

Diss. ETH No. 17529

Optimal Modulation and Wideband Current Sensing for Three-Level PWM Rectifiers

A dissertation submitted to the
ETH ZURICH

for the degree of
DOCTOR OF TECHNICAL SCIENCES

presented by

LUCA DALESSANDRO

M.Sc. El. Eng. Politecnico di Bari
born 29. April 1978
Italian citizen

accepted on the recommendation of

Prof. Dr. Johann W. Kolar, examiner
Prof. Dr. Paolo Mattavelli, co-examiner

2007

*To my parents and
my twin brother,*

for their love, support and guidance.

Quando mi diparti' da Circe,

[...]

né dolcezza di figlio, né la pieta
del vecchio padre, né 'l debito amore
lo qual dovea Penelopé far lieta,

vincer potero dentro a me l'ardore
ch'i' ebbi a divenir del mondo esperto,
e de li vizi umani e del valore.

Dante Alighieri, Inferno, Canto XXVI

When I escaped from Circe,

[...]

Nor fondness for my son, nor reverence
Of my old father, nor return of love,
That should have crown'd Penelope with joy,
 Could overcome in me the zeal I had
To explore the world, and search the ways of life,
Man's evil and his virtue.

Dante Alighieri, *Inferno*, Canto XXVI

© 2007

Luca Dalessandro
All Rights Reserved

Contents

Acknowledgments	1
Abstract	3
Kurzfassung	7
Sommario	11
1 Introduction	15
1.1 Background	15
1.1.1 Three-phase Power Factor Correction Circuits	15
1.1.2 Current Control Strategies	21
1.1.3 Current Sensor Technologies	28
1.1.4 Wide Bandwidth Operating Range	29
1.2 Motivation	31
1.3 Dissertation Objectives and Contributions	32
1.4 Publications	34
1.5 Selected Invited Lectures	35
1.6 Dissertation Organization	35
2 Pulse-Coordinated Decoupling Hysteresis Control	37
2.1 Introduction	37
2.1.1 Conventional Hysteresis Current Control	39
2.1.2 Conventional Carrier-based Current Control	40

2.2	Decoupling Hysteresis Control: Principle of Operation	42
2.2.1	High Frequency Injection	45
2.2.2	Low Frequency Control	46
2.2.3	Output Partial Voltages Balancing	49
2.2.4	Average Switching Frequency	51
2.3	Variable Hysteresis Band	52
2.4	Phase Switching Synchronization	55
2.5	Experimental Analysis	57
2.6	Conclusion	60
3	Center-Point Voltage Control	65
3.1	Introduction	65
3.1.1	Center-Point Voltage Balancing Methods	65
3.1.2	Effect of the Center-Point Current	67
3.2	Interdependence of AC-side and DC-side Controllers	68
3.3	Space Vector Analysis	73
3.3.1	Balanced Output Partial Voltages	73
3.3.2	Unbalanced Partial Output Voltages	75
3.4	On the Inherent Stability of the Center-Point	82
3.5	Impact of the Current Reference Offset	83
3.5.1	Effect of the Offset on Switching Frequency and on Center-Point Voltage Drift	83
3.5.2	Dependence of the Center-Point Current on the Current Reference Offset	84
3.6	Center-Point Voltage Control	88
3.6.1	Center-Point Characteristic	88
3.6.2	Design of the Center-Point Voltage Controller	90
3.6.3	Stationary Operation	92
3.6.4	Dynamic Operation	93
3.7	Conclusion	94
4	Discontinuous Space Vector Modulation	97
4.1	Introduction	97
4.2	Discontinuous Modulation Schemes	100
4.2.1	Space Vector Representation	101

4.2.2	Modulation Functions	106
4.3	Comparison of Continuous and Discontinuous Modulation Schemes	107
4.3.1	Calculation of Switching Frequency Increase	109
4.3.2	Impact of the Redundant Switching States Distribution on AC-side Currents	111
4.3.3	Impact of the Redundant Switching States Distribution on DC-side Currents	113
4.4	Experimental Verification	115
4.5	Discussion	121
4.6	Rectifier Loading Capability	123
4.6.1	Load on the Output Capacitors	125
4.7	Conclusion	129
5	HF Characterization of Magnetic Components	131
5.1	Introduction	131
5.2	The Capacitance-Permeance Analogy	133
5.2.1	Transformer Equivalent Circuit	134
5.2.2	Properties of the Equivalent Circuit	139
5.3	Core Material Characterization	140
5.3.1	Measurements of Complex Permeability	140
5.3.2	Prototype Construction	141
5.3.3	Winding Arrangement	141
5.3.4	Modeling the Nonlinear Magnetic Core	142
5.4	Empirical Characterization of the Current Transformer	147
5.4.1	Open Circuit Impedance	147
5.4.2	Transimpedance Gain	147
5.4.3	Magnetic Flux Distribution	150
5.5	High Frequency Effects	156
5.5.1	High Frequency Model of Ferrite Material	156
5.5.2	Magnetic Skin Depth and Dimensional Resonance	160
5.5.3	High Frequency Winding Resistance	169
5.5.4	Winding Losses	175
5.5.5	Losses in Magnetic Components	178
5.6	Conclusion	180

6	Electrostatic Analysis of Wound Ferrite Components	183
6.1	Introduction	183
6.1.1	Calculation Approaches	184
6.1.2	Assumptions	184
6.2	Basic Cell for the Capacitance Calculation	186
6.2.1	Transformer Characteristics	186
6.2.2	Single-Turn Capacitance	188
6.2.3	Basic Cell: Turn-to-Turn Capacitance	190
6.3	Influence of the Core on the Electric Field Distribution	192
6.4	Capacitance of the Secondary Winding	196
6.4.1	Single Layer Capacitance	196
6.4.2	Layer-to-Layer Capacitance	198
6.4.3	Effect of the Connection Between Adjacent Layers	200
6.4.4	Effect of the Voltage Ratio and Spacing Between Adjacent Layers	202
6.5	Capacitance towards Screen	204
6.6	Experimental Results	207
6.7	Conclusion	214
7	Isolated Planar DC Current Transformer	217
7.1	Introduction	217
7.2	Principle of Operation	219
7.2.1	Ideal Sensor	220
7.2.2	Real Sensor	224
7.3	Realization of the Prototype	226
7.4	Experimental Results	230
7.4.1	Current Step Response	230
7.4.2	Core Saturation	230
7.4.3	dv/dt Immunity Test	234
7.5	Conclusion	235
8	Conclusion	237
8.1	Dissertation Summary	237
8.2	Dissertation Conclusion	239

8.3 Recommendations for Future Work	241
Bibliography	242
Appendix	243
A.1 Switch Signal and Input Rectifier Voltage for the First Sector . . .	243
A.2 Space Vectors Duty Cycle Calculation for the First Sector	244
A.3 Switching Loss Calculation	246
A.4 Output Capacitors rms Current	247
A.5 FEM Formulation in Terms of Weighted Residuals	249
Curriculum Vitæ	267

Acknowledgments

First and foremost, I would like to thank my *Doktorvater*, Professor Johann W. Kolar. He made my ETH experience unique by welcoming me into an unsurpassed academic environment, by offering me such exciting research topics and providing me with excellent guidance while leaving at the same time independence. I will be forever thankful for his confidence and trust in me, for his continuous support and for the priceless opportunity to work in one of the most celebrated and leading research groups.

My gratitude extends to the other Member of my Thesis committee, Prof. Paolo Mattavelli of the University of Padova, Italy. I really appreciated his interest in this work and his kindness to review and referee this Dissertation.

I would like to quote at this point my previous supervisor, Prof. Antonio DeSimone, who *discovered* me in the past 1999 and to whom I am eternally grateful. Among the many precious pieces of advice which he gave me, he mentioned once that the *acknowledgements* can become somehow the most important part of a Thesis, for both writer and reader. One can risk to spend quite some time to write them down (or perhaps to read them as well) ... Well, from my side, I confess: I've spent more time on this section than expected!

I owe so much to many great individuals I have met during the last four years; I will try to mention them all.

I am particularly indebted to my colleague and friend, Dr. Nico Karrer for his continuous guidance and encouragement. Since the very beginning of my PhD, I had the priceless opportunity to benefit of the experience and the encyclopedic knowledge of Nico in current measurements and electrical engineering in general. Thank-you for your great advice, for your illuminating discussions and of course for your friendship!

A special mention and note of appreciation goes to Prof. Hardus Odendaal, who played an important, influential role in my education. I had the honour and pleasure of meeting him at a very delicate moment of my PhD, at which point he was kind enough to support me in my research. I admire and I am indebted to Dr. Odendaal for his ideas, for the many fruitful discussions, for his

Acknowledgments

patience and kindness, and for his bright eloquence.

My academic formation has been greatly influenced and enriched by my colleague, mentor and friend, Prof. Avijit Mukherjee. Thank-you for your many pieces of advice, for your overwhelming generosity and precious guidance.

It has been a great pleasure and honour working and collaborating with Dr. Simon Round, whose guidance and friendship I acknowledge.

I have been pleased and lucky to share the office (ETL I14) with very special colleagues. I thank Patrick Furrer, Chuanhong Zhao, Fabiana Cavalcante and John Schönberger for the great time and for their friendship. My gratitude extends to all my colleagues of the Institute, for their friendship and conversations, all which made the time at the PES Laboratory more enjoyable.

I also owe a lot to the many students who I have supervised or that have been helping me in the teaching activity. They have been a continuing source of motivation and enthusiasm for me. A special mention goes to my *historical* PPS Assistants, with whom I spent four years of my PhD coordinating: Matthias Grüetter, Thomas Kaufmann, Simon Mall, Lukas Bolliger, Philipp Simka and Patrick Bichsel.

I would like to acknowledge the support of the Staff of the Power Electronics System Laboratory of the ETH: Dr. Beat Seiler, the secretaries, Gabriela Spek-Fey, Roswitha Coccia-Kunz and Prisca Maurantonio, and the technicians Markus Berger, Peter Albrecht, Peter Seitz and Hansueli Altdorfer. I would also express a kind thought for Joachim Bazali, a former *Oberassistent* at the Institute.

I wouldn't have been able to keep my good mood and a sane equilibrium between work and private life without my wonderful friends in Zurich: Júlia Relat, Alessia Neuronì, Blanca Serda, Remo Sigrist, Xavier Calderon and Hardy Happle. I also extend my gratitude towards my relatives in Zurich, zia Pina and Luciano. You made me feel like I was almost living at home.

Thanks for the friendship and the great time to Boris Grbić and Daniel Trzesianiak. You have been most excellent traveling companions on this PhD journey, which we all started together on the 2nd of September, 2002.

I would like to manifest my deepest gratitude and affection to my wonderful parents, Michele and Letizia, for their unconditional love and for their overwhelming support. Without their exemplary guidance or the precious harmony of our family, I would have never been able to keep my serenity, to achieve many goals and to even realize this work that I uniquely devote to you, as a very little sign of my love for you.

Finally, my greatest appreciation and admiration is for my twin brother, Dr. Antonio; for his immense affection and loyalty as a friend, for his exceptional strength and perseverance as a crew-mate, for his bright intelligence and creativity as an advisor and visionary for many projects and publications. I owe you much more than words can ever express.

Abstract

For high power three-phase rectifiers the use of unity power factor control is becoming an industrial requirement. In particular, multilevel voltage-source-rectifiers are of special interest as they offer reduced input current ripple and lower switching device blocking voltages. Besides the advantages related to the converter's topology, further improvement of the overall system performance, in terms of efficiency and realization effort, depends on the modulation strategy employed. Furthermore, high switching frequency is desirable to increase the power density and to improve current control dynamic performance. While a switching frequency of few kHz is sufficient in most inverter applications, a PFC converter is operated at higher frequency, e.g., 20-200 kHz in the kilowatt power range. Thus, a wide current sensor bandwidth is required and more important for PFC circuits than for inverters.

With this scenario, the Dissertation deals in its first part with innovative and optimal modulation strategies for three-phase three-level PWM rectifiers. Both direct and indirect methods are considered and the advantages and drawbacks of conventional techniques critically presented. The novel current control concepts are based on decoupling hysteresis current control and voltage oriented control (Space Vector Modulation), respectively.

The design of a high-performance current sensor is addressed in the second part of this Dissertation. Current sensor technologies are reviewed and the sensor's design parameters that facilitate broadband performance are analyzed. Since the current sensor proposed has a current transformer as the main sensing device, the frequency-dependent characteristics of ferrite wound components are analyzed in detail.

The contribution presented for the direct modulation deals with a hysteresis current control concept for three-phase three-level PWM rectifiers based on a virtual connection of the output center point and the mains star point and achieves a decoupling of the three phases. This control technique, named Decoupling Hysteresis Control, besides having the advantages of a classical hysteresis

control, provides a more regular switching of the power transistors and an intrinsic stability of the output center point voltage, and allows a full utilization of the modulation range. Furthermore, a pre-control and synchronization signal for the hysteresis band is implemented to obtain coordinated switching between the phases and results in a near constant switching frequency and a current ripple performance that is similar to conventional carrier-based PWM controllers. These modulation strategies have been verified on a 5 kW *Vienna Rectifier*.

The presented technique to balance the output center-point voltage of a hysteresis current-controlled three-level PWM rectifier is based on adding an offset to the input current-reference. It is shown that the strategy of augmenting the current reference by an offset in direct (hysteresis) modulated three-level rectifiers is equivalent to the utilization of the redundant switching-states in indirect (voltage-oriented) PWM modulation. The space-vector representation of the input rectifier voltage and current is chosen to explain the effect of the current-offset injection on the output center-point voltage. The influence of the offset-current injection on the mains currents as well as the control and center-point characteristics are analyzed and verified by measurements.

A further new contribution of the Dissertation is the implementation and experimental verification of two discontinuous pulse-width modulation (DPWM) methods for three-phase, three-level rectifiers. DPWM's features, such as improved waveform quality, lower switching losses, reduced AC-side passive component size, are investigated and compared to the conventional continuous pulse-width modulation (CPWM). These features allow higher power density and/or efficiency to be achieved and are important targets for the next generation of power rectifiers. The implementation of the two DPWM strategies is explained by means of a space-vectors representation and modulation functions. The analysis of the center point loading capability and of the interdependence of AC-side and DC-side optimal PWM controllers is presented.

The design of a high-performance current sensor, to which is devoted the second part of the Dissertation, is presented as the result of a detailed analysis of the frequency dependent characteristics of ferrite wound components, which enhance broadband performance.

A permeance model of the core is implemented to model the magnetic circuit. The model includes a linear lumped element equivalent circuit to approximate the non-linear complex permeability of the core, which was measured empirically. The measured and simulated results of open-circuit impedance from the secondary winding and the transimpedance gain of the current sensor are compared and discussed. The flux distribution within the ferrite is modeled using the electromagnetic wave propagation theory and the dimensional resonance effect is explained. Derivations for the losses in the core and in the winding are included. A review of the literature dealing with the calculation

of the frequency-dependent winding resistance is presented and the winding impedance for the case study is calculated by a modified Dowell formula.

Particular emphasis is given to the calculation of transformer's parasitics, in particular of its self capacitance, which is a fundamental step for predicting the frequency behavior of the device, to reduce the capacitance's value and moreover for more advanced aims of capacitance integration and cancellation. A comprehensive procedure for calculating all contributions to the self-capacitance of high-voltage transformers is presented, as well as a detailed analysis of the problem, based on a physical approach.

Finally, a novel, planar current sensor, comprised of a magnetic current transformer and a Hall-effect element is presented. The sensor has a broad frequency bandwidth from DC up to 30 MHz, a high current rating (40 A DC), superior linearity, high EMI immunity, small size, robustness and low realization cost. The main design formulations are given analytically; simulations and finite element results are presented for verification. Experimental results of current step response and dv/dt immunity are included.

Kurzfassung

Für leistungselektronische Dreiphasen-Gleichrichtersysteme ist in der Industrie zunehmend der Einsatz von Leistungsfaktorkorrektur-Schaltungen erforderlich. Besonders Multilevel-Spannungsgleichrichter sind von besonderem Interesse, da diese eine geringere Eingangsstromwelligkeit und niedrigere Sperrspannungen der Schalter aufweisen. Allerdings hängt die Systemperformance hinsichtlich Wirkungsgrad und Realisierungsaufwand in hohem Mass von der angewandten Modulationsstrategie ab. Daher beschäftigt sich der erste Teil der vorliegenden Dissertation mit innovativen, optimalen Modulationsstrategien für dreiphasige Drei-Level PWM-Gleichrichter. Dabei werden sowohl direkte als auch indirekte Modulationsmethoden betrachtet und die Vor- und Nachteile gegenüber konventionellen Techniken aufgezeigt.

Um die Leistungsdichte von Gleichrichtersystemen zu erhöhen und das dynamische Verhalten der Stromregelung zu verbessern, sind generell hohe Schaltfrequenzen erstrebenswert. Während für die meisten Motor-Umrichter eine Schaltfrequenz von einigen Kilohertz ausreichend ist, wird ein Konverter mit Leistungsfaktorkorrektur (PFC) im Kilowattbereich typischerweise mit 20-200 kHz betrieben. Aus diesem Grund wird eine grosse Bandbreite der für die Regelung notwendigen Stromsensoren benötigt. Der zweite Teil dieser Dissertation widmet sich daher der Analyse und dem Design eines breitbandigen Stromsensors. Dabei werden unterschiedliche Stromsensortechniken untersucht und die Designparameter für die Stromsensoren, welche die Messbandbreite bestimmen, analysiert. Da der vorgeschlagene Stromsensor als Hauptkomponente einen Stromtransformator besitzt, werden die frequenzabhängigen Charakteristika von bewickelten Ferritelementen detailliert analysiert.

Der Beitrag zur direkten Modulationsmethode im ersten Teil der Arbeit befasst sich mit einem Hysteresestrom-Regelungskonzept für dreiphasige Drei-Level-PWM-Gleichrichter und basiert auf einer virtuellen Verbindung des Ausgangsmittelpunktes zum Netzsternpunkt. Dadurch wird eine Entkopplung der drei Phasen erreicht. Diese Regelungsmethode wird als *Decoupling Hystere-*

sis Control (Entkoppelte Hystereseregung) bezeichnet. Sie besitzt die Vorteile einer klassischen Hystereseregung, bietet jedoch zusätzlich den Vorteil nahezu konstanter Schaltfrequenz der Leistungstransistoren, eine inhärente Stabilität der Ausgangsmittelpunktspannung und erlaubt die vollständige Nutzung der Modulationsbreite. Um ein koordiniertes Schalten zwischen den Phasen und somit eine nahezu konstante Schaltfrequenz zu erhalten, wird ein Vorregelungs- und Synchronisationssignal implementiert. Die resultierende Stromwelligkeit ist vergleichbar mit konventionellen Trägersignal-basierten PWM Regelungen. Diese Modulationsstrategien werden an einem 5 kW *Vienna*-Gleichrichter experimentell nachgewiesen.

Im darauffolgenden Teil wird eine Technik zum Abgleich der Ausgangsmittelpunktspannung eines Hysteresestrom-geregelten Drei-Level PWM-Gleichrichters durch Hinzufügen eines Offsets zur Eingangsstromsreferenz vorgestellt. Es wird gezeigt, dass diese Strategie in direkten (Hysteres-) modulierten Drei-Level-Gleichrichtern gleichbedeutend mit der Verwendung von redundanten Schaltzuständen bei der indirekten (spannungsorientierten) PWM-Modulation ist. Die Raumzeigerdarstellung der Eingangsgleichrichter-Größen (Spannung und Strom) wird zur Erklärung der Auswirkung des Stromoffsets auf die Ausgangsmittelpunktsspannung gewählt. Der Einfluss des Stromoffsets auf den Netzstrom, ebenso wie die Regelung und die Mittelpunktcharakteristik werden analysiert und durch Messungen verifiziert.

Anschließend werden zwei diskontinuierliche pulswidenmodulierte (DPWM) Methoden für dreiphasige Drei-Level-Gleichrichter implementiert und experimentell untersucht. Die Besonderheiten der DPWM, so wie zum Beispiel veringertes Strom-Oberwellenanteil, geringere Schaltverluste und geringere Komponentengröße der netzseitigen, passiven Elemente werden untersucht und mit der konventionellen kontinuierlichen Pulsweitenmodulation (CPWM) verglichen. Diese Eigenschaften erlauben sowohl eine höhere Leistungsdichte als auch einen besseren Systemwirkungsgrad, was wichtige Ziele für die zukünftige Generation von leistungselektronischen Gleichrichtersystemen sind. Die Implementierung der zwei DPWM-Strategien wird mittels Raumzeigerdarstellung und Modulationsfunktionen erklärt. Abschliessend werden die Belastungsfähigkeit des Mittelpunktes und die Unabhängigkeit von Gleichspannungs- und Wechselspannungsseite der optimalen PWM-Regler analysiert.

Der zweite Teil der Dissertation ist der detaillierten Analyse der frequenz-abhängigen Charakteristika von bewickelten Ferritkomponenten und dem Design eines breitbandigen Hochleistungsstromsensors gewidmet. Zunächst wird ein Permanenzmodell des Kerns entwickelt, um den magnetischen Kreis zu modellieren. In diesem Modell sind die Ersatzschaltbilder mit linear konzentrierten Elementen enthalten, um die nichtlineare komplexe Permeabilität des Kerns zu approximieren, welche empirisch gemessen wurde. Die gemessenen

und simulierten Ergebnisse der Leerlaufimpedanz der Sekundärwicklung und die Transferimpedanz-Verstärkung der Stromsensoren werden verglichen und diskutiert. Die Flussverteilung im Ferrit wird unter Verwendung der elektromagnetischen Wellenausbreitungstheorie modelliert und das Ausmass der Resonanzeffekte erläutert. Zusätzlich werden die Verluste im Kern und in den Windungen hergeleitet. Ein Überblick über die Literatur zur Berechnung des frequenzabhängigen Wicklungswiderstandes wird präsentiert und die Wicklungsimpedanz wird für den vorliegenden Fall mit einer abgewandelten Dowell-Formel berechnet.

Ein besonderer Schwerpunkt wird auf die Berechnung der parasitären Eigenschaften des Transformators gelegt, vor allem der Eigenkapazität. Dies stellt eine wichtige Grundlage zur Vorhersage des Frequenzverhaltens des Bauteils dar, sowie zur Reduktion des Kapazitätswerts, wie auch zur Integration und auch Auslöschung der Kapazität. Es wird eine umfassende Prozedur zur Berechnung aller Anteile der Eigenkapazität von Hochspannungstransformatoren vorgestellt, ebenso wie eine detaillierte Analyse des Problems, basierend auf physikalischen Methoden.

Zum Abschluss wird ein neuer, planarer Stromsensor präsentiert, der einen magnetischen Stromtransformator und ein Halleffektelement beinhaltet. Der Sensor hat eine Bandbreite vom Gleichstrombereich bis zu Frequenzen von 30 MHz, eine hohe Strombelastbarkeit (40 A Gleichstrom), ausgezeichnete Linearität, hohe Robustheit gegenüber elektromagnetischer Störbeeinflussung, eine geringe Grösse, eine hohe mechanische Robustheit und geringe Herstellungskosten. Das Design wird analytisch erarbeitet und Ergebnisse aus Simulationen und Finite-Elemente-Berechnungen werden als Bestätigung präsentiert. Abschliessend wird das Design mittels experimenteller Ergebnisse der Stromsprungantwort und der dv/dt -Störfestigkeit bestätigt.

Sommario

Il fattore di potenza unitario per i raddrizzatori trifase e' oggi un requisito per le applicazioni industriali. Le topologie di raddrizzatori a piu' livelli di tensione sono di particolare interesse, in quanto offrono una migliore qualita' delle forme d'onda della corrente lato rete ed una ridotta tensione di blocco sui dispositivi semiconduttori. L'esercizio del raddrizzatore, in termini di efficienza e costi d'implementazione, dipende non solo dalla scelta opportuna della topologia, ma puo' essere migliorato a seconda della tecnica di controllo della corrente che si implementa. Inoltre, un'elevata frequenza di commutazione e' opportuna per aumentare la densita' di potenza e per migliorare la dinamica del sistema di controllo. Se una frequenza di commutazione di pochi kHz e' sufficiente per la gran parte delle applicazioni di invertitori, un convertitore che effettua la correzione del fattore di potenza (PFC) e' di solito operato a piu' elevate frequenze, ad esempio 20-200 kHz per potenze dell'ordine dei kW. Pertanto, l'impiego di un sensore di corrente con larga banda passante e' piu' importante per un circuito PFC che per un invertitore.

Con queste premesse, la presente Dissertazione tratta nella prima parte tecniche innovative ed ottimizzate di modulazione per raddrizzatori trifase a tre livelli. Sono stati esaminati sia i metodi diretti di modulazione che quelli indiretti; inoltre i vantaggi e gli svantaggi delle tecniche convenzionali di controllo sono discussi. Le nuove strategie di modulazione sono basate sul controllo ad isteresi *disaccoppiato* e sulla modulazione dei vettori di spazio.

La seconda parte della Dissertazione e' dedicata alla progettazione di un sensore di corrente a banda larga. Le tecnologie per la misura di corrente sono rivisitate ed i parametri progettuali, che consentono di estendere la banda di frequenza, sono analizzati. Poiche' il sensore di corrente proposto ha un trasformatore di corrente come dispositivo di misura principale, le caratteristiche dipendenti dalla frequenza dei dispositivi magnetici *avvolti* su nucleo di ferrite sono analizzate in dettaglio.

Il contributo presentato per la modulazione diretta riguarda un metodo

di controllo ad isteresi per raddrizzatori trifase a tre livelli che si basa sulla connessione virtuale del terminale centrale dell'uscita a tre livelli e del neutro della rete d'alimentazione. Questa tecnica di modulazione, denominata Controllo ad Isteresi Disaccoppiato, conserva i vantaggi della classica modulazione ad isteresi, ed in piu' garantisce una piu' regolare frequenza di commutazione ed una intrinseca stabilita' della tensione del terminale centrale in uscita, ed inoltre la completa utilizzazione dello spettro di modulazione. Inoltre, un segnale pre-controllo e di sincronizzazione che va ad aggiungersi alla banda di isteresi e' stato implementato per ottenere la commutazione coordinata delle tre fasi, risultando in una quasi costante frequenza di commutazione ed in oscillazioni della corrente lato rete paragonabili a quelle ottenibili dai convenzionali controllori a rampa. Queste tecniche di modulazione sono state verificate su un raddrizzatore trifase *Vienna* di 5 kW.

La tecnica presentata per controllare la tensione del morsetto centrale (lato carico DC) per un raddrizzatore trifase a tre livelli controllato ad isteresi, e' basata sull'aggiunta di un offset al segnale di riferimento per la corrente lato rete. Viene dimostrato che, per un raddrizzatore modulato in maniera diretta (modulazione ad isteresi), la strategia di aggiungere al segnale di riferimento un opportuno offset, e' equivalente all'uso degli stati di commutazione ridondanti nelle tecniche di modulazione indiretta. La rappresentazione della tensione e della corrente d'ingresso del raddrizzatore mediante vettori di spazio, e' utilizzata per spiegare l'effetto dell'offset sulle variazioni della tensione del punto centrale dell'uscita. L'influenza dell'offset sulla corrente lato rete e le caratteristiche di controllo sono analizzate e verificate sperimentalmente.

Un ulteriore contributo della Dissertazione riguarda l'implementazione e la verifica sperimentale di due strategie di modulazione discontinua per raddrizzatori trifase a tre livelli. Le caratteristiche della modulazione discontinua quali la migliore qualita' della corrente lato rete, le ridotte perdite di commutazione, la ridotta dimensione dei componenti passivi lato rete, sono investigate e confrontate con la convenzionale tecnica di modulazione continua. Queste caratteristiche consentono di aumentare la densita' di potenza e l'efficienza, che sono obiettivi importanti per la prossima generazione di raddrizzatori di potenza. L'implementazione di due strategie di modulazione discontinua e' spiegata per mezzo della rappresentazione tramite vettori di spazio e delle funzioni di modulazione. L'analisi della capacita' di carico del punto centrale d'uscita e della mutua dipendenza dei controllori lato rete e carico sono anche presentate.

La progettazione di un sensore di corrente con elevate prestazioni tecniche, a cui e' incentrata la seconda parte della Dissertazione, e' presentata quale il risultato di una dettagliata analisi di tutti quei parametri dipendenti dalla frequenza che consentono di estendere la banda d'esercizio.

Un equivalente circuitale basato sull'analogia tra capacita' e permeanza e'

utilizzato per modellare il circuito magnetico. Il modello comprende un circuito equivalente che approssima la permeabilità complessa non-lineare del materiale del nucleo, che è stata anche misurata. I risultati simulati e misurati dell'impedenza secondaria e della funzione di trasferimento sono confrontati e discussi. La distribuzione del flusso all'interno del nucleo è modellata utilizzando la teoria della propagazione delle onde elettromagnetiche e gli effetti dimensionali sono spiegati. Le formulazioni delle perdite nel nucleo e degli avvolgimenti sono incluse nel capitolo. Una revisione dei contributi fondamentali in letteratura relativi al calcolo della resistenza dell'avvolgimento ad alte frequenze è presentata e l'impedenza d'avvolgimento per il caso-studio analizzato è calcolata mediante una formula di Dowell modificata.

Particolare enfasi è conferita al calcolo dei parametri parassiti di un trasformatore ed, in particolare, della sua capacità parassita. Tale calcolo è fondamentale per predire il comportamento in frequenza del dispositivo, per ridurre il valore della capacità parassita ed inoltre per scopi più avanzati di integrazione o cancellazione della capacità. Una procedura completa per calcolare tutti i contributi che costituiscono la capacità parassita di un trasformatore di alta tensione è presentata, così come una dettagliata analisi del problema, basata su un approccio fisico.

Infine, un nuovo sensore planare, costituito dalla combinazione di un trasformatore di corrente e di un sensore Hall è presentato. Il sensore ha ampia banda in frequenza da DC fino a 30 MHz, elevata portata (40 A DC), comportamento lineare, alta immunità elettromagnetica, ridotte dimensioni, compattezza e basso costo realizzativo. Il principio operativo è spiegato analiticamente; simulazioni e risultati FEM sono presentati come verifica. I risultati sperimentali di risposta all'impulso e di immunità ad elevati dv/dt sono inoltre mostrati.

Chapter 1

Introduction

"Is there, I ask, can there be,
a more interesting study than
that of alternating currents?"

Nikola Tesla

1.1 Background

1.1.1 Three-phase Power Factor Correction Circuits

Electricity is typically generated and distributed in the form of alternating currents (AC) yet most of the electronic devices and many industrial applications require direct current (DC) to operate. The need of AC to DC conversion was the birth of modern solid-state power electronics in the 1940's and 1950's. The first components that signaled the era of rectification were the selenium diodes, and then the progress in the rectification technology has been driven by the appearance of successive generations of controllable semiconductor devices [1]; beginning with the point-contact transistor by the Bell-Labs in the 1948, followed in 1951 by the junction transistor, the MOSFET (Metal Oxide Semiconductor Field Effect Transistor) in the 1960's, the insulated gate bipolar transistors (IGBT) in the 1980's and recently the Silicon Carbide (SiC) devices [2], [3]. These latter power semiconductor devices are capable of being operated at higher voltages, frequencies and temperatures than silicon power devices [4]. Thus, the latest switches technologies have gradually taken over more and more of the applications and power ratings previously dominated by silicon controlled

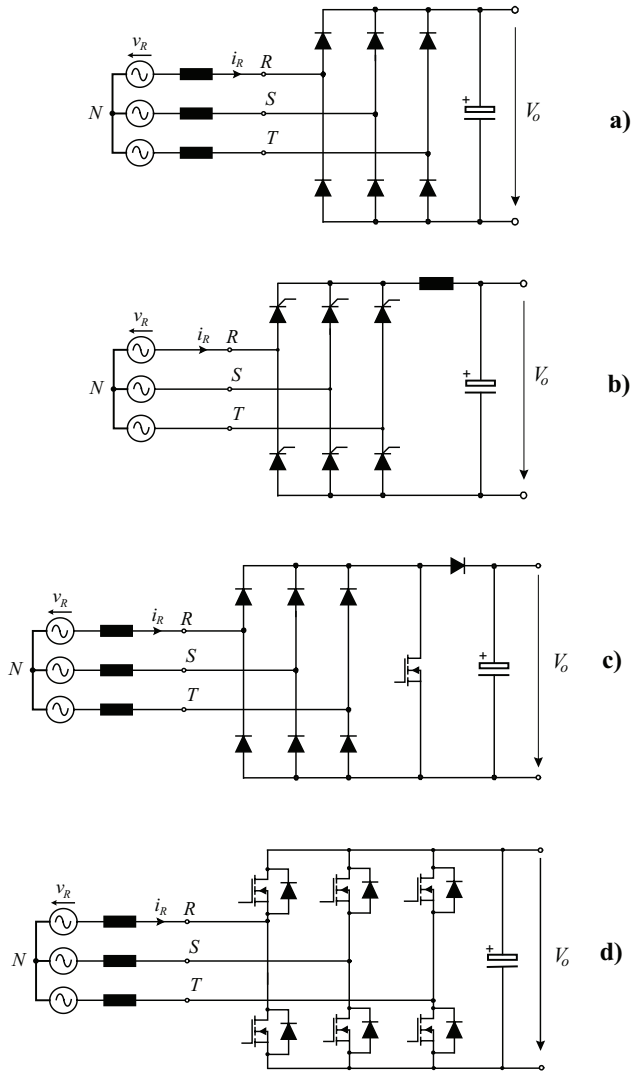


Figure 1.1: Conventional rectifier systems: (a) line commutated diode bridge, (b) thyristor bridge, (c) DCM boost rectifier, and (d) voltage source, boost-type two-level PWM rectifier.

rectifiers (SCRs) and gate turn-off thyristors (GTO - firstly developed by the GE company in 1958). The improvements in semiconductor technology, which offer higher voltage and current ratings as well as better switching characteristics, have allowed the growth and the expansion of application areas of power converters.

Although nowadays there exists more than in the past a large availability of power switches and key systems components, the challenge of rectification technology is to install the most suitable and reliable system architecture for the specific application.

The earliest three-phase rectifier architectures were constituted by line commutated rectifiers or diode bridges. They are usually supplied by an inductive AC source and drive a voltage-type load [5]. They have found extensive applications and often occur as interface in battery charger/power supply systems, such as employed in automotive (for inst. as interface of a Lundell alternator [6]) and aerospace applications. Three-phase diode bridge rectifiers have the disadvantages of lagging displacement factor with respect to the voltage of the utility (hence consumption of reactive power for large AC side inductors) and generate odd non-triplen harmonics (5th, 7th, 11th, 13th, ...) in the AC line current.

More advanced rectification technology is constituted by the line commutated controlled rectifiers or *thyristor rectifiers* which allows the control of the DC output by delaying the firing current pulse applied at the gate terminal of the thyristors. The most common topology is shown in Fig. 1.1.b, in which the six diodes of Fig. 1.1.a are replaced by Silicon Controlled Rectifiers (SCRs). A conventional and important application for thyristor rectifiers is found in machine drives, for controlling the torque and the speed of a DC motor by the firing angle of the thyristors. However, also this latter category of rectifiers suffer the same disadvantages of a diode bridge, as concerns the poor quality of the input currents.

A great improvement in the performance of the diode rectifier was obtained by adding the classical self commutated topology an active power factor correction stage [7]. The obtained *single-switch rectifiers* feature approximately sinusoidal input currents, resistive mains behavior and controllability of the output DC voltage. In Fig. 1.1.c a three-phase single-switch *boost-type* rectifier is shown [8]; similarly, there exists also the *buck-type* realization of the rectifier.

However, the use of a PFC stage increases the number of switching devices, which results in a higher failure rate and mean time to repair (MTTR). Although the diode and thyristor bridge offer a high reliability, there are problems associated with their inability to control the non-sinusoidal input currents, which are responsible for harmonic distortion in the utility.

In this scenario, active rectifier technology is the most promising technology from a power quality viewpoint and valid competitor for traditional solutions such as diode and thyristor bridges. A conventional six-switch three-phase

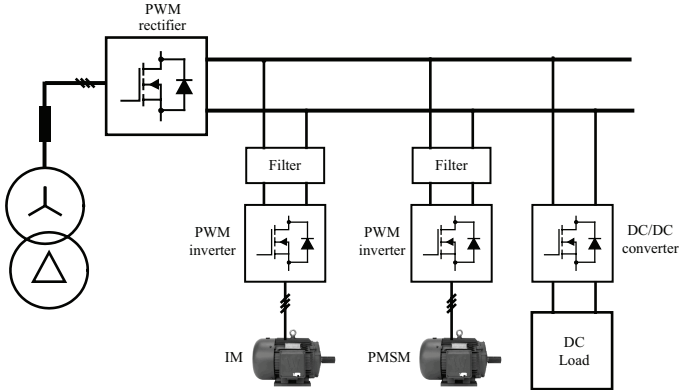


Figure 1.2: DC Distributed Power System.

pulsewidth-modulated (PWM) rectifier is shown in Fig. 1.1d. Active rectification is a more interesting solution for industrial applications due to advantages such as:

1. low harmonic distortion of line current;
2. power factor correction (PFC) capability ($\cos\varphi=1$) and, in particular, regulation of input power factor to unity; [9];
3. adjustment and stabilization of DC-link voltage;
4. reduced size of the passive components, in particular of the AC side boost inductors and the DC filter capacitor size;
5. possibility of bidirectional power flow.

Active rectifiers are now in use as standard products for both low- and medium-voltage applications. Particularly voltage source rectifiers (VSRs), employing pulse width modulation, are the widest used power converters for applications within:

1. telecommunication power supply systems;
2. electrical drives [9];
3. welding power supplies;
4. uninterruptible power supplies (UPS);
5. air conditioning and ventilation;
6. battery chargers;

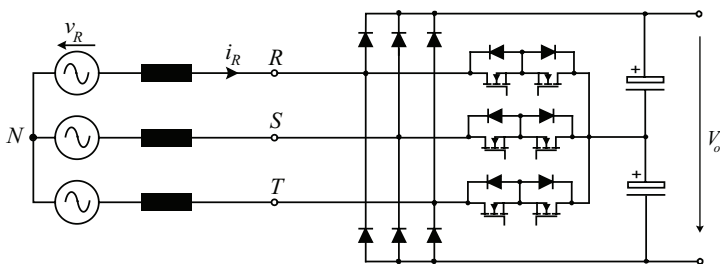


Figure 1.3: Three-phase, three-level, PFC low-frequency PWM rectifier for high power applications [10].

7. distributed power systems (DPS) [11];
8. aircraft power supplies [12];

For instance, a multisection AC drive system (cf. Fig. 1.2) typically uses a DC bus supply that is common to multiple inverters. AC/DC converters using thyristors for this common DC supply have the following inherent drawbacks: the power factor decreases when the gate firing angle increases and the size of the AC-side filter circuits becomes bulky, since the content of harmonics of the line current is relatively large.

PWM rectifiers are applied by most global companies within AC/DC/AC converters (back-to-back) or DC distributed power systems (Fig. 1.2). Furthermore, thanks to advances in power semiconductor devices and digital signal processors, it is possible to implement sophisticated control algorithms which allow fast operation and cost reduction. Appropriate control can provide both the rectifier performance improvements, in terms of efficiency and reliability, and reduction of the filtering effort [14].

Although active rectifiers are commonly used for both low- and medium-voltage applications, this technology is currently not common for high-power rectifier applications, partly due to the unavailability of suitable cost-effective power electronic devices. Nevertheless, due to the regulations mandating and recommending low-harmonic equipment (IEEE 519-1981, IEC 61000-3-2, IEC 61000-3-4) and in view of the advantages in terms of controllability, active PWM rectifiers represent the future also for high-power applications. As the voltage and current ratings and switching characteristics of power semiconductor devices are steady improving, hence the range of applications will continue to expand in areas such as power supplies for motion control, multi-megawatt industrial drives, and electric power transmission and distribution.

An example of a high-power three-level rectifier is shown in Fig. 1.3 [10]. This unit is modulated at low frequency [15] and it is used as low-cost front-end

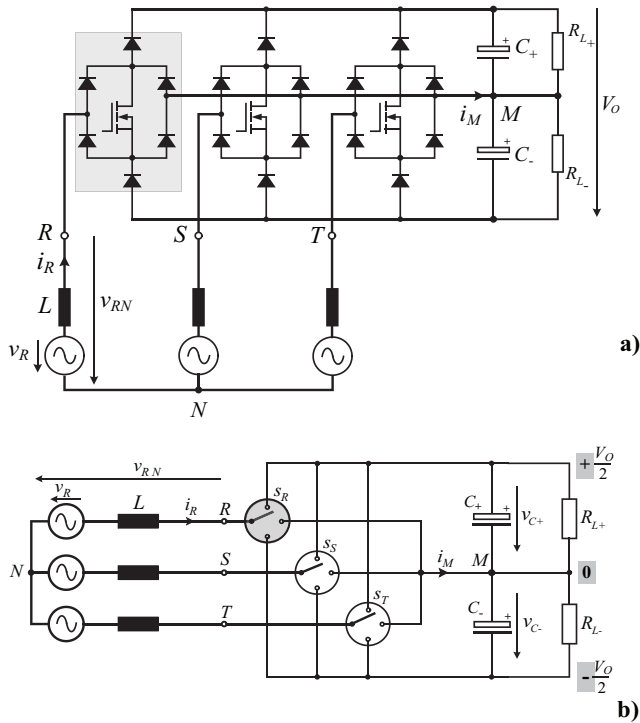


Figure 1.4: a) Power circuit of a three-phase, three-level, *Vienna* rectifier [13] and b) simplified model of a three-level rectifier. The clamping of an input rectifier phase-terminal to the positive or negative bus occurs when the switch is off and the input current flows through the upper or lower diodes to the output bus.

PFC circuit for high-power applications. In Fig. 1.4 is represented a boost-type, three-phase, three-switch, three-level PWM *Vienna* Rectifier and its simplified equivalent circuit model.

Multilevel Voltage Source PWM Rectifiers (VSR) are of particular interest for future high power applications [16]. They typically synthesize a staircase voltage wave from several levels of DC capacitor voltage and they are able to produce current waveforms with lower harmonic content than conventional two-level topologies. Fig. 1.5 shows the input rectifier voltage for a three-level rectifier. A major advantage of the converter for high voltage application is the reduced DC

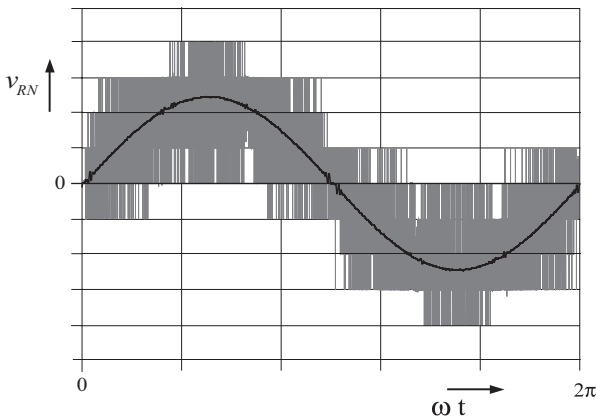


Figure 1.5: Simulation of the pulsewidth-modulated, input rectifier phase voltage referred to the mains star point and normalized over $\frac{V_0}{6}$ for a three-level PWM rectifier. This voltage and the mains supply voltage provide sinusoidal guidance to the input rectifier current.

maximum voltage applied to the switching devices. However a further effort in the unit control is required since the voltage at the midpoint of the bus-splitting capacitors needs to be regulated.

For the sake of completeness, it should be mentioned that the power factor correction can be achieved not only by a forced commutated (active) PWM rectifier, but also by means of three-phase *passive* circuits, based on multi-phase transformer or autotransformer-based diode rectifiers, and by *hybrid* solutions, like the *Minnesota* rectifier [17], based on the principle of harmonic injection [18] (cf. Fig. 1.6).

1.1.2 Current Control Strategies

Due to their key role for feeding variable speed AC motors, the current control strategies for PWM voltage source inverters have received a great deal of attention in the last three decades and they have been the subject of numerous publications [19, 20]. The current control techniques have been compared with emphasis on their performance in steady-state and in transient conditions and to the switching frequency.

On the other hand, most of the current control techniques proposed for voltage source rectifiers have been borrowed from the drives technology, since it is a quite straightforward approach due to the many analogies between inverters

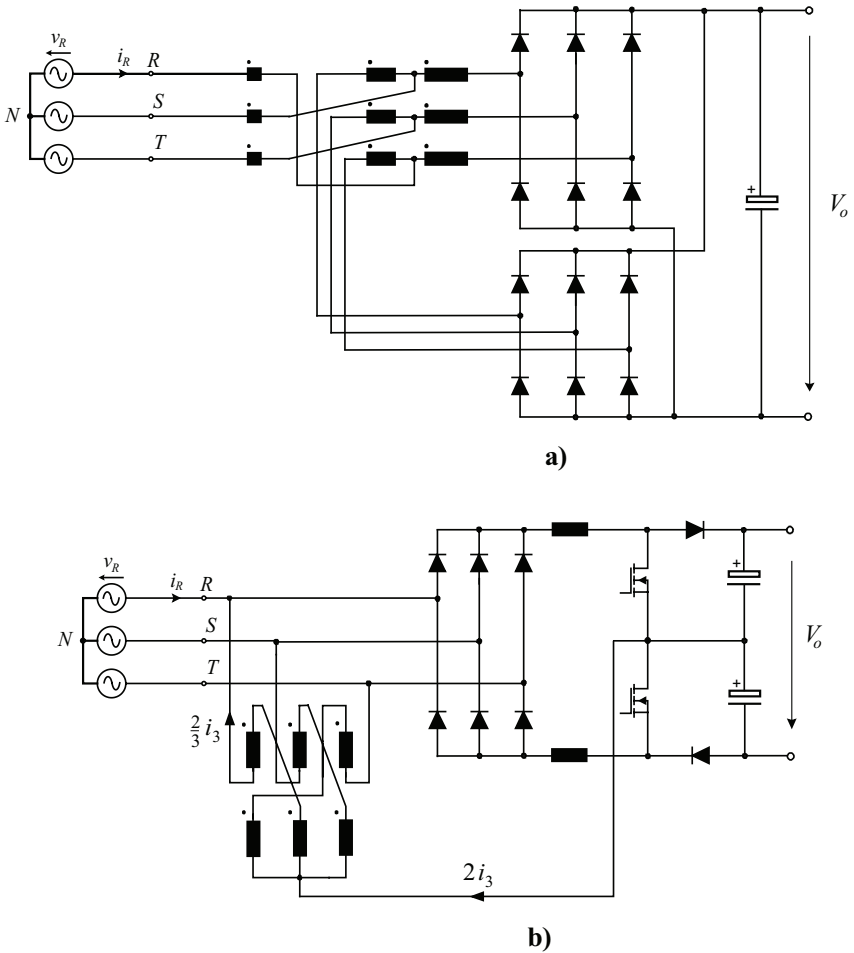


Figure 1.6: Three-phase rectifiers with low effect on the mains: a) Passive (12-pulse rectifier) and b) hybrid (*Minnesota* [17]) three-phase power factor correction circuits.

and rectifiers. Nevertheless, the application of the control strategy for a rectifier unit is not an immediate task but can only be performed after a careful evaluation and a thorough review of all critical requirements for the optimal operation of the rectifier. The main differences between rectifiers, and in particular PFC

circuits, and inverters deal with the following issues:

1. The quality of the input current, usually measured by the *input current total harmonic distortion* (THD), is an important requirement for the rectifier in order to reduce the pollution to the utility. The restriction to impose to the THD (typically limited $< 5\%$) makes the control design of a rectifier more critical than in inverters.
2. The electromagnetic interference (EMI) emissions are a great concern in PFC applications. The high-speed switching action of a PFC converter generates both differential mode and common-mode noise at the input and output of the PFC at high frequencies. The assessment of the common (CM) and differential (DM) radiated and conducted emissions is of great importance [21]. Passive filtering is widely used to reduce the electromagnetic interference into the utility.
3. Higher frequencies are desirable to reduce the size and weight of passive components, especially of the boost inductors, and improve the current control dynamic performance. Therefore the switching frequency in PFC applications (up to 500 kHz [22, 23]) is higher than in inverter applications (usually up to 20 kHz). For PFC application, the current sensing needs therefore to be accurate.
4. The input currents are generally in phase with the input voltages and bidirectional power flow is usually not required in PFC.

The switching associated to a particular modulation generates, as shown in Fig. 1.5, a pulsewidth-modulated input rectifier voltage of sinusoidal frequency content, which is formed by switching between the available DC output voltage levels. For three-level rectifiers (for inst. the *Vienna* rectifier), besides the potential of the positive and negative DC voltage bus, also the neutral point potential is available for the voltage formation. The DC bus voltages are thus converted in three-phase switching waveforms that are filtered to produce a symmetrical three-phase sinusoidal system. The *filtering* and *storage* roles of the passive elements, such as capacitors and inductors at the DC and AC side respectively, are essential for the basic operating of the rectifier. The Voltage Source Rectifier adopts a DC capacitive storage instead of an inductive storage, like in the current source rectifiers. The DC capacitor is firstly charged to a certain voltage. Then, the AC current can be controlled by the difference of AC mains voltage and the PWM voltage waveform (this difference is the voltage across the boost inductor), which is built at the input of the rectifier by switching among the available DC voltages levels according with the modulation strategy.

The AC power level can be controlled by varying the AC current amplitude and, if converter losses are neglected, this allows to control the DC power as

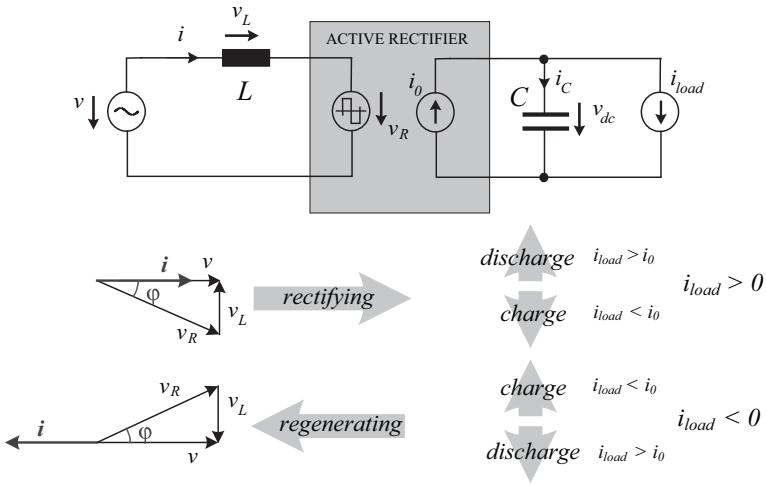


Figure 1.7: Voltage source rectifier operating principle, consisting in two operating modes, rectification and regeneration, and the two processes, charge and discharge of the DC-side capacitor.

well, thus resulting in a charge and discharge of the DC capacitor. The process *DC capacitor charge/AC current control/DC voltage control* is based on the possibility of energy storage of the dc capacitor (cf. Fig. 1.7). The *filtering* action is necessary because of the PWM signals are present both on the DC side and on the AC side.

The passive elements are charged/discharged during the switching period, ensuring the smoothing of the AC currents and of the DC voltage. The characteristics of the filtering components influence the performance of the implemented control technique. The dynamics of the rectifier’s input-current and output-voltage controllers depend on the time constants of the two filter stages. Therefore the overall design, that accounts for both filtering and control issues, is a trade-off between high filtering and fast dynamics.

In most applications, three-phase voltage source converters have a control structure comprising an internal *input current feedback loop* besides the *output voltage feedback loop*, as represented in Fig. 1.8. The control principle of a PWM rectifier is such that the reference current signal i_{ref} of the feedback current control is built out of the information of the current magnitude, provided by the output voltage V_o feedback loop for a given power level and by a normalized sinusoidal reference, derived directly by the grid voltage v_i .

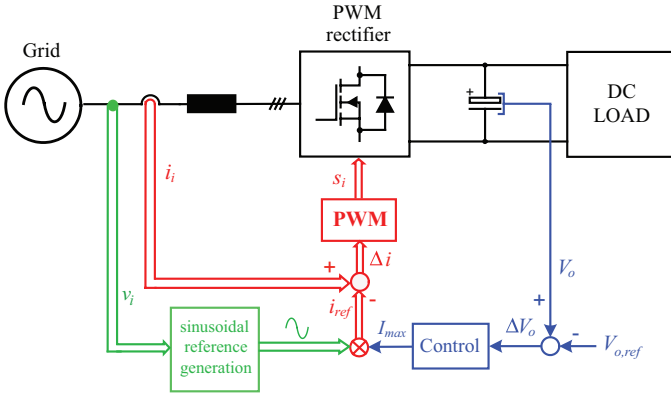


Figure 1.8: Control principle of a PWM rectifier. The reference current signal i_{ref} of the feedback current control is built out of the information of the current magnitude, provided by the output voltage V_o feedback loop for a given power level, and by a normalized sinusoidal reference, derived directly from the grid voltage v_i .

There exists a number of current control techniques that employ PWM modulation, and they differ for the type of controller used. Historically, the first current control methods were introduced for the DC to AC voltage source converters, and in particular three-phase, two-level inverters. Pulse-width modulated, current-controlled (PWM CC) converters have found extensive application especially because they exhibit, in general, better safety, better stability and faster response than the voltage controlled ones [19]. Moreover they have several additional advantages [24]. The PWM CC is applied to active rectifier in order to ensure DC-link voltage regulation [25]. Thus, the PWM CC rectifier is usually applied to front-end operation in AC drives with DC-link voltage regulation [26, 27].

The status of art of the PWM CC concepts for VSC and the evolution of the control methods in order to fulfill the needs of the technology is provided by some authoritative works [19, 24, 28, 20, 29].

Since PWM CC techniques for three-phase rectifiers are in most cases directly borrowed from the control concepts developed for the inverters [30], there does not exist a classification of the current control techniques for VS PWM rectifiers like for inverters [20, 29, 31, 32]. The current controllers for three-phase active rectifiers can be divided into two main groups:

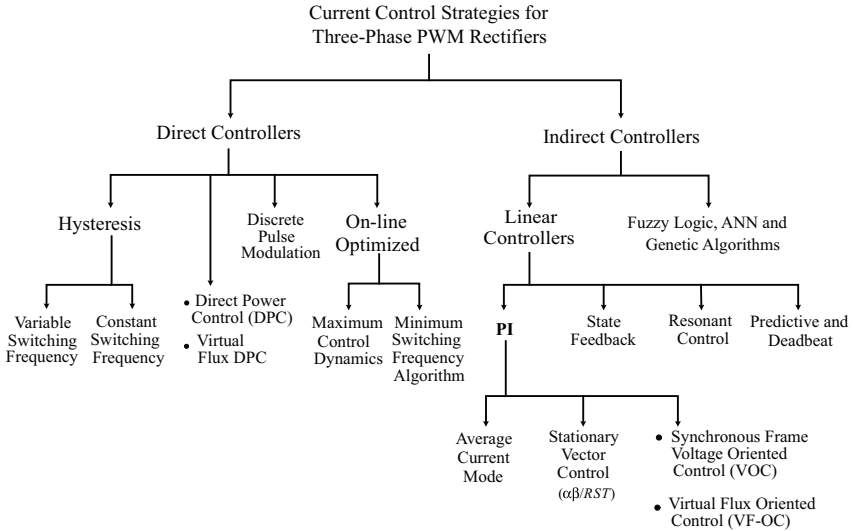


Figure 1.10: Overview of the current control strategies for three-phase PWM rectifiers. These methods are typically used for the current control of inverters and their application can be extended to three-level topologies, where the center-point control is integrated into the phase-current control loop.

In particular, in soft-switched resonant three-phase rectifiers [46, 47], the commutation process is restricted to *discrete* time instances, when the DC-link voltage pulses are zero.

Therefore, a special technique called *delta modulation* (DM) or *Pulse Density Modulation* (PDM) or *Discrete Pulse Modulation* is used [48, 49].

On the other hand, the indirect controllers are divided into:

1. Linear controllers are: *PI*, *State feedback* [39], *Resonant Controllers* [39], *Predictive* [50, 51, 52] and *Deadbeat* [31];
2. Nonlinear controllers, which are Fuzzy Logic, Artificial Neural Network (ANN) and Genetic Algorithms (GAs).

The group of PI current controllers comprises: Average Current Mode Control [53, 54]; Stationary Vector Controllers ($\alpha\beta/RST$) [39] and Synchronous-frame, Voltage Oriented Control (VOC) [43, 55, 56] and the Virtual-Flux Oriented Control (VF-OC) [43].

Fuzzy logic based control has been applied to modulation optimization [57], PI based controllers [58, 59], to start-up optimization [60] and feedforward control

and modulation [61]. Furthermore, soft computing techniques, such as genetic algorithms, can be used for optimizing the design of rectifier systems [62] or to adapt the parameters of advanced controls such as active damping [63].

1.1.3 Current Sensor Technologies

Industrial electronics equipment for measurement [64], control [65], protection [66] and diagnostics [67] often require high-performance current sensors with features such as:

1. wide frequency bandwidth;
2. high current rating;
3. high dv/dt immunity;
4. linearity and stability with temperature variations;
5. compatibility with integration processes;
6. low realization effort and low cost.

The types of current sensors that have appeared in recent publications were based on numerous different physical effects, for instance magnetic coupling [?, 68, 69], magneto resistance [70, 71], Faraday induction [72], Hall effect [73] and zero flux [74]. However, as some recent comparative studies have shown [75, 76, 77, 78], none of these sensors have really met all the requirements above listed in one device. An overview of current sensor technologies is provided in Fig. 1.11. The main differentiation is between sensors based on magnetic coupling and sensors that use other principles. The magnetic coupling based sensor are further split into sensors that use a magnetic core and coreless sensors.

A large bandwidth from DC [79] to several MHz has been the most difficult objective, but is also one of the most crucial characteristics for modern current controlled converters having switching frequencies up to 1 MHz and fast dynamics [80, 81]. Accuracy and low-cost of the sensing device are important requirements for current controlled converters. They are particularly crucial for direct pulsewidth modulation, such as hysteresis and direct power control, or for current sensor-based active ripple filters [82]. To circumvent these issues, many *sensorless* control techniques for converters and drives have been developed over recent years [39]. Another important aspect is the immunity of the sensor against external fields. For instance, a current sensor that is physically located near a SiC J-FET, can be affected severely by dv/dt transients up to several tens of $kV/\mu s$ [4]. The parasitic coupling associated with the sensor itself can couple these transients into the sensing part causing distortion in the output.

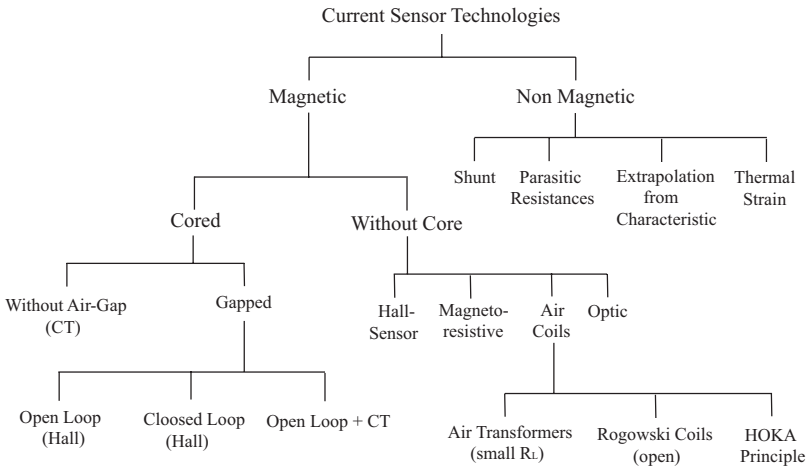


Figure 1.11: Overview of current sensors technologies.

1.1.4 Wide Bandwidth Operating Range

Increasing the switching frequency has been the traditional approach to reduce the converter size and improve dynamic performance. However, the increase in switching frequency leads to increased power loss density, in particular in magnetic components, thus causing a raise of the device operating temperature. The thermodynamic analysis of the system and the study of the energy and heat flows are of great importance for the devices design and for assessing the system's performance and reliability [83]. The high switching frequency operation contributes to a significant increase of the parasitic electric and magnetic coupling among components and generates the phenomena of electromagnetic interference.

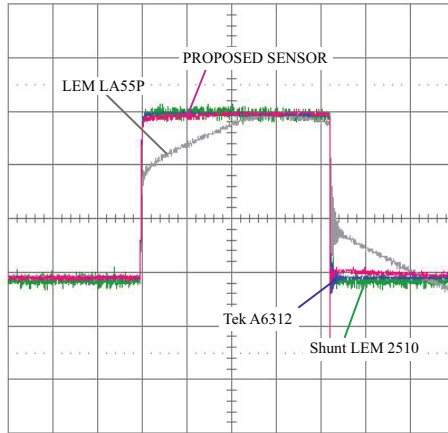
Besides the issues related to the optimal high-frequency layout of the converter topology, one has to select properly the current sensor. This latter should possess a frequency bandwidth at least one decade larger than the switching frequency, i.e. converters switching in the hundreds of kilohertz range should be equipped with current sensors in the Megahertz bandwidth range.

Fig. 1.13 clearly shows two of the major issues for the high-performance, high-frequency operation of a current sensor. The ability of the current sensor to follow the raising edge of a current pulse is dependent on the upper limit of its frequency bandwidth. If the sensing element or the process electronic are not

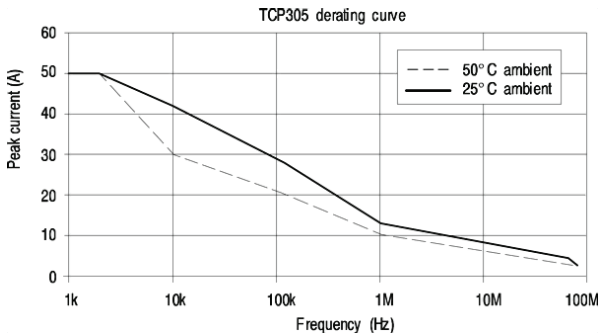


Figure 1.12: Commercial current sensors: a) Current transformer, 20 MHz; b) Closed-loop, DC to 200 kHz current sensor; c) DC to 100 kHz magnetostrictive sensor; d) zero-flux, DC to 100 MHz current probe; e) 100 MHz shunt; f) DC to 10 kHz, Hall-effect element.

fast enough, the current sensor is able to sense only a part of the current to be measured, as displayed in Fig. 1.13a. Another important issue is constituted by the losses dependent on the operating frequency. Especially for a magnetic core based sensor, the eddy current losses in the core and in the winding are such that the sensor current rating needs to be reduced for increasing frequency in order to control thermal offset and dissipation. These challenges are faced in the second part of this Dissertation.



(a)



(b)

Figure 1.13: Examples of high-frequency issues for current sensors. a) Current step response of devices having MHz-range bandwidth (Tektronix Probe, Shunt, Proposed Sensor-Ch. 8) compared to a narrow bandwidth device. Vertical scale: 5 A/div, time scale: 0.5 μ s/div. b) Thermal derating for a Tek A6312 Probe.

1.2 Motivation

For high power three-phase rectifiers the use of unity power factor control is becoming an industrial requirement. In particular, multilevel voltage-source-

rectifiers are of special interest as they offer reduced input current ripple and lower switching device blocking voltages. Besides the advantages related to the converter's topology, further improvement of the overall system performance depends on the modulation strategy employed. The selection of an appropriate current control technique allows an improvement of the rectifier's efficiency and to reduce the realization effort.

Up to now, the research of three-phase converters has been heavily focused on inverter applications. Although most current control techniques developed in the inverter area can be used in PFC applications, a PFC circuit has its unique characteristics and, therefore, deserves some special treatment. In particular special attention has to be paid to the quality of the input current. High switching frequency is desirable to reduce the size and weight of reactive components, especially inductors, and to improve current control performance.

While a switching frequency of few kHz is sufficient in most inverter applications, a PFC converter is operated at higher frequency, e.g., 20-200 kHz in the kilowatt power range. Thus, a wide current sensor bandwidth is required and is more important for PFC circuits than for inverters. Accordingly, the issues related to the high-frequency characterization of ferrite wound components and in particular of current sensors are of special interest to model and predict the frequency behaviour of the device.

1.3 Dissertation Objectives and Contributions

The dissertation deals with innovative and optimal modulation strategies for three-phase, three-level rectifiers. Both direct and indirect modulations are considered and the advantages and drawbacks of conventional techniques critically presented. The novel current control concepts are based on decoupling hysteresis current control and voltage oriented control (Space Vector Modulation), respectively. The goal of the novel controllers is to overcome the drawbacks of the conventional control schemes and to retain the advantages thus leading to an improvement of the converter performance in terms of efficiency, robustness and low implementation cost. Moreover, the Dissertation addresses other control issues for three-level PWM rectifiers, such as the output center point voltage control for three-level topologies, the center point loadability, and the interdependence of AC-side and DC-side optimal PWM control. The influence of the modulation method on the switching losses is also undertaken, and two discontinuous modulation methods are considered.

Besides the current control issues, the design of a high-performance current

sensor is also addressed. For this aim current sensor technologies are reviewed and the sensor's design parameters that dictate broadband performance are analyzed. Since the current sensor proposed has a current transformer as the main sensing device, the frequency properties of ferrite materials are analyzed in detail. A non-linear model of a gapped transformer, based on the capacitance-permeance analogy, is used for the frequency analysis. A high-performance, isolated current sensor, comprised of a planar current transformer with multilayer PCB winding and a Hall-effect element is presented. All these topics are analyzed in detail in the dissertation, the principles of operation of the new concepts are explained and theoretical and simulation results are systematically verified by experiments.

The contributions of the Dissertation deal with the analysis, experimental verification of the following topics:

1. Decoupling Hysteresis Current (DHC) control for three-level rectifiers;
2. variable tolerance-band, synchronized DHC for three-level rectifiers;
3. loadability analysis of the center-point for three-level rectifiers;
4. study of the interdependence of the AC-side and DC-side optimization for three-level rectifiers;
5. two discontinuous SVM methods for three-level rectifiers;
6. broad-band comprehensive model for the losses of a transformer based on the capacitance-permeance analysis;
7. frequency characterization of ferrite materials, including magnetic skin depth and dimensional resonance;
8. electrostatic analysis of ferrite wound components;
9. a planar, isolated current sensor for high performance power electronics applications.

1.4 Publications

1. L. Dalessandro, U. Drogenik, S. Round, and J. W. Kolar, "A Novel Hysteresis Current Control for Three-Phase Three-Level PWM Rectifiers", Proc. Applied Power Electronics Conf. pp. 501-507. 2005;
2. L. Dalessandro, W. G. Odendaal, J. W. Kolar, "HF Frequency Characterization and Nonlinear Modeling of a Gapped Toroidal Magnetic Structure", IEEE Trans. Power Electronics, Vol. 21, no. 5, pp. 1165-1175, Sept. 2006 and presented at the 36th Power Electronics Specialist Conference, Recife, Brazil, June 2005;
3. S. Round, L. Dalessandro, and J. W. Kolar, "Novel Phase Decoupling and Coordinating Tolerance Band Current Control for Three-Phase Three-Level PWM rectifiers", Proc. PCIM 2005, pp. 285-291;
4. L. Dalessandro, N. Karrer, and J. W. Kolar, "High-Performance Planar Isolated Current Sensor for Power Electronics Applications", IEEE Trans. Power Electronics, vol. 22, no. 5, pp. 1682-1692, Sept. 2007 and presented at the 21st Applied Power Electronics Conf, Dallas, March 2006;
5. L. Dalessandro, F. Cavalcante, and J. W. Kolar, "Self-Capacitance of High Voltage Transformers", IEEE Trans. Power Electronics, vol. 22, no. 5, pp. 2081-2092, Sept. 2007;
6. L. Dalessandro, S. Round, U. Drogenik, and J. W. Kolar, "Discontinuous Space-Vector Modulation for Three-Level PWM Rectifiers", IEEE Trans. Power Electronics, vol. 23, no. 2, pp. 530-542, March 2008;
7. L. Dalessandro, S. Round, and J. W. Kolar, "Center-Point Voltage Balancing of Hysteresis Current Controlled Three-Level PWM Rectifiers", IEEE Trans. Power Electronics, September 2008, (to appear);
8. M. L. Heldwein, L. Dalessandro, and J. W. Kolar, "Modeling and Performance Improvements for the Three-Phase Common Mode Inductor", IEEE Trans. Power Electronics, (submitted).

1.5 Selected Invited Lectures

1. L. Dalessandro, "Optimal Modulation and Wideband Current Sensing for Three-Level PWM Rectifiers", Massachusetts Institute of Technology (MIT), Laboratory for Electromagnetic and Electronic Systems (LEES), Stata Center, ROOM 32-155, March 16th 2006, 4:00 PM;
2. L. Dalessandro, "Optimal Modulation and Wideband Current Sensing for Three-Level PWM Rectifiers", Virginia Polytechnic Institute and State University (Virginia Tech), National Science Foundation (NSF-ERC) Engineering Research Center for Power Electronics Systems (CPES), Whittemore Hall, ROOM 300, March 24th, 2006, 12:20 AM;
3. L. Dalessandro, "Electromagnetics Applied to Power Electronics and Optimal Direct Current Control for Three-Level PWM Rectifiers", Asea Brown Boveri (ABB), Corporate Research Center, Baden-Dättwil, May 15th, 2006, 4:00 PM;
4. L. Dalessandro, "Current Measurement Principles for Integrated Power Electronics Modules", Japanese National Institute for Advanced Industrial Science and Technology (AIST), Power Electronics Section, and TO-SHIBA Japan, Semiconductor Company (Dr. Ogura), ETH Zurich, June 2nd 2006, 4:30 PM.

1.6 Dissertation Organization

In Chapter 2, a novel decoupling hysteresis current control concept for three-phase three-level PWM rectifiers is presented. Another method that uses a pre-control signal for the hysteresis band is implemented to obtain coordinated switching between the phases and results in a near constant switching frequency and a current ripple performance that is similar to conventional carrier-based PWM controllers.

Chapter 3 deals with the center-point voltage control issue for three-level converter topologies. The balancing of the output center-point voltage of a hysteresis current-controlled three-level PWM rectifier is realized by adding an offset to the input current reference. The main characteristics of direct and indirect current control methods for three-phase active rectifiers are presented, with particular emphasis on the degree-of-freedom one can use to balance the center-point in three-level topologies.

In Chapter 4, the implementation and experimental verification of two discontinuous pulse-width modulation (DPWM) methods for three-phase, three-level rectifiers are presented. A detailed analysis of both AC-side and DC-side current waveforms is presented, and there is excellent agreement between the

analytical, simulated and experimental results for the mains current ripple amplitude and output center point current over the practical modulation range.

In Chapter 5, the frequency dependent characteristics of a gapped toroidal structure are extracted empirically over a bandwidth that exceeds 30 MHz. The flux distribution within the ferrite is modeled using the electromagnetic wave propagation theory and the dimensional resonance effect is explained. Derivations for the losses in the core and in the winding are included in the chapter.

Chapter 6 deals with the electrostatic analysis of ferrite wound component, and a particularly complex architecture, a high-voltage transformer, is selected to analyze with a broad perspective, the electric field distributions.

Chapter 7 presents a novel, planar current sensor, comprised of a magnetic current transformer and a Hall-effect element. The main design formulations are given analytically; simulations, finite element results and measurements are presented for verification.

Chapter 8 summarizes and concludes. An outlook on further research topics and open issues is provided.

Chapter 2

Pulse-Coordinated Decoupling Hysteresis Control

2.1 Introduction

Three-phase PWM based rectifiers are desirable as the input phase currents can be controlled to have a sinusoidal shape. By using a three-level topology, such as the circuit in Fig. 2.1, the voltage stress on the switches is reduced to half that of a two-level topology. The control of the input current waveform shape for the three-level rectifiers can be divided into two categories, either the conventional carrier-based controller (CCC) or the conventional hysteresis (or tolerance band) controller (CHC) [24].

The CCC employs in each phase a P-type controller, a PWM triangular carrier and a comparator to generate the gate drive signal of the corresponding transistor. The main advantages of the carrier-based method are a fixed frequency, which simplifies the EMI filter design and features natural center point stability. However, the CCC requires a control-oriented modeling of the system [53] and a mains voltage pre-control signal in order to insure a sinusoidal input current shape with low control error [54]. In addition, the CCC has a relatively low dynamic performance and requires additional control effort to compensate for non-idealities such as differences in the switch delay times.

In comparison, the CHC directly compares the line current with the reference current and controls the switches appropriately to force the line current to follow the reference. Hysteresis control is much easier to implement than a carrier-based controller and the transient response is extremely fast since the

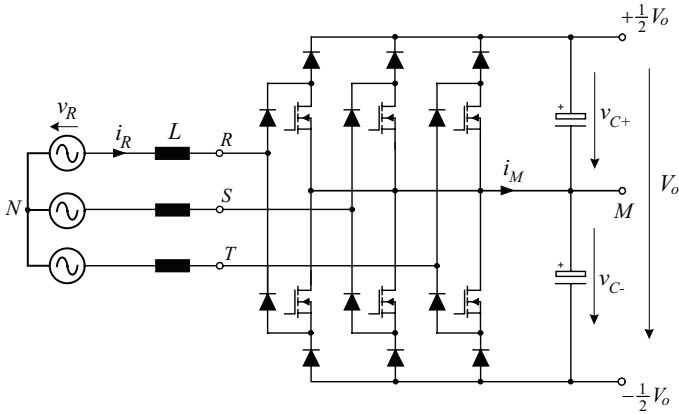


Figure 2.1: Basic power circuit structure of a three-phase, three-level, six-switch PFC rectifier.

current instantaneously follows any change in the reference signal. However, the main disadvantage is that the switching frequency is not regular as the actual switching frequency depends on the input inductor value, the hysteresis band amplitude and on the input and output voltage levels. For three-phase inverters and rectifier systems the CHC is implemented independently for each phase current. However, it is well known that the switching of each phase is not independent as there is coupling and/or interaction between the phases [32].

Therefore, both control methods present advantages and drawbacks. For three-phase two-level PWM rectifier systems with CHC additional circuitry has been proposed to limit the maximum switching frequency [45, 84], or to keep it even constant [35, 25, 37, 31]. In particular, [25] proposes a hysteresis control method for two-level PWM inverters that eliminates the interaction between the phases thus allowing a phase-locked loop control of the modulation frequency of the switches.

An analogous approach would be interesting for three-phase three-level rectifiers (cf. Fig. 2.1). This Chapter proposes such control concept, which decouples the three phases by extending the actual phase currents by a zero sequence current component and results in a virtual connection of the mains star point N and of the output center point M . Accordingly, the proposed current control is named Decoupling Hysteresis Control (DHC). The decoupling provides a more regular switching and a natural stability of the output center point. Furthermore, the advantages of the conventional hysteresis control such as excellent dynamic performance, low complexity of implementation, and direct compen-

sation of non-idealities (e.g. of gate drive and switching delay times and power semiconductor on-state voltage drops) are maintained.

In this Chapter the DHC concept for three-level rectifiers is further extended so that the rectifier is operated with a constant switching frequency and the switching of each phase is synchronized and aligned to reduce the current ripple and to achieve a phase current waveform similar to that of a CCC.

2.1.1 Conventional Hysteresis Current Control

For three-phase, three-level PWM rectifier systems the CHC, shown in Fig. 2.2, is implemented independently for each phase. Each current controller directly generates the switching signal, s_i , (2.1), where i indicates the phase R , S or T . For the case of positive input current, if the error between the phase current, i_i , and the reference sinusoidal current, i_i^* , exceeds the upper hysteresis limit $+h$, the power transistor of the corresponding phase is turned off, causing i_i to decrease. Once i_i reaches the lower hysteresis limit $-h$, the power transistor is turn on again, the phase current increases and the cycle repeats.

$$s_i' = \begin{cases} 0 & \text{if } i_i > i_i^* + h \\ 1 & \text{if } i_i < i_i^* - h \end{cases} \quad (2.1)$$

The final switching decision, s_i , is determined considering the direction of the mains phase current [8] or the sign of the corresponding reference current i_i^* as given in (2.2) or of the related mains phase voltage v_i .

$$s_i = \begin{cases} s_i' & \text{if } i_i^* \geq 0 \\ \text{NOT } s_i' & \text{if } i_i^* < 0 \end{cases} \quad (2.2)$$

In Fig. 2.2 this is considered in the block labeled with (2.2). The resulting input current waveform (cf. Fig. 2.2) exhibits time intervals where no switching occurs. This clearly indicates a mutual influence of the phase current control circuits. Furthermore, as shown in [85] the rectifier output center point is not naturally stable and therefore must be actively controlled. This could be achieved in the simplest case by a P-type control in Fig.2.2) which generates an offset, i_{dc} , of the phase current reference values in case an output center point voltage shift

$$\Delta v_M = \frac{1}{2}(V_{C+} - V_{C-}) \quad (2.3)$$

occurs (V_{C+} and V_{C-} are the upper and the lower output partial voltages). The

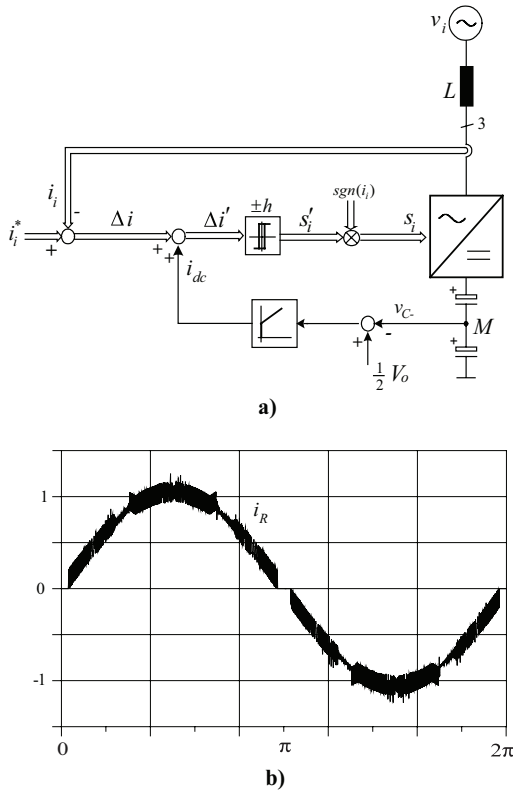


Figure 2.2: a) Block diagram of a conventional hysteresis current controlled (CHC) rectifier and b) phase current.

CHC has among its advantages, simplicity of implementation, robustness, and excellent dynamics but results in irregular switching and is characterized by a dependency of the average switching frequency on the mains voltage and output voltage transfer ratio, the absolute mains voltage level, the input inductor value and the width of the hysteresis band.

2.1.2 Conventional Carrier-based Current Control

For CCC, the switching decision s_i' , is the result of a comparison of the dynamically weighted current error (in the simplest case only a P-type control

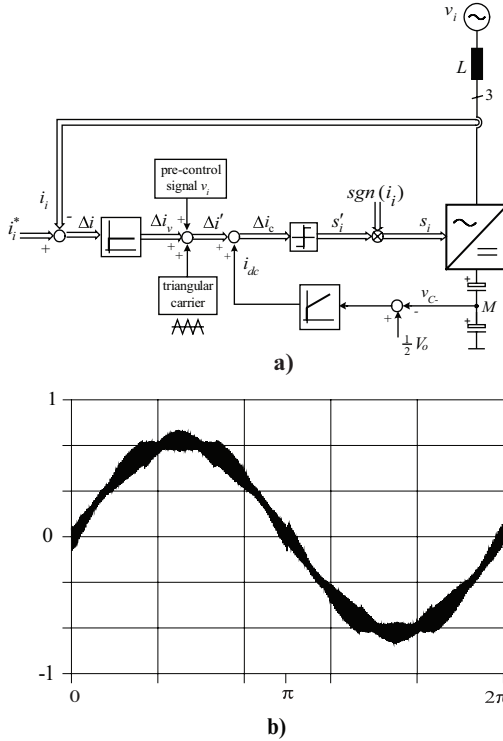


Figure 2.3: a) Block diagram of a conventional carrier-based current controlled (CCC) rectifier and b) phase current.

is employed) with a triangular carrier signal, as shown in Fig. 2.3. The use of a triangular carrier results in a constant switching frequency. As with the hysteresis control, the final switching decision, s_i , depends on the sign of the corresponding mains phase current reference value.

In order to ensure a low current control error and/or a sinusoidal input current shape also for P-type control, a mains voltage pre-control signal, v_i , is added to the current controller output. The time behavior of the pre-control signal can be derived from an analysis of the input voltage formation [54] resulting

in

$$v'_i = \begin{cases} \hat{I}_{CS} \left(\frac{4v_i}{V_{out}} - 1 \right) & \text{if } i_i \geq 0 \\ \hat{I}_{CS} \left(\frac{4v_i}{V_{out}} + 1 \right) & \text{if } i_i < 0. \end{cases} \quad (2.4)$$

As the output voltage center point of the rectifier for CCC is naturally stable [85], theoretically no output voltage center point control would have to be provided. However, in a practical realization an asymmetry of the partial output voltages can occur due to non-idealities such as different switching and gate drive delay times of the phases. Therefore, a control of the center point voltage is implemented following the same concept as for the CHC.

For the switching state sequence of the CCC a subsequent rectifier switching state is achieved by changing always only the switching state of one phase. Compared to that the switching of the CHC is highly irregular, what results in a higher average switching frequency for equal input current ripple rms value.

2.2 Decoupling Hysteresis Control: Principle of Operation

The basic concept of the proposed control can be clearly shown based on an equivalent circuit of the AC part of the three-phase PWM rectifier depicted in Fig. 2.4. The shape of the input phase current i_i , (index i indicates phase R, S

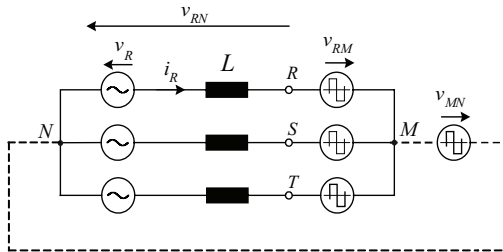


Figure 2.4: Equivalent circuit of the AC part of a three-phase PWM rectifier.

or T) is defined by the voltage across the input inductors $v_{L,i}$

$$\begin{cases} L \frac{di_R}{dt} = v_{L,R} = v_R - v_{RN} \\ L \frac{di_S}{dt} = v_{L,S} = v_S - v_{SN} \\ L \frac{di_T}{dt} = v_{L,T} = v_T - v_{TN} \end{cases} \quad (2.5)$$

where v_{iN} are the rectifier input voltages referred to N . As the mains star point, N , and the rectifier center-point M are not connected, hence the rectifier input voltages are given by

$$\begin{cases} v_{RN} = v_{RM} + v_{MN} \\ v_{SN} = v_{SM} + v_{MN} \\ v_{TN} = v_{TM} + v_{MN} \end{cases} \quad (2.6)$$

where v_{iM} are the rectifiers input voltage referred to M , and v_{MN} is the zero sequence voltage occurring between the mains star point and output center point. Furthermore, the sum of the phase currents is forced to zero

$$i_R + i_S + i_T = 0 \quad (2.7)$$

In addition for a symmetric mains

$$v_R + v_S + v_T = 0 \quad (2.8)$$

is valid. Taking (2.7) and (2.8) into account, it follows from (2.5) and (2.6)

$$v_{MN} = -\frac{1}{3}(v_{RM} + v_{SM} + v_{TM}) \quad (2.9)$$

which corresponds to a mutual coupling of the three phases. In case M and N would be connected ($v_{MN} = 0$), and/or

$$v_{iN} = v_{iM} \quad (2.10)$$

the current in each phase would only be dependent on the respective rectifier phase and mains phase voltage and a zero sequence current driven by v_{MN} would flow in the center point to neutral connection. For the proposed DHC, the connection of N and M is virtually established (shown by a dashed line in Fig. 2.4) by adding a zero sequence current i_0 to the actual phase current ($i'_i = i_i + i_0$, cf. Fig. 2.5) where i_0 is generated by the integration of the measured zero sequence voltage v_{MN}

$$i_0 = \frac{1}{L} \int_T v_{MN} dt \quad (2.11)$$

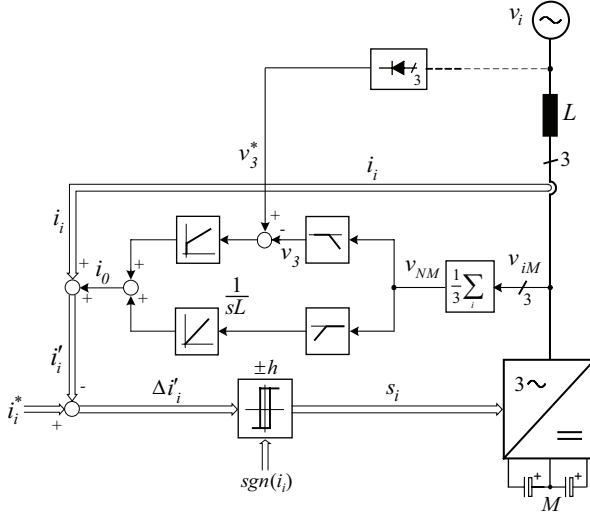


Figure 2.5: Decoupling hysteresis current control implementation.

where L denotes the phase inductance. Therefore, the controller processes the same error signal as for an actual connection of N and M . Accordingly, a decoupling of the three phases is realized. In Fig. 2.6, the simulated time behavior of the virtual phase current i'_i and of the corresponding actual phase i_i is shown. The control error $\Delta i_i = i_i^* - i'_i$ processed by the hysteresis controller is depicted in Fig. 2.6d, the ripple of the actual phase current is shown in Fig. 2.6b.

The decoupling hysteresis controller (DHC), as shown in Fig. 2.5, has the same basic outer structure as the standard CHC where the phase current is subtracted from a current reference and the hysteresis controller generates a switching signal from the current error. The DHC has an additional control loop that generates i_0 . By summing the measured line current, i_i , with i_0 a virtual current i'_i is formed. With the correct formation of i_0 the switching of the hysteresis controller can occur without any interaction between each of the phase controllers. The operation of the DHC can be seen from the simulation results in Fig. 2.6a where the virtual phase current i'_i has a current ripple that is always maintained within the hysteresis band. Fig. 2.6c shows the actual line current i_R and it can be seen that it does not have the same current ripple as the virtual current. Compared to the phase current produced using the CHC (Fig. 2.2) the phase current is now being continuously switched over the complete mains period.

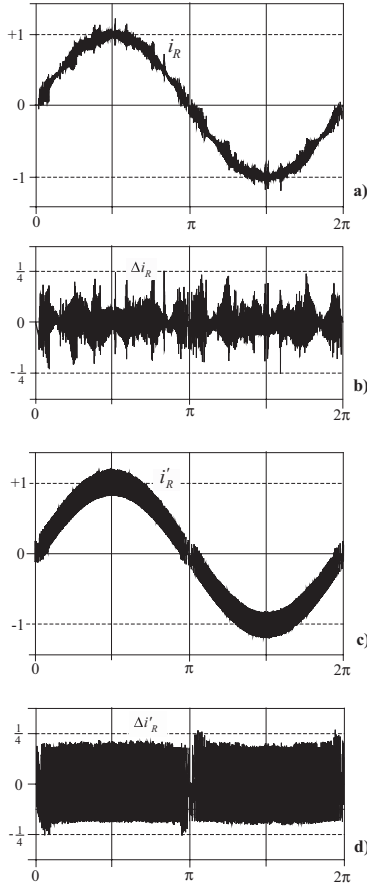


Figure 2.6: Simulated time behavior of the actual mains current i_R (a) and of $i'_R = i_R + i_0$ (cf. Fig.2.5) (c) within one mains period in case of DHC. The respective current ripples are shown in (b) and (d).

2.2.1 High Frequency Injection

The aim of the high frequency injection is to decouple the phases and/or avoid the interaction of the phase switching. The phase interaction is caused because the mid point to neutral voltage is not constant, as it is dependent on each of the rectifier input voltages as given by (2.5),(2.6) and (2.9) . The v_{NM} voltage is

determined, either from direct measurement or by summing the input to mid-point voltages and high pass filtering to extract the high frequency or switching components of the voltage. From this voltage a current signal is generated by using an integrator with a gain of $1/L$, where L is the input phase inductance, as given by 2.13. This current signal is then summed with the actual current (as this is the controlled quantity). The high frequency components of the current i_0 now modify the measured phase current signal. This now virtually decouples each phase switching action, thus producing a regular switching that has no interference from the other phases.

$$v_{MN} = +\frac{1}{3}(v_{RM} + v_{SM} + v_{TM}) \quad (2.12)$$

$$i_0 = \frac{1}{L} \int_T v_{MN} dt \quad (2.13)$$

The operation of the DHC can also be explained using the equivalent circuits depicted in Fig. 2.7. Fig. 2.7a shows the case where the mid-point of the two output capacitors is directly connected to the mains neutral. In this case there is no mechanism for any coupling between the phases as the current, i_i , that flows in each phase is only dependent on the total voltage measured to the mid-point, v_{iM} . The fundamental current is produced by the voltage difference of the mains voltage, v_i , and the fundamental voltage at the input of the rectifier, $v_{iM,1}$. The current ripple is created from the high frequency switching voltage at the input of the rectifier.

In the case where the mid-point point is disconnected (Fig.2.7b), there is now coupling between the phases as each phase current must return via the other two phases. In terms of the equivalent circuit there are now two additional voltage components formed because of the interaction (cf. 2.12). There is a low frequency voltage \bar{v}_{MN} and a high frequency switching voltage, $v_{MN,r}$. For high frequency considerations the low frequency component is ignored. The addition of the decoupling controller now effectively shifts the switching component of v_{MN} into each of the phases (Fig.2.7c). This effectively makes the point M' look like it is connected to the mains neutral point and that is the reason why the high frequency switching does not have any interaction with the other phases.

2.2.2 Low Frequency Control

From the equivalent circuit and 2.12 there is still a low frequency component, \bar{v}_{MN} , in the voltage v_{MN} , that represent namely the degree of freedom in the modulation. By applying a low frequency controller to the DHC system it is possible to properly shape this low frequency component. In conventional PWM

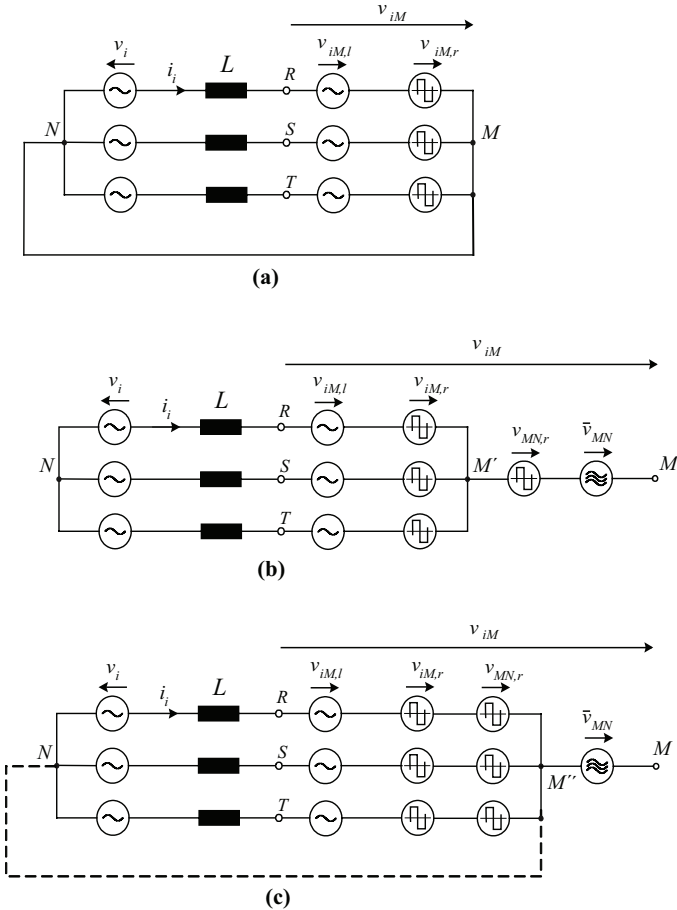


Figure 2.7: Equivalent circuits of DHC implementation (a) physical connection of M and N (b) DHC (c) virtual connection of M and N .

systems it is desirable to add a third harmonic component to the reference so that the modulation range is extended [86]. It is also desirable to extend the modulation range for the three-level rectifier, therefore the low frequency controller is used to shape the low frequency component to be a third harmonic or zero sequence component. Fig. 2.5 shows the low frequency control path where the low pass filtered voltage v_{NM} is used as one input to the controller.

This voltage is then compared against a reference third harmonic voltage. This reference voltage can be generated either from a three-phase bridge rectifier connected to the mains voltage or through digital calculation. The error between the reference and the measured voltage is processed by a PI controller to generate a low frequency component of current i_0 that is superimposed on the phase currents. From [87] and [85] it is shown that i_0 at the control level causes a simultaneous change in the mid-point current and a zero sequence voltage in the input rectifier voltage. In this control case the controller produces a small change to i_0 . In the case of the three-level rectifier the gain between i_0 and v_{MN} is very high. This can be seen from Fig 2.8a where the rectifier input voltage waveform now has a significant zero sequence component caused from the zero sequence voltage reference. Fig. 2.8c shows that the low frequency component of i_0 has a magnitude of 20 mA while the low frequency component of \bar{v}_{MN} is 80 V, resulting in a gain of the order of 4000. This high gain can also be seen from the Fig.2.8(b) where the reference and the measured voltage are almost identical. It is interesting to note that the current i_0 has high peak values that are caused when the phase currents go through zero and that the controller is increasing its control value to maintain v_{MN} at the reference voltage level.

Since the system has a very high gain between i_0 and v_{NM} it is not necessary to use the proportional part of the PI controller. Only an integrator is necessary to take the error voltage and generate the controlling current. An integrator with a gain of $1/L$ is sufficient to act as a controller, therefore both the low and high frequency branches be combined together to produce a single control loop as is shown in Fig 2.9. This significantly reduces the complexity of the controller and does not change the performance of the system.

A further advantage of the DHC compared to the CHC is that the mid-point voltage is naturally stable. The bandwidth of this inherent mid-point control is determined by the system parameters and the operating point. To ensure that the control of the mid-point voltage has a defined bandwidth an additional output voltage center point controller can be added as shown in Fig. 2.9. The mid-point voltage is compared against a reference, which is normally half of the total output voltage, and a proportional controller produces a DC current, i_{dc} , from the error and is added into the DHC. It was shown in [85] that a current i_{dc} causes a mid-point current and this mid-point current then causes the voltage on the capacitors to change reducing the error.

The DHC has been shown to produce switching with no phase interactions and has inherent stability of the capacitor mid-point voltage [88]. Although DHC makes the switching frequency more regular than a CHC it is desirable to have the rectifier operating with a constant switching frequency as this makes the EMI filtering task simpler. Implementing constant frequency switching in hysteresis control system, as has been shown in the literature for single- and

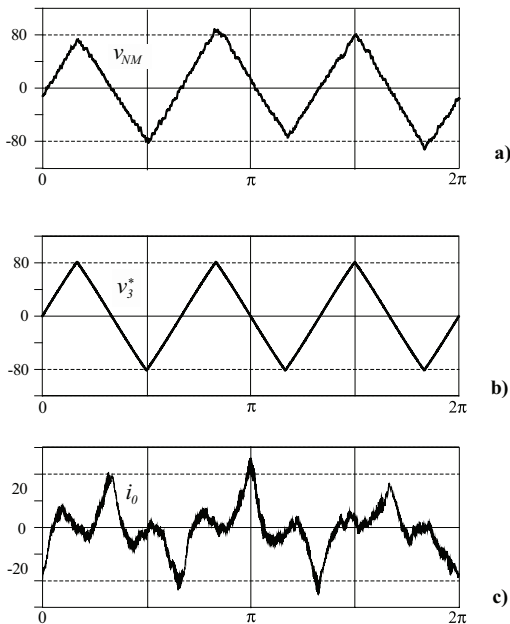


Figure 2.8: Simulated time behavior within one mains period of the triangular signal v_3^* injected in the control loop to allow the extension of the rectifier modulation range and resulting low pass filtered rectifier input voltage, a) low frequency components of v_{MN} , b) reference v_3^* , and c) i_0 . Simulation parameters are: $L = 450 \mu\text{H}$, $V_o = 700 \text{ V}$, $\hat{V} = 327 \text{ V}$, $\hat{I} = 21 \text{ A}$.

three-phase inverter systems, is achieved by varying the hysteresis band amplitude as the input voltage level changes [36, 35].

2.2.3 Output Partial Voltages Balancing

The proposed current control results in the natural stability of the rectifier output center point M and/or exhibits a self balancing of the output capacitor voltages V_{C+} and V_{C-} . In Fig. 2.10 the dependency of the midpoint current (global) average I_M on the output center potential shift ΔV_M defined in (2.3) is depicted for CHC (dashed line, for a proof of the instability of M in case of CHC see [36]) and for the proposed DHC (bold solid line). Furthermore, an approximation of the characteristic of the DHC (thin line) is included which could be analytically derived as follows.

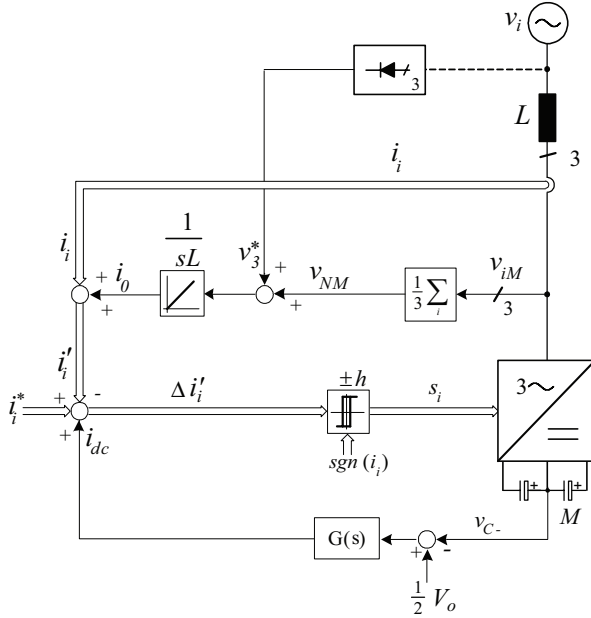


Figure 2.9: Combining high frequency and low frequency paths and using single integrator control.

If one assumes the three phases to be decoupled, each phase circuit can be considered as conventional single-phase boost converter where the total mid-point current i_M of the three-phase system can be calculated as

$$i_M = i_{MR} + i_{MS} + i_{MT} \quad (2.14)$$

For each boost converter the output current i_{Mi} is related to the respective input current i_i by the duty cycle d_i

$$i_{Mi} = d_i \cdot i_i \quad (2.15)$$

where d_i is defined by

$$d_i = \begin{cases} 1 - \frac{v_i}{\frac{1}{2}V_0 + \Delta V_M} & \text{if } v_i, i_i \geq 0 \\ 1 - \frac{v_i}{\frac{1}{2}V_0 - \Delta V_M} & \text{if } v_i, i_i < 0 \end{cases} \quad (2.16)$$

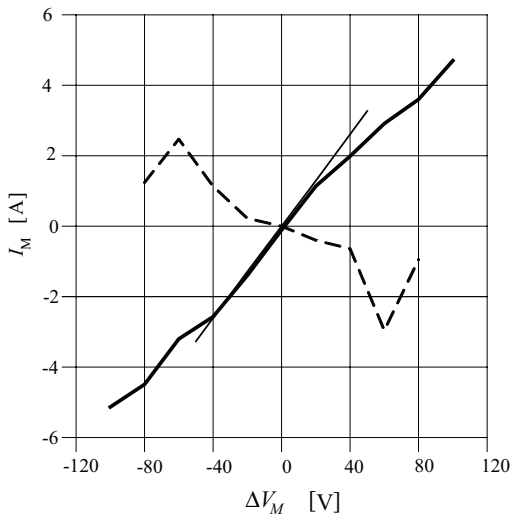


Figure 2.10: Natural stability of the output center point for DHC (bold line) and instability for CHC (dotted line); analytically derived characteristic of the DHC shown by thin line.

This clearly shows that, e.g. for $\Delta V_M > 0$ ($V_{C+} > V_{C-}$ results for $v_i > 0$ in a reduction and for $v_i \leq 0$ in an increase of the corresponding power transistor turn-on time. Accordingly, in the average over the half period $v_i > 0$ a lower share of the phase current $i_i > 0$ is switched to the output center point M than drawn from M within $v_i \leq 0$ ($i_i \leq 0$). This results in a global average value of the center point current $I_M < 0$, charging $C-$ and discharging $C+$ what finally decreases ΔV_M . The corresponding characteristic is depicted in Fig. 2.10. Analogous to CHC (cf. Fig. 2.2) a zero sequence voltage v_{dc} can be used for DHC to implement a feedback control of the midpoint current average value I_M and/or of the midpoint potential shift ΔV_M , as shown in Fig. 2.9.

2.2.4 Average Switching Frequency

The average switching frequency f_{avg} can be calculated starting from the time distribution of the switching state commutations \hat{s}_i , where $\hat{s}_i = 1$ for each change of switching state. The local switching frequency is then provided by the number of commutations of \hat{s}_i within a sliding time window Δt centered in t_{loc} , $0 \leq t_{loc} \leq T/2$, and given by

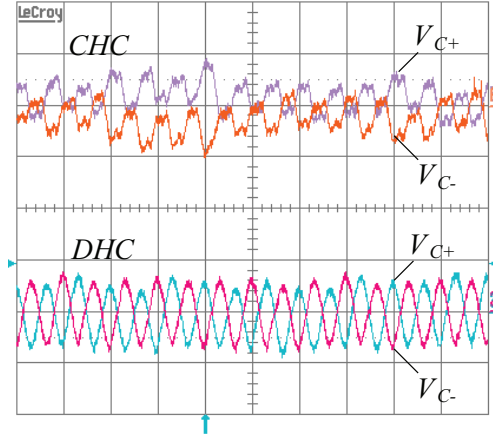


Figure 2.11: Experimental verification of the natural stability of the output center point for DHC while the traces of the partial output voltages for CHC are diverging. Vertical scale 5 V/div.

$$f_{loc} = \frac{1}{2 \Delta t} \sum_i \tilde{s}_i |_{\Delta t} \quad (2.17)$$

Fig. 2.12 shows the switching frequency distribution derived for a window of $\Delta t = 300 \mu s$ according to (2.17), in case of CHC, CCC, and DHC. In this latter case, the switching frequency is nearly constant whereas for CHC a highly irregular switching occurs. The parameters of the simulations in this paper have been set to obtain the same current ripple rms value for the three control concepts.

2.3 Variable Hysteresis Band

Since the switching frequency or time the switch is on and off is dependent on the width of the hysteresis band, the voltage difference across the inductor and the inductor value, the switching frequency can be kept constant by adjusting the width of the hysteresis band depending on the mains voltage. Fig. 2.13 is used to help derive an expression for three-level systems to vary the hysteresis band in order to keep the switching frequency constant. In order to derive a relatively simple expression for the hysteresis band it is assumed that during

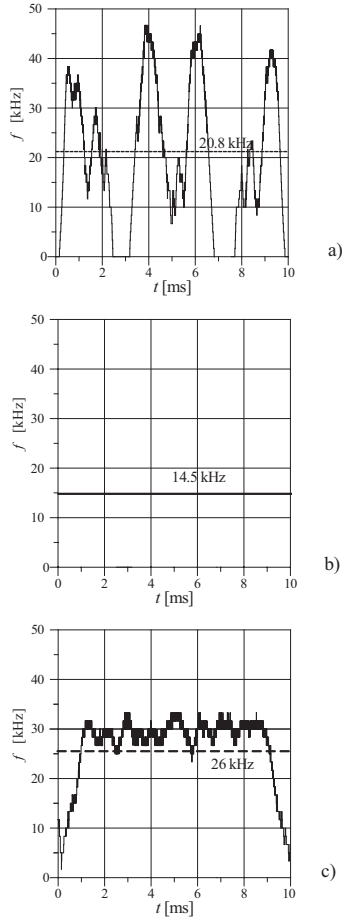


Figure 2.12: Time behavior of the switching frequency distribution within a half mains period in case of a) CHC, b) CCC and c) DHC.

one switching period the fundamental voltage is constant. During the positive half cycle of the mains voltage the turning on and off of the phase switch either impresses zero or half the output voltage at the input of the rectifier. When the switch is on the input rectifier voltage is zero and the current increases until the upper hysteresis band is reached. At that time the switch is turned off and the rectifier input voltage becomes $0.5V_o$ since the upper diode is conducting.

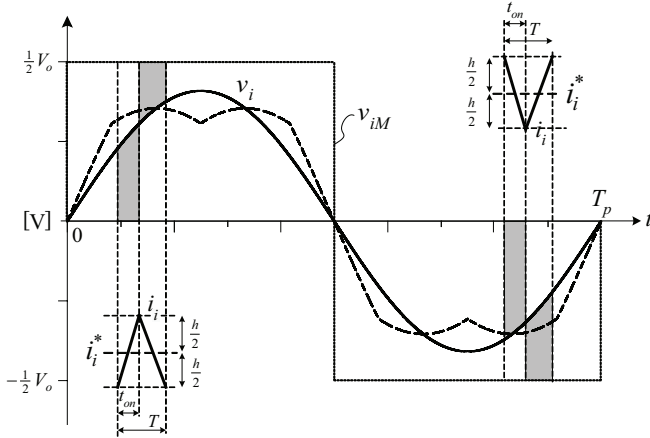


Figure 2.13: Example of three-level switching waveforms.

This causes the current to decrease until the current reaches the lower hysteresis band. Together these two switching times represent one switching cycle. By considering the positive half cycle the switching time, T , can be derived as

$$T = \frac{h \cdot L \cdot \frac{1}{2} V_o}{v_i \left(\frac{1}{2} V_o - v_i \right)} \quad (2.18)$$

For the negative half cycle the switching time, T , is similarly determined. Combining the switching time equations and rearranging the hysteresis band, h , required to produce a constant frequency is expressed as

$$h = \frac{T \cdot |v_i| \left(\frac{1}{2} V_o - |v_i| \right)}{L \cdot \frac{1}{2} V_o} \quad (2.19)$$

For sinusoidal input rectifier voltage, v_{iM} , the shape of the hysteresis band for one mains period is shown in Fig. 2.14, where the magnitude has been normalized by dividing by the peak value of the reference current. At the peak of the mains voltage the hysteresis band has to be decreased to maintain a constant frequency. The hysteresis band has to be also substantially decreased as the mains voltage approaches zero.

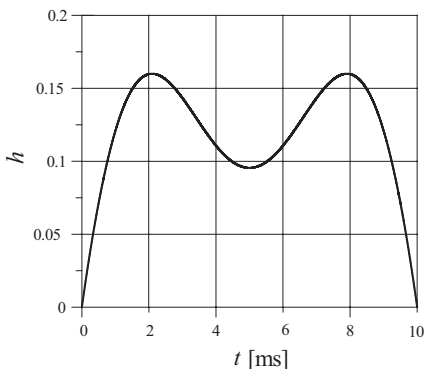


Figure 2.14: Normalized hysteresis band shape for one half a mains period that allows to keep the switching frequency constant at 32 kHz. Normalized to a peak current of 1A.

2.4 Phase Switching Synchronization

The use of a variable hysteresis band produces nearly uniform switching frequency of each of the virtual phase currents. However the switching for each phase is still independent and is not coordinated in anyway. By synchronizing the switching actions of each phase to a common frequency reference an input current waveform shape similar to that produced by a CCC could be achieved. This waveform would have a reduced rms current ripple than produced by the CHC and DHC.

The synchronization and the achieving of constant switching frequency has been previously proposed [89]. In this paper the authors presented a method using a phase-locked-loop (PLL) that generated a varying hysteresis band to force the synchronization of phase switching. The switching signal was used as one input into a Type II phase detector (PD), and a reference frequency was used as the other input. The use of the switching signal as an input to the PLL would make alignment of the switching difficult to achieve over the full range of duty cycles. This may explain why the alignment of the switching signals in Fig. 22 of [89] is not as good as that produced by CCC. The proposed method (Fig. 2.15) uses a PLL and a pre-control signal for the hysteresis band, as presented in the previous Section and shown as the block that produces the signals $h_{R,S,T}$. The pre-control ensures that the switching frequency is already close to the required switching frequency. The synchronization circuit then adjusts the level of the hysteresis band to force the switching signals to become locked to

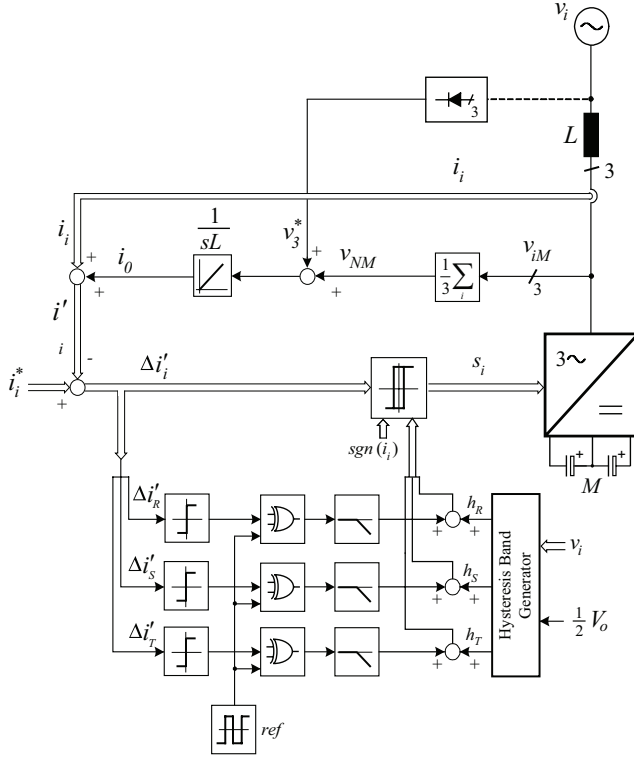


Figure 2.15: Extension to DHC to synchronize the switching of each phase to produce input current waveforms similar to CCC.

a reference signal.

To reproduce a synchronized switching pattern as in CCC requires the switching signals to be centered to a common point. In this method the current error, $\Delta i_i'$, the difference between the current reference and the virtual current, is used to synchronize the switching action. Since the current error is an equally positive and negative signal, it can be compared with a zero reference to produce a 50% duty cycle logic signal. In CCC the current error signals are aligned therefore by aligning the current error logic signal with a reference signal the synchronization of the switching can be achieved. To adjust the switching of each phase a PLL is used to slightly modify the hysteresis band level. The PLL loop is implemented with a Type I (XOR) phase detector that when locked

produces a 50% duty cycle output. The output of the phase detector is then low pass filtered and attenuated to produce the small change in the hysteresis band.

Fig. 2.17 shows the waveforms generated by the synchronization control scheme. The reference signal is a 50% duty square wave. When each of the PLLs is locked, then the hysteresis bands have been modified such that the current error waveforms, $\Delta i_{R,S,T}$, are all in phase. The resulting output of the comparators, $t_{R,S,T}$, are in phase with the common reference signal. The switching signals, $s_{R,S,T}$, are also centered around the rising edge of the reference signal.

The use of a Type I XOR PD allows a simple and inexpensive implementation. The low pass filter that is designed to have a fast locking time as it should be able to track changes in less than 1 ms. The loop filter has been designed to have a cutoff frequency of 6 kHz.

The steady state performance of the synchronization can be seen in the phase current waveform of Fig. 2.21. The current waveform and frequency spectrum has a very similar characteristic to that produced by CCC. This shows that DHC with phase synchronization can have the advantages of both hysteresis and carrier-based current controllers.

Fig. 2.16 shows the frequency spectrum of input phase current ripple for the case of a CHC and a DHC with variable hysteresis band. In Fig. 2.16a it can be seen that the switching is occurring over a relatively wide frequency range for CHC compared to DHC with varying hysteresis band where the switching frequency is more centered around 32 kHz.

2.5 Experimental Analysis

The experimental evaluation of the DHC is achieved by using a *Vienna* rectifier as the three-phase, three-level rectifier. The *Vienna* rectifier is connected to a three-phase 200 V rms line-to-line, 50 Hz voltage source and operated with an output voltage of 380 V_{dc} at an output power of approximately 1 kW. The current controller is implemented with analog circuitry to achieve accurate hysteresis current switching. The three reference currents and variable hysteresis bands are generated digitally using an Analog Devices ADSP21991 DSP, which is a 16-bit, 160 MHz processor, although a standard control microprocessor could be used. The experimental results for the CHC, DHC with a fixed hysteresis band and DHC with a varying hysteresis band are shown in Figs. 2.18-2.20. For CHC (Fig. 2.18) it can be seen for the R phase switching signal, v_{GS} , that there are periods where no switching occurs and the switch is turned off (a high v_{GS} indicates the switch is off). For the case of DHC with a fixed hysteresis band (Fig. 2.19) there is now more uniform switching occurring during the mains pe-

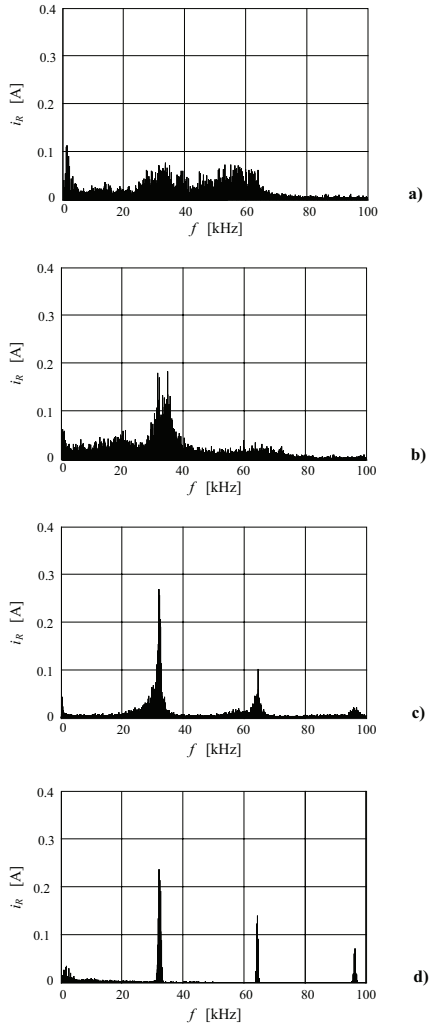


Figure 2.16: Frequency spectrum of the input current i_R , in case of a) CHC, b) DHC, c) DHC with variable hysteresis band and d) DHC with variable band and synchronization of pulse patterns. The switching frequency is 32 kHz and the fundamental is omitted.

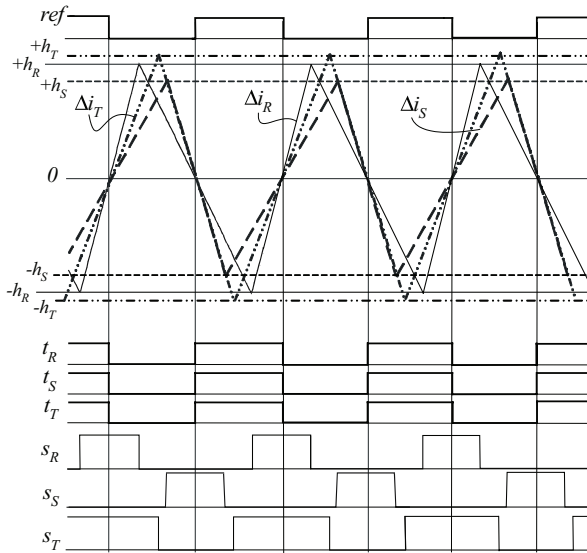


Figure 2.17: Idealized waveforms produced by the DHC with synchronization.

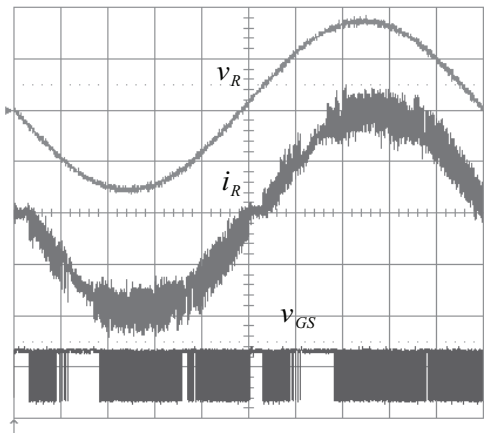


Figure 2.18: Phase voltage (100 V/div), phase current (2 A/div) and gate signal (5 V/div) for CHC.

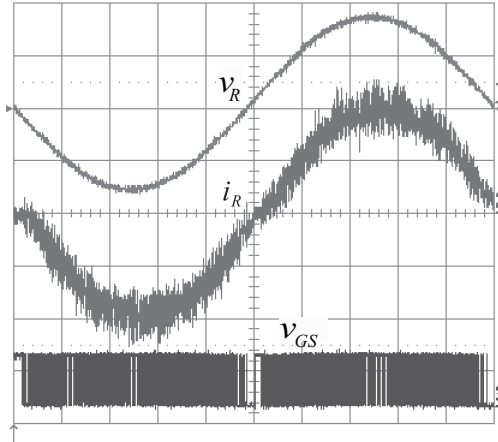


Figure 2.19: Phase voltage (100 V/div), phase current (2 A/div) and gate signal (5 V/div) for DHC.

riod although there is some variability in the switching frequency. For the case of DHC with a varying hysteresis band (Fig. 2.20), the shape of the hysteresis band can be seen and that the switching is more uniform.

2.6 Conclusion

In this Chapter, a novel hysteresis current control based on the decoupling of the phases by the injection of a zero sequence, has been proposed. A further extension to the proposed decoupling hysteresis controller concept for three-level three-phase rectifiers produces a constant switching frequency and synchronized switching. The DHC takes advantage of the decoupling of the three phases by employing a virtual connection of the mains star point and the output center point in the control loop and removes the phase interaction at the control level. By using a varying hysteresis band, rather than a fixed band, the switching frequency of the rectifier can be made almost constant. The DHC control strategy with and without a varying hysteresis band has been verified through simulation and experimental implementation in a Vienna rectifier.

Through the use of a common fixed frequency reference signal and current error signal a PLL for each phase can slightly adjust the varying hysteresis band produced by the pre-controller to produce synchronized switching of all three

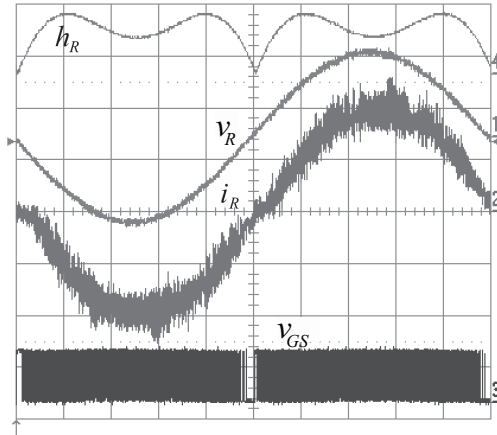


Figure 2.20: Phase voltage (100 V/div), phase current (2 A/div) and gate signal (5 V/div) for DHC with varying hysteresis band.

phases. The synchronized switching produces a phase current waveform with reduced current ripple that has the same quality as achieved with conventional carrier-based controllers.

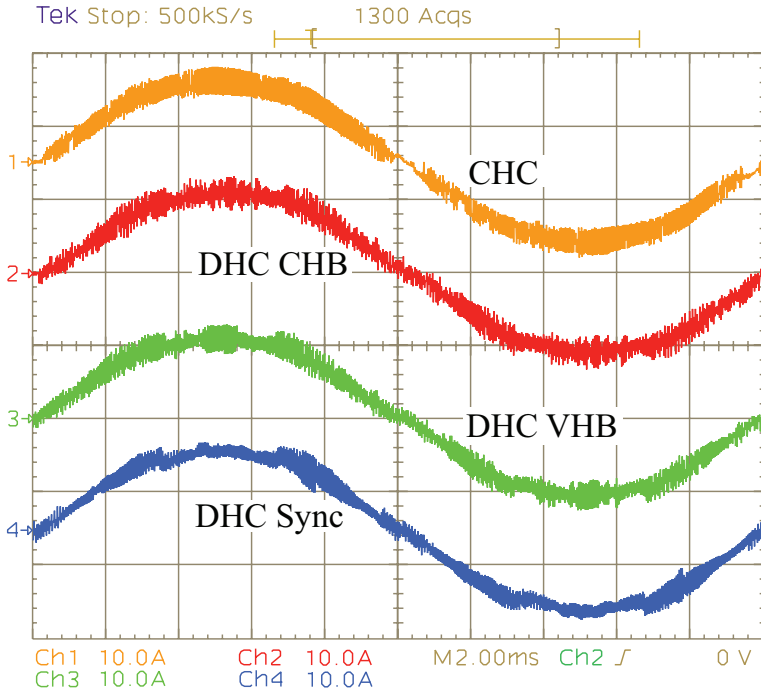


Figure 2.21: Comparison of experimental phase R currents generated by the different hysteresis controllers, i.e. conventional hysteresis control (CHC), decoupling hysteresis control with constant hysteresis band (DHC CHB), DHC with variable constant hysteresis band (DHC VHB), synchronized DHC (DHC Sync). Current scale: 10 A/div, time scale: 2ms/div.

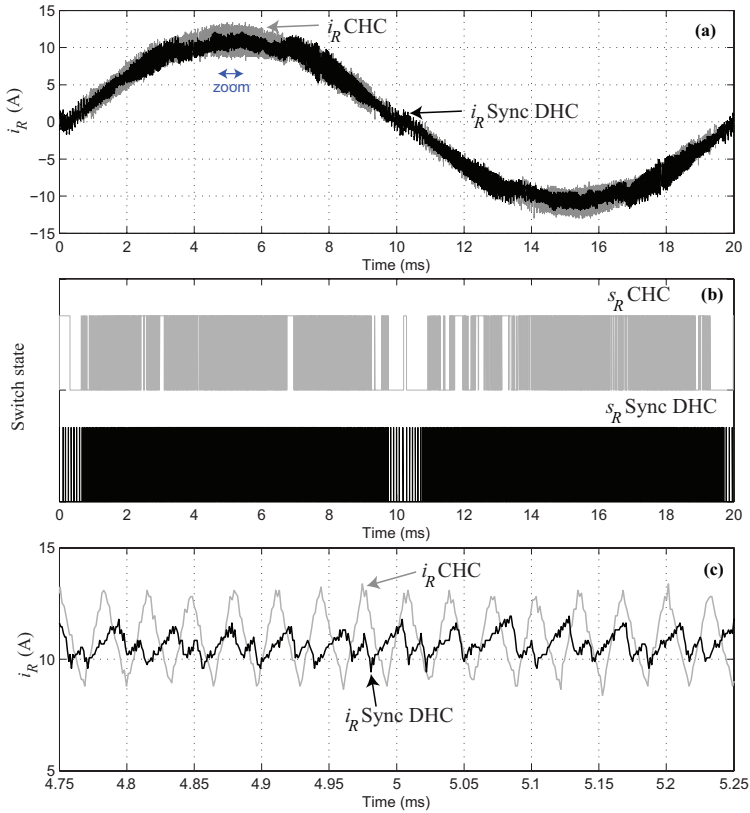


Figure 2.22: Experimental performance comparison of CHC and synchronized DHC; a) phase R current i_R , b) phase R switch signal s_R , c) zoomed view of i_R , showing the reduced current ripple level for the synchronized DHC.

Chapter 3

Center-Point Voltage Control

3.1 Introduction

The three-phase, current-controlled, voltage-source, PWM rectifier has found extensive application as front-end stage in AC drives [90, 91], in distributed power systems [92], as input power-supply for welding processes [93], within more-electric aircraft [94] due to several advantages such as:

1. regulation of input power factor to unity;
2. low harmonic distortion of line current;
3. adjustment and stabilization of DC-link voltage;
4. reduced size of the boost inductors.

Three-level topologies, as the circuit shown in Fig. 3.1 [95], have further advantages with respect to the conventional two-level topologies in terms of lower blocking voltage across the power switches and reduced input current ripple. However, a larger number of semiconductors is needed and the modulation becomes more complex. In addition, the balancing of the output capacitor voltages has to be ensured, in order to prevent over-voltage stress across the semiconductors and the output capacitors and to avoid low-frequency harmonics in the input rectifier voltage [96, 97, 85, 87].

3.1.1 Center-Point Voltage Balancing Methods

The problem of controlling the center-point voltage variations has been widely recognized for three-phase three-level inverters [87, 96, 97, 98, 99, 100, 101].

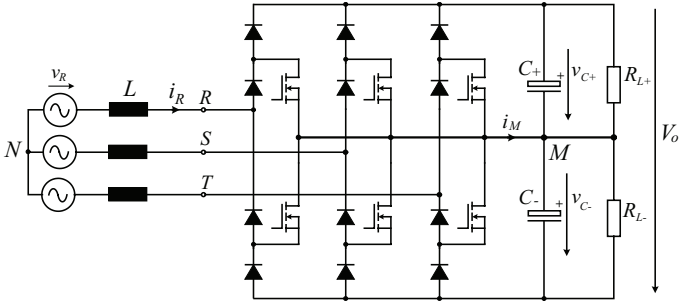


Figure 3.1: Power circuit of a unidirectional, three-phase, three-level, boost-type PWM rectifier [95].

The possibility of influencing the center-point voltage of a three-level rectifier is based on the existence of a degree of freedom in the modulation, constituted by the zero-sequence (common mode) voltage v_{NM} between the star point N of the supplying mains and the center point M of the DC-link (see Fig. 3.1). The voltage v_{NM} can be suitably shaped and used to optimize the modulation strategy [102, 98]. For indirect modulation of a three-level rectifier, the control variable that influences the voltage v_{NM} and controls the center-point voltage uses the redundant switching states that form identical rectifier input voltage space vectors. These switching states are characterized by opposite loading of the center point, i.e. the corresponding center point current has opposite signs. The appropriate selection of the redundant switching states enables the balancing of the center point voltage to be ideally independent of the control of the rectifier input voltage space vector. However, the use of the redundant switching states to control the center-point voltage besides the phase currents, introduces further switching transitions and can deteriorate the harmonic performance of the modulation [103].

On the other hand, direct (hysteresis) modulation uses actually the same degree of freedom but the control variable is constituted by the shaping of the hysteresis band and/or of the current reference signal. Several high-performance direct (hysteresis) modulation strategies have been proposed by suitably modifying the tolerance band and the most common objective is to stabilize the switching frequency [104, 36, 88]. This paper presents a method for the control of the output center-point voltage of unidirectional three-level PWM rectifiers, obtained by augmenting the current reference by an offset term. Independent hysteresis controllers are used to guide the phase currents along the mains-voltage shaped reference current. The modelling and dimensioning of the

center-point voltage control circuit are treated.

The stability of the center-point is then investigated, based on the analysis of the generation of the center-point current, in dependency on the converter switching states. It is shown that an asymmetry of the output partial voltages without control action results in a mean value of the center-point current, which increases the asymmetry. Thus, because of the intrinsic instability of the center-point, stable operation of a hysteresis current controlled rectifier is only possible when a center-point voltage control is implemented.

Due to the absence of the neutral current path, the mains current shape is not influenced by the offset injection. The following sections show how the offset signal affects the distribution and the frequency of the switching states used for the guidance of the mains current, which influences the value of the center-point current. Finally, the design of the center-point voltage control circuit is presented and its stationary and load-step performances are experimentally demonstrated.

3.1.2 Effect of the Center-Point Current

The center-point current i_M should be controlled in such a way that the output capacitors are symmetrically charged and the output partial voltages are equal. Since the center-point current is formed by segments of the mains currents, whose shape depends on the selected current control method, and since the charging/discharging of the output capacitors is dependent on i_M , hence the action of i_M represents the link between mains current controller and center-point voltage controller. The two controllers are therefore mutual dependent and the correct control of i_M is fundamental to ensure a proper operation of the three-level PWM rectifier.

It can be shown, [87], that the expression of the center-point current for a three-level PWM rectifier is given by

$$i_M(M, v_{NM}) = \hat{I}M\left(\frac{1}{2} + \cos 2\varphi\right) - \hat{I}\frac{v_{NM}}{\hat{V}}2\sin\varphi \quad (3.1)$$

where $\varphi = 2\pi ft$, f is the mains frequency, and \hat{I} and \hat{V} are the current and voltage peak values, respectively.

From (3.1), it follows that the value of the modulation index M and the shape of the zero-sequence voltage v_{NM} have direct influence on i_M , where the modulation index is defined as

$$M = \frac{\hat{V}}{\frac{1}{2}V_0} \quad (3.2)$$

and V_0 represents the total output voltage. In particular, it is well documented in

literature for three-level inverters, [96, 97, 98, 99, 100], how the proper selection of the redundant switching states in SVM (indirect modulation) affects the shape of v_{NM} , thus allowing the implementation of high-performance current and center-point voltage control strategies.

In direct, hysteresis modulation, the zero-sequence voltage v_{NM} can be controlled through the injection of a common-mode signal at a control level [87, 88]. The following sections show that a common signal added to each of the current references represents a control variable for the system analogous to the use of the redundant switching states in Space Vector Modulation. The conventional space vector representation is adopted hereafter to show the impact of the center-point voltage unbalance and the influence that the common signal has on the distribution and the frequency of the space vectors for the hysteresis current-controlled three-level PWM rectifier.

3.2 Interdependence of AC-side and DC-side Controllers

Three-phase three-level rectifiers possess redundant switching states concerning the formation of the local average values of the line-to-line input voltages. Fig. 3.2 shows the sum of the redundant switching states duty cycles as a function of the phase angle and of the modulation index. The duty cycles of the redundant switching states are mutually dependent by the parameter ρ defined as

$$\rho = \frac{\delta_-}{\delta_- + \delta_+}. \quad (3.3)$$

The opportune selection of ρ represents a degree of freedom of the control of these system which is usually applied for balancing the output capacitor center-point voltage. However the same degree of freedom can be used to minimize the rms value of the switching frequency mains current harmonics. Therefore, if the goal is the optimization of the overall system's control performance, then one has to pose the questions: (1) by which increase of the capacitor loading one has to pay for the optimization of the mains-side performance or, viceversa, (2) to which extend does a minimization of the load on the capacitors contribute to an increase of the ripple of the mains current. To obtain the balanced output voltages and/or a stable neutral point voltage, the neutral point current has to be minimized.

$$\frac{d}{dt} v_{M,avg} = \frac{1}{2C} i_{M,avg} \quad (3.4)$$

In this way, both the voltage stress across the switches (and hence the switching losses) and the low frequency harmonics of i_M are reduced. The optimization

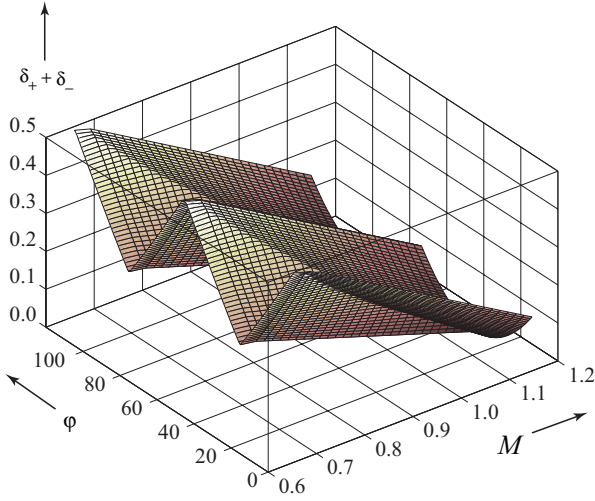


Figure 3.2: Sum of the relative on-time of the redundant switching states depending on M and φ .

criterion for the DC-side can be defined as:

$$i_{M,avg} \rightarrow 0. \quad (3.5)$$

The minimization of the square *rms* value of the input current ripple is a criterion to optimize the AC-side performance:

$$\sum \Delta i_{N,rms}^2 \rightarrow min. \quad (3.6)$$

The physical interpretation of this criterion is that the square of the global *rms* value of the phase current ripple is proportional to the losses. Figs. 3.3-3.5 show the distribution ρ of redundant switching states, the average center-point current $i_{M,avg}$ and the rms value of the ripple square, $\Delta i_{N,rms}^2$ when only one of these quantities is optimized.

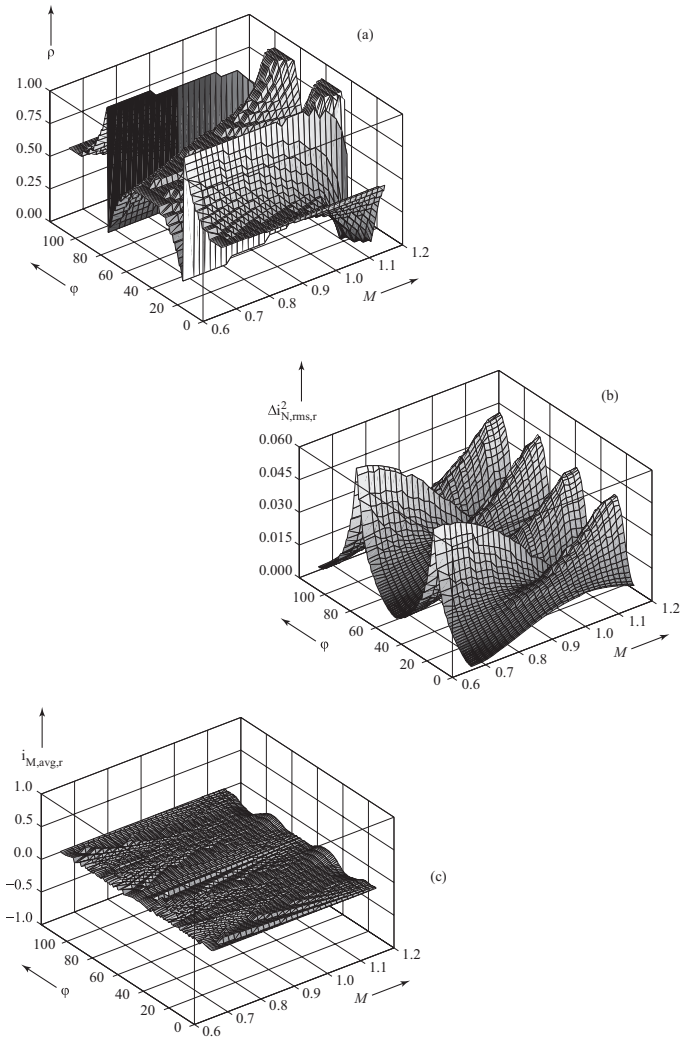


Figure 3.3: For DC-side optimization ($i_{M,avg} \rightarrow 0$): (a) distribution of the redundant switching states ρ , (b) local mains current ripple $\Delta i_{N,rms}^2$ and (c) local neutral point current $i_{M,avg}$.

3.2. INTERDEPENDENCE OF AC-SIDE AND DC-SIDE CONTROLLERS

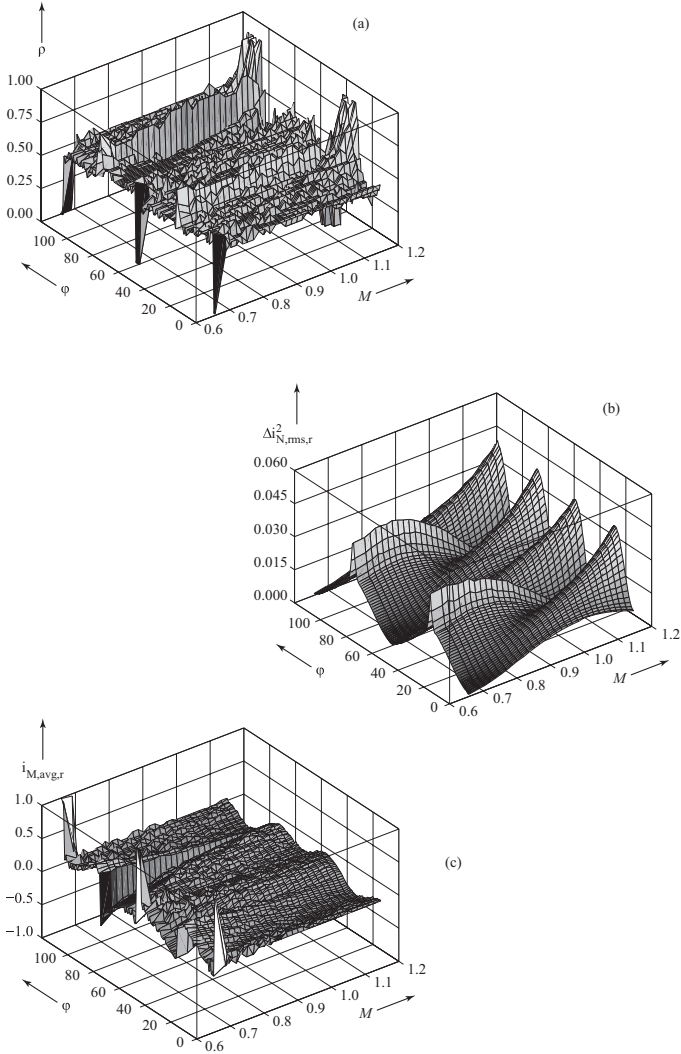


Figure 3.4: For AC-side performance optimization ($\Delta i_{N,rms}^2 \rightarrow Min$): (a) distribution of the redundant switching states ρ , (b) local mains current ripple $\Delta i_{N,rms}^2$ and (c) local neutral point current $i_{M,avg}$.

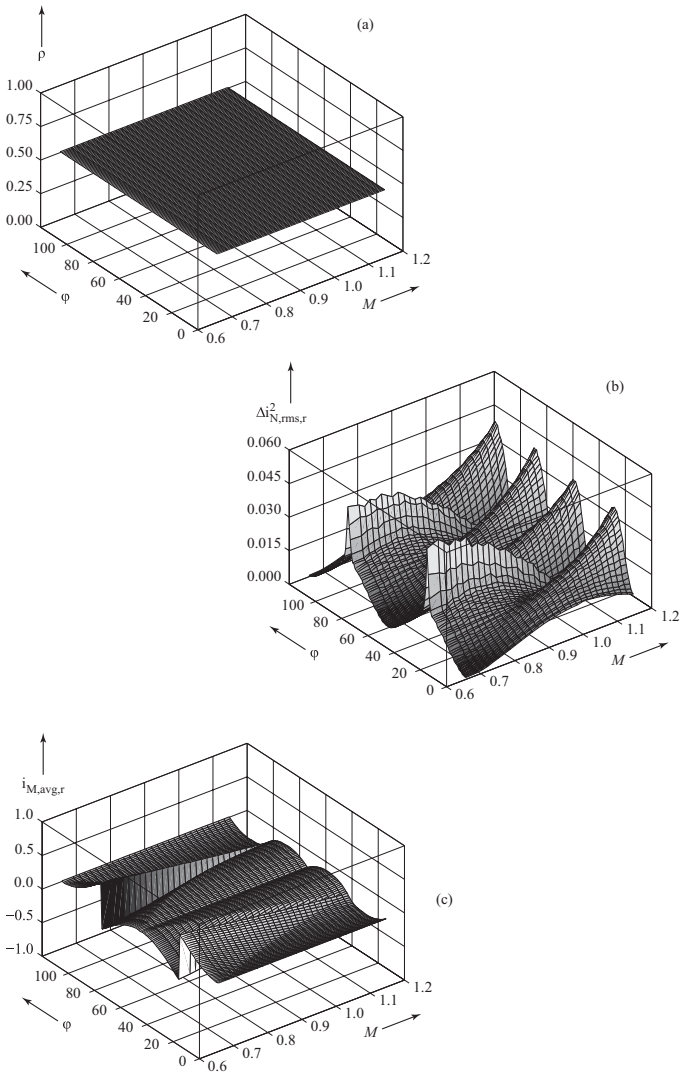


Figure 3.5: For constant control parameter $\rho = 0.5$: (a) distribution of the redundant switching states ρ , (b) local mains current ripple $\Delta i_{N,rms,r}^2$, (c) local neutral point current $i_{M,avg}$

3.3 Space Vector Analysis

In voltage-oriented control (indirect modulation), the rectifier input voltage is formed as the time average of the three nearest voltage space vectors available according to the mains phase angle, the modulation index and the switches' status. The space vector diagram in the stationary frame is usually used to represent all the space vectors available in a mains period. In indirect modulation, it is possible to directly select the space vectors and, in particular, the redundant space vectors in order to implement a specific control strategy.

In direct, hysteresis modulation, the space vector representation can be used to show how an offset of the phase current reference values (the control variable) affects the selection of the rectifier input voltage space vectors and, in particular, of the redundant switching states, in the same fashion as for indirect modulation. With this in mind, the effect of the center point voltage unbalance Δv_M on the space vector diagram is shown (Section 3.3.2) and then the influence of a current reference offset (Section 3.5).

3.3.1 Balanced Output Partial Voltages

The input current of a boost-type PWM rectifier is defined by the voltage drop \underline{v}_L across the input inductors L ,

$$\underline{v}_L = L \frac{d\hat{i}}{dt} = \underline{v} - \underline{v}_r \quad (3.7)$$

where \hat{i} is the input current phasor, as depicted in Fig. 3.7a, \underline{v}_r is the input rectifier phasor and

$$\underline{v} = \hat{V} e^{j\varphi} \quad (3.8)$$

is the mains voltage phasor.

The voltage space vectors available in the mains phase interval $\varphi \in (-\frac{\pi}{6}, +\frac{\pi}{2})$ for a three-level PWM rectifier are shown in Fig. 3.7a. Each switching space vector is denoted by the triple (t_R, t_S, t_T) formed by the phase switching functions t_i , where $t_i = \text{sgn}\{v_{iM}\} = \{+, 0, -\}$ if the respective phase input rectifier terminal is clamped to the positive rail, to the center-point or to the negative rail, respectively. The space vectors are usually classified into zero voltage vectors, small vectors which are the vertices of the inner hexagon, medium vectors which are the midpoints of the sides of the outer hexagon and large vectors comprising of the vertices of the outer hexagon.

The control unit of the converter has to guarantee the symmetry of the partial output voltages, v_{C+} and v_{C-} (see Fig. 3.1). The basis for controlling the center-point voltage is given by the knowledge of the center point currents

i_M resulting for different switching states. The center-point voltage unbalance Δv_M is defined as

$$\Delta v_M = \frac{1}{2}(v_{C-} - v_{C+}). \quad (3.9)$$

Accordingly, since $v_{C+} + v_{C-} = V_0$, then the output partial voltages are

$$v_{C-} = \frac{1}{2}V_0 + \Delta v_M \quad v_{C+} = \frac{1}{2}V_0 - \Delta v_M. \quad (3.10)$$

The current i_M loads the capacitive center point and is formed by sections of the phase currents in dependency on the switching states s_i of the power transistors

$$i_M = s_R i_R + s_S i_S + s_T i_T. \quad (3.11)$$

The voltage shift of the center point is hence given by

$$\frac{d\Delta v_M}{dt} = \frac{1}{2C} i_M \quad (3.12)$$

for constant output voltage V_0 and equal capacitor value $C_+ = C_- = C$. It should be noted that since the output partial voltages affect the center-point voltage shift in the same direction,

$$\frac{dv_{C+}}{dt} = -\frac{dv_{C-}}{dt},$$

the variation of the center-point voltage is determined only by i_M . Moreover, because of the constant output voltage, regulated by the output voltage controller $F(s)$, the parallel connection $2C$ of both capacitors is acting. The center point current (3.11) resulting for the possible combinations of values of the phase switching functions for $\varphi \in (-\frac{\pi}{6}, +\frac{\pi}{6})$ (see Fig. 3.6) can be taken directly from Fig. 3.8 and they are summarized in Tab. 3.1. In Fig. 3.8 the contribution to i_M of three different types of rectifier input space vectors or switching states is represented. Exemplarily, the space vectors for sector 1 are chosen (cf. Fig. 3.7). The short space vectors of $(0 - -)$ and $(+00)$, corresponding to the redundant switching states, provide the largest contribution to i_M in opposite directions. This is indicated in Tabs. 3.1 and 3.2 through a double contribution $(++$ or $--)$, respectively. The medium vectors contribute also to i_M , like $(+0-)$ in Fig. 3.8, and are indicated in Tabs. 3.1 and 3.2 by a single sign, $+$ or $-$, according to the direction of i_M . Long vectors, like $(+ - -)$ in Fig. 3.8, do not contribute to i_M .

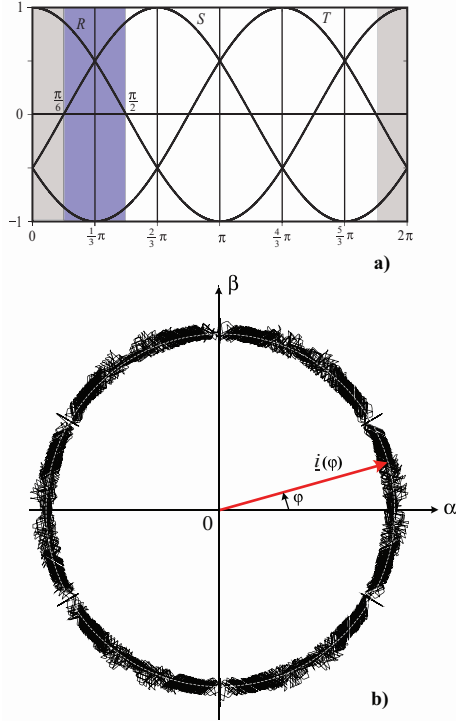


Figure 3.6: a) Three-phase reference signals. b) Phase current phasor trajectory in the complex plane for hysteresis current controlled three-level PWM rectifier.

3.3.2 Unbalanced Partial Output Voltages

In case of asymmetry of the partial output voltages, the input rectifier voltage phasor \underline{v}'_r is given by the sum of the vector \underline{v}_r as defined for balanced conditions and a distortion space vector $\Delta\underline{v}$ that is dependent on converter switching states,

$$\underline{v}'_r = \underline{v}_r + \Delta\underline{v}, \quad (3.13)$$

where the phasor \underline{v}_r is defined as

$$\underline{v}_r = \frac{2}{3} (v_{RM} + \alpha v_{SM} + \alpha^2 v_{TM}), \quad \alpha = e^{j\frac{2}{3}\pi} \quad (3.14)$$

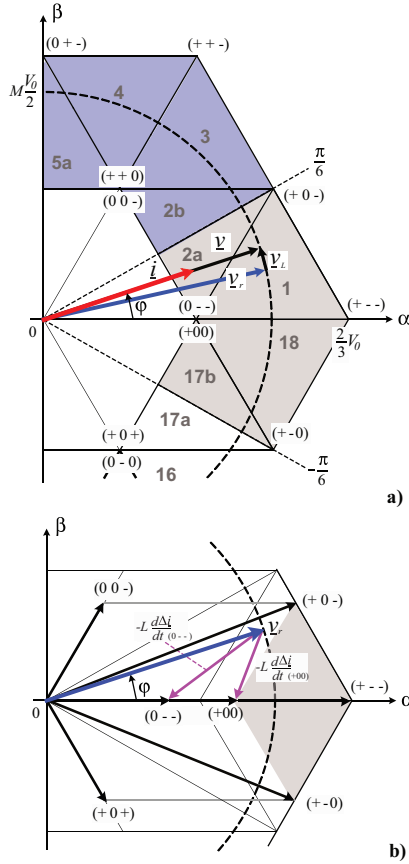


Figure 3.7: a) Space vector diagram in the interval $\varphi \in (-\frac{\pi}{6}, +\frac{\pi}{2})$ for a three-level rectifier: $\underline{v}(\varphi)$ and $\underline{i}(\varphi)$ are the mains voltage and current space vectors, respectively; $\underline{v}_r(\varphi)$ is the input rectifier voltage space vector. b) Space vector diagram for the case of unbalanced center-point voltage, $\Delta v_M < 0$ in the interval $\varphi \in (-\frac{\pi}{6}, +\frac{\pi}{6})$.

and the distortion vector is given by

$$\Delta \underline{v} = \frac{2}{3} \Delta v_M (s_R + \alpha s_S + \alpha^2 s_T). \quad (3.15)$$

Table 3.1: Influence of the switching states on the center-point current i_M , average voltage shift, and average voltage shift weighted with the relative switching state on-time δ within the interval $\varphi \in \left(-\frac{\pi}{6}, +\frac{\pi}{6}\right)$.

t_R	t_S	t_T	i_M	$\left(\frac{d\Delta v_M}{dt}\right)_{\text{avg}}$	$\delta \left(\frac{d\Delta v_M}{dt}\right)_{\text{avg}}$
+	-	-	0	0	0
+	-	0	i_T	-	--
+	0	-	i_S	-	--
+	0	0	$-i_R$	--	--
0	-	-	$+i_R$	++	++
0	-	0	$-i_S$	+	+
0	0	-	$-i_T$	+	+

Table 3.2: Influence of the switching states on the center-point current i_M , average voltage shift, and average voltage shift weighted with the relative switching state on-time δ within the interval $\varphi \in \left(+\frac{\pi}{6}, +\frac{\pi}{2}\right)$.

t_R	t_S	t_T	i_M	$\left(\frac{d\Delta v_M}{dt}\right)_{\text{avg}}$	$\delta \left(\frac{d\Delta v_M}{dt}\right)_{\text{avg}}$
+	+	-	0	0	0
+	+	0	i_T	--	--
+	0	-	i_S	+	++
+	0	0	$-i_R$	-	-
0	+	-	$+i_R$	+	++
0	+	0	$-i_S$	-	-
0	0	-	$-i_T$	++	++

The distortion space vectors for the interval $\varphi \in \left(-\frac{\pi}{6}, +\frac{\pi}{6}\right)$ are given in Tab. 3.3.

If the capacitive center-point M is not loaded (long space vectors and $i_M = 0$) a voltage shift Δv_M does not influence the corresponding voltage space vectors. In this case, the rectifier input voltage is only determined by the total amount of the output voltage. The distortion space vectors $\Delta \underline{v}$ of the switching states associated with the short and medium space vectors show a constant absolute value and are defined directly by the asymmetry.

The resultant voltage space vectors for $\Delta v_M < 0$ and $\varphi \in \left(-\frac{\pi}{6}, +\frac{\pi}{6}\right)$ are shown in Fig. 3.7b. For hysteresis current control the switching frequency, which is dependent on the intersection of the phase current ripple with the respective tolerance band, is influenced by the absolute values of the corresponding space vectors $\frac{d\Delta i}{dt}$ defining the time behavior of the current error.

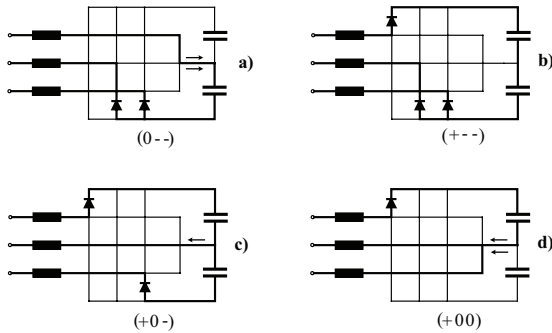


Figure 3.8: Dependence of the center-point current on the converter switching state for Sector 1. In particular the schematics a) and d) are referred to the redundant switching states or short space vectors, b) to the long vectors (no center-point current) and c) to the medium vectors.

The change of the on-time of the space vectors is a direct consequence of the variation of the mutual position of the space vectors in case of partial output voltages asymmetry. Thus the space vectors that in the unbalanced case are closer to the trajectory of the rectifier input voltage reference (proportional to the current reference) have therefore a longer relative on-time. In particular, for $\Delta v_M < 0$ the space vectors associated with the redundant switching states have different length. According to Fig. 3.7b, the asymmetry $\Delta v_M < 0$ leads to the change of the length of the space vectors $v_{(0-)}$ and $v_{(+00)}$ by the same amount in the opposite directions, besides a rotation of the vectors of the switching

Table 3.3

t_R	t_S	t_T	Δv
+	-	-	0
+	-	0	$+\frac{2}{3}\Delta v_M \alpha^2$
+	0	-	$+\frac{2}{3}\Delta v_M \alpha$
+	0	0	$-\frac{2}{3}\Delta v_M$
0	-	-	$+\frac{2}{3}\Delta v_M$
0	-	0	$-\frac{2}{3}\Delta v_M \alpha$
0	0	-	$-\frac{2}{3}\Delta v_M \alpha^2$

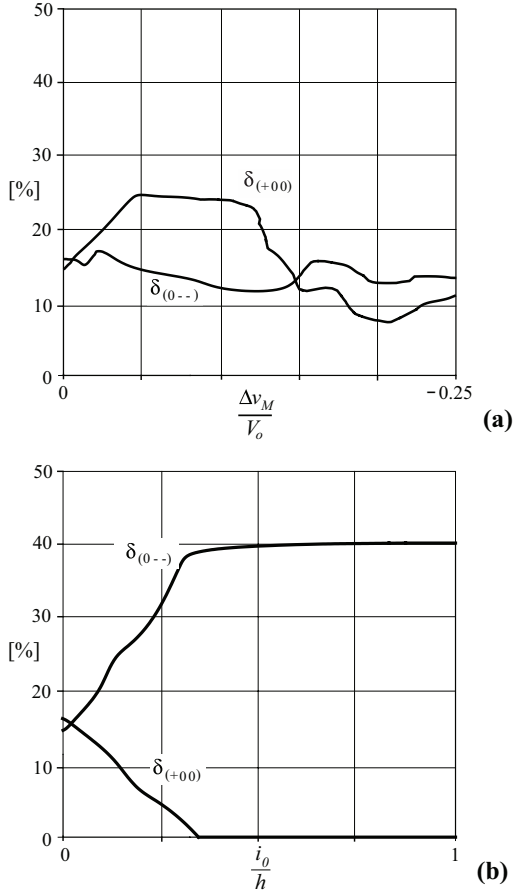


Figure 3.9: Average relative on-time $\delta_{(+00)}$ and $\delta_{(0--)}$ of the redundant switching states (+00) and (0 --) in Sector 1 as function of (a) of the center point voltage shift Δv_M normalized to the total output voltage V_o and (b) of the current offset i_o normalized to the hysteresis band amplitude h .

states (+0-) and (+ - 0). According to the space vector representation in Fig. 3.7b and the simulated relative on-time in Fig. 3.9a, for modulation index $M \in \left[\frac{2}{3}, \frac{2}{\sqrt{3}} \right]$ the switching state (+00) is preferred as compared to (0 --).

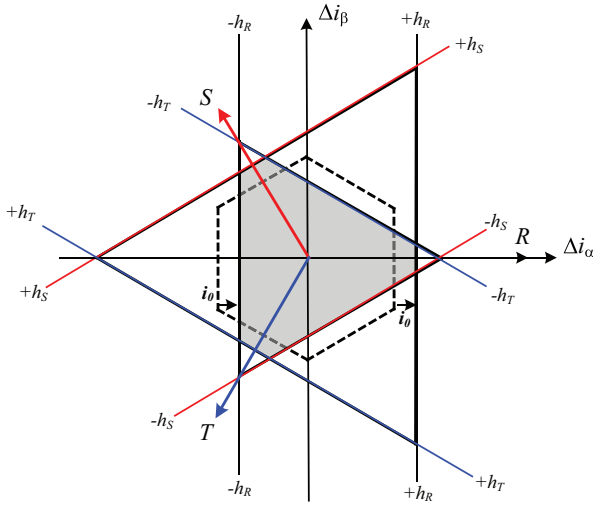


Figure 3.10: Space vector representation of the current ripple Δi for offset $i_o = 0$ (dashed line) and $i_o > 0$. The positive and negative hysteresis thresholds, $+h_i$ and $-h_i$ (index $i = R, S, T$) respectively, vary according to the value of i_o . For $i_o = \frac{1}{3}h$ the positive switching thresholds are touched by the tolerance area only in one point.

Moreover, the unbalance affects the position of the medium space vector, which also contributes to the center point current. If the relative on-time, δ , is defined as

$$\delta = \frac{t_{on, \Delta v_M < 0}}{t_{on, \Delta v_M = 0}}, \quad (3.16)$$

then the center point current is weighted by a factor proportional to δ , as indicated in the Tabs. 3.1 and 3.2 by the quantity

$$\delta \left(\frac{d\Delta v_M}{dt} \right)_{\text{avg}}. \quad (3.17)$$

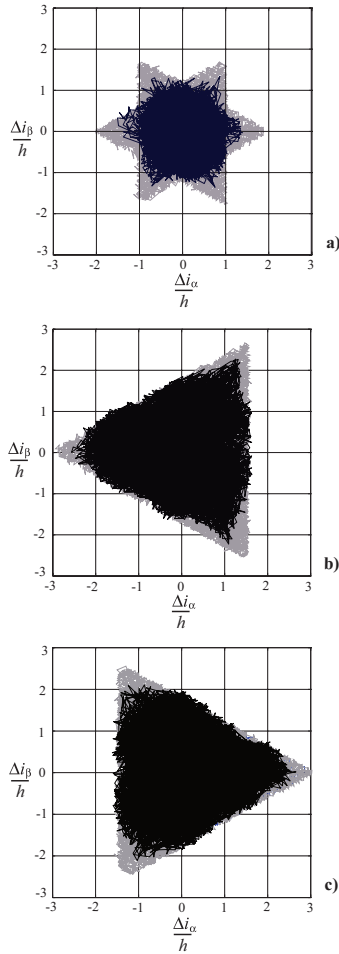


Figure 3.11: Experimentally measured (black line) and simulated trajectories (gray line) in the complex plane of the current-error space-vector $\Delta \dot{\mathbf{i}}$ for hysteresis modulated three-level PWM rectifier. a) $i_o = 0$, b) $i_o = +0.5 h$ and c) $i_o = -0.5 h$, where $2h$ is the width of the hysteresis band. The specifications and operating point of the experimental three-level rectifier are given in Tab. 3.6.2.

3.4 On the Inherent Stability of the Center-Point

In order to maintain stationary stability for higher modulation index and/or in case of unbalanced, non-linear loads or no load operation, one has to investigate whether a voltage shift Δv_M causes an increase or decrease of the mean center-point current value I_M and if a center-point loading effect of the current i_M leads to an instability of the center-point voltage.

If a constant switching frequency is assumed, i.e. equal switching on-time and uniform distribution within the phase interval $\Delta\varphi$, no mean voltage shift of the capacitor center point voltage results, which is given by the sum of the contributions $\left(\frac{d\Delta v_M}{dt}\right)_{\text{avg}}$ due to the different switching states. However, for hysteresis control of the phase currents, the switching states resulting in a lower current variation $\frac{d\Delta i}{dt}$, i.e. the space vectors lying in the vicinity of the trajectory of the input rectifier voltage phasor \underline{v}_r , have a greater mean existence interval and/or higher relative on-time δ . In particular, the effect of the medium space vectors has an influence on the average center-point current $i_{M,\text{avg}}$, where $i_{M,\text{avg}}$ denotes averaging over a $\frac{\pi}{3}$ -wide interval.

For the segment of the mains period $\varphi \in (-\frac{\pi}{6}, +\frac{\pi}{6})$ there results, according to the reference signals shown in Fig. 3.6a, an increase of v_{C+} over v_{C-} . The space vectors diagram is consequently modified, as shown in Fig. 3.7b. Therefore, as shown in Tab. 3.1, a negative mean value $i_{M,\text{avg}}$ results. An analog analysis of the center point current for the angle interval $\varphi \in (+\frac{\pi}{6}, +\frac{\pi}{2})$ leads to the values compiled in Tab. 3.2. There results a positive mean value $i_{M,\text{avg}}$, which is opposite to the previous interval. The analysis of further angle intervals leads to alternating positive and negative contributions of $i_{M,\text{avg}}$. Accordingly, the fundamental frequency of the center point current i_M is defined by $3f$, where f is the mains frequency, as known also from three-level PWM inverters [87]. Based on the previous considerations and on ideally equal system behavior within the different angle intervals one would not expect a voltage shift in the average over a mains period. However, due to the mutual influence of the three independent hysteresis phase current controllers, there results a stochastic [105, 106] or chaotic [107] sequence and/or large variation in the on-times and distributions of the different switching states. Thus, the center point current i_M shows in general a small DC component I_M (mean value over a mains period) or a low frequency harmonic, lying below the mains frequency. This leads to an asymmetry of the partial output voltages and/or to a shift Δv_M of the output voltage center point, which acts in the direction to further increase the asymmetry, as apparent from the center-point characteristic shown in Fig.3.17.

3.5 Impact of the Current Reference Offset

The center-point voltage control of a hysteresis current controlled three-level PWM rectifier needs to be implemented because the center point voltage is unstable. In analogy to the Space Vector Modulation, the switching states should be selected such that the corresponding input rectifier space vectors generate a center-point current flow with zero average over a mains period. Since the switching decisions s_i' are derived directly from the comparison of the phase current ripple and the hysteresis band, the possibility of controlling the frequency of the different switching states is limited to a modification of the reference value and/or to a variation of the hysteresis band shape.

3.5.1 Effect of the Offset on Switching Frequency and on Center-Point Voltage Drift

The control action consists of the modification of the tolerance band, or equivalently, of the current reference, by means of the addition of an offset component i_o ,

$$\begin{aligned} i_R^{*'} &= i_R^* + i_o \\ i_S^{*'} &= i_S^* + i_o \\ i_T^{*'} &= i_T^* + i_o \end{aligned} \quad (3.18)$$

Since the rectifier's output center-point is not connected to the mains neutral point, the sum of the mains phase currents is forced to zero at all times and therefore, the offset i_o cannot be produced by the phase current controllers and does not influence the mains current shape. The space vector representation of the control errors of the phase currents $\Delta i_i = i_i - i_i^{*'}$, whose complex components are given by

$$\begin{aligned} \Delta i_\alpha &= \Delta i_R - i_o \\ \Delta i_\beta &= \frac{1}{\sqrt{3}} (\Delta i_S - \Delta i_T), \end{aligned} \quad (3.19)$$

clearly shows that i_o has influence on the form of the tolerance area (see Fig. 3.10) defined by the intersection of the tolerance bands of each phase current controllers. Therefore, the offset has influence on the frequency of the switching states used for guidance of the mains current and consequently the value of the center point current.

For $i_o = 0$, the tolerance area shows the characteristic form of an equilateral hexagon, limited by segments of the positive and negative switching thresholds of equal length (see Fig. 3.10). Accordingly, for both switching thresholds there

exists equal switching frequency,

$$f_+ = f_-$$

where f_+ and f_- indicate the number of intersections of the current ripple with the positive and negative threshold, respectively.

If now the switching thresholds are shifted due to an offset i_o of the phase current reference values, the tolerance area is distorted and the conditions in (2.1) are now given by:

$$s'_i = \begin{cases} 0 & \text{if } i_i > i_i^* + h + i_o \\ 1 & \text{if } i_i < i_i^* - h + i_o \end{cases} . \quad (3.20)$$

For $i_o > 0$, an increase of the contribution of the negative switching thresholds is given in Fig. 3.10. Accordingly, for guidance of Δi within the tolerance area the switching frequency f_- is increased and f_+ decreased, respectively. Therefore, the on-switching states, $(s_{R'}, s_{S'}, s_{T'}) = (1xx), (x1x), (xx1)$ are used more often, leading to a positive center-point voltage shift ($\frac{d\Delta v_M}{dt} > 0$). This effect is shown in Fig. 3.12, where the shape of the center point current for a discrete value of the offset i_o is represented for a mains period, along with the phase current R . The resulting experimentally measured trajectories of the space vector Δi (3.19) are given in Fig. 3.11 for $i_o = 0, 0.5 h$ and $-0.5 h$. Fig. 3.9(b) shows the change in the average relative on-times $\delta_{(0--)}$ and $\delta_{(+00)}$ of the redundant switching states $(0--)$ and $(+00)$ ($\varphi \in (-\frac{\pi}{6}, +\frac{\pi}{6})$) for increasing values of the offset current. It can be seen that the switching state $(0--)$ becomes dominant for a positive i_o .

For $i_o < 0$, an analog consideration leads to $f_+ > f_-$ and finally to $\frac{d\Delta v_M}{dt} < 0$. Therefore, the offset signal i_o offers the possibility of an active symmetrization of the partial output voltages and/or of a control of the voltage of the output voltage center point.

3.5.2 Dependence of the Center-Point Current on the Current Reference Offset

The average value I_M resulting for a defined shift i_o of the reference values and/or the gain

$$k_M = \frac{\Delta I_M}{\Delta i_o} \quad (3.21)$$

of the output signal i_o of the center-point voltage controller has been experimentally measured and the resulting control characteristic $I_M = I_M(i_o)$ is shown in Fig. 3.13. In this case the partial capacitor voltages are externally forced to be equal, $\Delta v_M = 0$, and there is a constant output voltage V_0 and a constant

3.5. IMPACT OF THE CURRENT REFERENCE OFFSET

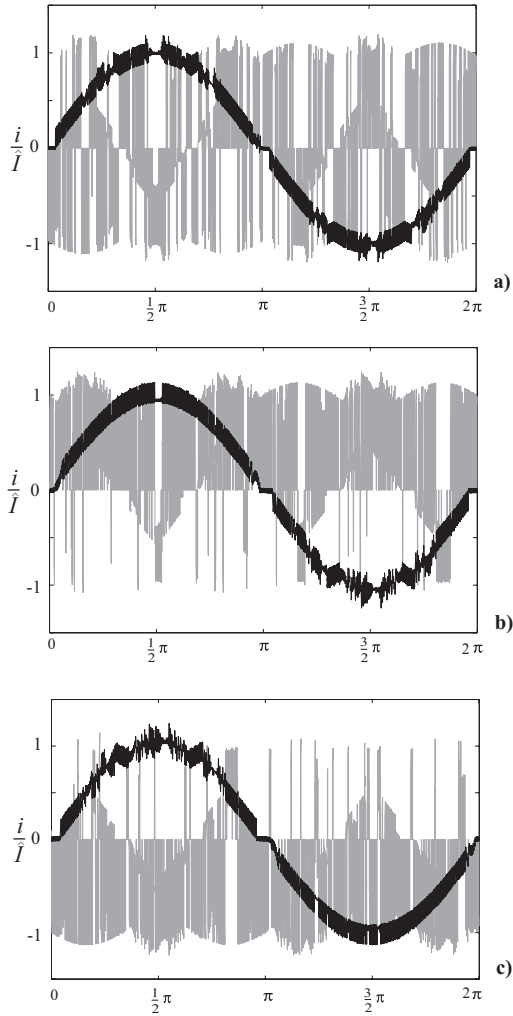


Figure 3.12: Simulated time behavior of the phase current i_R (black line) and of the center-point current i_M (gray line) for different values of i_o . a) $i_o = 0$, b) $i_o = +0.5 h$ and c) $i_o = -0.5 h$, where h is the hysteresis band amplitude.

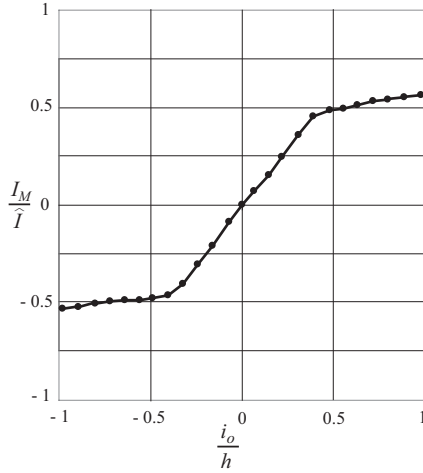


Figure 3.13: Experimentally measured and normalized output center-point control characteristic. The current offset i_o is normalized to the amplitude of the hysteresis band h , while the resulting center point current average value I_M is normalized to the mains current amplitude \hat{I} .

amplitude of the phase current reference values \hat{I}^* . The characteristic can be approximated by a straight line around the origin,

$$i_M = I_{M,\Delta v_M=0} + k_M i_o \quad (3.22)$$

where, $I_{M,\Delta v_M=0}$ describes the average value of the center point current related to a mains period, occurring without control input ($i_o = 0$) and for symmetric partition $\Delta v_M = 0$ of the output partial voltages.

The center point current i_M shows in a first approximation a linear dependency on the amplitude of the phase current reference values \hat{I}^* , as apparent from (3.11) and Fig. 3.13. It should be noted that a reduction of the mains voltage amplitude \hat{V} and/or a reduction of the modulation index M leads to an increase of the absolute value of I_M resulting for a defined value i_o (3.1).

The saturation in the control characteristic (see Fig. 3.13) for $i_o = \pm \frac{1}{3}h$ becomes clear by inspection of Fig. 3.10. For $i_o = +\frac{1}{3}h$ the positive switching thresholds are touched by the tolerance area at only one point. Therefore, the tolerance area assumes the form of a triangle and is limited exclusively by negative switching thresholds (cf. Fig. 3.11). Thereby, the limit of an approximately

3.5. IMPACT OF THE CURRENT REFERENCE OFFSET

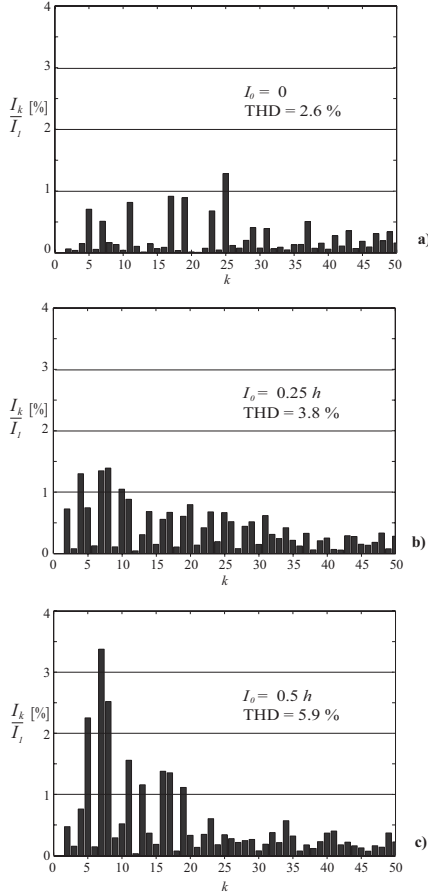


Figure 3.14: Frequency spectrum of the mains current of a hysteresis current controlled three-level PWM rectifier. The k -harmonics ($k = 2 \dots 50$) amplitudes referred to the fundamental are shown for: a) $I_o = 0$, b) $I_o = +0.25 h$ and c) $I_o = +0.5 h$, where h is the hysteresis band amplitude. The THD values are calculated up to the 50th harmonic.

linear influence of i_o on the relative on-times δ_+ and δ_- of the redundant switching states is reached. A further increase of i_o has no importance in practice and results only in a small increase of the average value I_M .

It is of interest to analyze if the offset i_o produces low frequency harmonics, especially those of even order, due to the asymmetry of the positive and negative half cycles caused by i_o . Fig. 3.14 shows the analysis of the amplitude spectrum of the mains current shape. The low frequency spectral components of the mains current are significantly influenced only for very large values i_o . For the stationary value,

$$I_{0,\Delta v_M=0} = \frac{1}{k_M} I_{M,\Delta v_M=0},$$

adjusted in practice by the center point voltage controller, there results in no low frequency distortion of the mains currents.

3.6 Center-Point Voltage Control

The block diagram for the control of the center-point voltage is shown in Fig. 3.16 and is considered in the following for dimensioning the center point voltage controller $G(s)$ (see Fig. 3.15).

The center point voltage control represents actually a fixed command control $\Delta V_M^* = 0$. Therefore, the control loop has to be designed with respect to its disturbance response. A disturbance of the symmetrical voltage partition can result, from a change of the system load status. Hence, the output voltage controller $F(s)$ changes the amplitude of the mains phase current reference values within a mains period. Due to the direct coupling between center point current and mains current (3.11) this results in the occurrence of a transient mean value of i_M . A direct loading of the center-point can result from an asymmetric partition of the load supplied by the rectifier among the partial output voltages. The disturbance influence is considered in Fig. 3.16 by the current I_Z .

3.6.1 Center-Point Characteristic

Fig. 3.17 shows that the deviation of the partial output voltages from the symmetrical case results in a mean value I_M , which produces further asymmetry and is proportional, in a first approximation, to ΔV_M . This behavior can be described by a positive feedback,

$$g_M = \frac{\Delta I_M}{\Delta V_M} \quad g_M > 0 \quad (3.23)$$

corresponding to the slope of the characteristic $I_M(\Delta V_M)$ at the origin. Therefore, the system $S(s)$ to be controlled by the center point voltage control (see

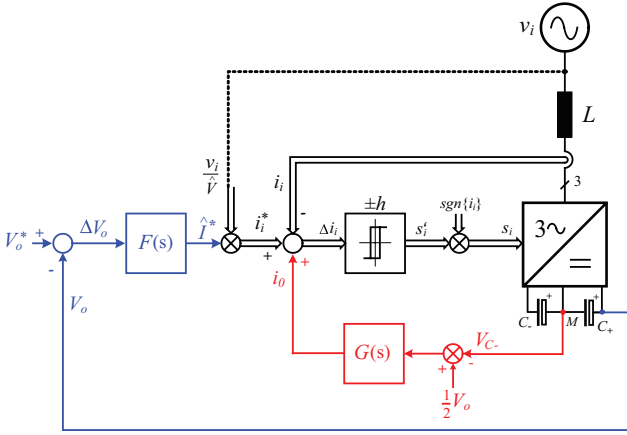


Figure 3.15: Control block diagram of a three-level PWM rectifier showing the feedback control of output rectifier voltage V_o , the input current feedback control and output center-point voltage feedback control.

Fig. 3.16) shows a pole in the right-hand s -half-plane

$$S(s) = \frac{1}{s - \frac{g_M}{2C}}. \quad (3.24)$$

It should be noted that the rectifier modulation index (3.2) has influence on the value of the gain g_M . A reduction of the mains voltage (reduction of M) and/or relative reduction of the mains voltage peak value (defining the trajectory of the fundamental of \underline{v}_r) results in an increase of the gain g_M for $M \in \left[\frac{2}{3}, \frac{2}{\sqrt{3}}\right]$. This is true since in general a larger relative on-time of the switching states associated to the short space vectors is given, which contribute mostly to the center-point current.

The fundamental frequency of the center point current is given by $3f$ due to the operating principle of the system. In order to avoid a mutual influence of the phase current control and of the center point voltage control, the cross-over frequency should occur sufficiently below $3f$. Thus the model shown in Fig. 3.16, based on averaging over a fundamental period, can be directly applied for dimensioning of the controller.

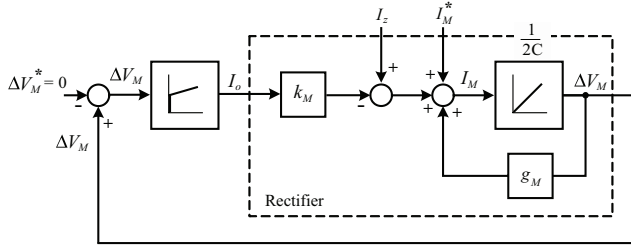


Figure 3.16: Block diagram of the center point voltage control based on averaging the quantities ΔV_M and I_M related to one mains period.

3.6.2 Design of the Center-Point Voltage Controller

If $G(s)$ is realized, with respect to the stationary operation $\Delta V_M = 0$, as a PI-controller such that

$$G(s) = k_p + \frac{k_I}{s}, \quad (3.25)$$

it follows that the disturbance response is

$$\frac{\Delta V_M(s)}{I_Z(s)} = k \frac{s}{1 + 2d \frac{s}{\omega_0} + \left(\frac{s}{\omega_0}\right)^2} \quad (3.26)$$

with

$$k = \frac{1}{k_I k_M} \quad \omega_0 = \sqrt{\frac{k_I k_M}{2C}} \quad d = \frac{k_P k_M - g_M}{2\sqrt{2C k_I k_M}}. \quad (3.27)$$

Therefore, for a step function disturbance $I_Z(s) = \frac{I_Z}{s}$ the center point voltage has a shape corresponding to an impulse response of a second-order transfer function with gain k , characteristic frequency ω_0 and damping d . Based on the impulse response of such a function, the controller parameters k_P and k_I can be easily calculated and used for a desired transient response and/or damping and characteristic frequency.

For determining the gain k_P of the P-component of the controller, the limitation of the correcting value introduced for values $i_o > \frac{b}{3}$ (Fig.3.17) needs to be considered as well as the increase in the variation of Δv_M with a frequency $3f$, for increasing k_P .

For low load there results a reduction in the damping of the control loop and a decrease of the characteristic frequency ω_0 (3.27), due to a decrease of

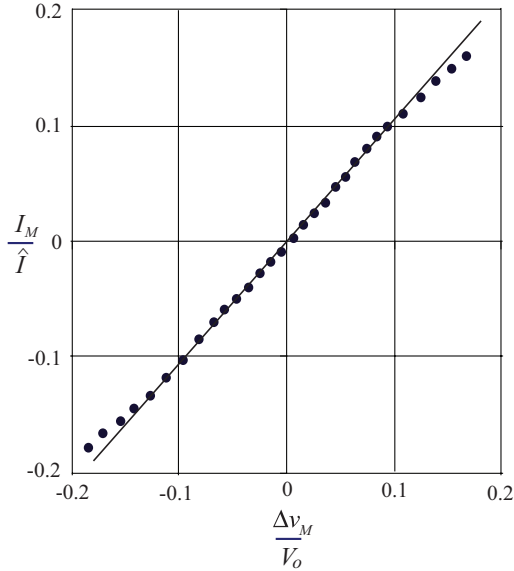


Figure 3.17: Experimentally measured and normalized center-point characteristic. The center-point voltage shift ΔV_M is referred to the output voltage V_o while the center-point current I_M is referred to the mains-current amplitude \hat{I} .

the gains k_M and g_M , which are proportional to the mains current amplitude in a first approximation. Concerning the assumption of a constant output voltage it should be noted, that there is a certain decoupling between the controller of the output partial voltages (center-point control) and the total output voltage

Table 3.4: Experimental Setup Parameters

parameter	symbol	value
mains voltage	v_{rms}	30 V
output voltage	V_o	115 V
peak reference current	\hat{I}^*	5 A
hysteresis band	$\pm h$	± 0.5 A
input inductance	L	1 mH
output capacitance	C	940 μ F

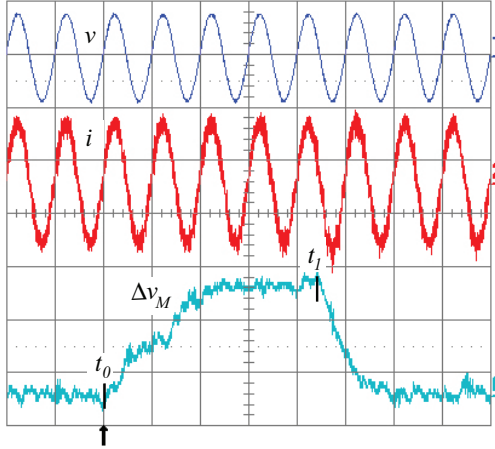


Figure 3.18: Measured input voltage (Ch. 1, 50 V/div) phase current (Ch. 2, 2 A/div) and center point voltage Δv_M (Ch. 4, 20 V/div) for open ($t = t_0$) and closed ($t = t_1$) center-point voltage control loop. The total output voltage is $115 V_{DC}$. Time scale: 20 ms/div.

controller. The dynamics of the two controllers are different since for the center-point voltage control the dynamically active capacitance of the output circuit is defined by the parallel circuit of the partial capacitors ($2C$), while for the output voltage control by the series connection ($\frac{1}{2}C$). Furthermore, the center point current oscillates with three times the mains frequency. This requires a relatively low cross-over frequency of the center point voltage controller. Contrary to this, there is an ideally constant power flow for output voltage control. Therefore, the controller dimensioning can be performed without taking consideration of the low-frequency variation of the controlled quantity.

3.6.3 Stationary Operation

Verification of the performance of the center-point voltage controller has been undertaken using a three-level *Vienna* rectifier [13] with the specifications and operating point given in Table 3.6.2. Fig. 3.18 shows the variation of Δv_M during the operation and non-operation of the center point voltage control loop. It can be seen that the center point voltage difference is initially controlled to be zero ($\Delta V_M^* = 0$) until $t = t_0$. As can be expected due to the I-component of

the controller $G(s)$ (3.25), no stationary error results. At $t = t_0$ the center-point voltage controller is turned off and the voltage shows a shape corresponding to the step response of an integrator with positive feedback. The step disturbance is given there by the absence of the controller output $k_M I_{0, \Delta v_M = 0}$ compensating the average value of the center point current due to the statistic sequence of the switching states of the system. An almost identical shape of the step response of the linear model (3.24) of the real system is given only in the vicinity of $\Delta v_M = 0$. According to Fig. 3.17, an increasing asymmetry is associated with a reduction of the positive feedback. The control loop is activated again at $t = t_1$, accordingly the asymmetry of the partial voltages is controlled back to zero. and that there is very little overshoot of the voltage. As shown in Fig. 3.18, the sinusoidal guidance of the phase currents is slightly influenced by the asymmetric partition of the output voltage, this is due to the hysteresis control. It can also be seen that a relatively large shift of the center point ($\Delta v_M \approx 0.2 V_o$) leads to no significant distortion of the mains current shape.

3.6.4 Dynamic Operation

In order to analyze the dynamic behavior of the center point voltage control the center point M is loaded by a step function of an external current disturbance i_Z . The value i_Z of the distortion function is fitted to the respective mains current amplitude and it is changed to be proportional to the output power of the system. This corresponds, in a first approximation, to the disturbance to be expected for loading of the center point by a converter connected in series. The measured shape of the center point voltage for a load step from 2.9 A to 5.4 A is shown in Fig. 3.19. It can be seen that this results in a deviation of 4 V from a 57.5 V average center-point voltage.

The dynamic quality of the control is influenced by the output power and/or by the mains current amplitude which influences directly the parameters g_M and k_M . With decreasing output power, the oscillation tendency of the system increases and the settling time rises accordingly. A control quality constant for a wide load range can be obtained only by adaption, i.e. by varying the controller gains proportional to $1/\hat{I}^*$ (3.27). An alternative is given by elimination of the load dependency of k_M by a current proportional variation of the hysteresis width.

The amount of the control error is limited to values $< 2\% V_o$. The ripple of the center point voltage Δv_M is caused by the center point current variations with three times the mains frequency. The open loop gain of the control is $\ll 1$ for $3f$, hence the voltage ripple is not influenced by the feedback due to $G(s)$.

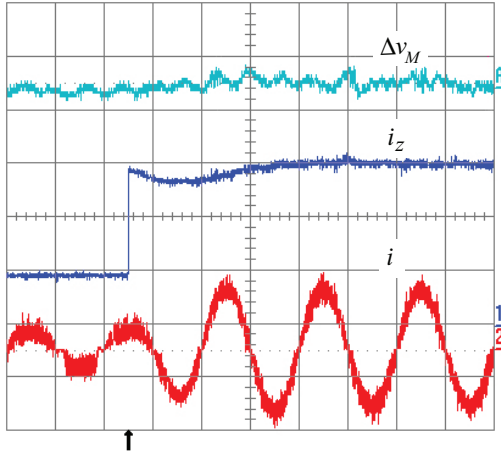


Figure 3.19: Measured line current (Ch. 2, 4 A/div), load current (Ch. 3, 0.5 A/div) and center-point voltage Δv_M (Ch. 4, 10 V/div) for a load-step. The total output voltage is $115 V_{DC}$. Time scale: 5 ms/div.

3.7 Conclusion

A center-point voltage controller for a three-level PWM rectifier is implemented by augmenting the current reference value by a common offset, which has a loading effect on the center-point. The mains current guidance is realized by three independent hysteresis controllers.

A space vector representation of the input rectifier voltage and current is used to show that the proposed control method is equivalent to the conventional use of the redundant switching states in indirect (voltage-oriented) PWM modulation. The center-point characteristic $I_M(\Delta V_M)$ is derived and the intrinsic instability of the center-point for hysteresis current controlled PWM rectifiers shown. The impact of the offset I_o injection and of the center-point voltage shift ΔV_M on the selection and the frequency of the switching states is analyzed and experimentally verified with a three-level *Vienna* rectifier.

A design of the center-point controller is presented based on the detailed analysis of the center-point voltage shift ΔV_M due to the effect of both the current I_M and the offset I_o . The controller performance has been experimentally verified and it proved to possess excellent dynamics and to have minimum impact on the mains current shape.

The essential advantages of the control concept for the voltage control of the output voltage center point of a unidirectional three-phase three-level PWM rectifier system are (1) the very straightforward realizability by practical circuits and (2) the possibility of a direct inclusion into a high-dynamic (analog) hysteresis control of the mains current. Therefore, the method can be applied also for low-power rectifier systems and for switching frequencies greater than 100 kHz.

Chapter 4

Discontinuous Space Vector Modulation

4.1 Introduction

Three-phase, boost-type, DC voltage link PWM rectifiers have, in general, no connection between the star point N of the supplying mains and the center point M of the output DC voltage (see Fig. 4.1). Hence only the differences between the phase voltages formed at the input of the rectifier and the mains voltages have influence on the formation of the mains phase currents. The zero-sequence voltage v_{MN} between M and N can therefore adopt any value and its waveform shape depends on the selected modulation strategy. As consequence, the rectifier input sinusoidal reference voltage can be augmented by a suitably selected zero-sequence voltage to modify the duty-cycle of the rectifier switches and thus implement high-performance modulation strategies [108, 109, 103, 110].

One modulation method to form sinusoidal currents is by switching only two rectifier phase legs while the third phase leg (where the selected phase changes in a cyclic manner over one mains period) is clamped to an output voltage bus. This can be obtained by using zero-sequence discontinuous-type signals to augment the sinusoidal reference [109, 102]. The method of clamping of a phase leg input voltage to the output bus is called Discontinuous Pulse-Width Modulation (DPWM) and has reduced switching losses compared to using conventional modulation approaches, where there is constant switching of the power devices, such as in Continuous Pulse-Width Modulation (CPWM) [102, 111, 112, 113]. For a defined value of allowable switching loss, this allows an increase of the

DPWM was first used for three-phase, two-level voltage-source inverters (VSI) [114, 111, 112] in order to reduce the switching losses and improve the efficiency of the converter, due to the reduced number of device switching instances and the absence of switching in the vicinity of peaks of the phase current [112]. In [102], the analytical derivations of the expression of the modulation signals used to implement the DPWM for two-level VSI are presented. It is shown in [115] that, for the same class of converters, DPWM is superior to CPWM for high values of the modulation index, in terms of linear modulation range, voltage gain and harmonic distortion. Therefore it is advantageous to switch between different modulation methods according to the modulation index [108]. An improved DPWM method for a two-level VSI used in an active power filter application is presented in [116], where the modulation method includes an algorithm to predict the peak values of the inverter current and consequently calculate the position of the phase clamping intervals. The advantages of DPWM have been recently verified on multilevel VSI, a class of topologies that offer many benefits for higher power application, such as the ability to synthesize voltage waveforms with lower harmonic content than two-level inverters and operation at higher DC voltages using series connected semiconductor switches. In particular, [103] presents the implementation of DPWM methods for three-level VSIs and [110] investigates the possibility of implementing DPWM strategies for five-level and seven-level VSIs.

Since the main goal of DPWM is to reduce the switching losses, the phase clamping intervals should occur around the peaks of the respective phase current. Therefore, one has to consider the typical current phase lag in ac motor drive VSI applications, where the clamping interval occurs for a phase angle of 60° of the fundamental period [112]. In particular, the total clamping interval per phase lasts 120° and can be continuous (one phase clamped either to the positive or negative DC rail exclusively) or split up into $2 \times 60^\circ$ or $4 \times 30^\circ$ intervals, using both rails [111, 102]. In [113], DPWM is applied to a two-level PWM rectifier, which operates with a wide power factor range.

This chapter investigates and experimentally verifies the application of discontinuous modulation to a three-phase, three-level *Vienna* Rectifier (Fig. 4.1a) [117]. The *Vienna* rectifier is a unity power factor (zero phase angle) rectifier with only a unidirectional power flow. Three-level rectifiers have the advantages of lower blocking device voltage and improved quality of the current waveform compared with two-level rectifiers. On the other hand, the balancing of the center point M voltage has to be assured [98, 118, 119]. Two discontinuous modulation methods can be implemented by eliminating either the first or the last state in the switching sequence, or equivalently, by using only one of the redundant vectors. With this in mind, the analysis presented in this chapter shows to what extent the operational behavior of a three-level rectifier, modulated by

DPWM, is improved as compared to continuous modulation. This chapter's contribution is to present the performance of discontinuous modulated three-level rectifiers from a more practical standpoint, comparing the theoretical analysis with a comprehensive experimental verification using a three-switch, three-level *Vienna* rectifier.

In Section 4.2 it is shown how the degree of freedom in the modulation is used to implement the discontinuous schemes. In particular, both a space vector representation and a modulation function are used as a means to explain the two discontinuous modulation methods introduced in this chapter and to clearly show the clamping intervals of the switches. Section 4.3 presents a comparison between the two DPWM strategies and CPWM, in terms of mains current ripple and switching losses. Experimental measurements comparing the differences between CPWM and DPWM in terms of the input and center point current waveforms and relative ripple currents over the practical modulation range are presented in Section 4.4.

4.2 Discontinuous Modulation Schemes

The absence of the neutral current path in three-phase rectifiers provides a degree of freedom in determining the input converter voltage, that constitutes the sinusoidal guidance for the line current according to

$$L \frac{di_i}{dt} = v_i - v_{iN} \quad \text{index } i = R, S, T \quad (4.1)$$

where v_i and v_{iN} are the mains voltage and the input rectifier voltage for phase i (referred to the star point N potential), i_i is the phase i current and L the input inductance. The degree of freedom provided is that the voltage v_{MN} from the center point M to the mains star point N can assume any value. Therefore, zero sequence signals can be added to the pre-control signal to improve the performance of the modulation [109, 108, 88], and the voltage v_{MN} will be shaped according to the zero-sequence signal injected in the modulator part of the current control loop. The zero-sequence (or common mode) voltage v_{MN} is related to the input rectifier voltage v_{iN} by

$$v_{iN} = v_{iM} + v_{MN} \quad \text{index } i = R, S, T \quad (4.2)$$

where v_{iM} is the input rectifier voltage referred to the center point M of the DC-link capacitors. Since the input rectifier voltage v_{iN} is defined according to (4.2), then its local average value waveform must be sinusoidal in order to generate the required sinusoidal line current. For a current-commutated voltage-source rectifier, like the *Vienna* rectifier [117] used for the experiments, the generation

of the voltage v_{iM} is dependent on the direction of the phase current and is defined as:

$$v_{iM} = \begin{cases} \operatorname{sgn}\{i_i\} \frac{V_0}{2} & \text{if } s_i = \operatorname{sgn}\{i_i\} \\ 0 & \text{if } s_i = 0 \end{cases} \quad (4.3)$$

where V_0 is the output rectifier voltage (see Fig. 4.1). According to the value assumed by the phase switching function s_i , the respective input rectifier phase terminal can be clamped to the positive output-voltage rail ($s_i = +$), to the negative rail ($s_i = -$) or to the output center point ($s_i = 0$). For the *Vienna* rectifier, the case when $s_i = 0$ occurs when the power switch is turned on.

In contrast, for a forced-commutated, conventional 6-switch rectifier the switching function s_i ($i = R, S, T$) is independent of the phase current sign and the rectifier input terminals are clamped to the positive output-voltage rail or the negative rail according to the switches status.

4.2.1 Space Vector Representation

All the space vectors available in a mains period for a three-level PWM rectifier are represented in the complex plane as shown in Fig. 4.2. The space vectors are usually classified into zero voltage vectors, small vectors which are the vertices of the inner hexagon, medium vectors which are midpoints of the sides of outer hexagon and large vectors comprising of the vertices of the outer hexagon. Each switching state vector is denoted by the triple of quantities (s_R, s_S, s_T) formed by the phase switching function s_i . The rectifier input reference voltage phasor

$$\underline{V}^* = \frac{1}{2} M V_0 e^{j\varphi(t)} \quad (4.4)$$

is formed by averaging the three-nearest available space vectors over a switching period, where M indicates the modulation index, which is defined as

$$M = \frac{\hat{V}_{iN}}{\frac{1}{2} V_0}, \quad (4.5)$$

where \hat{V}_{iN} is the peak value of the rectifier input voltage and $\varphi(t) = 2\pi f t$ is the phase angle dependent on the mains supply frequency f . Hereafter only the interval

$$M \in \left[\frac{2}{3}, \frac{2}{\sqrt{3}} \right] \quad (4.6)$$

will be considered, which is a typical modulation index range for a practical realization. For example, in a three-phase 400 V line-to-line application the output voltage would be typically limited to $800 V_{DC}$ since commonly available capacitors have a rated voltage of $450 V_{DC}$. If the input voltage is considered to range from 320V to 480V, then a modulation index from 0.65 to 0.99 would

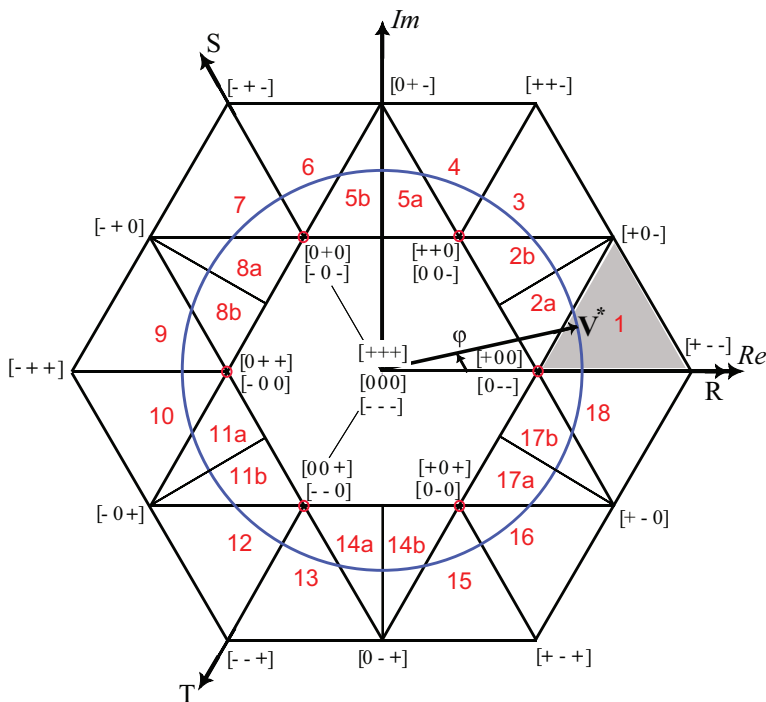


Figure 4.2: Switching intervals for continuous SVM (CPWM).

result.

For the current-commutated *Vienna* rectifier, the available space vectors depend on the sign of the phase currents and accordingly, there are eight available space-vectors every 60 degrees [120]. In the direct digital implementation, that uses the space-vectors concept to calculate the duty cycle of the rectifier switches [109], the degree of freedom appears as the partitioning of two redundant switching states. There are six pairs of redundant space-vectors represented by the small vectors in Fig. 4.2. Each pair generates the same line-to-line voltage and this results in a center point current i_M of same value but the direction of i_M depends on the selected switching state [118]. If δ_- represents the duty-cycle for one pulse period of the redundant switching state that generates a negative i_M (according to the direction indicated in Fig. 4.1), and δ_+ is the duty-cycle of the space-vector causing positive flowing i_M , then the control parameter that

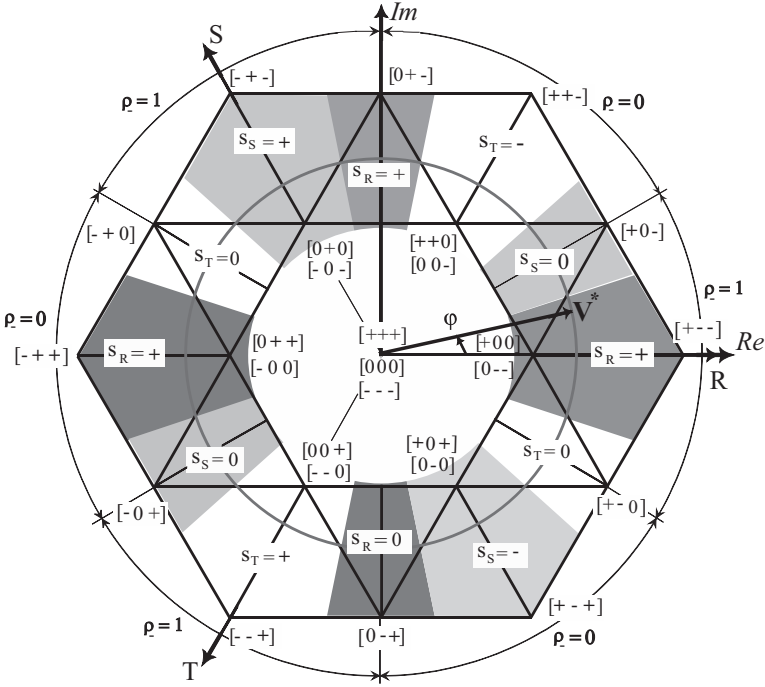


Figure 4.3: Switching intervals for discontinuous SVM method A (DPWMA), characterized by variable intervals, depending on the modulation index M . The shaded regions indicate the clamping intervals of the i -phase, $i = R, S, T$, to the positive rail ($s_i = +$), the negative rail ($s_i = -$) or to the center point ($s_i = 0$). Moreover, the value of the control variable ρ_- (4.7), either 0 or 1, is indicated as a function of the angle φ .

expresses the degree of freedom in the SVM can be defined as

$$\rho_- = \frac{\delta_-}{\delta_- + \delta_+} \quad \rho_- \in [0, 1] \quad (4.7)$$

and represents namely the relative on-time of the space-vector producing a negative center-point current i_M . Therefore, the center point voltage balance can be performed by varying the control parameter ρ_- and it results that the center to neutral point voltage v_{MN} for SVM is shaped according to the modulation

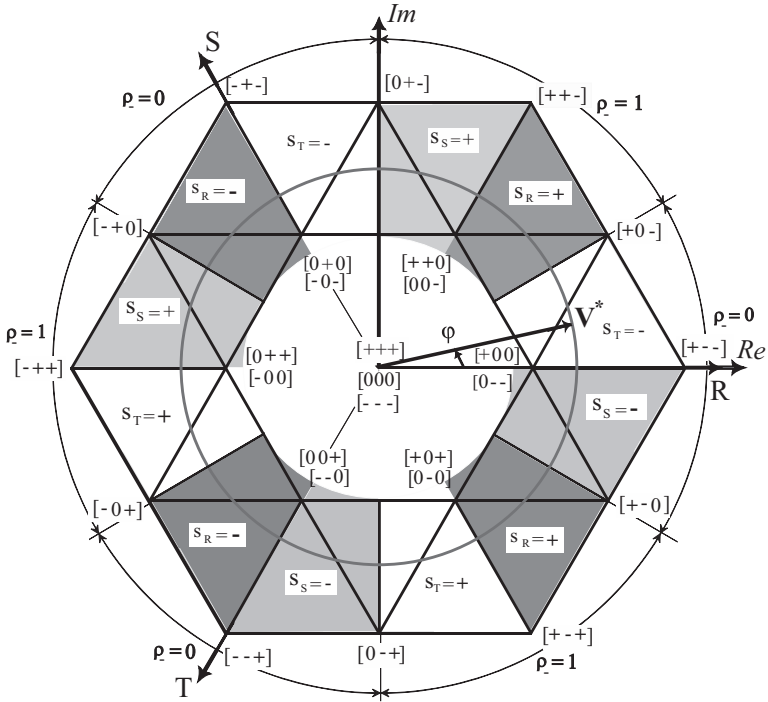


Figure 4.4: Switching intervals for discontinuous SVM method B (DPWMB) with fixed intervals. The shaded regions indicate the clamping intervals of the i -phase, $i = R, S, T$, to the positive rail ($s_i = +$), the negative rail ($s_i = -$) or to the center point ($s_i = 0$). Moreover, the value of the control variable ρ – (4.7), either 0 or 1, is indicated as a function of the angle φ .

strategy implemented and specifically, to the zero-sequence signal added to the pre-control signal or redundant switching vectors selected [118]. The denominator of (4.7), $\delta_- + \delta_+$, is dependent on the modulation index.

In order to minimize the transistors switching the switching states within each pulse half period can be arranged in such a way that the subsequent state can always be obtained by switching of only one bridge leg [103]. For a three-phase rectifier, using CPWM, the minimum number of switching transitions in one switching period is three, i.e. one per phase leg. The duty cycle of the redundant space vector is split such that the redundant vector occurs at the

first and the last position of the switching sequence. To minimize the current ripple, the duty-cycles δ_+ and δ_- are selected to have the same value and this results in ρ_- being equal to 0.5 [110]. Consider sector 1, as shaded in Fig. 4.2 for CPWM, if $(0 - -)$ is selected, arbitrarily, as the initial switching state, this results within each pulse period T_P a switching state sequence of

$$\begin{aligned} \dots \Big|_{t=0} (0 - -) \rightarrow (+ - -) \rightarrow (+0-) \rightarrow (+00) \Big|_{t=\frac{1}{2}T_P} & \quad (4.8) \\ (+00) \rightarrow (+0-) \rightarrow (+ - -) \rightarrow (0 - -) \Big|_{t=T_P} \dots \end{aligned}$$

The main goal for implementing the discontinuous modulation strategy is to minimize the switching losses; hence the switching of the power transistor has to be preferably avoided around the maxima of the associated phase current. This basic idea, in connection with providing a zero average value of the center point current within a mains period, results in the discontinuous modulation scheme A (DPWMA), shown in Fig. 4.3. Here, the different colored shaded regions indicate the clamping of a particular phase. For example, in sector 1 where the voltage reference vector V^* is positioned, the input phase R is clamped to the positive bus. This is achieved by turning the power transistor of bridge leg R off, and since the input phase R current is flowing into the rectifier it must flow to the positive output bus, which results in the input rectifier voltage being clamped to the output-voltage positive rail ($s_R = +$). As the angle φ advances, into the next phase clamping region the switch in phase S is turned on and phase S is clamped to the center point voltage ($s_S = 0$).

Discontinuous modulation is implemented by eliminating the first or the last state (corresponding to the redundant vector) in the switching sequence (4.8), or equivalently by selecting $\rho_- = 0$ or 1. If now $\rho_- = 1$ is set in sector 1 of the space vector plane (see Fig. 4.3) this results a switching state sequence or DPWMA of

$$\begin{aligned} \dots \Big|_{t=0} (\underline{+}00) \rightarrow (\underline{+}0-) \rightarrow (\underline{+} - -) \Big|_{t=\frac{1}{2}T_P} & \quad (4.9) \\ (\underline{+} - -) \rightarrow (\underline{+}0-) \rightarrow (\underline{+}00) \Big|_{t=T_P} \dots \end{aligned}$$

where the input rectifier voltage of phase R is clamped to the output-voltage positive rail ($s_R = +$).

The other discontinuous control scheme (DPWMB), which is independent of the modulation index M , can be obtained by inverting the values of the control parameter ρ_- as compared to DPWMA. The DPWMB clamping intervals, as shown in Fig. 4.4, are now different from DPWMA. If $\rho_- = 0$ is set in sector 1 of the space vector plane (see Fig. 4.4) this results in the following switching

state sequence

$$\begin{aligned} \dots \Big|_{t=0} (0 \text{ -- } \underline{-}) \rightarrow (+ \text{ -- } \underline{-}) \rightarrow (+0\underline{-}) \Big|_{t=\frac{1}{2}T_P} & \quad (4.10) \\ (+0\underline{-}) \rightarrow (+ \text{ -- } \underline{-}) \rightarrow (0 \text{ -- } \underline{-}) \Big|_{t=T_P} \dots \end{aligned}$$

Here the switch of the phase T is turned off for the complete pulse period and the input rectifier voltage is clamped to the negative output-voltage rail ($s_T = -$). For DPWMB, the clamping takes place in 30° -wide intervals that are shifted by $\pm 45^\circ$ from the maxima of the respective mains phase currents.

4.2.2 Modulation Functions

The calculation of the duty cycles of the rectifier switching devices can be determined from the phase modulation functions m_i [121, 122]. For phase i , the equation of the modulation function is expressed as

$$\begin{aligned} m_i &= \frac{v_{iM}}{\frac{1}{2}V_0} = \frac{v_{iN}}{\frac{1}{2}V_0} - \frac{v_{MN}}{\frac{1}{2}V_0} \\ &= m'_i + m_0 \quad \text{index } i = R, S, T \end{aligned} \quad (4.11)$$

where the sinusoidal reference m'_i is augmented by a zero-sequence waveform, m_0 . The signal m_0 and the average value of the neutral point voltage v_{MN} are directly proportional, whereas the average input rectifier voltage v_{iM} can be calculated from (4.3).

Considering Sector 1 in Fig. 4.2 and using switching pattern and input rectifier voltages given in the Appendix 8.3, the modulation functions for the three phases are

$$\begin{aligned} m_R &= \delta_{(+--)} + \delta_{(+0-)} + \delta_{(+00)} \\ m_S &= -\delta_{(0--)} - \delta_{(++-)} \\ m_T &= -\delta_{(0--)} - \delta_{(++-)} - \delta_{(+0-)}. \end{aligned} \quad (4.12)$$

The zero-sequence part of the modulation function m_0 is given by

$$\begin{aligned} m_0 &= \frac{1}{3}(m_R + m_S + m_T) \\ &= -\frac{1}{3}\delta_{(++-)} + \frac{1}{3}\delta_{(+00)} - \frac{2}{3}\delta_{(0--)} \\ &= -\frac{1}{3}\delta_{(++-)} + \left(\rho_- - \frac{2}{3}\right)(\delta_{(+00)} + \delta_{(0--)}) \end{aligned} \quad (4.13)$$

where the control parameter ρ_- , defined in (4.7), has the form for Sector 1 of

$$\rho_- = \frac{\delta_{(+00)}}{\delta_{(+00)} + \delta_{(0--)}}. \quad (4.14)$$

The modulation functions of the sinusoidal references m'_i for each of the three phases can then be determined from (4.11)-(4.13) as

$$\begin{aligned} m'_R &= \frac{2}{3}(1 + \delta_{(+--)} + \frac{1}{2}\delta_{(+0-)}) \\ m'_S &= -\frac{1}{3}(1 + \delta_{(+--)} - \delta_{(+0-)}) \\ m'_T &= -\frac{1}{3}(1 + \delta_{(+--)} + 2\delta_{(+0-)}). \end{aligned} \quad (4.15)$$

From equations (4.13) and (4.15) it is apparent that a change of ρ_- influences only the zero-sequence part of the modulation function.

Fig. 4.5 shows the modulation functions of the CPWM, DPWMA and DPWMB for a modulation index $M = 0.815$. For the two discontinuous methods the bridge legs are not switched continuously during one mains period and the clamping intervals of the input rectifier voltage to the positive, negative and center point, characteristic of the discontinuous modulation are apparent from Fig. 4.5. Note that for the DPWMA there are clamping intervals during the phase current zero-crossings and this is an advantage as the generation of the modulation waveforms is not dependent on accurately determining the mains phase voltage zero crossing.

4.3 Comparison of Continuous and Discontinuous Modulation Schemes

One of the advantages of discontinuous modulation over the continuous modulation is the reduction of the switching losses. For a defined value of the switching loss, this allows an increase of the switching frequency thus leading to a decrease in the current ripple. The harmonic components of the switching frequency are therefore shifted to higher values for discontinuous modulation.

In order to obtain an independency of the simulations and experiments from the selected specific parameters and to derive results which are not limited to specific operating parameters and device characteristics, the calculated average and rms current values are related to the peak value \hat{I}^* of the mains current reference value. The normalized rms value of the power transistor current is

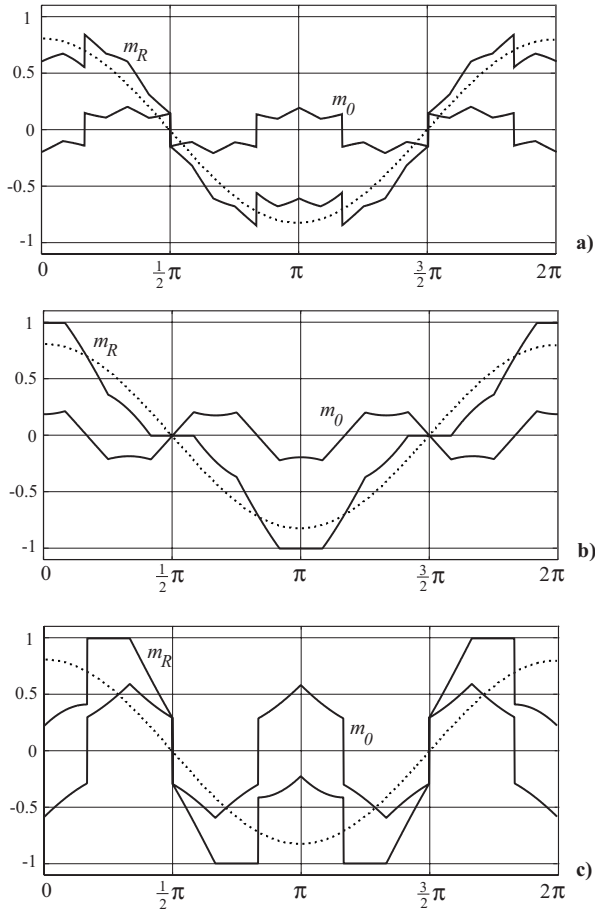


Figure 4.5: Modulation functions for the phase R and for modulation index $M = 0.815$. The modulation function m_R (proportional to the rectifier input voltage average value v_{RM}) and its zero-sequence component m_0 (proportional to the average value of v_{MN}) are shown for: a) CPWM, b) DPWMA and c) DPWMB.

then

$$I_{\text{rms},r} = \frac{I_{\text{rms}}}{\hat{I}^*}. \quad (4.16)$$

The normalization basis of the rms value of the mains current ripple ΔI_{rms} is set to

$$\Delta I_r = \frac{V_0 T_P}{8L}. \quad (4.17)$$

Thus,

$$\Delta I_{\text{rms},r} = \frac{\Delta I_{\text{rms}}}{\Delta I_r} \quad (4.18)$$

and represents a characteristic value which is independent from the switching frequency f_P and the input inductance value L in a first approximation. The subscript r indicates the normalization.

4.3.1 Calculation of Switching Frequency Increase

The admissible increase of the switching frequency for equal thermal stress on the switches is now calculated. As shown in [117] the global (over a mains period) switching losses of the transistor of a *Vienna* rectifier phase leg can be calculated by averaging the local switching losses $p_T = \frac{1}{T_P} w_P$ according to

$$P_T = \frac{1}{\frac{\pi}{2}} \int_0^{\frac{\pi}{2}} p_T d\varphi \quad (4.19)$$

where the integration can be limited to $\frac{1}{4}T_N$ or $\frac{\pi}{2}$ due to symmetry reasons and T_N is the mains period. The switching loss w_P within one pulse period T_P , given by the sum of the turn-on loss and the turn-off loss, can be expressed as a linear function the switched phase current

$$w_P = k_f i \quad (4.20)$$

where k_f is a constant dependent on the voltage across the switch and the switch characteristics and i indicates the phase current.

Assuming for CPWM a purely sinusoidal shape of the switched current (see Appendix 8.3), it follows

$$P_{T,CPWM} = \frac{2}{\pi} k_f \hat{I} f_P \quad (4.21)$$

where \hat{I} is the peak value of the phase currents and f_P is the pulse frequency. For discontinuous modulation, the clamping intervals shown in Fig. 4.3 and Fig. 4.4 have to be omitted from the integration (4.19). Since the integration interval for DPWMA is dependent on the modulation index M , then also the resulting switching losses $P_{T,DPWMA}$ show a dependency on the modulation

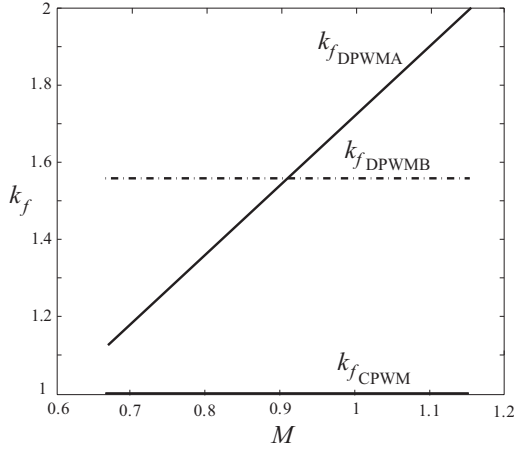


Figure 4.6: Factors k_f as a function of the modulation index M , indicating the increase of switching frequency for a) DPWMA ($k_{f,DPWMA}$) and b) DPWMB ($k_{f,DPWMB}$), with respect to c) CPWM ($k_{f,CPWM}$).

index M as given by

$$P_{T,DPWMA} = \frac{2}{\pi} \frac{1}{\sqrt{3}M} k_f \hat{I} f_P . \quad (4.22)$$

Close to the overmodulation limit, $M = M_{max}$ (4.6), the switching losses (4.22) are reduced with by a factor of 2 as compared to continuous modulation, and for $M = \frac{2}{3}$ there is a reduction by a factor of $\frac{\sqrt{3}}{2}$. As shown in [111], the conduction losses are in good approximation independent of the modulation scheme (continuous or discontinuous modulation). Therefore, under the assumption of equal thermal stress on the power transistors as in continuous modulation (4.21) the switching frequency of DPWMA can be increased by a factor of

$$k_{f,DPWMA} = \sqrt{3}M \quad (4.23)$$

A similar consideration shows for DPWMB the possibility of increasing the switching frequency by a constant factor of

$$k_{f,DPWMB} = \frac{2}{3 - \sqrt{3}} \approx 1.58 . \quad (4.24)$$

In contrast to the DPWMA, there is no dependency of k_f on M for DPWMB (see Fig. 4.6). This can be explained by the independency of the relative duration and position of the clamping intervals of M for DPWMB.

4.3.2 Impact of the Redundant Switching States Distribution on AC-side Currents

As compared to continuous modulation, discontinuous modulation has in general a lower ripple of the mains phase current due to the higher effective switching frequency. Besides the switching frequency, the ripple of the mains phase current is also influenced by the distribution of the redundant switching states between the beginning and end of one pulse half period as illustrated in Fig. 4.7. As shown in [110], the rms value of the mains current ripple can be minimized for continuous modulation by defining $\rho_- \approx 0.5$ in wide intervals of the mains period. Therefore, for discontinuous modulation, characterized by values of the control parameter of $\rho_- = 0$ or 1 (see Fig. 4.2), an increase in the current ripple has to be expected. However, there is a reduction in the ripple through the increasing of the switching frequency by a factor k_f , (4.23)-(4.24). The normalized mains current ripple can be calculated analytically for the continuous and discontinuous modulation methods by determining the equations of the squared and normalized current sum averaged over the switching period for each sector. Appendix 8.3 describes the basis for this calculation. The analytical equations for the squared current ripple of CPWM, DPWMA and DPWMB are given in (4.25)-(4.27) respectively. The results from these equations are plotted over the practical modulation index range in Fig. 4.8 where they are compared with simulation and experimental results. It can be seen that at lower modulation indexes the current ripple for CPWM is lower than both the DPWM schemes, however for $M > 0.95$ DPWMA starts to have a much lower current ripple than

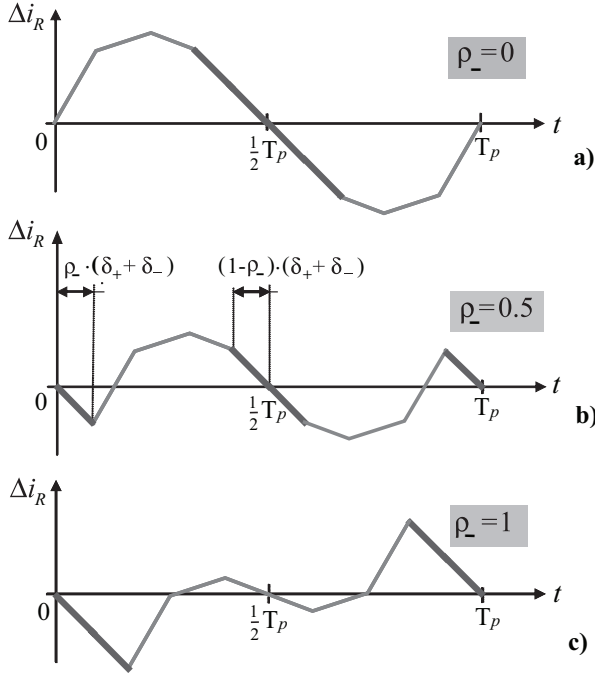


Figure 4.7: Representation of the impact of the redundant switching states distribution on the mains current ripple Δi_R over a pulse period T_P . The duty cycles δ_- and δ_+ of the redundant space vectors are expressed as a function of the control parameter ρ_- (4.7).

CPWM.

$$\begin{aligned}
 \Delta I_{rms,r,CPWM}^2 &= \left[\frac{2\pi - 3\sqrt{3}}{9\pi} + \frac{4}{9\pi} \arcsin \left(\frac{1}{\sqrt{3}M} \right) \right] \\
 &+ M \cdot \left(-\frac{4}{\pi} + \frac{22}{9\sqrt{3}\pi} \sqrt{1 - \frac{1}{3M^2}} \right) \\
 &+ M^2 \cdot \left[\frac{2}{\pi} \arcsin \left(\frac{1}{\sqrt{3}M} \right) + \frac{3\pi - \sqrt{3}}{2\pi} \right] \\
 &+ M^3 \cdot \left(\frac{-72 + 16\sqrt{3}}{9\pi} + \frac{8}{3\sqrt{3}\pi} \sqrt{1 - \frac{1}{3M^2}} \right) \\
 &+ M^4 \cdot \left(\frac{3\pi - 3\sqrt{3}}{4\pi} \right)
 \end{aligned} \tag{4.25}$$

$$\begin{aligned}
 \Delta I_{rms,r,DPWMA}^2 &= \frac{1}{3M^2} \left\{ \frac{20}{9} \right. \\
 &+ \frac{2}{\pi} \left[\sqrt{3} - \frac{28}{9} \arcsin \left(\frac{1}{\sqrt{3}M} \right) \right] \\
 &- \frac{308}{9\sqrt{3}\pi} M \sqrt{1 - \frac{1}{3M^2}} \\
 &+ M^2 \left[13 + \frac{5\sqrt{3}}{\pi} - \frac{34}{\pi} \arcsin \left(\frac{1}{\sqrt{3}M} \right) \right] \\
 &- \frac{2}{3\sqrt{3}\pi} M^3 \left(4 + 83 \sqrt{1 - \frac{1}{3M^2}} \right) \\
 &\left. + \frac{3}{2} M^4 \left(1 + \frac{3\sqrt{3}}{2\pi} \right) \right\}; \tag{4.26}
 \end{aligned}$$

$$\begin{aligned}
 \Delta I_{rms,r,DPWMB}^2 &= \frac{(3 - \sqrt{3})^2}{4} \left\{ \left[\frac{4}{3} - \frac{8}{9\pi} \arcsin \left(\frac{1}{\sqrt{3}M} \right) \right] \right. \\
 &- M \cdot \left[\frac{12 + 16\sqrt{3}}{3\pi} + \frac{44}{9\sqrt{3}\pi} \sqrt{1 - \frac{1}{3M^2}} \right] \\
 &+ M^2 \cdot \left[-\frac{4}{\pi} \arcsin \left(\frac{1}{\sqrt{3}M} \right) + \frac{17\pi + 21\sqrt{3}}{3\pi} \right] \\
 &- M^3 \cdot \left[\frac{-9 + 104\sqrt{3}}{9\pi} + \frac{16}{3\sqrt{3}\pi} \sqrt{1 - \frac{1}{3M^2}} \right] \\
 &\left. + M^4 \cdot \left[\frac{6\pi + 3\sqrt{3}}{4\pi} \right] \right\}. \tag{4.27}
 \end{aligned}$$

4.3.3 Impact of the Redundant Switching States Distribution on DC-side Currents

The implementation of discontinuous modulation schemes by setting the control parameter ρ_- equal to 1 (DPWMA) or 0 (DPWMB) has also a direct influence on the shape of the center point current i_M through the shape of the neutral point voltage v_{MN} . The center point current i_M is dependent on the phase currents according to

$$i_M = t_R i_R + t_S i_S + t_T i_T \quad t_i = \begin{cases} 1 & \text{if } s_i = 0 \\ 0 & \text{else} \end{cases} \tag{4.28}$$

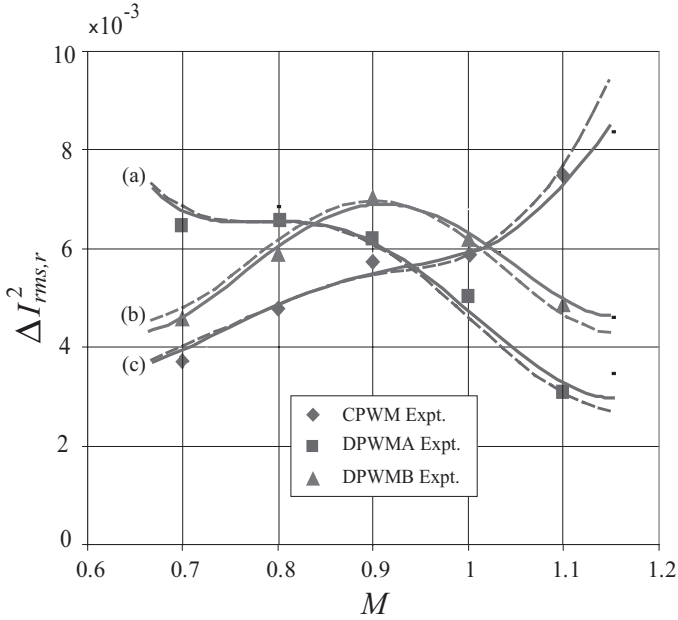


Figure 4.8: Analytical (solid lines), simulated (dashed lines) and experimental (marked points) results showing the dependency of the square of the rms value of the phase current ripple on the modulation index M for (a) DPWMA, (b) DPWMB and (c) CPWM.

where the function t_i (index $i = R, S, T$) is unitary only when the phase input terminal is clamped to the center point. In [118] it is clearly shown that only short (redundant) and average vectors contribute to the center point current. Redundant switching states result in center point current i_M of same value but different sign. In particular, for sector 1 in Fig. 4.2), the center point current corresponding to the redundant switching states (0--) and (+00) is calculated as

$$i_M = \begin{cases} -i_R & \text{for } (0--) \\ +i_R & \text{for } (+00) \end{cases} \quad (4.29)$$

while the local average within a pulse half period in the same sector is given by

$$i_{M,\text{avg}} = (\delta_{(0--)} - \delta_{(+00)})i_R + \delta_{(+0-)}i_S. \quad (4.30)$$

Since ρ_- (4.14) alternates between 0 and 1 six times the mains frequency (see Fig. 4.3 and Fig. 4.4), and from (4.28) and (4.30), a relative high amplitude of the third harmonic in the center point current waveform has to be expected.

4.4 Experimental Verification

The continuous and the two discontinuous modulation schemes are experimentally evaluated using a 5 kW, 115 V, three-level *Vienna* rectifier. The current control, modulation and switch signals are implemented digitally using an Analog Devices ADSP21992 160 MHz DSP. The line currents and output voltages are sampled at the switching frequency and are used by the DC output voltage and current controllers to generate the duty cycles for the PWM generator. The modulation strategies are implemented in the DSP using a synchronous-frame voltage-oriented current control scheme. The voltage-oriented control for a unity power-factor only requires the control of the synchronous d -component of the current phasor. Inaccurate detection of the phase current zero-crossings can result in additional low frequency distortion when using conventional modulation, however with DPWMA, one phase is clamped during the zero-crossing and therefore does cause any additional distortion. To complement the experimental results, the three modulation schemes have been simulated using Simpler for different modulation index values using the same experimental parameters as listed in Table I. The switching frequency for continuous modulation is set equal to 10 kHz whereas for the discontinuous schemes the coefficients (4.23) and (4.24) are considered since equal switching losses are assumed as the basis for the comparison. In particular, the switching frequency for the DPWMA is dependent on the modulation index and it assumes the maximum value for $M = \frac{2}{\sqrt{3}}$.

In order to evaluate the waveform quality over the whole modulation range, the line and center point current, and input rectifier voltage (v_{iM}) have been recorded for the three modulation strategies (CPWM, DPWMA and DPWMB) and for five discrete values of the modulation index. The variation of the modulation index (4.6) is obtained by keeping the output voltage V_0 constant while changing the supply voltage amplitude. As an example, a set of waveforms are shown in Fig. 4.9 for a modulation index $M = 0.9$ and for each modulation scheme. Here the phase and the center point currents are seen in channels 2 and 4 and the rectifier input voltage (4.3) in channel 3 where the clamping intervals characteristic of discontinuous modulation are apparent in Fig. 4.10

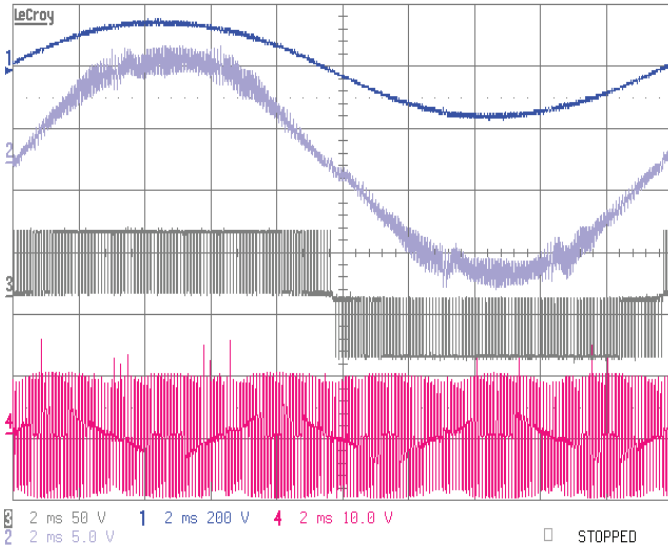


Figure 4.9: Experimental waveforms recorded for CPWM. The modulation index is $M = 0.9$. Ch1: mains voltage (200 V/div). Ch2: mains current (5 A/div). Ch3: rectifier input voltage (200 V/div). Ch4: neutral point current i_M (10 A/div). Time base: 2ms/div.

and Fig. 4.11.

Fig. 4.12 shows the input current ripple waveform and frequency spectrum for modulation depth $M = 0.7$ normalized by the fundamental component. The switching frequency for the discontinuous schemes is calculated according to the

Table 4.1: Experimental Setup Parameters

parameter	symbol	value
mains voltage	V_{rms}	115 V
output voltage	V_0	350 V
rms line current	I	6 A
switching frequency	f_P	10 kHz
input inductance	L	500 μ H

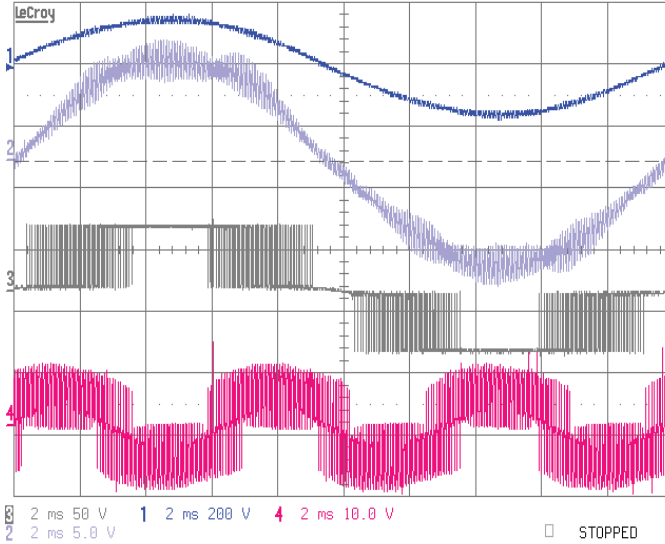


Figure 4.10: Experimental waveforms recorded for DPWMA. The modulation index is $M = 0.9$. Ch1: mains voltage (200 V/div). Ch2: mains current (5 A/div). Ch3: rectifier input voltage (200 V/div). Ch4: neutral point current i_M (10 A/div). Time base: 2ms/div.

coefficients (4.23) and (4.24). The harmonic components of the mains current, which are grouped around multiples of the switching frequency are shifted to higher frequencies for both discontinuous schemes and this is advantageous in dimensioning of the input EMI filter. In particular for DPWMA, the relative position of the harmonic components in the frequency spectrum is dependent on the modulation index M in order to ensure the same switching loss. The frequency spectrum of the DPWMB is independent on the modulation index and the relative position of the harmonic components with respect to continuous modulation is always as shown in Fig. 4.12.

A conventional criteria to evaluate the waveform quality of different modulation schemes is the the square rms value of the current ripple [111]. The comparative evaluation of the current ripple for the three modulation strategies, normalized according to (4.25)-(4.27), is shown in Fig. 4.8. The results from experimental measurements show a very good correspondence to the analytical equations and simulation results shown as solid and dashed lines respectively. If

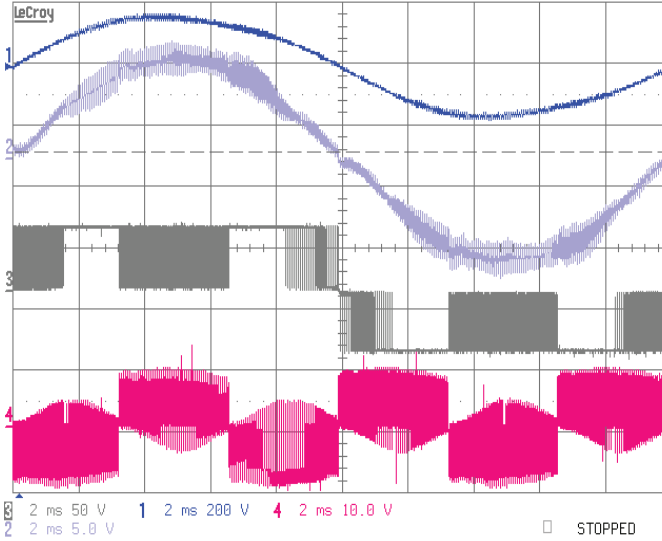


Figure 4.11: Experimental waveforms recorded for DPWMB. The modulation index is $M = 0.9$. Ch1: mains voltage (200 V/div). Ch2: mains current (5 A/div). Ch3: rectifier input voltage (200 V/div). Ch4: neutral point current i_M (10 A/div). Time base: 2ms/div.

the rectifier is operated close to the overmodulation limit in case of DPWMA, then the harmonic losses are reduced by a factor of ≈ 3 with respect to CPWM (the rms value of the mains current harmonics is then reduced by a factor of $\sqrt{3}$). The use of DPWMB results in a reduction of the switching losses by factor 2 (the rms value of the mains current harmonics is then reduced by a factor of $\sqrt{2}$). For practical realization, therefore, DPWMA has to be preferred to DPWMB although the calculation effort for DPWMA is higher due to the dependency of the clamping intervals on the modulation index M . The results are also in general agreement with the comparative evaluations carried out for continuous and discontinuous modulation schemes of two-level converters [108, 102, 111].

According to (4.14) and (4.30), the maximum negative and the maximum positive local average value $i_{M,\text{avg}}$ of the center point current occurs during one pulse period for $\rho_- = 0$ and $\rho_- = 1$, respectively. The switching of ρ_- between 0 and 1 with three times the mains frequency (see Fig. 4.3 and Fig. 4.4), which is characteristic for discontinuous modulation, results in a relatively high

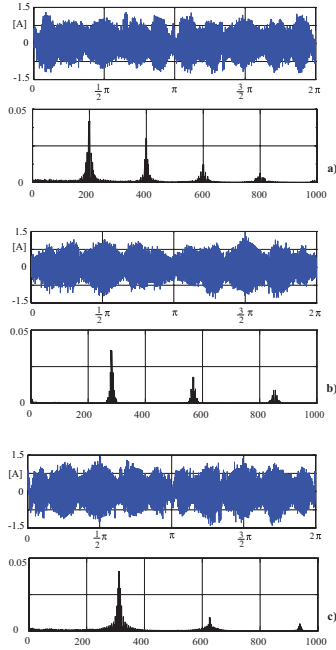


Figure 4.12: Measured input current ripple waveform and frequency spectrum for: a) CPWM, b) DPWMA and c) DPWMB. The modulation index is $M = 0.7$ and the amplitudes are normalized by the fundamental component of the current ($6 A_{rms}$) while the frequency components are multiples of the mains frequency (50 Hz).

amplitude of the third harmonic of the center point current (see Fig. 4.13). In contrast, for optimized continuous modulation (characterized by $\rho_- \approx 0.5$) there is on average a cancellation of the positive and negative portion of i_M within one pulse period. Therefore, the low-frequency harmonics $\hat{I}_{M,(n)}$ ($n = 3, 9, 15, \dots$) of i_M show relatively low amplitudes. In order to limit the potential shift of the center point caused by the low frequency harmonics $\hat{I}_{M,(n)}$ of the center point current to a given maximum value, a higher output capacitor value has to be used for discontinuous modulation.

As shown in Fig. 4.14 for DPWMA there is an approximately linear decline of the amplitude of the third harmonic of the center point current for increasing modulation index M . This can be explained by the decreasing value of the sum

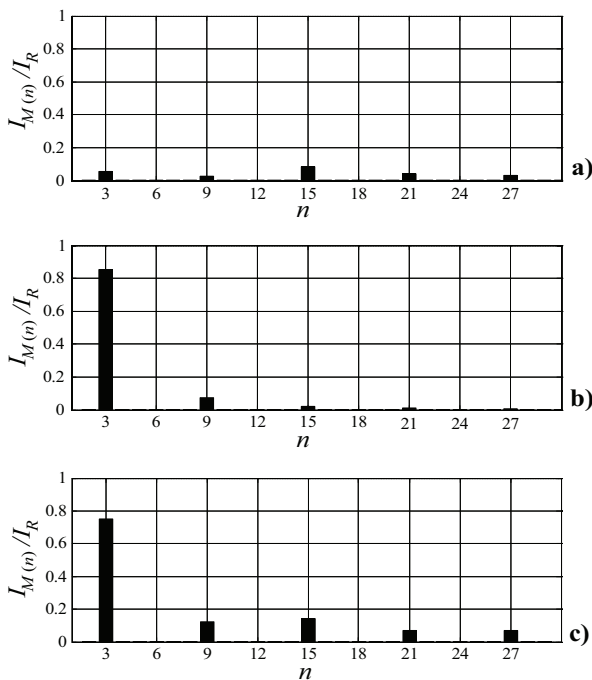


Figure 4.13: Experimental neutral point current harmonic components $I_{M(n)}$ normalized to the fundamental component of the mains current ($6 A_{rms}$) and multiples of the mains frequency (50 Hz) for modulation index $M = 0.8$. a) CPWM, b) DPWMA and c) DPWMB.

of the redundant switching states durations (4.7), which is also linear with M and which results in a proportional reduction of the local average value and amplitude of the low-frequency harmonics of the center point current. For a high modulation index the base for calculating the necessary output capacitance (using electrolytic capacitors) is therefore the rms value of the capacitor current $I_{C,rms}$ rather than the above described potential shift of the center point.

In contrast to the low-frequency harmonics of i_M the rms value of the output capacitor current is *not* influenced by the control parameter ρ_- for balanced partial output voltages and can, therefore, be derived (see Appendix 8.3) for CPWM ($\rho_- = 0.5$), DPWMA and DPWMB as

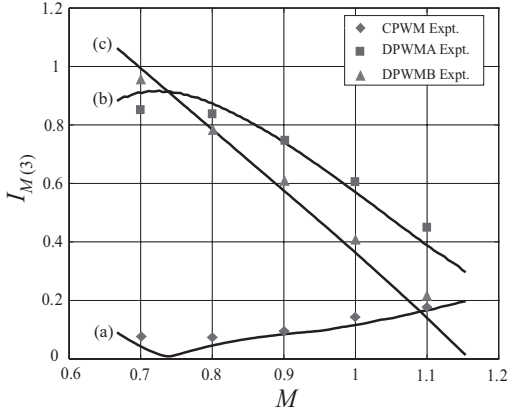


Figure 4.14: Experimental and simulated results showing the dependency of the normalized amplitude $I_{M(3)}$ of the third harmonic of the center point current on the modulation index M for a) CPWM, b) DPWMA and c) DPWMB.

$$I_{C,rms,r}^2 = \frac{10\sqrt{3}M}{8\pi} - \frac{9M^2}{16}. \quad (4.31)$$

For the redundant switching states the center point current shows different signs but equal absolute value (4.28). Therefore, the rms value of the current being fed into the capacitive center point M and being distributed between the both output capacitors equally and/or the output capacitor rms value are independent of ρ_- .

4.5 Discussion

The control of the center point voltage should be implemented and has been addressed in several publications [98, 118, 103, 119]. Although the partial DC-link output voltages are balanced over one mains period for both continuous and discontinuous modulations under ideal conditions, the main task is to maintain long-term stability for higher modulation depth (where the relative duty-cycle of the redundant switching states becomes smaller) and/or in case of unbalanced, nonlinear loads or no-load operation. The center point balancing control strategies are based on the same degree of freedom used to implement the current control, and specifically on the addition of a zero-sequence component to

the sinusoidal reference [98] and on adjusting the redundant switching sequences [118]. These approaches would introduce further switching transitions and deteriorate the harmonic performance of the modulation as discussed in [103]. A center point balancing control strategy based on variation of the input current amplitudes rather than the use of redundant switching states is proposed in [119] and its performance with no-load or low-load operation is demonstrated. This control strategy could be combined with a discontinuous modulation scheme, at the expense of line current harmonic distortion; nevertheless the suppression of low frequency ripple of the center point current and/or additional phase current harmonics represent a minor issue for which other conventional balancing strategies can be applied [103, 119].

The main advantage of discontinuous modulation as compared to continuous modulation is the possibility of increasing the effective switching frequency. The reduction of the rms value of the mains current ripple is then a consequence. If the EMI-filter (which has to be provided at the input side of the rectifier for a practical realization) size is set as basis for the comparison among the modulation schemes, then for a second order filter with a cut-off frequency considerably lower than the switching frequency, the doubling of the switching frequency will result in an increase of the attenuation by a factor of 4. This increase in attenuation is by far more effective than the reduction of the rms value of the mains current ripple due to the increase of the effective switching frequency (factor $\approx \sqrt{3}$). If the rms value of the mains current ripple is thought to be concentrated in a single harmonic with effective switching frequency, the total improvement of the damping of mains current harmonics caused by discontinuous modulation results to a factor of $\approx 4\sqrt{3} \approx 7$.

As is shown in Fig. 4.14, both DPWM methods have a larger third harmonic center point current, which is more significant at lower modulation indices, than CPWM. This current flows into the parallel connection of the output capacitors (with an effective value of $2C$). Therefore, to maintain the same level of third harmonic voltage ripple, as in CPWM, would require the increase of output capacitance value, especially at low values of M . This would result in a decrease of the power density of the rectifier. However, in a practical three-phase rectifier application there is the requirement of a defined hold-up time and/or operation under a phase-loss condition. When operating with only two phases, the output capacitors now have a significant second harmonic current flowing in the series connected output capacitors (with effective value of $C/2$). Overall, the required value of the capacitors for the hold-up and/or phase-loss requirements dominates over the increase in capacitor value due to increased third harmonic current of the DPWM methods at low values of M . Therefore, in a practical *Vienna* rectifier implementation the use of DPWM compared to CPWM would not change the power density when only the output capacitors are considered.

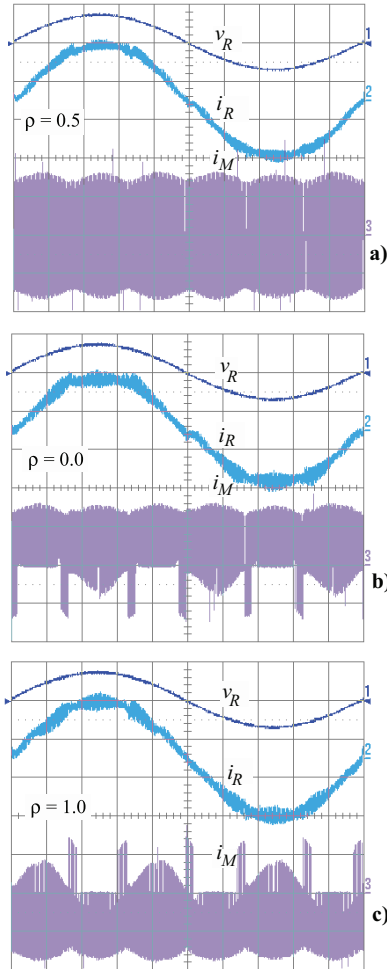


Figure 4.15: Experimental measurements showing the mains voltage v_R and the mains current i_R and center point current i_M for (a) $\rho_- = 0.5$, (b) $\rho_- = 0.0$ and (c) $\rho_- = 1.0$. Time base: 2ms/div, v_R : 200V/div, i_R and i_M : 4A/div.

4.6 Rectifier Loading Capability

The positive maximum value of the center-point current I_M is formed for $\rho_- = 0$, the negative maximum value for $\rho_- = 1$. The measurements shown in Fig.

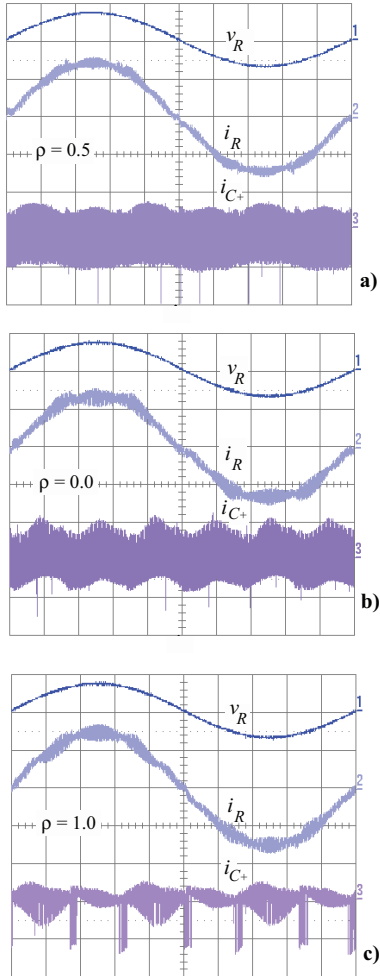


Figure 4.16: Experimental measurements showing the mains voltage v_R and the mains current i_R and positive bus capacitor current i_{C+} for (a) $\rho_- = 0.5$, (b) $\rho_- = 0.0$ and (c) $\rho_- = 1.0$. Time base: 2ms/div, v_R : 200V/div, i_R and i_{C+} : 4A/div.

4.16 show this dependence of the center-point current from ρ_- .

The general dependency of I_M on ρ_- and on the modulation index M for values $\rho_- \in [0, 1]$ which are constant over φ . For a controls point of view we assume therefore a control of the center point current (and of the center point potential) with low dynamics.

If a purely sinusoidal shape of the mains current is assumed, the average value of i_M in dependency on the parameter ρ_- and on the modulation index M can be calculated analytically:

$$I_{M,avg,r} = \frac{3}{\pi}(1 - 2\rho_-) \left[1 + \frac{1}{2M}(\sqrt{3M^2 - 1} - \frac{1}{\sqrt{3}}) - \frac{\sqrt{3}M}{4} \left(1 + \frac{2\pi}{\sqrt{3}} - 2\sqrt{3} \arcsin\left(\frac{1}{\sqrt{3}M}\right) \right) \right]. \quad (4.32)$$

Equation (4.32) represents a very good approximation of the exact dependency $I_{M,avg,r} = I_{M,avg,r}\{M, \rho_-\}$ which is shown in Fig. 4.17. For $\rho_- = 0.5$ in a first approximation the average value of the center point current is zero. According to Fig. 4.17 $I_{M,avg,r}$ shows an approximately linear dependency on the control input ρ_- and on the modulation index M . The maximum values of $I_{M,avg}$ resulting for $\rho_- = 1$ and $\rho_- = 0$ show equal absolute values. Therefore, basically a symmetric controllability $I_{M,avg}\{\rho_-\} = -I_{M,avg}\{1 - \rho_-\}$ of the center point current average value is given. The decrease of the maximum obtainable average value with increasing M is a consequence that for increasing values of M the overall on-time of the redundant switching states is reduced. In general this can also be explained by the fact that, in order to form a high amplitude of the fundamentals of the phase voltages (high M) the current flow has to be provided especially via the positive or negative free-wheeling diodes. Therefore, the power transistors have only relatively short on-times. In the average, only a low contribution of the phase currents is fed into the center point. The dependence of $I_{M,avg}$ on the amplitude \hat{I} of the mains current becomes immediately clear.

4.6.1 Load on the Output Capacitors

The output capacitors C_+ and C_- of the system (which in general are realized as electrolytic capacitors) have to be dimensioned with respect to rms current stress and admissible low-frequency ripple of the center point potential. In order to not exceed a given maximum value of the amplitude $\hat{V}_{M,(k)}$ in the capacitor voltage (as caused by the low-frequency harmonics $\hat{I}_{M,(k)}$ of the center point

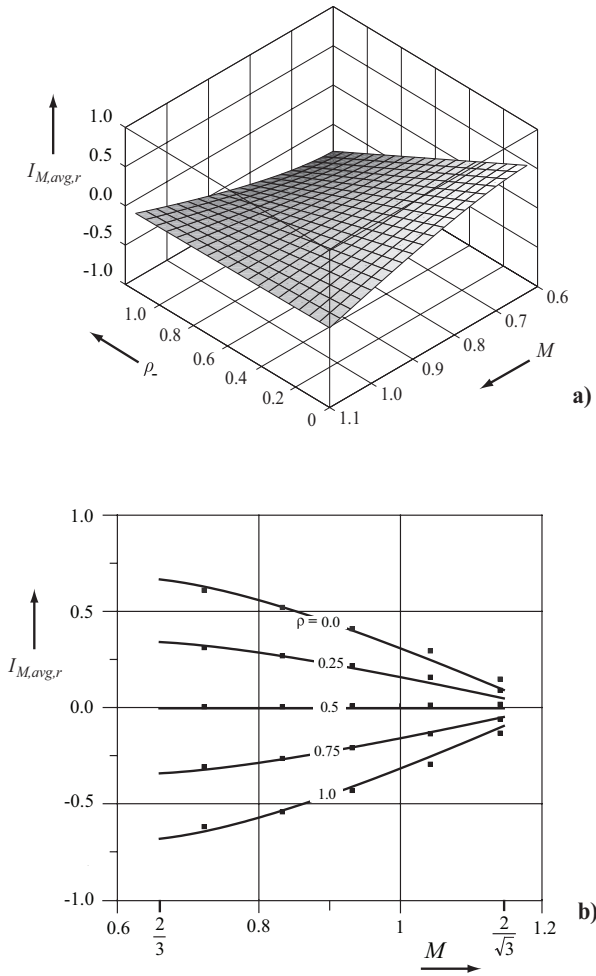


Figure 4.17: Dependency of the normalized average value of the center-point current i_M on the modulation index M and on ρ . Dots indicate experimental results.

current) we have to select

$$C \geq \frac{1}{k \omega \hat{V}_{C,(k)}} \hat{I}_{C,(k)} . \quad (4.33)$$

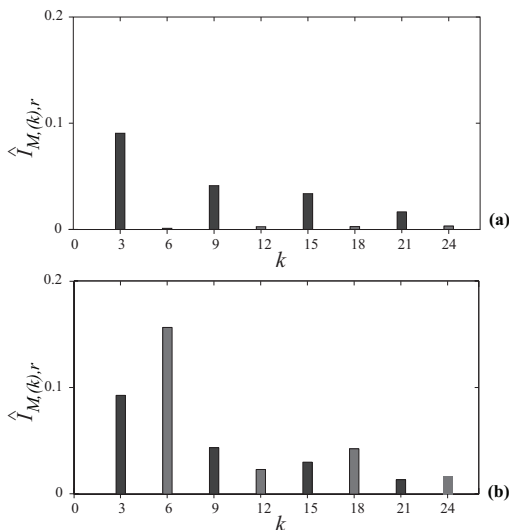


Figure 4.18: Amplitude spectrum of the center point current (normalized with respect to the amplitude of the mains current fundamental) as determined by digital simulation for $\rho_- = 0.5$ (cf. (a)) and $\rho_- = 0.0$ (cf. (b)).

($\hat{V}_{M,(k)}$ is set typically to $0.01V_o$.) There, k denotes the order of the current and voltage harmonics with respect to the mains frequency. For constant total output voltage V_o (controlled with high dynamics) a parallel connection of the output capacitors C_+ and C_- exists concerning the harmonics of the current i_M flowing into the center point M . Therefore, the center point current harmonics are divided into equal parts in both output capacitors. They shift the voltage center point, but they do not change to overall voltage V_o . Therefore, the harmonics of a capacitor current are calculated from the harmonics of i_M by

$$\hat{I}_{C,(k)} = \frac{1}{2} \hat{I}_{M,(k)}. \quad (4.34)$$

A typical spectrum of harmonics of i_M (where the DC term $I_{M,\text{avg}}$ is omitted) is shown in Fig. 4.18. For symmetrical control of the system ($\rho_- = 0.5$) the spectrum shows the amplitudes of the triplen harmonics ($k = 3, 9, 15, \dots$). With increasing asymmetry of the control (i.e., $\rho_- \rightarrow 0$, cf. Fig. 4.18(b), or $\rho_- \rightarrow 1$) the spectrum shows increased harmonics for $k = 6, 12, 18, \dots$ (even multiples of 3).

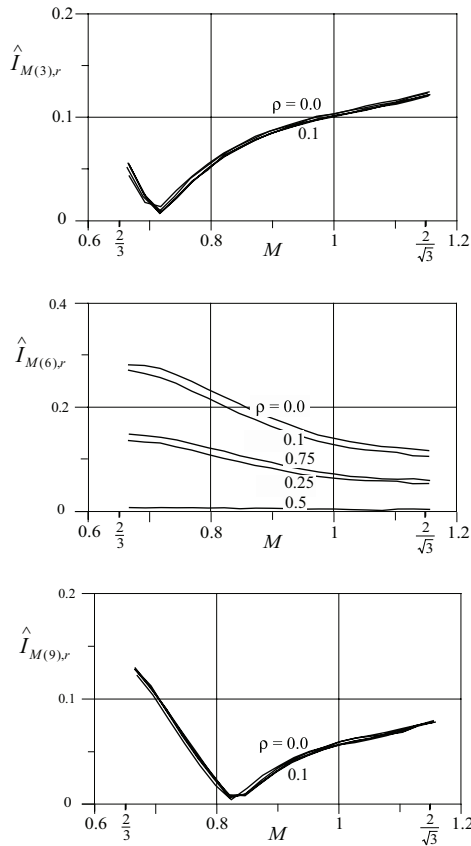


Figure 4.19: Dependency of the amplitudes of the low-frequency harmonics (ordinal number (k), $k = 3, 6, 9$) of the center point current on the modulation index M for different values ρ_- , as determined by digital simulation.

The dependency of the amplitudes of the low-frequency harmonics $k = 3, 6, 9$ (which are of special importance for the dimensioning) on the modulation index M and on the control parameter ρ_- is shown in Fig. 4.19. Basically, ρ_- influences only the amplitudes of the even-order center point current harmonics. The amplitudes of the odd-order center point current harmonics remain unchanged in a first approximation.

Besides the amplitudes of the harmonics of the center point and/or capacitor

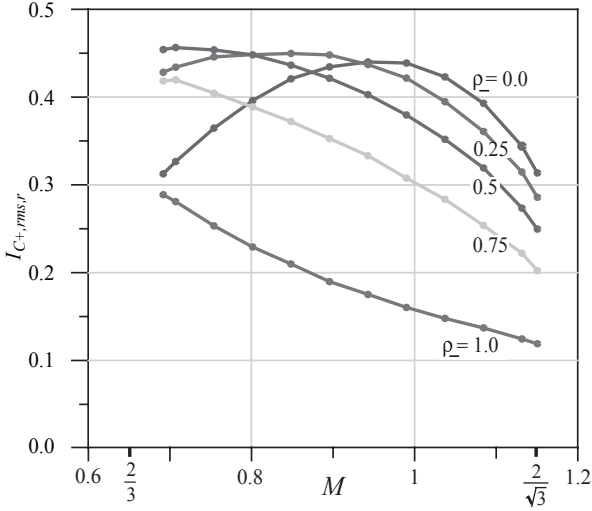


Figure 4.20: Experimental measurement of the normalized value $I_{C_+,rms,r}$ of the current in the output capacitor C_+ showing the dependency on the modulation index M and on ρ_- . The current load of C_- (associated with a value ρ_-) can be determined by reading the rms value of $I_{C_+,rms,r}$ for $\rho'_- = 1 - \rho_-$.

current, the value of the output capacitors is selected with respect to the rms value of the capacitor current. The experimental measured current stress resulting for C_+ with dependency on M and ρ_- is shown in Fig. 4.20. For increasing load unsymmetry on the partial output voltages the current stress on the output capacitors C_+ and C_- is changed in opposite directions. Only for symmetric load (and/or for $\rho_- = 0.5$) both capacitors have equal current stress

$$I_{C_+,rms,r}^2|_{\rho_-=0.5} = \frac{10\sqrt{3}M}{8\pi} - \frac{9M^2}{16}. \quad (4.35)$$

4.7 Conclusion

This chapter has investigated the application of discontinuous modulation schemes for three-level rectifiers. Based on the knowledge of discontinuous PWM as implemented for two-level converters, a theoretical and experimental analysis of two discontinuous PWM methods is compared with continuous PWM. The

main advantage of the discontinuous modulation implemented for three-level rectifiers is the possibility of increasing the switching frequency, which allows the reduction of the input current ripple as well as a considerable reduction of the input EMI filter size. The switching losses are also lower compared to continuous modulation.

The presented DPWMA has demonstrated to have better performance than DPWMB and CPWM, especially for high modulation indices ($M > 0.93$). However, it is shown that discontinuous modulation results in a dominant third harmonic in the center point current and the implementation of the center point voltage control may introduce further switching transitions, hence resulting in a poorer harmonic performance of the modulation.

For practical realization of the current control of a three-level rectifier, discontinuous modulation is preferred to continuous modulation, especially if high power density and/or low filtering effort and/or small size of the AC-side passive components are required. Since the advantages of the discontinuous modulation are recognized for higher modulation indices, it may be a good strategy to swap between different modulation strategies according to rectifier's operating point, thus realizing a high-performance adaptive modulation algorithm [108, 103].

Chapter 5

HF Characterization of Magnetic Components

5.1 Introduction

The wide-band characteristics of passive components are becoming increasingly important even for high power applications, for which there has been a steady increase in switching frequencies over recent years. Modern circuit simulation software running on present computers is more able to cope with high frequencies, and enables tighter control bandwidth. The ability to predict conducted EMI in power electronics circuitry before even constructing a prototype has also become a reality. These are only some of the reasons why high frequency behavior will gain increasing interest for the accurate characterization, modeling and design of circuit components, such as filters, inductors, capacitors and sensors, for frequencies typically up to 30 MHz.

Current transformers with high frequency bandwidths are of special interest, since they are widely used in EMC compliance testing to measure disturbances as well as in power electronics circuits with high switching frequencies and wide-band control functions [123]. This manuscript investigates the high frequency behavior of a gapped toroidal magnetic structure which is intended for a current sensor application. In practice the application includes a Hall-effect element, which is physically positioned in the air-gap as shown in Fig. 5.1, for DC and low frequency components of the measured current. The higher frequencies, to which the Hall-sensor is insensitive, are detected magnetically. The magnetic structure, which will be considered herein, thus consists of a toroidal core with

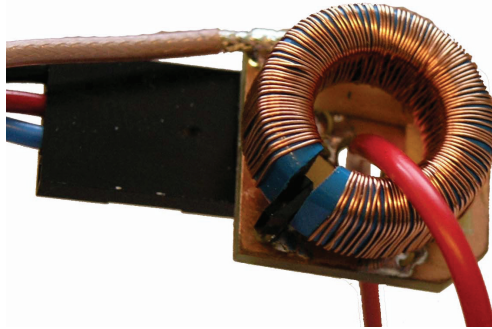


Figure 5.1: Prototype of DC-broadband CT showing the wound toroid with a Hall-element positioned in the air gap.

an air-gap, a single-turn primary passing through the center window of the core, and a multi-turn secondary winding connected to the detection circuitry via a small load resistor. Even though this is in principle a rather simple structure, its behavior at high frequencies is affected by several factors that can produce highly non-linear response signals. Firstly, a large air-gap (necessitated by the physical dimensions of the Hall-element) in a toroidal core produces a large distribution of fringing flux that leaks through the window of the core instead of passing through the air gap. This irregular distribution of flux depends on the winding arrangement. Secondly, the core characteristics become non-linear due to the frequency-dependent behavior of the ferrite core. At higher frequencies rotational magnetic losses dominate, and the dielectric properties of the material play an increasing role. Lastly, the secondary winding itself exhibits enough stray capacitance and stray inductance to affect performance, notwithstanding the internal impedances which give rise to a substantial higher resistance due to eddy current effects. The complexity of its behavior due to the combination of the above effects does not only affect the modeling of the structure, but also its empirical characterization. In [124] the difficulties and trade-offs associated with wide-band characterization of a current probe by means of frequency domain, S-parameter testing and time domain testing were discussed. In this study a lumped element model is extracted using impedance measurements and the dominating design parameters that dictate broadband performance are also identified. A permeance-based model of the core is implemented to model the magnetic circuit and stray capacitance and inductance of the winding are also

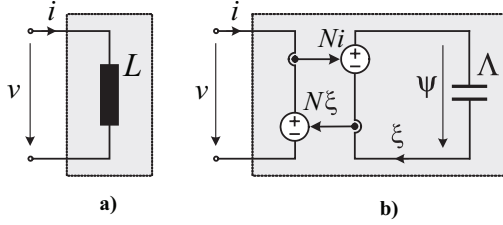


Figure 5.2: Electrical circuitual model of a coil: a) conventional equivalent and b) permeance-capacitance analogy based model with coupling between electrical and magnetic circuits using a Tellegen gyrator.

included. The model includes a linear lumped element equivalent circuit to approximate the non-linear complex permeability of the core, which was measured experimentally. A set of gyrators is used to couple the electric and magnetic models for circuit simulation.

5.2 The Capacitance-Permeance Analogy

The conventional electrical equivalent of a coil is shown in Fig. 5.2 a, where i and v are the current and voltage at the winding terminals related by

$$v = L \frac{di}{dt} \quad (5.1)$$

and L is the self-inductance value. In order to highlight the properties of the core we recall the relations

$$\begin{aligned} v &= N\xi \\ \psi &= Ni \end{aligned} \quad (5.2)$$

being N the number of turns, ξ the induced voltage per turn and ψ the magnetomotive force (MMF). It should be noted that equations (5.2) represent Faraday's and Ampere's Laws respectively (see page 186 of [125]).

Greek letters indicate the magnetic quantities to better distinguish them from the electric ones. The permeance Λ of the magnetic core is defined as

$$\Lambda = \frac{\phi}{\psi} = \frac{\mu A}{l} \quad (5.3)$$

where μ is the core permeability, A and l the core cross-section and the magnetic flux pathlength, respectively. The relation between the MMF ψ and the magnetic flux ϕ in a magnetic system

$$\xi = \frac{d\phi}{dt} = \Lambda \frac{d\psi}{dt} \quad (5.4)$$

can be written analogous to the relation between charge q and voltage v across a capacitor:

$$i = \frac{dq}{dt} = C \frac{dv}{dt}. \quad (5.5)$$

From (5.4) and (5.5) it follows that the MMF ψ is used analogous to the voltage v , whereas the induced e.m.f. ξ is used analogous to the electrical current i .

Accordingly the magnetic circuit can be modelled by an electrical loop (cf. Fig 5.2b) where the permeance Λ is modelled by a capacitor, the current flowing is the flux rate ξ (5.4) and the voltage across the capacitor is the MMF ψ . The magnetic and the electric circuits are coupled by a Tellegen gyrator defined by the relations (5.2).

This model based on the permeance-capacitance analogy [126, 127] presents numerous advantages:

1. the implementation of frequency dependent components and complex permeability;
2. the simulation of a magnetic network by an electrical circuit;
3. it allows access to the flux rate ξ and the MMF ψ ;
4. geometry and number of turns are included in the model;
5. since a resistance element in the permeance model represents core losses (unlike the conventional magnetic reluctance model where resistance represents energy storage), core losses could be also extracted using this method [126].

5.2.1 Transformer Equivalent Circuit

Fig. 5.3 depicts a sketch of a gapped current transformer comprised of N_1 and N_2 primary and secondary turns of resistance R_1 and R_2 , respectively, a load resistor R_L , and a gapped magnetic core, of air-gap δ , cross sectional area A and flux pathlength l in the core.

The transformer equivalent model shown in Fig. 5.4 has been drawn using the capacitance-permeance analogy. All the set of equations that describe a transformer can be written by inspection of the circuit in Fig. 5.4.

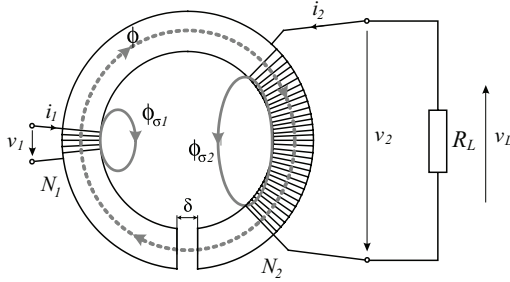


Figure 5.3: Sketch of a gapped current transformer.

Accordingly, the equations of the electric loops are:

$$\begin{aligned} v_1 &= R_1 i_1 + N_1 \xi_1 = R_1 i_1 + N_1 \frac{d\phi_1}{dt} \\ v_2 &= R_2 i_2 + N_2 \xi_2 = R_2 i_2 + N_2 \frac{d\phi_2}{dt} \end{aligned} \tag{5.6}$$

whereas the relations associated to the nodes of the magnetic circuit are

$$\begin{aligned} \phi_1 &= \phi_{\sigma 1} + \phi \\ \phi_2 &= \phi_{\sigma 2} - \phi \end{aligned} \tag{5.7}$$

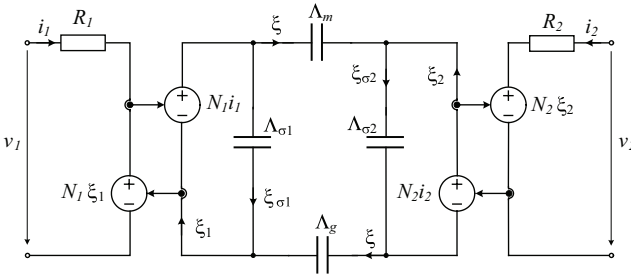


Figure 5.4: Equivalent model of a transformer based on the permeance-capacitance analogy. In particular Λ_m and Λ_g indicate the permeances of the magnetic core and the air-gap, respectively; $\Lambda_{\sigma 1}$ and $\Lambda_{\sigma 2}$ the shunt permeances of the primary and secondary leakage fluxes.

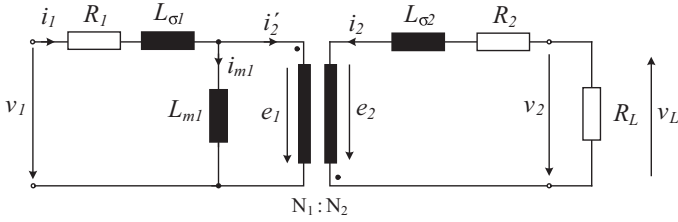


Figure 5.5: Equivalent electric circuit of a current transformer.

and

$$\begin{aligned}
 \phi_{\sigma 1} &= \Lambda_{\sigma 1} N_1 i_1 \\
 \phi_{\sigma 2} &= \Lambda_{\sigma 2} N_2 i_2 \\
 \phi &= \left(\frac{\Lambda_m \Lambda_g}{\Lambda_m + \Lambda_g} \right) (N_1 i_1 - N_2 i_2).
 \end{aligned} \tag{5.8}$$

The primary and secondary leakage fluxes, $\phi_{\sigma 1}$ and $\phi_{\sigma 2}$, are dependent on the permeances $\Lambda_{\sigma 1}$ and $\Lambda_{\sigma 2}$ of the leakage paths whereas the magnetizing flux ϕ is proportional to the resultant MMF and to the permeance of the air gap Λ_g which is much smaller than the core permeance Λ_m ,

$$\Lambda_g = \frac{\mu_0 A}{\delta} \ll \frac{\mu_0 \mu_r A}{l} = \Lambda_m \tag{5.9}$$

where μ_0 and μ_r air and core permeability, respectively. By substituting (5.7) and (5.8) in (5.6) and considering (5.9), the primary voltage v_1 is given by

$$\begin{aligned}
 v_1 &= R_1 i_1 + N_1 \frac{d\phi_{\sigma 1}}{dt} + N_1 \frac{d\phi}{dt} \\
 &= R_1 i_1 + \Lambda_{\sigma 1} N_1^2 \frac{di_1}{dt} + \Lambda_g N_1^2 \frac{di_1}{dt} - \Lambda_g N_1 N_2 \frac{di_2}{dt}
 \end{aligned} \tag{5.10}$$

where

$$\begin{aligned}
 L_{\sigma 1} &= \Lambda_{\sigma 1} N_1^2 \\
 L_{m1} &= \Lambda_g N_1^2 \\
 M &= \Lambda_g N_1 N_2 \\
 L_1 &= L_{\sigma 1} + L_{m1}
 \end{aligned}$$

are *leakage*, *magnetizing*, *mutual*, and *self*- inductances, respectively, of the pri-

mary winding. L_1 and M can be measured, L_{m1} can be calculated and $L_{\sigma 1}$ can be derived. These parameters can be determined by means of the well known open-circuit and short-circuit tests [128]. Equation (5.10) can be further arranged as follows

$$\begin{aligned} v_1 &= R_1 i_1 + L_{\sigma 1} \frac{di_1}{dt} + L_{m1} \frac{d}{dt} \left(i_1 - \frac{N_2}{N_1} i_2 \right) \\ &= R_1 i_1 + L_{\sigma 1} \frac{di_1}{dt} + L_{m1} \frac{di_{m1}}{dt} \end{aligned} \quad (5.11)$$

which corresponds to the primary side of the electrical circuit in Fig. 7.3. There, the currents i'_2 and i_{m1} are defined respectively as:

$$i'_2 = \frac{N_2}{N_1} i_2 \quad (5.12)$$

$$i_{m1} = i_1 - i'_2 \quad (5.13)$$

In a similar fashion, the output voltage v_2 can be written from (5.6) and (5.7) as

$$v_2 = R_2 i_2 + N_2 \frac{d\phi_{\sigma 2}}{dt} - N_2 \frac{d\phi}{dt} \quad (5.14)$$

and the *leakage*, *magnetizing*, *mutual*, and *self*-inductances of the secondary winding can be defined analogous to the primary as follows:

$$\begin{aligned} L_{\sigma 2} &= \Lambda_{\sigma 2} N_2^2 \\ L_{m2} &= \Lambda_g N_2^2 \\ M &= \Lambda_g N_2 N_1 \\ L_2 &= L_{\sigma 2} + L_{m2}. \end{aligned}$$

The e.m.f. e_2 induced in the secondary by the mutual flux ϕ , is defined as

$$e_2 = N_2 \frac{d\phi}{dt} \quad (5.15)$$

and it drives the secondary current i_2 . The e.m.f. e_1 induced across the primary winding is similarly given by

$$\begin{aligned} e_1 &= N_1 \frac{d\phi}{dt} \\ &= L_{m1} \frac{di_{m1}}{dt} \end{aligned} \quad (5.16)$$

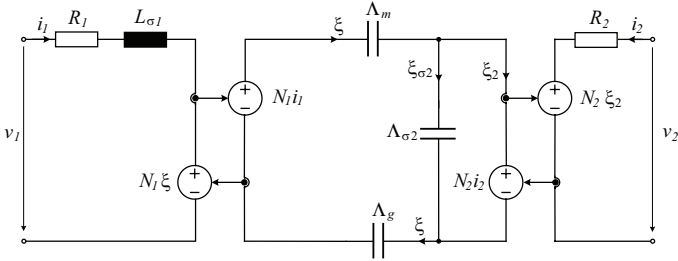


Figure 5.6: Equivalent model of the transformer based on the permeance-capacitance analogy: significance of the leakage inductance.

and it is related to e_2 through the transformer ratio:

$$\frac{e_2}{e_1} = \frac{N_2}{N_1}. \quad (5.17)$$

This latter and (5.12) constitute the equations of an ideal transformer, *i.e.* core permeability μ_r infinite and magnetic flux ϕ zero.

The (5.14) can be written as

$$e_2 = R_2 i_2 + L_{\sigma 2} \frac{di_2}{dt} - v_2 \quad (5.18)$$

Let define R_L and v_L as the load resistor and load voltage:

$$\begin{aligned} v_L &= R_L i_2 \\ &= -v_2. \end{aligned} \quad (5.19)$$

Considering (5.13), (5.16), (5.17) and (5.19), it follows

$$\begin{aligned} \frac{N_2}{N_1} \left(L_{m1} \frac{d}{dt} \left(i_1 - \frac{N_2}{N_1} i_2 \right) \right) &= R_2 i_2 + L_{\sigma 2} \frac{di_2}{dt} + v_L \\ M \frac{di_1}{dt} - L_{m2} \frac{di_2}{dt} &= R_2 i_2 + L_{\sigma 2} \frac{di_2}{dt} + R_L i_2 \\ M \frac{di_1}{dt} &= R_2 i_2 + L_2 \frac{di_2}{dt} + R_L i_2 \end{aligned} \quad (5.20)$$

Using the Laplace transform, where s indicates the Laplace operator, from

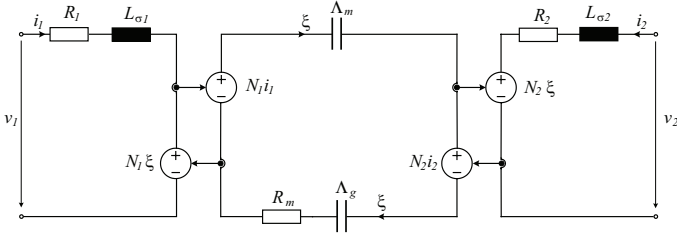


Figure 5.7: Equivalent model of the transformer based on the permeance-capacitance analogy: significance of the resistance in the magnetic loop.

(5.20) the ratio between primary and secondary currents is then provided by:

$$\begin{aligned}
 \frac{I_2(s)}{I_1(s)} &= \frac{sM}{R_2 + R_L + sL_2} \\
 &= \frac{N_1}{N_2} \frac{sL_{m2}}{R_2 + R_L + sL_2} \\
 &= \frac{N_1}{N_2} \frac{s \frac{L_{m2}}{R_2 + R_L}}{1 + s \frac{L_2}{R_2 + R_L}}. \tag{5.21}
 \end{aligned}$$

5.2.2 Properties of the Equivalent Circuit

Fig. 5.4 represents the equivalent circuit of a transformer based on the capacitance-permeance analogy. It is constituted of two electric loop, for the primary and secondary winding, and one magnetic loop that models the core and the magnetic flux paths.

As show in Fig. 5.6, the shunt capacitance in the magnetic loop, which accounts for the leakage flux permeance, can be replaced by an inductance in series in the electric loop, without varying the response and the properties of the model. Moreover, a resistance in the magnetic loop (see Fig. 5.7) accounts for the losses in the magnetic circuit, contrary to the resistance-reactance based model of the transformer, in which a resistance is a storage element.

5.3 Core Material Characterization

5.3.1 Measurements of Complex Permeability

Complete material information over a broad frequency bandwidth is not always available. Therefore the measurement of the fundamental ferrite parameters, i.e. permeability, permittivity and conductivity must often be performed by the magnetic designers themselves. For this aim, specific material samples must be used. The complex relative permeability $\mu_r = \mu' - j\mu''$ can be extracted by measuring the reactance of a thin toroidal core (cf. Fig. 5.8). Since the dimensional effects influence this kind of measurement, the core cross-section should be sufficiently small [129, 130, 131]. Moreover, the windings on the sample core should ideally wrap fully around the circumference of the toroid. This uniform winding reduces the amount of flux that leaves the core and forces a more uniform flux density distribution in the core. The impedance Z of an N -turn inductor L can be represented at any given frequency $\omega/2\pi$ by the series combination of a resistance, R_s , and a reactance, $j\omega L_s$.

$$\begin{aligned}
 j\omega L &= j\omega\mu_o\mu_r \left(\frac{N^2 A_e}{l_e} \right) \\
 &= j\omega\mu_o(\mu' - j\mu'') \left(\frac{N^2 A_e}{l_e} \right) \\
 &= j\omega \left(\frac{\mu_o\mu' N^2 A_e}{l_e} \right) + 2\pi f \left(\frac{\mu_o\mu'' N^2 A_e}{l_e} \right) \\
 &= j\omega L_s + R_s
 \end{aligned} \tag{5.22}$$

where A_e is the effective core cross section and l_e is the mean flux path length. The values of equivalent series circuit parameters R_s and L_s can be measured directly using an impedance analyzer.

The real and imaginary parts of the complex relative permeability are then obtained from:

$$\mu'(f) = L_s(f) \left(\frac{l_e}{\mu_o N^2 A_e} \right) \tag{5.23}$$

$$\mu''(f) = R_s(f) \left(\frac{l_e}{2\pi f \mu_o N^2 A_e} \right). \tag{5.24}$$

A R4 toroidal core of N30 ferrite, having dimensions $d_{ext} = 4$ mm, $d_{int} = 2.4$ mm, $h = 1.6$ mm, was used for the measurement. This thin toroid was fully wound with $N = 22$ turns. The impedance was measured with an AGILENT A294A Precision Impedance Analyzer with an oscillation level of 0.5 mA. The

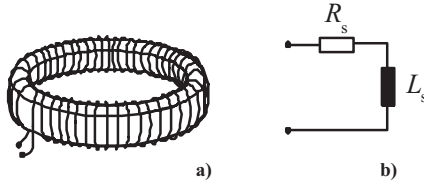


Figure 5.8: (a) Fully wound thin toroid for the measurement of complex permeability and (b) its equivalent circuit.

results shown in Fig. 5.9 are in good agreement with similar measurements obtained for larger cores [132].

5.3.2 Prototype Construction

The magnetic cores selected for the measurements were R16 toroidal cores of N30 ferrite. Two designs were prototyped for testing; one having an air gap of 1.6 mm and another without an air gap as shown in Fig. 5.10.

5.3.3 Winding Arrangement

High immunity against external fields is important especially for current measurement applications. The winding arrangement must therefore be chosen carefully so that any external magnetic fields will not influence the sensor accuracy [133]. If a traditional winding is realized, as in Fig. 5.11a, then the area linked with the external magnetic field is about equal to the internal circumference of the toroid. If one of the two terminals is returned back along the outer circumference of the toroid, then the loop area is reduced as in Fig. 5.11b. This solution is usually used for realizing Rogowski coils [134, 135, 136]. If the return conductor is also wound as in Fig. 5.11c, then the loop area is further reduced. For a gapped toroid, this latter winding strategy can be realized as shown in Fig. 5.11d.

The secondaries of the prototypes consisted of 120 turns of 0.2 mm magnet wire.

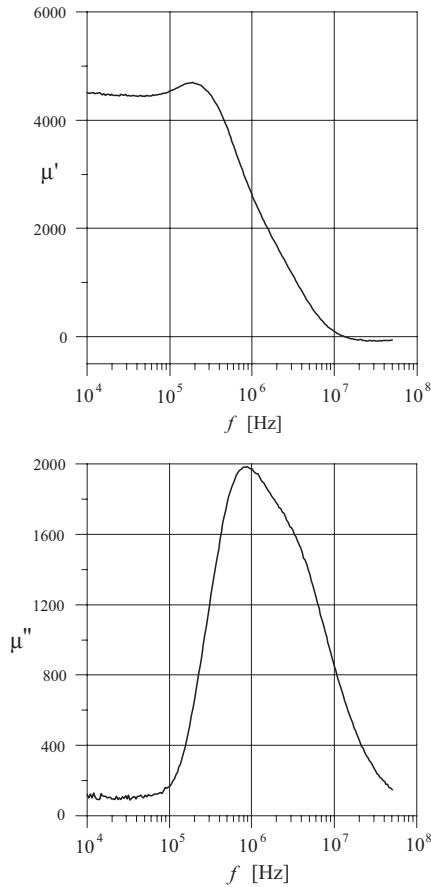


Figure 5.9: Frequency plot of the real and imaginary parts, μ' and μ'' respectively of the complex relative permeability for N30 ferrite at 25°C.

5.3.4 Modeling the Nonlinear Magnetic Core

The capacitance-permeance model [137, 138, 139] was chosen to model the rotational magnetization losses of the magnetic core. The model allows electrical simulation of a non-linear magnetic structure, through an analogous transformation of field quantities and the implementation of a gyrator.



Figure 5.10: Prototypes of the broadband DC-CT. Ungapped toroids were used for empirical characterization.

In a circuit simulator the magnetic circuit can thus be constructed using capacitor elements to represent all of the permeances. In the magnetic domain, the flux path may be broken into series capacitor elements representing permeances, whereas the flux cross section may be broken into parallel capacitor elements representing permeances. For instance, a core with an air gap is modeled as a capacitor for the core permeance in series with a capacitor representing the permeance of the air gap. The connection to the electrical circuit can then be represented by the Tellegen gyrator according to (5.2), comprising a controlled voltage source producing ψ (in series with the two capacitors), and another controlled voltage source producing the electrical voltage.

If the frequency dependency of the ferrite core permeability is to be included in the model, then a simple curve fit may be implemented to approximate the complex permeability as a function of frequency. For frequencies up to 200 MHz, the permeability is then approximated by assuming that

$$\mu_r(j\omega) = 1 + \frac{\chi_1}{1 + j\omega\chi_1\tau_1} + \frac{\chi_2}{1 + j\omega\chi_2\tau_2} \quad (5.25)$$

Formula (5.25) is a description of the complex permeability through relaxation effects. χ_1 and χ_2 represent the low frequency susceptibilities of the domain wall movement and rotational magnetic losses respectively. The time constants τ_1 and τ_2 are material properties. For a toroid having a cross section, A and a magnetic path length l , the non-linear permeance of the core can be represented by a circuit comprising linear elements as shown in Fig. 5.12. For N30 ferrite, Table 5.1 lists the curve-fitted values that were obtained empirically

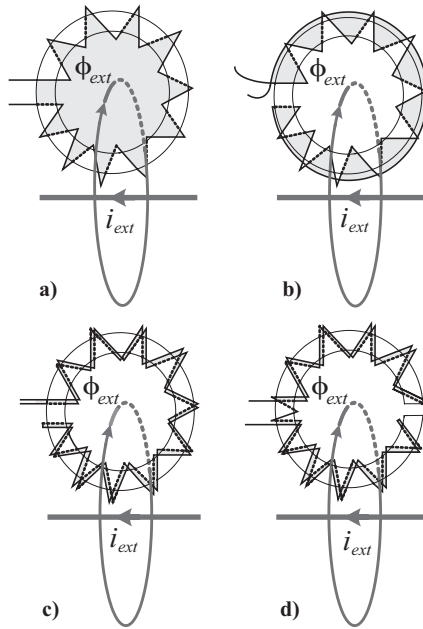


Figure 5.11: Effect of an external magnetic field for different winding arrangements on toroidal magnetic cores. The cross sectional area of flux linkage in (a) becomes smaller if a conductor is returned to the starting position as shown in (b). This loop area reduces further if the return conductor is wound as shown in (c). For a gapped toroid, such as in (d), the arrangement must be repeated twice.

and subsequently used in the simulations.

Fig. 5.12 depicts the equivalent lumped element circuit for representing the frequency-dependent complex permeability of the core. The complex permeability is assumed to obey the function (5.25).

The admittance of this circuit in the frequency domain is:

$$\begin{aligned}
 Y(j\omega) &= j\omega \frac{\mu_0 \mu_r(j\omega) A}{l} &= j\omega C_o \mu_r(j\omega) \\
 & &= Y_o(j\omega) \mu_r(j\omega)
 \end{aligned} \tag{5.26}$$

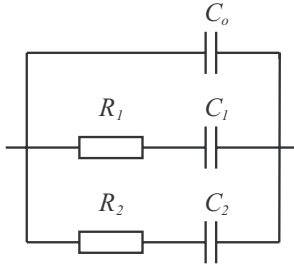


Figure 5.12: Equivalent magnetic circuit for the complex permeability using linear lumped electrical elements.

where:

$$C_o = \frac{\mu_0 A}{l} \quad (5.27)$$

Since C_o can be calculated directly from the geometry, the other four parameters are more easily obtained by subtracting this value:

$$\begin{aligned} \frac{Y(j\omega) - Y_o(j\omega)}{Y_o(j\omega)} &= \frac{Y(j\omega) - j\omega C_o}{j\omega C_o} = \mu_r(j\omega) - 1 \\ &= \left(\frac{C_1/C_o}{1 + j\omega(\frac{C_1}{C_o})(\frac{R_1}{C_o})} + \frac{C_2/C_o}{1 + j\omega(\frac{C_2}{C_o})(\frac{R_2}{C_o})} \right) \end{aligned} \quad (5.28)$$

By inspection, all of the equivalent circuit element values are then identified

Table 5.1: Parameters for complex permeability of N30 ferrite

μ_r		permeance	
name	value	name	value
χ_1	2.621×10^3	C_o	671.5 pF
χ_2	1.599×10^3	C_1	1.76 μ F
τ_1	4.385×10^{-11}	C_2	1.074 F
τ_2	6.943×10^{-11}	R_1	65 m Ω
		R_2	103 m Ω

as follows:

$$\begin{aligned}
 C_1 &= \chi_1 C_o \\
 C_2 &= \chi_2 C_o \\
 \tau_1 &= \chi_1 R_1 \\
 \tau_2 &= \chi_2 R_2
 \end{aligned}$$

The values of χ_1 , χ_2 , τ_1 and τ_2 can also be obtained by a simple method involving graphical inspection of measured data of the complex permeability. Equation (5.25) can be simplified:

$$\begin{aligned}
 \mu_r(j\omega) - 1 &= \frac{\chi_1}{1 + j\omega\chi_1\tau_1} + \frac{\chi_2}{1 + j\omega\chi_2\tau_2} \\
 &= \frac{\chi_1 + \chi_2 + j\omega\chi_1\chi_2(\tau_1 + \tau_2)}{(1 + j\omega\chi_1\tau_1)(1 + j\omega\chi_2\tau_2)} \\
 &= A_o \frac{1 + j\omega/\omega_{12}}{(1 + j\omega/\omega_1)(1 + j\omega/\omega_2)} \tag{5.29}
 \end{aligned}$$

where:

$$\begin{aligned}
 A_o &= \chi_1 + \chi_2 \\
 \omega_1 &= (\chi_1\tau_1)^{-1} \\
 \omega_2 &= (\chi_2\tau_2)^{-1} \\
 \omega_{12} &= \frac{\chi_1 + \chi_2}{\chi_1\chi_2(\tau_1 + \tau_2)} \\
 &= \frac{A_o}{\frac{\chi_2}{\omega_1} + \frac{\chi_1}{\omega_2}} \tag{5.30}
 \end{aligned}$$

The approximate values of ω_1 , ω_2 and ω_{12} can be determined graphically by identifying asymptotes in a bode plot of the measured $\mu_r - 1$.

The plot of the complex relative permeability of N30 ferrite indicates that it is fair to assume that $\omega_1 < \omega_{12} < \omega_2$. The frequency $(2\pi\tau_2)^{-1}$ is Snoek's limit, which is typically in the order of several gigahertz for video head ferrites, whereas $(2\pi\tau_1)^{-1}$ lies somewhere between 0.1 and 3 GHz.

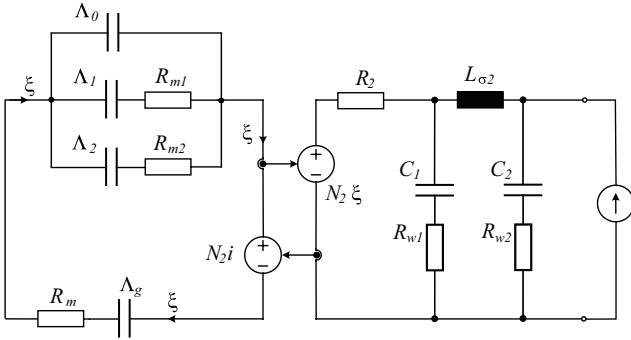


Figure 5.13: Equivalent circuit with core permeances model and extracted winding impedances for simulating the output impedance measurement.

5.4 Empirical Characterization of the Current Transformer

5.4.1 Open Circuit Impedance

The device under test is in essence a current transformer (CT) with a single conductor in the primary. A model for the secondary winding was extracted by measuring its output impedance with an open-circuited primary conductor still present. Rigorous methods for modeling winding impedances are given in [140, 141]. The measured and simulated results are plotted in Fig. 5.14 and the equivalent circuit for the simulation is depicted in Fig. 5.13. The lumped equivalent circuit model for the winding approximates the effects of winding stray capacitances, the winding leakage impedance and the high frequency ac resistance for the frequency range of interest. It can be extended to include higher order resonances that occur for frequencies beyond 30 MHz.

5.4.2 Transimpedance Gain

The primary was fed by a signal of constant amplitude over the frequency range 250 kHz to 30 MHz using a signal generator and a power amplifier as shown in Fig. 5.15, and a list of the equipment is given in Table 5.2. The primary of the CT consists of a custom designed coaxial construction that provides a constant resistance of 50Ω up to 30 MHz. It allows better stability over this frequency range and also matches the output impedance of the power amplifier. At each

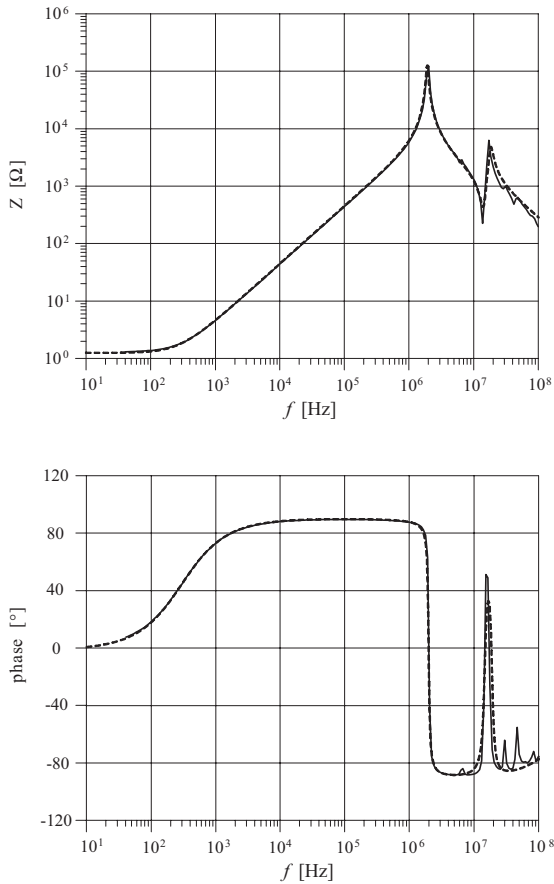


Figure 5.14: Plots of measured (solid line) and simulated (dashed line) output impedance.

frequency, the primary (input) current amplitude I_1 and the secondary (output) voltage amplitude V_L across the load resistor R_L are measured, along with the time delay between the two signals i_1 and v_L , that provides the difference $\Delta\varphi$ between the phases of the measured signals. The ratio between output voltage and input current provides the transfer function (TF) as a transimpedance gain V_L/I_1 , while the phase of the TF is given by $\Delta\varphi$.

5.4. EMPIRICAL CHARACTERIZATION OF THE TRANSFORMER

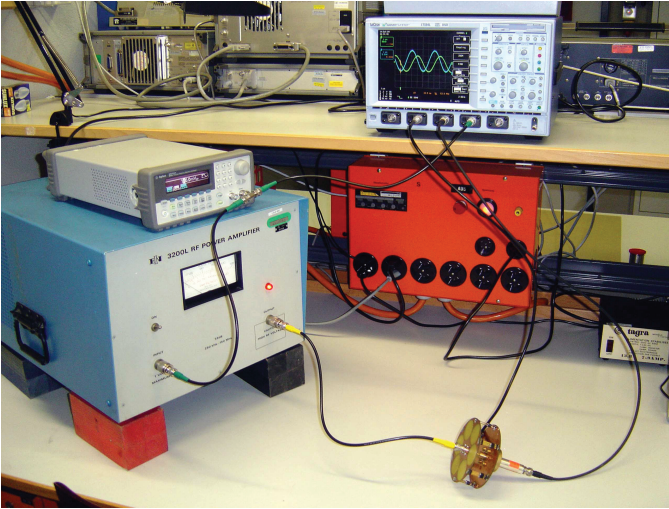


Figure 5.15: Photograph of the experimental setup.

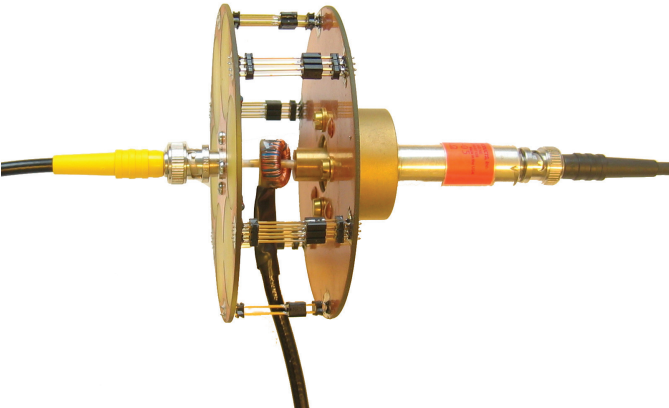


Figure 5.16: Detail of the experimental setup.

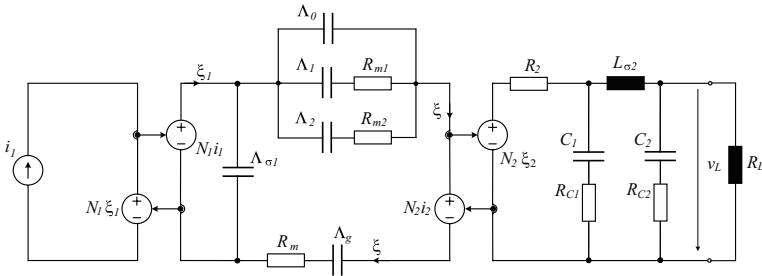


Figure 5.17: Equivalent circuit used to simulate the transimpedance gain of the current transformer.

The equivalent circuit of the current transformer for the transimpedance gain simulation is shown in Fig. 5.17. It includes the core permeances model for the non-linear core, the equivalent winding impedance, and the two Tellegen gyrators for the secondary winding and the single-turn primary winding.

5.4.3 Magnetic Flux Distribution

Each circuitual parameter used to model the gapped toroid has a specific physical meaning and influences the frequency behavior of the overall device to some degree according to the frequency of the exciting signal. In particular, the slope of the impedance curve in Fig. 5.14 depends mainly on the value of the air gap

Table 5.2: List of Equipment

Signal Generator	Agilent 33250A 80 MHz function/arbitrary waveform generator
Power Amplifier	ENI 3200L RF Power Amplifier gain 55 dB, 250 kHz-150 MHz
50 Ω Coaxial Primary	custom design 50 MHz bandwidth
50 m Ω Shunt	T&M Research Products Model A-1-05, $E_{max} = 20$ J
Oscilloscope	LeCroy Waverunner LT584L 1 GHz
Voltage Probe	LeCroy PP006A 500 MHz

5.4. EMPIRICAL CHARACTERIZATION OF THE TRANSFORMER

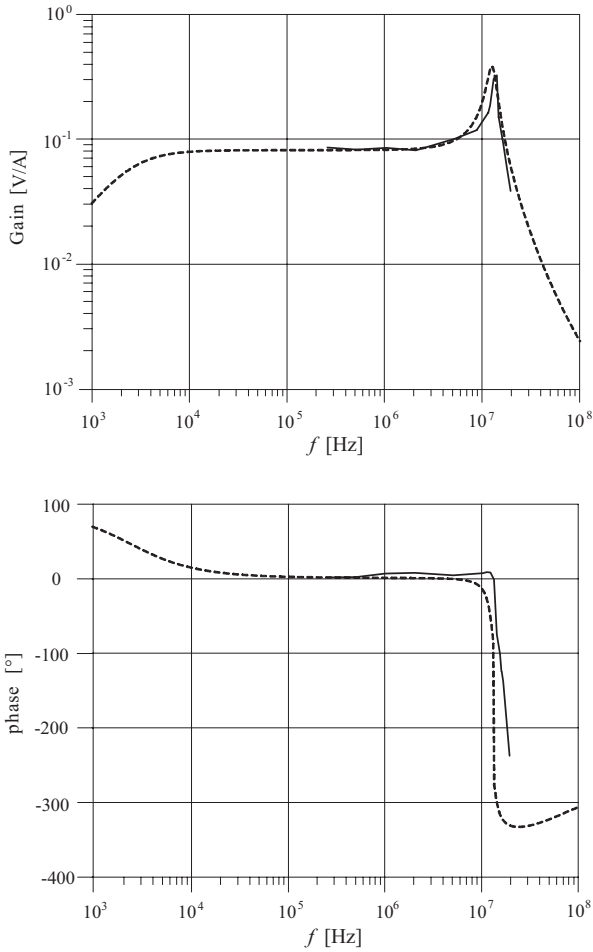


Figure 5.18: The measured (solid line) and simulated (dashed line) results of the transimpedance gain of the current transformer.

permeance C_g (Λ_g), since most of the magnetic field concentrates in the air gap. The first peak is provided by the parallel resonance between the magnetizing inductance and the winding self-capacitance, the second peak is given by the

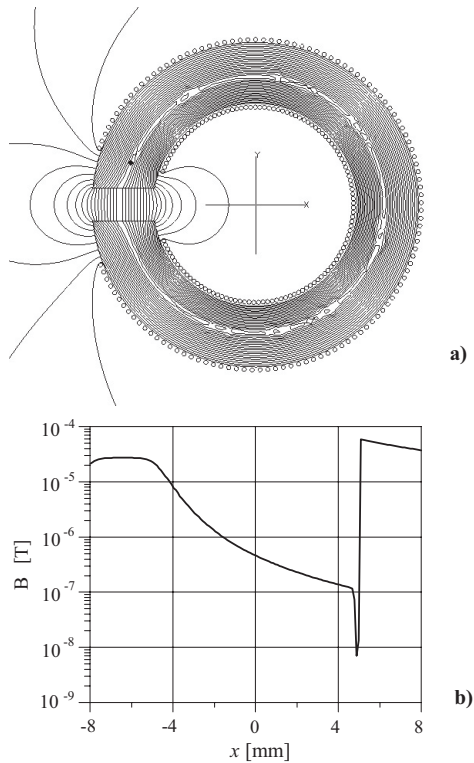


Figure 5.19: (a) Magnetic flux distribution for the inductor excited by a MMF of 10 A at 100 kHz and (b) the magnetic flux density B along the x -axis.

series resonance between winding leakage inductance L_s and self-capacitance and the third peak by the parallel resonance between L_s and winding self-capacitance. The damping associated with the second and third resonance peaks in the impedance plot, as well as the damping associated with the resonant peak in the transimpedance gain curve (cf. Fig. 5.18), are modeled by the two large resistors R_{C1} and R_{C2} . In fact, the core shunt capacitances, C_{w1} and C_{w2} , cannot simply be grounded since a ferrite material is a poor conductor and the resistors account for the high resistivity of the ferrite.

When the transimpedance gain is calculated (cf. Fig. 5.17), then the equiva-

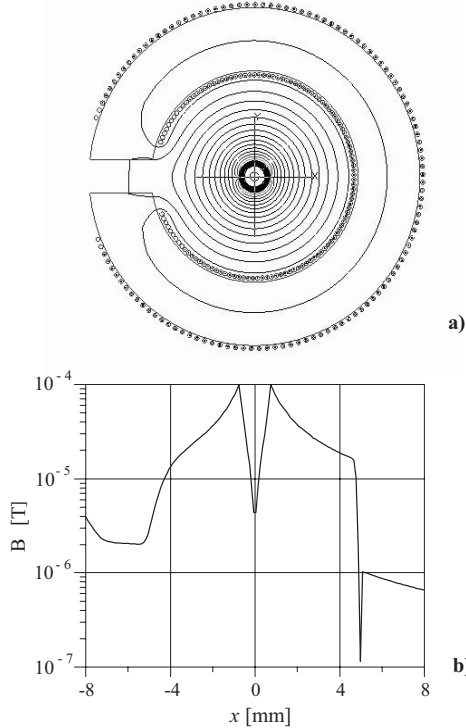


Figure 5.20: (a) Magnetic flux distribution for the current transformer excited by a primary current of 10A at 100 kHz and (b) the magnetic flux density B along the x -axis.

lent circuit remains the same except for the introduction of another gyrator that accounts for the primary and the secondary, which is then closed across a load resistor R_L . A small capacitor between the Tellegen gyrators takes into account leakage flux in the core window that reduces the coupling between the primary conductor and the secondary winding. It is well known that the expression of the transimpedance gain of a transformer for low frequency, i.e. neglecting all

HF effects and stray capacitance is

$$\frac{U_L}{I_1} = R_L \left(\frac{sM}{R_L + sL} \right) \quad (5.31)$$

where L is the self-inductance of the secondary and M is the mutual inductance between primary and secondary [142]. If there is good magnetic coupling between primary and secondary, which is typical for a toroid, then M/L equals the ratio of primary to secondary turns. Accordingly the low corner frequency and the transimpedance gain are defined respectively as

$$f_L = \frac{R_L}{2\pi L} \quad (5.32)$$

and

$$\left| \frac{U_L}{I_1} \right| = \frac{R_L}{N} \quad (5.33)$$

For this case study these values correspond to $f_L = 2.27$ kHz and $|U_L/I_1| = 83$ m Ω , where $L = 700$ μ H, $R_L = 10$ Ω and $N = 120$ turns. These theoretical values have been verified by the proposed transfer function model (cf. Fig. 5.18). If the coupling is not ideal, then the self inductance of the secondary L and the mutual inductance M are not proportional to one another. Therefore, the presence of a small capacitance between the Tellegen gyrators accounts for the non-ideal coupling. Accordingly the transimpedance gain will be lower and provided by the general expression

$$\left| \frac{U_L}{I_1} \right| = R_L \left(\frac{M}{L} \right) \quad (5.34)$$

Since the leakage inductance L_s is proportional to N^2 and the winding self capacitance C is proportional to N , reducing the number of turns N should extend the frequency band. The drawback of this solution is that the self inductance L will also decrease, thus increasing the lower corner frequency.

The value of the load resistor R_L plays a crucial role in current transformers. Firstly, both the lower corner frequency and the transimpedance gain depend on R_L . If R_L is increased, then a lower amplitude current will flow in the secondary, since the impressed e.m.f. (electro motive force) sMI_1 remains the same. Therefore the MMF due to the secondary current will compensate just part of the magnetic field associated with the primary current. The magnetic field density and flux line distribution for the inductor are shown in Fig. 5.19. The compensation of the primary magnetic field by the one in the secondary is evident by examining Fig. 5.20, where the device operates in the flat part (100 kHz) of its frequency response. For large values of the load resistor or even for open secondary, the primary MMF is not compensated. The flux in the core is basically given by the primary MMF and the device behaves just like an

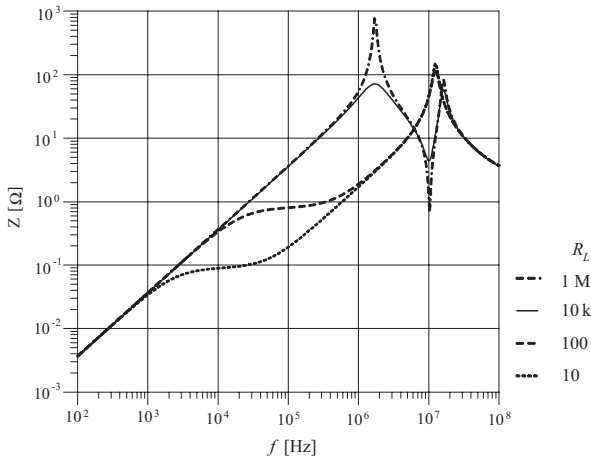


Figure 5.21: Frequency behavior as a function of the value of the load resistor R_L of the open loop secondary winding voltage or flux derivative or current in the magnetic circuit over a sinusoidal excitation of 1 A. In particular, the curve for $R_L = 1\text{M}\Omega$ provides the measured open loop impedance, just rescaled by the turn ratio. The curves were derived by using the equivalent circuit of the current transformer.

inductor. The magnetizing inductance assumes therefore a larger value and the frequency plots in Figs. 5.21-5.22 show a prominent first parallel resonance due to the large magnetizing inductance. If R_L is small, then more current will flow in the secondary. Ideally its amplitude should be equal to the primary current scaled by the turns ratio. In this case, the magnetizing inductance is very small due to flux cancellation so that the resultant flux within the transformer core is negligible. Consequently for small values of R_L , the magnetizing inductance will have no major influence on the frequency behavior, as is clearly evident from the curves in Figs. 5.21-5.22.

Fig. 5.21 depicts the voltage e (cf. Fig. 7.3) impressed across the secondary winding for a sinusoidal excitation of 1A. The voltage e is equal to the flux derivative, which is equivalent to the current flowing in the magnetic loop. In other words, this curve represents the impedance of the secondary winding rescaled by the turn ratio, since it is the primary which is being fed. In particular, the impedance plot in Fig. 5.14 corresponds to one of the curves in Fig. 5.21, which was obtained for the largest value of the load resistor. Moreover,

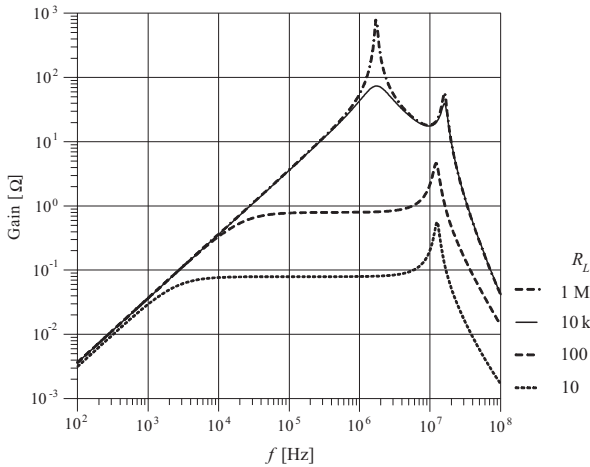


Figure 5.22: Transimpedance gain of the current transformer as a function of the value of the load resistor R_L . In particular, the curve for $R_L = 10\Omega$ corresponds to the case study. The curves are derived by using the equivalent circuit of the current transformer.

the influence of the magnetizing inductance or of the resulting magnetic flux on the shape of the impedance frequency plot is directly apparent from the plots. The results of a similar procedure for the transimpedance gain are depicted in Fig. 5.22.

5.5 High Frequency Effects

5.5.1 High Frequency Model of Ferrite Material

Ferrite materials show very complex high frequency behavior. The combination of high frequency excitation and physically large magnetic cores can result in losses and field distributions (dimensional effects) that are not encountered in low power and lower frequency devices. The research in this area has always been very limited although ferrite core devices are components present in many power electronic circuit [?, 130, 143, 144].

Ferrites are semiconductor materials that provide a preferential path for the magnetic field's lines and increase the stored magnetic energy. The definition

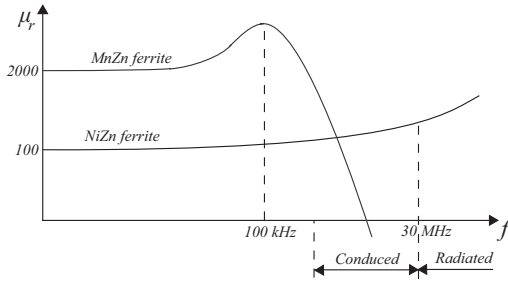


Figure 5.23: Frequency response of the relative permeability of MnZn and NiZn ferrites.

of the ferrite as a semiconductor allows one to point out its conducting properties, accounted by a conductivity σ . A well known effect, due to the finite conductivity of the ferrite, is the stray capacitance of the windings to the core, dependent on the electric field lines that can terminate on the ferrite core.

Ferrites are the most important compounds for applications where high permeability and low loss are the main requirements. They are composed of oxides containing ferric ions as the main constituent, and they are divided into two main categories: Manganese Zinc ferrites ($MnZnFe_2O_4$, $\mu_r = 4000 \dots 10000$) and Nickel Zinc ferrites ($NiZnFe_2O_4$, $\mu_r = 100 \dots 1000$). The *MnZn* ferrites has larger permeability value than the *NiZn* ones, hence they relax (dispersion phenomena) before than the *NiZn* which are therefore more suitable for high frequency applications. Typical value of the relaxation frequency for *MnZn* ferrites are in the range of hundred of kHz up to some MHz. At this frequency, the ferromagnetic material ($\mu_r > 0$) becomes diamagnetic ($\mu_r < 0$) and expels the magnetic field for frequencies higher than the relaxation's one. Fig. 5.23 represents the imaginary part of the complex permeability

$$\dot{\mu} = \mu' - j\mu'' \quad (5.35)$$

In order to better explain the dielectric behavior of the material, it is important to understand its structure. Polycrystalline ferrites may be regarded as compound dielectric consisting of semiconducting grains (crystallites) surrounded by thin boundaries having much higher resistivity. In the ferrite, core grains are combined by the organic binder during the manufacturing process (see Fig. 5.24). The dielectric effects between adjacent grains become significant when the frequency reaches the kHz-MHz range. These effects depends on the complex permittivity

$$\dot{\epsilon} = \epsilon' - j\epsilon'' \quad (5.36)$$

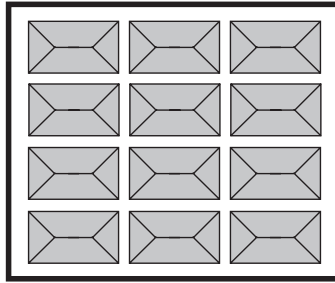


Figure 5.24: Idealized structure of ferrite where one crystal coincides with one grain. The grain constitutes the magnetic material itself while the surrounding boundaries (white) have dielectric characteristics.

f	μ'	μ''	ϵ'	ϵ''	σ
100 Hz	4220	20	$1.130e^5$	$1.820e^7$	$6.00e^{-4}$
1 kHz	4220	20	$1.010e^5$	$1.800e^6$	$5.50e^{-3}$
100 kHz	4294	70	$5.750e^4$	$3.875e^4$	0.32
200 kHz	4490.5	306.8	$5.378e^4$	$5.863e^4$	0.32
1 MHz	3150	2240	$3.125e^4$	$1.580e^4$	1.74
30 MHz	-34.4	102.1	$1.890e^3$	$1.535e^4$	3.15

Table 5.3: Material parameters of Ferrite N30

It should be noted that ferrites differ from metallic magnetic material because their eddy current losses, dependent on the conductivity σ , are considerably smaller and hence often negligible. Nevertheless the combination of a high dielectric constant, a high permeability and finite resistivity that ferrite cannot be treated either as a good conductor or a good insulator. This combination of material characteristics in combination with the operating frequency, leads to geometrical or dimensional resonances and significant eddy-current losses. If the dielectric constant and relative permeability have rather high values, then the electrical wavelength in the ferrite material is significantly shorter than in free space.

In order to characterize and analyze phenomena of dimensional resonance, the measurement of the material parameters (σ , $\hat{\mu}$, $\hat{\epsilon}$) is of fundamental importance [?, 130]. Table 5.3 shows the measured parameters for ferrite N30 as a function of frequency. Usually the dimensions of the ferrite sample used for measure the magnetic properties (the complex permeability) are small enough to neglect the

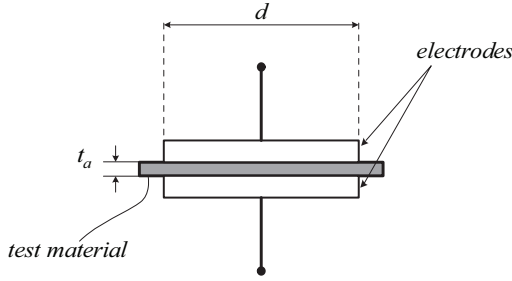


Figure 5.25: Contacting Electrode Method (Rigid Metal Electrode)

dimensional effects and the eddy currents losses. The information on the material is independent on the size and may be used to magnetically characterize all the devices made out of the same kind of material. In [130] is shown that once adequate material information is available as input, even relatively simple numerical solvers can provide reasonable prediction of device performance.

The dielectric constant can be calculated from the capacitance value measured by a dielectric test fixture when the ferrite is interposed between the electrodes (cf. Fig. 5.25). The *Contacting Electrode Method (Rigid Metal Electrode)* was used to measure the ferrite dielectric constant. This method uses a rigid electrode which make contact directly on the surface of the test material. The merits of the procedure are that the measurement the capacitance as well as the equations to obtain dielectric constant are simple. As drawback, an air film error might occur, which is caused by the air-gap between the electrodes and the surfaces of the test material. In order improve the contact between the ferrite sample and the electrodes, a thin film of silver was interposed. The real part ϵ'_r of the complex permittivity ϵ_r is obtained from:

$$\epsilon'_r = \frac{t_a}{\epsilon_0 A} C_p(f) \quad (5.37)$$

where t_a is the average thickness of test material, A is the area of guarded electrode (the diameter of Electrode-B is 5mm). The imaginary part ϵ''_r is given by

$$\epsilon''_r = D \epsilon'_r \quad (5.38)$$

where D is the dissipation factor

$$D = \tan \delta = \frac{\epsilon''_r}{\epsilon'_r} = \frac{1}{\omega C_p R_p} = \frac{1}{\omega \frac{\epsilon'_r A}{t_a} \frac{t_a}{\sigma A}} = \frac{\sigma}{\omega \epsilon'} \quad (5.39)$$

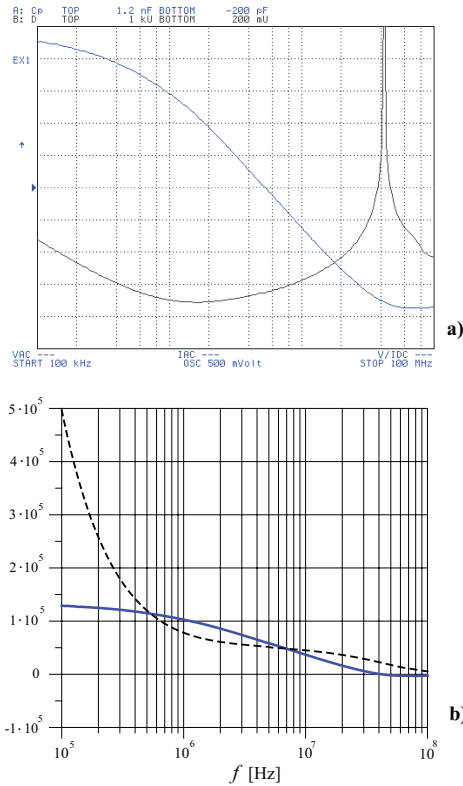


Figure 5.26: a) Measured equivalent parallel capacitance and dissipation factor for N30 test material. b) Computed complex permittivity. Solid line: real part; dashed line: imaginary part.

The experimental results of the parallel capacitance, dissipation factor and the computed complex permittivity for samples of ferrite material of grade N30 and N87 respectively are represented in Figs. 5.26 and 5.27.

5.5.2 Magnetic Skin Depth and Dimensional Resonance

The simplest type of wave propagation is the uniform plane wave. The term *plane* means that at any point in space the electric and magnetic field intensity

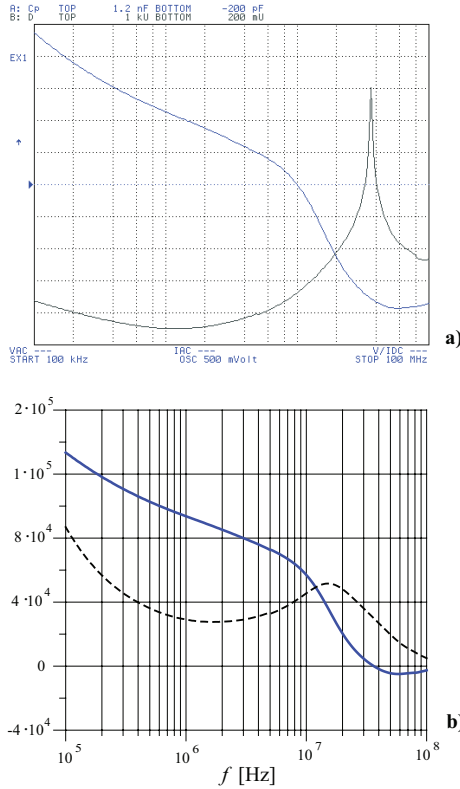


Figure 5.27: a) Measured equivalent parallel capacitance and dissipation factor for N87 test material. b) Computed complex permittivity. Solid line: real part; dashed line: imaginary part.

vectors lie in a plane and the planes at any two different points are parallel. The term *uniform* means that \mathbf{E} and \mathbf{H} are independent from the position in each plane. Lets assume that the electric and magnetic field intensity vectors lie in the xy plane and in particular the electric field intensity vector is directed in the x direction.

$$\mathbf{E} = E_x(z, t)\mathbf{e}_x \quad (5.40)$$

The condition that the field vector is uniform yields that it must be independent from x and y (or constant along x and y):

$$\frac{\partial E_x}{\partial x} = \frac{\partial E_x}{\partial y} = 0 \quad (5.41)$$

the vector can be a function of only z and, of course of the time t . Similarly for \mathbf{H} :

$$\mathbf{H} = H_y(z, t)\mathbf{e}_y \quad (5.42)$$

$$\frac{\partial H_y}{\partial x} = \frac{\partial H_y}{\partial y} = 0 \quad (5.43)$$

Substituting these results (5.41) and (5.43) into Faraday's and Ampère's laws

$$\begin{aligned} \text{rot}\mathbf{E} &= -\frac{\partial \mathbf{B}}{\partial t} = -\mu \frac{\partial \mathbf{H}}{\partial t} \\ \text{rot}\mathbf{H} &= \mathbf{J} + \frac{\partial \mathbf{D}}{\partial t} \end{aligned} \quad (5.44)$$

we obtain two differential equations

$$\frac{\partial E_x(z, t)}{\partial z} = -\mu \frac{\partial H_y(z, t)}{\partial t} \quad (5.45)$$

$$-\frac{\partial H_y(z, t)}{\partial z} = \sigma E_x(z, t) + \varepsilon \frac{\partial E_x(z, t)}{\partial t}. \quad (5.46)$$

For sinusoidal, steady-state variation:

$$\frac{d\hat{E}_x(z)}{dz} = -j\omega\mu\hat{H}_y(z) \quad (5.47)$$

$$\frac{d\hat{H}_y(z)}{dz} = -(\sigma + j\omega\varepsilon)\hat{E}_x(z) \quad (5.48)$$

These two differential equations are coupled and, differentiating with respect to z and subtracting the other and vice versa, one can obtain the well known Helmholtz's Equations, where the only dependence on the z direction is considered:

$$\begin{aligned} \frac{d^2\hat{E}_x(z)}{dz^2} - \hat{k}^2\hat{E}_x(z) &= 0 \\ \frac{d^2\hat{H}_y(z)}{dz^2} - \hat{k}^2\hat{H}_y(z) &= 0. \end{aligned} \quad (5.49)$$

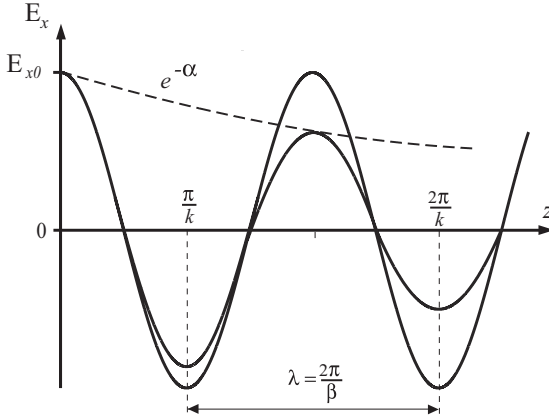


Figure 5.28: Representation of the propagation of the electric field wave in a lossy medium, characterized by the attenuation constant α and the constant of phase β .

The solutions of these equation are respectively

$$\begin{aligned}\hat{E}_x &= \hat{E}_m^+ e^{-j\hat{k}z} + \hat{E}_m^- e^{+j\hat{k}z} \\ \hat{H}_y &= \frac{\hat{E}_m^+}{\hat{\eta}} e^{-j\hat{k}z} + \frac{\hat{E}_m^-}{\hat{\eta}} e^{+j\hat{k}z}\end{aligned}\quad (5.50)$$

where \hat{k} is the complex propagation constant defined as

$$\begin{aligned}\hat{k} &= \sqrt{j\omega\mu(\sigma + j\omega\varepsilon)} \\ &= \alpha + j\beta\end{aligned}\quad (5.51)$$

α is also called attenuation coefficient and β is the phase constant. The intrinsic wave impedance in the medium having properties $(\sigma, \varepsilon, \mu)$ is accordingly given by

$$\hat{\eta} = \sqrt{\frac{j\omega\mu}{\sigma + j\omega\varepsilon}}\quad (5.52)$$

measured in Ω . Equations (5.51) and (5.52) can be rewritten as

Table 5.4: Skin depth for Copper

frequency	δ
60 Hz	8.53 mm
1 MHz	66.1 μm
10 MHz	20.9 μm
100 MHz	6.6 μm
1 GHz	2.09 μm

$$\hat{k} = j\omega \sqrt{\mu\varepsilon \left(1 + \frac{\sigma}{j\omega\varepsilon}\right)} \quad (5.53)$$

$$\hat{\eta} = \sqrt{\frac{\mu}{\varepsilon \left(1 + \frac{\sigma}{j\omega\varepsilon}\right)}}. \quad (5.54)$$

One can distinguish between a good conductor and a dielectric if

$$\begin{cases} \frac{\sigma}{\omega\varepsilon} \gg 1 & \text{good conductor} \\ \frac{\sigma}{\omega\varepsilon} \ll 1 & \text{good dielectric} \\ \sigma = 0 & \text{lossless} \end{cases} \quad (5.55)$$

In particular, for a good conductor

$$\begin{aligned} \hat{k} &= \sqrt{(j\omega)^2 \mu\varepsilon \left(1 + \frac{\sigma}{j\omega\varepsilon}\right)} \\ &\approx \sqrt{j\omega\mu\sigma} \\ &= \sqrt{j} \sqrt{\omega\mu\sigma} \\ &= \left(\frac{1}{\sqrt{2}} + j\frac{1}{\sqrt{2}}\right) \sqrt{\omega\mu\sigma}. \end{aligned} \quad (5.56)$$

Therefore the wave number can be written as

$$\begin{aligned} \hat{k} &= \alpha + j\beta \\ &= \sqrt{\frac{\omega\mu\sigma}{2}} + j\sqrt{\frac{\omega\mu\sigma}{2}} \end{aligned} \quad (5.57)$$

where the skin depth is defined as

$$\delta = \frac{1}{\alpha} = \frac{1}{\sqrt{\pi f \mu \sigma}}. \quad (5.58)$$

If the proprieties of the material (μ , ε) are complex, as is for the ferrite, see

equations (5.35) and (5.36), the constant of propagation assumes the form

$$\hat{k} = \sqrt{j\omega\dot{\mu}(\sigma + j\omega\dot{\epsilon})} \quad (5.59)$$

$$\begin{aligned} &= \sqrt{j\omega(\mu' - j\mu'')(\sigma + j\omega(\epsilon' - j\epsilon''))} \\ &= \sqrt{j\omega(\mu' - j\mu'')(j\omega(\epsilon' - j\epsilon'' + \frac{\sigma}{j\omega}))} \\ &= \sqrt{j\omega(\mu' - j\mu'')(j\omega(\epsilon' - j(\epsilon'' + \frac{\sigma}{\omega})))} \\ &= \sqrt{j\omega(\mu' - j\mu'')(j\omega(\epsilon' - j(\tilde{\epsilon}''))) } \end{aligned} \quad (5.60)$$

and it can also be written as

$$\hat{k} = j\omega\sqrt{\dot{\mu}\dot{\epsilon}} \quad (5.61)$$

$$= j\omega\sqrt{(\mu'\epsilon' - \mu''\tilde{\epsilon}'') - j(\mu''\epsilon' + \mu'\tilde{\epsilon}'')} \quad (5.62)$$

whose real and imaginary part are

$$\Im(\hat{k}) = \frac{\omega}{\sqrt{2}} \left(\sqrt{|\dot{\mu}||\dot{\epsilon}|} + (\mu'\epsilon' - \mu''\tilde{\epsilon}'') \right) \quad (5.63)$$

$$\Re(\hat{k}) = \frac{\omega}{\sqrt{2}} \left(\sqrt{|\dot{\mu}||\dot{\epsilon}|} - (\mu'\epsilon' - \mu''\tilde{\epsilon}'') \right) \quad (5.64)$$

The phase speed is given from

$$v = \frac{dz}{dt} = \frac{\omega}{\beta} = \frac{1}{\sqrt{\mu\epsilon}} \quad (5.65)$$

In air, $\mu_0 = 4\pi \times 10^{-7}$ H/m and $\epsilon_0 = 1/36\pi \times 10^{-9}$ F/m. It results that the light speed in the vacuum is $v_0 = 3 \times 10^8$ m/s.

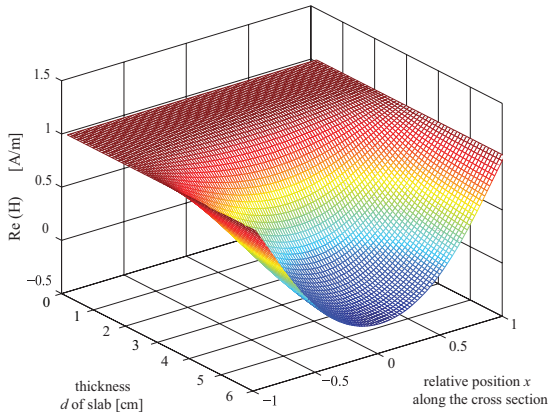
The unit of measure of β is rad/m, β is a change in phase of the wave with respect to the distance of propagation. The distance between two correspondent points of a wave is the *wavelength* defined as

$$\lambda = \frac{2\pi}{\beta} = \frac{v}{f} \quad (5.66)$$

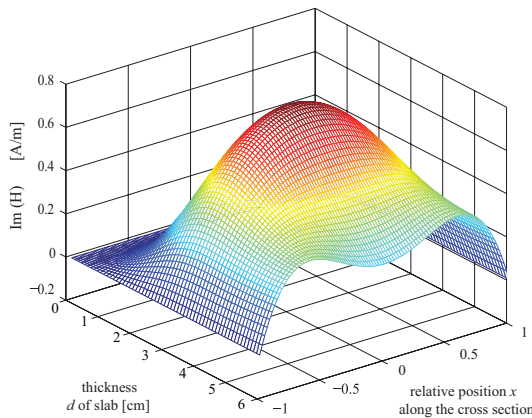
The general expression of the wavelength λ within a ferrite material is

$$\lambda = \frac{2\pi}{\beta} = \frac{2\pi}{\Im(\hat{k})} = \frac{\sqrt{2}c_0}{f\sqrt{|\dot{\mu}||\dot{\epsilon}| + (\mu'\epsilon' - \mu''\tilde{\epsilon}'')}} \quad (5.67)$$

$\dot{\mu}$ and $\dot{\epsilon}$ are the complex relative permeability and permittivity of the material



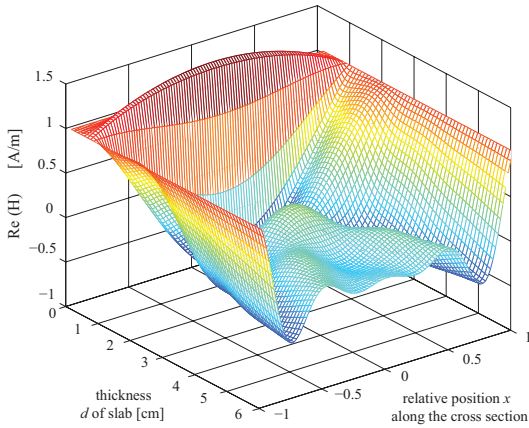
(a)



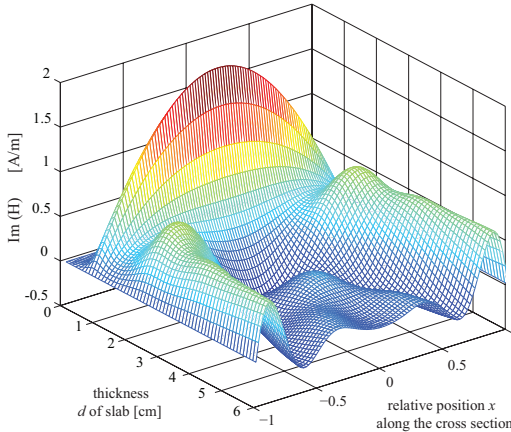
(b)

Figure 5.29: Simulation of the distribution of the magnetic field H along the cross-section d of a slab for an excitation frequency of 100 kHz and ferrite grade N30. The real part (a) and the imaginary part (b) of the field are plotted as a function of the size of the slab and of the relative position $\frac{2x}{d}$.

respectively; these quantities are all frequency dependent. Since the permeability μ and the permittivity ϵ depend on the frequency, then the wavelength λ generally decreases for increasing frequency values. In addition, at high fre-



(a)



(b)

Figure 5.30: Simulation of the distribution of the magnetic field H along the cross-section d of a slab for an excitation frequency of 1 MHz and ferrite grade N30. The real part (a) and the imaginary part (b) of the field are plotted as a function of the size of the slab and of the relative position $\frac{2x}{d}$.

quency the distribution of the flux density \mathbf{B} is not anymore uniform across the

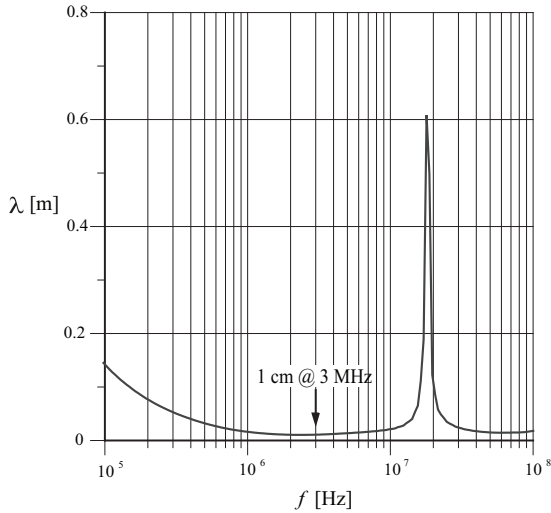


Figure 5.31: Wavelength λ of Ferrite N87 material

section of the core, because of the high values of μ and ϵ give rise to standing electromagnetic waves within the ferrite. This is called dimensional resonance. This latter is characterized by the observed permeability dropping to zero if the smallest cross-sectional dimension of the core is $\lambda/2$ and since there is a corresponding standing wave in the electric flux density \mathbf{D} , the permittivity is also affected by a similar dispersion. In addition, a peak in the magnetic loss curve μ'' and in the dielectric loss curve ϵ'' occur about the resonance.

The solution for the magnetic field in the slab is given by

$$H(x) = H_0 \frac{\cos(j\hat{k}x)}{\cos(j\hat{k}\frac{d}{2})} \quad (5.68)$$

where \hat{k} is the propagation constant (5.61). According to (5.68) the field in the slab for N30 ferrite grade and for 100 kHz and 1 MHz are shown in Fig.5.29 and Fig.5.30, respectively.

From the data of the measurements of the Ferrite N87 we computed the value of the wavelength in function of the frequency, the result is represented in Fig. 5.31.

Let us define now the loss tangents that relate the real and complex parts of the complex permittivity and permeability respectively:

$$\tan \delta_m = \frac{\mu''}{\mu'} \quad (5.69)$$

$$\tan \delta_e = \frac{\varepsilon''}{\varepsilon'} \quad (5.70)$$

In [?], Snelling states that if $\tan \delta_m \tan \delta_e \ll 1$ then dimensional resonance will be observed. If $\tan \delta_m \tan \delta_e \gg 1$ the material will not support standing waves and there is no dimensional resonance. Instead the flux will be attenuated as it is propagated through the cross-section and there will be a penetration depth δ defined as:

$$\delta = \frac{1}{\alpha} = \frac{1}{\Re(\hat{k})} = \frac{\sqrt{2}c_0}{2\pi f \sqrt{|\hat{\mu}| |\hat{\varepsilon}| - (\mu' \varepsilon' - \mu'' \varepsilon'')}} \quad (5.71)$$

A description of such effects where λ and δ are a function of the complex wave number \hat{k} is presented in [130].

From the data of the measurements of the Ferrite N87 we computed the value of δ in function of the frequency, the result is represented in Fig. 5.32.

5.5.3 High Frequency Winding Resistance

The winding loss and hence the winding resistance increases at high frequency because the current density \mathbf{J} is not uniform in the cross-section of the conductor, but the current lines are gathered only in part of it, and this is caused by eddy-current effects. There are two kinds of eddy current effects: *skin effect* and *proximity effect* (see Figs. 2-3 in [145]). When an AC current flows in a conductor, the current density decreases from the surface to the center of the conductor and thus the power loss increases for higher frequency. This is called skin effect. The proximity effect is similar but it is caused by a nearby conductor. The current in the nearby conductor causes a time-varying field and induces circulating currents inside the conductor [146]. Therefore the knowledge of the *spatial* distribution of the extern magnetic field \mathbf{H}_{ext} caused by the current flowing in the winding and the value of the magnetic field \mathbf{H}_{int} internal at the conductor are essential to quantify and determine the eddy currents-effects hence the value of the resistance.

The value of the stray inductance L_σ is dependent on the energy stored in the magnetic field \mathbf{H} within the conductor and in the space between the conductors (the presence of a magnetic material is not considered in this case). The stray

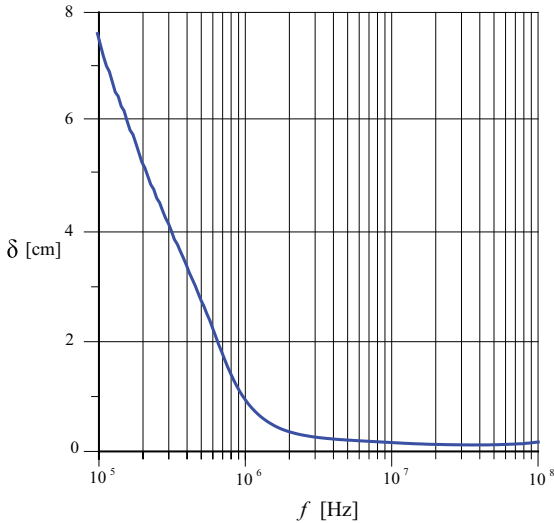


Figure 5.32: Skin effect depth δ of Ferrite N87 material.

inductance and the AC resistance represent respectively the contributes conservative (L_σ) and dissipative (high-frequency resistance $R_{h,f}$) and of the same phenomenon and therefore they are usually calculated at the same time.

The magnetic field \mathbf{H} has a strong influence on the current density distribution \mathbf{J} . Hence the accurate determination of \mathbf{H} is the first step for the calculation of the high frequency winding resistance expression.

The determination of \mathbf{H} is not an easy problem, especially in case of complex core geometries.

At high frequency, the values of the winding resistance and of the leakage inductance are strongly dependent on the magnetic component's geometry and operating frequency.

In particular, the dependency on the geometry can be better expressed in terms of dependence on the *shape* and on the *dimensions* of the transformer or inductor. In fact, according with the device's shape, the field's distribution can be assumed one- dimensional (1-D), two-dimensional (2-D) or, for complex geometries, three-dimensional (3-D). On the other side, the variation of the component's dimensions may generate a new problem even if the shape of the device is not changed (re-scaling of the problem). Let us consider, for instance the case of a toroidal shape, which can be solved with a 1-D approach [147] if the diameter is large. However, for very small toroids such an approach is no more valid,

and one should solve a 3-D problem [148]. The integration of the Maxwell's equations in order to derive the field for the particular geometry is therefore in general not an easy task.

One of the earliest analytical derivation of the high frequency resistance, is the well-know 1-D study case presented by Dowell in 1966 [149] who employed the same approach of used in [150] by Bennett and Larson (1940) and in [151] by Long (1945). Dowell studied in his paper the case of a pot transformer. Under the assumptions of sinusoidal excitation and magnetic field parallel to the windings, he derived a binomial expression of the AC resistance, where the terms account for the skin and proximity effect, respectively. Further assumptions in Dowell's paper: the transformation of the layer of conductors having circular cross-section into an equivalent foil by introducing a porosity factor that has been object of many argumentations [152, 153].

Moreover the edge effects are neglected by stretching the equivalent layer and assigning it the same length of the window. In addition an extended experimental verification is presented [145].

Dowell's formula is able to reliably predict the increased resistance in cylindrical windings where the foil or layer thickness is less than 10% of the radius of curvature. As mentioned by Hurley in [154], the formula has been utilized in many application such as *planar magnetics* by Kassakian and Sullivan, *matrix transformer* by Williams, *toroidal inductors* by Cheng, *distributed air-gaps* by Evans and *slot bound conductors* by Hanselmann.

After Dowell's work several articles have been published on the subject. Although these papers cover a wide range of topics, they have as common aspect the study of skin and proximity effects.

Jongsma (1978, 1986), develops an extensive algorithm for design of transformers using an approximation based on Dowell's result.

Perry (1979), analyzes a general N-layer solenoid and derives power-loss expressions for each layer.

Ventrakaman (1984), applies Dowell results to non sinusoidal excitation using Fourier analysis.

Coonrod (1984), concentrates on the thermal effects of eddy-current losses in transformers.

Carsten (1986), [155], normalizes Ventrakaman's results using resistance of a conductor one skin depth height.

Rosa (1986), presents an equivalent circuit model of a multiwinding transformer for low-frequency sinusoidal currents.

Vandelac and Ziogas (1987), [156], incorporate aspects of Dowell, Jongsma, Carsten, and Ventrakaman to extend Perry's analysis.

Sayani et al. (1991), [157] extend the Dowell's approach to planar structures.

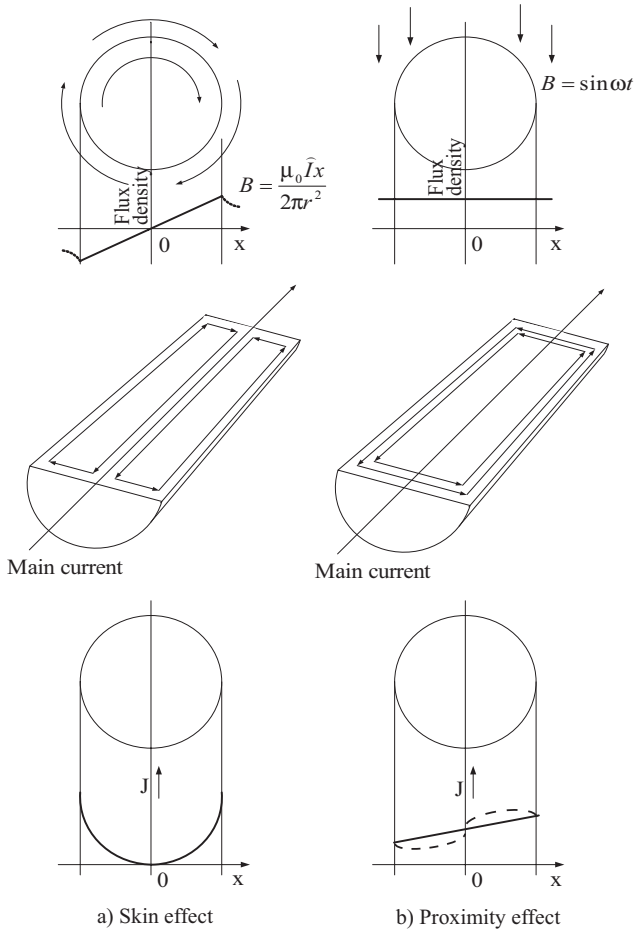


Figure 5.33: Skin effect and proximity effect in round conductors.

Keradec et al. (1991), [158], consider the modification of the field in a conductor due to eddy current in adjacent conductors along the direction of the field. The approximation does not account for the effect of the distance to conductors in the other direction.

Ferreira (1994), [152], applies the well known Bessel function solution for the field in a single isolated cylindrical conductor to get an expression for the ac resistance of the m-layer by assuming a 1-D field inside the winding. Moreover states that skin effect and proximity effect can be calculated separately due to the orthogonality between them.

Odendaal (1997), [159] shows that the various 1-D solutions for the eddy current distributions in a current carrying strip conductor with arbitrary field on its surfaces are all equivalent and skin and proximity current distributions can be decoupled as well. Furthermore, the structure can be analyzed by considering the penetration of two electromagnetic wave sources.

Hurley et al. (2000), [154], presents a new formula for the optimum - respect to ac losses due to nonsinusoidal excitation - foil or layer thickness, without the need of Fourier coefficients and calculation at harmonic frequencies.

Wallmeier (2001), [160], faces the 1-D case of a gapped inductor by using in the calculations the vector potential.

Robert et al. (2001), [161], propose a modified Dowell function based on FEM results to extend the formula validity to the 2-D case.

Nan and Sullivan (2003), [146], follow Robert's idea but propose a more general formula valid for the 2-D case and achieve higher accuracy. The formula is function of tabled coefficients.

To obtain the analytical expression of the winding resistance, one should derive the AC current density J distribution in coil winding. This can be done in two ways [162, 163].

A first method is to start from the Maxwell's equation and derive the differential equation for determining the current density J in the coil conductor is given by

$$\frac{\partial^2 J}{\partial r^2} + \frac{1}{r} \frac{\partial J}{\partial r} - (jk^2 + \frac{1}{r^2})J = -\frac{\partial^2 J}{\partial z^2} \quad (5.72)$$

where r and z are the radial and axial components respectively, and $k^2 = j\omega\sigma\mu$. As mentioned, the result of this problem is a complex quantity, whose reactive part is proportional to the stray inductance. Since only the current distribution in the winding is considered, the resulting value of the leakage inductance will be as much accurate, the larger the space filling factor of the inductor. The AC resistance R_{hf} and the leakage inductance L_σ are therefore calculated together. The AC resistance may be also derived by integrating the ordinal differential

equation in the magnetic field H

$$\frac{\partial^2 H}{\partial r^2} + \frac{1}{r} \frac{\partial H}{\partial r} - j\omega\mu_0\sigma H = 0. \quad (5.73)$$

The high frequency impedance of the winding of the current transformer shown in Fig. 5.1 has been calculated and verified by FEM. The *Dowell's Formula* [149] has been used, where the coefficients are calculated for a round wire. The impedance of one layer winding is provided by

$$\hat{Z}_w = R_{wdc}A(1+j) \coth A(1+j) \quad (5.74)$$

where

$$R_{wdc} = \frac{N_t \ell_t}{\sigma_c S_t} \quad (5.75)$$

is the winding DC-resistance, N_t is the number of turns, S_t the section of the round wire, ℓ_t the turn length. The parameter A is provided by

$$A = \left(\frac{\pi}{4}\right)^{\frac{3}{4}} \frac{\sqrt{d^3}}{\delta\sqrt{t}} \quad (5.76)$$

where d is the conductor diameter, t is the distance between the centers of two adjacent conductors and

$$\delta = \sqrt{\frac{1}{\pi\mu_0\sigma_c f}} \quad (5.77)$$

is the skin depth of the wire. The effective winding resistance and leakage inductance are therefore derived from the real and the imaginary part of the complex function \hat{Z}_w :

$$R_w = \Re(\hat{Z}_w) = R_{wdc}A \left(\frac{\sinh 2A + \sin 2A}{\cosh 2A - \cos 2A} \right) \quad (5.78)$$

$$L_\sigma = \Im(\hat{Z}_w) = R_{wdc} \frac{A}{2\pi f} \left(\frac{\sinh 2A - \sin 2A}{\cosh 2A - \cos 2A} \right) \quad (5.79)$$

This formula is dependent on the frequency, and on the geometry of the device. The capacitive parasitic effects between turns and turns against the core are neglected and hence the re-distribution of the current in the winding due to the displacement current. These formulae are derived for a 1-D problem. The Finite Element Analysis represents the only powerful method to solve in a quite straightforward way complex 3-D problems. The influence of an air gap on the AC resistance has been rarely faced in literature and could be studied methodically by FEM.

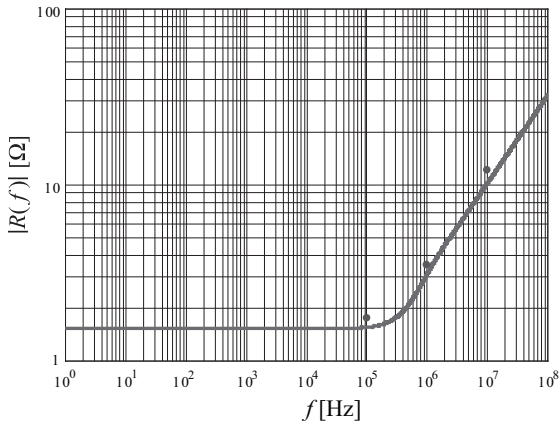


Figure 5.34: AC Winding Resistance: computed (line), simulated with FEM (dots). The simulation parameters correspond to the gapped prototype shown in Fig. 5.10.

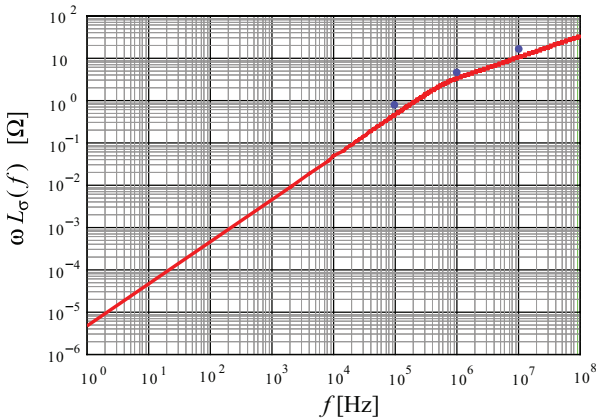


Figure 5.35: AC Winding Reactance: computed (line), simulated with FEM (dots). The simulation parameters correspond to the gapped prototype shown in Fig. 5.10.

5.5.4 Winding Losses

If a conductor is immersed in an alternating magnetic field, an electro motive force (e.m.f.) will be induced in it and these will give rise to eddy currents and

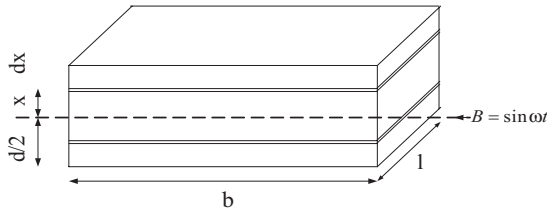


Figure 5.36: Calculation of Eddy currents in a thin tape

associated power losses. The magnetic fields may be due to currents flowing in other conductor or due to current flowing in the conductor in question. The losses may be represented as an increase in resistance of the current-carrying conductors above the value measured with direct current; this increase of resistance becomes larger as the frequency increases.

A conductor which is part of a current-carrying winding will in general experience the magnetic field due to its own alternating current (skin effect Fig. 5.33a) and also the field due to all the other current-carrying conductors in the vicinity (proximity effect Fig. 5.33b). These two contributions are added together.

Skin effect may be virtually eliminated by using conductors consisting of thin insulated strands composed so that individual strands wave cyclically from the center of the conductor to the outside and back as they run along the length of the conductor. Such a conductor is referred to as *Litz wire*; the stranding and transposition makes the current density uniform. But skin effect is not usually the most important form of eddy current loss in winding conductors. More important is the second effect, called *proximity effect*, that is the eddy current effect in a conductor due to the alternating field of other conductors in the vicinity.

To calculate the power loss due to proximity effect we consider a thin tape having width b and thickness d (cf. Fig. 5.36). An alternating magnetic flux density $B \sin \omega t$ is everywhere parallel to the plane of the tape. The e.m.f. induced in a loop consisting of the two elementary laminate is given by

$$E = \frac{2\omega Bxl}{\sqrt{2}} \quad (5.80)$$

The resistance of the elementary Eddy current circuit is given by

$$R = \frac{2\rho cl}{bdx} \quad (5.81)$$

Therefore the power loss due to proximity effect is

$$dP_{pe} = \frac{E^2}{R} = \frac{\omega^2 B^2 x^2 l b dx}{\rho_c} \quad (5.82)$$

$$P_{pe} = \frac{\omega^2 B^2 l b}{\rho_c} \int_0^{d/2} x^2 dx = \frac{\omega^2 B^2 l b d^3}{24 \rho_c} \quad (5.83)$$

For a round conductor of diameter d :

$$P_{pe} = \frac{\pi \omega^2 B^2 l d^4}{128 \rho_c} \quad (5.84)$$

If the transverse magnetic field is associated with a main current in the conductor, the Eddy currents cause a distortion of the current density, enhancing it on one side of the axis and diminishing it on the other (cf. Fig. 5.33b solid line). At higher frequencies the associated current distribution becomes non-linear as shown by the dotted line in Fig. 5.33b.

A reduction of the conductor diameter d will be very effective in reducing proximity effect but, by itself, this reduction will rapidly increase the value of R_{dc} and may result in a greater overall loss. The usual method of resolving proximity effect is to use bunched conductors consisting of n insulated strands of diameter d . At each end of winding the strands are soldered together; at low frequency the conductor has an effective area of $\frac{n\pi d^2}{4}$. The conductor is twisted so that, in its simplest form, each strand follows a helical path.

The total proximity effect loss in a winding consisting of a number of layers of closely-wound round conductors (of total length $l = Nl_w$) will be given by:

$$P_{pe} = \frac{\pi \omega^2 2 \bar{B}^2 l d^4}{128 \rho_c} = \frac{2\pi(\omega \mu_0 N I)^2 N l_w d^4 k}{3 \cdot 128 \rho_c b_w^2} \quad (5.85)$$

where \bar{B}^2 is the average value of B^2 and is $\bar{B}^2 = \frac{1}{3}(\frac{\mu_0 N I}{b_w})^2 k$ and k is a constant. The DC resistance of the same winding is:

$$R_{dc} = \frac{4 N l_w \rho_c}{\pi d^2} \quad (5.86)$$

and the power loss due to the DC resistance is

$$P_{dc} = I^2 R_{dc} = \frac{4 I^2 N l_w \rho_c}{\pi d^2} \quad (5.87)$$

The total winding loss is

$$P_{tot} = P_{pe} + P_{dc} = \frac{2\pi(\omega\mu_0NI)^2Nl_wd^4k}{3 \cdot 128\rho_cb_w^2} + \frac{4I^2Nl_w\rho_c}{\pi d^2}. \quad (5.88)$$

5.5.5 Losses in Magnetic Components

If an alternating magnetic field \mathbf{H} is applied to a ferrite material the resulting induction \mathbf{B} is periodic. As the ferromagnetic domains show a certain inertia to orient themselves along \mathbf{H} , then \mathbf{B} shows a delay with respect to \mathbf{H} . The relationship between the induction field and the magnetic field is defined by

$$\mathbf{B} = \hat{\mu}\mathbf{H} \quad (5.89)$$

where the permeability $\hat{\mu}$ is a complex quantity. In addition $\hat{\mu}$, which is a function of the frequency, is generally a tensor since \mathbf{B} and \mathbf{H} are not necessarily parallel and the negative imaginary part accounts for phase delay between \mathbf{B} and \mathbf{H} :

$$\hat{\mu} = \mu_0\mu_r = \mu_0(\mu'_r(f) - j\mu''_r(f)) = \mu' - j\mu'' \quad (5.90)$$

These considerations may be extended also to the relationship between the complex electric displacement vector \mathbf{D} and the complex electric field vector \mathbf{E} ,

$$\mathbf{D} = \hat{\epsilon}\mathbf{E} \quad (5.91)$$

where a frequency dependent complex permittivity is introduced

$$\hat{\epsilon} = \epsilon_0\epsilon_r = \epsilon_0(\epsilon'_r(f) - j\epsilon''_r(f)) = \epsilon' - j\epsilon'' \quad (5.92)$$

The formulas of the losses affecting a ferrite core inductor or transformer may be derived starting from the Maxwell's equations where the magnetic permeability and the dielectric permittivity are accounted as frequency-dependent complex quantities. In addition, if the amplitude of the magnetic flux density in the core is below its saturation limit and the exciting current waveform is sinusoidal, then \mathbf{B} , \mathbf{H} , \mathbf{E} and \mathbf{D} can be treated as phasors having effective values. The Maxwell's equations in terms of phasors can be expressed as

$$\text{rot}\mathbf{H} = \mathbf{J} + j\omega\mathbf{D} \quad (5.93)$$

$$\begin{aligned} &= \sigma\mathbf{E} + j\omega\hat{\epsilon}\mathbf{E} \\ &= (\sigma + j\omega\hat{\epsilon})\mathbf{E} \\ &= \dot{\sigma}\mathbf{E} \end{aligned} \quad (5.94)$$

$$\operatorname{rot}\mathbf{E} = -j\omega\mathbf{B} = -j\omega\dot{\mu}\mathbf{H} \quad (5.95)$$

where \mathbf{J} is the conduction current density, σ the conductivity of the core and $\dot{\sigma} = \sigma + j\omega\dot{\epsilon}$ its complex conductivity. The volume density of power loss due to the electric field may be calculated as the real part of the complex power $\mathbf{E} \cdot (\mathbf{J} + j\omega\mathbf{D})^*$:

$$\begin{aligned} \Re\{\mathbf{E} \cdot (\mathbf{J} + j\omega\mathbf{D})^*\} &= \Re\{\mathbf{E} \cdot (\sigma + j\omega\dot{\epsilon})^*\mathbf{E}^*\} \\ &= \Re\{\mathbf{E} \cdot (\sigma + \omega\varepsilon'' - j\omega\varepsilon')\mathbf{E}^*\} \\ &= \Re\{(\sigma + \omega\varepsilon'' - j\omega\varepsilon')\mathbf{E} \cdot \mathbf{E}^*\} \\ &= (\sigma + \omega\varepsilon'')E^2 \end{aligned} \quad (5.96)$$

The quantities σE^2 and $\omega\varepsilon'' E^2$ represent, respectively, the eddy current loss and the dielectric loss per unit of volume. In a similar way we can calculate the loss due to the magnetic field: this quantity with opposite sign is the external power *done on the field* [164] by the external e.m.f. which maintains the currents and is provided by

$$\Re\{-(-j\omega\dot{\mu}\mathbf{H}) \cdot \mathbf{H}^*\} = \Re\{(j\omega\mu' + \omega\mu'')\mathbf{H} \cdot \mathbf{H}^*\} = \omega\mu''H^2 \quad (5.97)$$

This latter is the magnetic hysteresis loss density. All the frequency-dependent contributions to iron loss are therefore:

$$P_h = 2\pi f\mu_0\mu_r''(f)H^2 \quad (5.98)$$

$$P_c = \sigma(f)E^2 \quad (5.99)$$

$$P_d = 2\pi f\varepsilon_0\varepsilon_r''(f)E^2 \quad (5.100)$$

respectively due to the magnetic hysteresis, eddy currents and dielectric loss. For the high frequency modelling of a ferrite core inductor or transformer one can not neglect the effect of the losses, the knowledge of which becomes crucial to predict with accuracy the frequency behavior of the components. The total core loss can be written as the sum of these three losses: static hysteresis loss P_h , classical eddy current loss P_c and the dielectric loss P_d .

$$P_v = P_h + P_c + P_d \quad (5.101)$$

This expression can be written in another manner considering static losses and dynamic losses

$$P_v = C_1 B_m^{\gamma_1} + C_2 f^{\gamma_2} \quad (5.102)$$

where B_m is the peak magnetic flux density, C_1 and C_2 are respectively coefficients of the static and dynamic losses.

It is known, according to Snelling [?], that for $B \rightarrow 0$ and $f \rightarrow 0$ the total core loss P_v is different from zero. This is due to the fact that exist some residual losses and they have to be insert in the incomplete equation (5.102), obtaining

$$P_v = C_1 B_m^{\gamma_1} + C_2 f^{\gamma_2} + C_3. \quad (5.103)$$

Simplifying this equation Steinmetz proposed a century ago a today well-known and normally used empirical approach to calculate the power loss of ferrite materials

$$P_v = C_m f^\alpha B_m^\beta \quad (5.104)$$

where C_m , α and β are empirical parameters obtained from experimental measurement under sinusoidal excitation. To estimate the power loss with nonsinusoidal excitation, a modified Steinmetz equation (MSE) was introduced

$$P_v = (C_m f_{eq}^{\alpha-1} B_m^\beta) f_r \quad (5.105)$$

where f_{eq} is the equivalent frequency of the nonsinusoidal induction waveform and f_r is the repeated frequency. Introducing the equivalent frequency, the MSE provides a good approximation of experimental measurements under triangular magnetization.

5.6 Conclusion

This chapter has presented a comprehensive high-frequency characterization of a magnetic device. Having as the basis of the analysis the particular case-study of a toroidal current sensor, the following characteristics have been studied in detail over a wide frequency band:

1. winding impedance
2. core impedance
3. non linear flux distribution
4. transfer function of two port device
5. eddy currents effects.

This investigation of a gapped toroidal magnetic structure for a current sensor dealt with its design, empirical characterization, parameter extraction and modeling over a wide frequency bandwidth up to 30 MHz. In the current sensing application, the Hall-effect sensor provides the low-frequency signal, whereas current transformer action is utilized for the high frequencies. A winding arrangement was presented which desensitizes the probe to the effects of external magnetic fields. The complex permeability of the magnetic core material was

measured and the non-linear behavior of the magnetic core was then modeled using a permeance model, which also accounts for the core losses. The output impedance was measured and all of the parameters associated with winding stray capacitances, leakage impedance and high frequency winding resistance were extracted for a lumped linear element equivalent circuit that could be linked to the magnetic permeances model via two Tellegen gyrators. The results from these open circuit measurements were compared to simulated results and good agreement was shown. A good agreement was also obtained between the measured transimpedance gain of the current transformer and simulated results. The influence of the load resistance in the secondary circuit on the transimpedance gain was also investigated empirically and numerically.

The permeance model allows access to the flux rate and the MMF in parts of the toroidal core, which provided further valuable information about the magnetic behavior of the magnetic structure. Since a resistance element in the permeance model represents magnetic losses (unlike the conventional magnetic reluctance model where resistance represents energy storage), core losses could also be extracted using this method.

The modeling procedure for a gapped toroidal current sensor that is presented herein demonstrates high accuracy for both the winding impedance and the transimpedance gain. From a practical standpoint, accurate measurement of the transfer function of a current transformer requires much more effort than measuring only its winding impedance, and the characterization of a two port device is generally more complicated than for a one port device. Since the winding impedance measurement and the characterization of the ferrite material allows extraction of all the parameters of the equivalent circuit of the current sensor electrically and magnetically, information about the transfer function of the component can be derived without having to perform any further two port measurements.

The upper bandwidth limit of the probe is mostly dependent on the winding impedances, in particular the stray winding capacitances [165], and this was also verified in simulations. The capacitive effects affect crucially the frequency behavior of magnetic components and they cause frequency resonances. Since there are different kinds of contributions to the self-capacitance and since there is a broad literature on the electrostatic analysis of wound components, this will be considered as an independent chapter in this Dissertation.

Chapter 6

Electrostatic Analysis of Wound Ferrite Components

6.1 Introduction

The electrostatic analysis of wound components has been a fascinating research field since the beginning of last century when the study of the surge performance of transformers became an increasingly crucial issue for predicting the devices' frequency behavior [166, 126]. As soon as wideband transformers began to appear in telecommunication systems in the 1940's [167, 168], so followed papers devoted to the frequency characterization of these magnetic components [169] and, in particular, to the calculation of their self-capacitance [170, 142, 171, 172, 173, 174]. The definition of a self-capacitance as a shunt lumped-element in the equivalent circuit of the wire-wound component is a very useful tool to justify and reproduce the first resonant frequency. However, the concept of *self capacitance* is well beyond any lumped-element circuit theory since it is an attempt to circumvent transmission line effects on wound-components when the current distribution begins to depart from its DC behavior [175, 176]. Recently, procedures for calculating the capacitance have been proposed for inductors [177], planar transformers [178, 179], magnetic components within SMPS [180], high-frequency transformers [181, 182] and power transformers [170, 142].

In this chapter, a comprehensive procedure for calculating the self-capacitance of high-voltage transformers is presented and all the factors that dictate the electrostatic behavior of these components are identified.

The high-voltage transformer has been selected as case-study, because its rel-

atively complex architecture gives the possibility to analyze several possible electric field configurations and to enrich the analysis of the stray capacitance of wound components.

The typical application of high-voltage transformers is within isolated DC/DC converters, where they step up the primary voltage and provide isolation [183]. For the high voltage transformer within a resonant DC/DC converter, where the switching frequency can rise up to 500 kHz [184], the parasitic parameters, in particular the self-capacitance, can heavily affect the performance of the converter. This capacitance is responsible for unwanted resonances and oscillations of the primary and secondary side currents, hence reducing the system's efficiency and reliability [185]. Thus the parasitics of the transformer, the leakage inductance and the parallel stray capacitance, have to be determined. These elements are usually used to form the resonant tank [186]. In order to predict the performance of the resonant converter and to be able to use the parasitics of the transformer as constitutive elements of the resonant circuit, the calculation of the stray capacitance is a fundamental issue [187].

6.1.1 Calculation Approaches

The analytical approach was used instead of FEM analysis for two reasons: firstly, in order to point out the physical relations of the electrostatics of wound components; secondly, to provide a simple and fast design tool that allows prediction rather than just reproduction of the capacitances. Moreover, the dependence of the capacitance value on the geometrical parameters and on the material properties is clearer when an analytical formulation of the problem is considered. On the other hand, numerical tools such FEM are able to model even complex structures and provide very accurate results, but at the cost of long simulation and overhead time required to draw the model and to set up the simulation parameters accurately. The FEM user might require some further time to learn a specific software package. Moreover, it is a good practice to verify the numerical results with another method, for instance an analytical one. Analytical tools are then a good tradeoff between speed to acquire results and their accuracy.

6.1.2 Assumptions

The main contributions to the self-capacitance in a high-voltage transformer whose secondary winding is divided into several sections made out of different layers of turns (cf. Fig. 6.3) are the following:

- a) the turn-to-turn capacitance;



Figure 6.1: Example of single layer, ferrite wounds components.

- b) the layer-to-layer capacitance;
- c) winding-to-magnetic core;
- d) winding-to-electrostatic screen;
- e) inter-winding interactions.

Although this chapter addresses calculation of the self-capacitance of step-up transformers, the analysis and the calculation procedure have general validity and the formulation can be adopted for other wound components.

The assumptions adopted herein for the calculation of the capacitance are:

- a) Static electric field: the electric field \mathbf{E} is independent of the magnetic induction \mathbf{B} . The displacement current $\partial\mathbf{D}/\partial t$ is neglected, and the problem is thus algebraic and not differential; accordingly, the incremental parasitic capacitance due to dynamic fields is neglected [188].
- b) No distributed charge between the electrodes. The volume charge ρ_T is neglected while only the surface charge σ_T is considered; this assumption and the previous one lead one to consider the equivalent winding like its DC or *electrostatic* equivalent.
- c) Uniform voltage distribution along the turns (equal magnetic flux linked to each turn) and all turns have the same length.



Figure 6.2: Photograph of a high-voltage transformer.

6.2 Basic Cell for the Capacitance Calculation

6.2.1 Transformer Characteristics

The typical high-voltage transformer's structure is depicted in Fig. 6.3. It is comprised of an E or U ferrite core and solid or Litz wire windings. The primary usually only has a few turns, realized by a foil conductor, while the secondary presents a larger number of turns, arranged in layers and split into several sections. The secondary coils are usually hosted within a dielectric coil-former that keeps the required distance between the windings parts and guarantees the electric breakdown limits with respect to the voltage level in operation. A grounded electrostatic screen is usually inserted between the windings in order to split and ground the interwinding capacitance. Furthermore, in order to increase the step-up ratio, the transformers are often built with multiple secondary windings, which are then series connected.

The three decisive factors that mainly affect the value of the self-capacitance

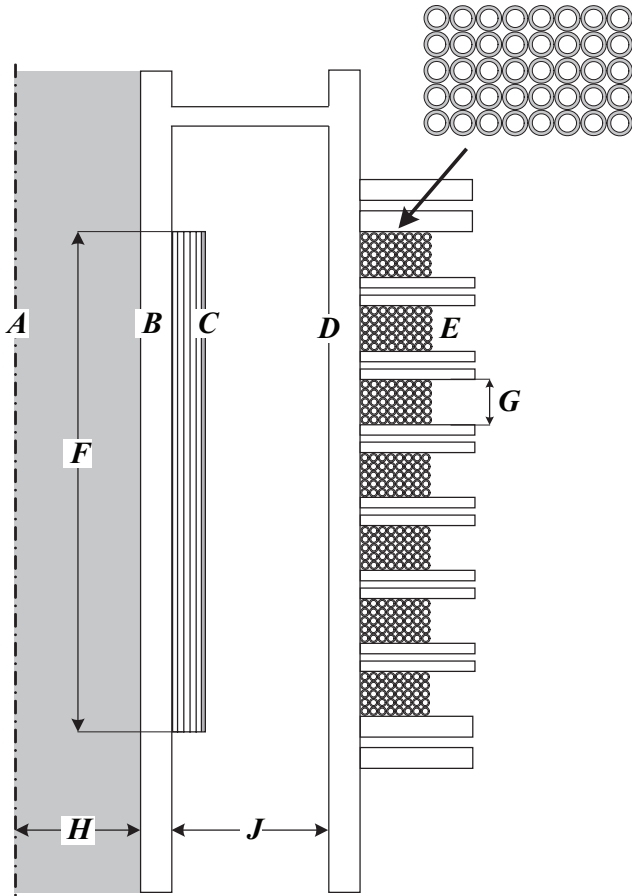


Figure 6.3: Cross section of a high-voltage transformer. A: central axis of the transformer (cylindrical symmetry); B: insulating cylindrical coil-former for the primary winding; C: primary winding realized with a foil conductor and outer electrostatic screen; D: coil-former for the secondary winding divided in sections; E: section made out of several layers of turns. F: width of the primary; G: section's width; H: magnetic core's leg radius; J: air-gap between windings.

are:

- a) the *dielectric constant* of the insulating materials interposed between the

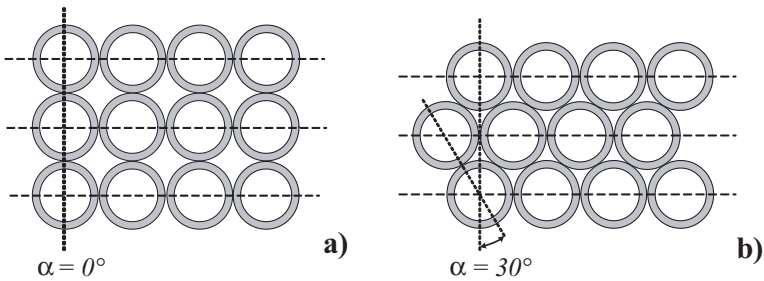


Figure 6.4: Arrangements of turns: (a) conductors aligned and (b) orthocyclic or hexagonal turns grid.

conductors;

- b) the *geometry*, i.e. diameter and dimension of the energized conductor, and the mutual spacing between wires and their distance to the screen or to the core;
- c) the *winding arrangement* and the strategy of connecting the different winding sections, which affect the distribution of the potential within each winding and between different windings and thus the amount of electrostatic energy stored (cf. Fig. 6.4).

6.2.2 Single-Turn Capacitance

Whenever an energized wire is in the proximity of another wire or of a ground plane, the electric field lines leaving the wire terminate on the surrounding conductors and they are distributed in the space such that the Laplace's equation

$$\nabla^2 \varphi = 0$$

is satisfied.

The turn-to-turn capacitance or the turn-to-ground (core or screen) capacitance are the elementary cells for the analysis of the electrostatic behavior of a wound component. For a cell constituted by two turns, the two conductors represent the electrodes and the electric field lines are distributed within the interposed dielectric and air. The wire can be solid or composed by several twisted strands. In this latter case, if t_w and t_L indicate the outer insulation thickness and the coating of each strand respectively (cf. Fig. 6.5a), then the equivalent dielectric

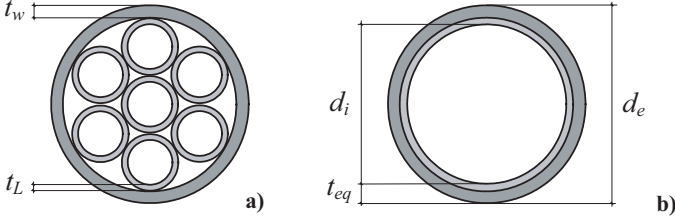


Figure 6.5: Cross-section of a Litz wire (a). To determine the equivalent isolation (b), the outer and the inner coating are considered as an equivalent dielectric of thickness t_{eq} and permittivity ε_{eq} .

constant ε_{eq} for a Litz wire is given by

$$\varepsilon_{eq} = \frac{\varepsilon_w \varepsilon_L (t_w + t_L)}{\varepsilon_L t_w + \varepsilon_w t_L} \quad (6.1)$$

where ε_w and ε_L are the dielectric constants of the outer insulation and of the coating of each strand respectively. The equivalent insulation thickness is provided by:

$$t_{eq} = t_w + t_L. \quad (6.2)$$

If the diameter d_L of each strand of a Litz wire is known, the outer diameter of the wire can be calculated as:

$$d_e = d_L \sqrt{\frac{4N_s}{\pi}} \quad (6.3)$$

where N_s is the number of strands [189].

In order to calculate the capacitance, it is first necessary to derive the electric field distribution, given the potential field φ (boundary conditions). For the elementary cell, such as the one depicted in Fig. 6.6a, the electric field \mathbf{E} along an electric flux line l_{PQ} is given by

$$\int_P^Q \mathbf{E} \cdot d\mathbf{l} = \Delta\varphi_{PQ} \quad (6.4)$$

where $\Delta\varphi_{PQ}$ is the voltage difference between the two points. Once that \mathbf{E} is calculated, the value of the corresponding capacitance C can be derived from the electrostatic energy stored in the volume Vol between the conductors,

$$C = \frac{1}{\Delta\varphi^2} \int_{Vol} \varepsilon_{eq} E^2 dv. \quad (6.5)$$

Accordingly, the expression of the capacitance per unit of length for a single wire of circular cross-section, uniformly charged, is given by

$$C_t = \varepsilon_0 \varepsilon_{eq} \frac{2\pi}{\ln\left(\frac{d_e}{d_i}\right)} \quad (6.6)$$

where $\varepsilon_0 = 8.854$ pF/m is the air permittivity, ε_{eq} is provided by (6.1), d_i and d_e are the inner and outer diameters (cf. Fig.6.5b), respectively.

6.2.3 Basic Cell: Turn-to-Turn Capacitance

Equation (6.6) overestimates the value of the capacitance between two conductors because it is derived under the assumption that the charge is uniformly distributed over the surface of the conductor. In a real system, however, the charge tends to gather along portions of turns that are closest to neighboring turns. Therefore, in order to take into account a more realistic charge distribution, the electric field between two wires can be derived considering field integration paths closer to the actual electric flux lines configuration. With this in mind, one can suppose either that the electric field lines remain radial until they reach the surface of the adjacent turn (cf. Fig.6.6a) or that they follow the shorter path in the air-gap between the turns (cf. Fig. 6.6b).

These two problems have already been faced by Koch [190] and Massarini [177], respectively. The calculation of the turn-to-turn capacitance corresponding to the configuration in Fig. 6.6a leads to

$$C_{tt,K} = 2\varepsilon_0 \left(m_L + \frac{2t_{eq}}{\varepsilon_{eq}d_e^2}(d_e - t_{eq})m_D \right), \quad (6.7)$$

where the coefficients m_L and m_D are given respectively by

$$m_L = \int_0^{\frac{\pi}{6}} \frac{\frac{1}{2} - \left(\sin^2 \theta + \cos \theta \sqrt{\cos^2 \theta - \frac{3}{4}} \right)}{\left[\cos \theta - \left(1 - \frac{2t_{eq}}{\varepsilon_{eq}d_e} \right) \left(\frac{1}{2} + \sqrt{\cos^2 \theta - \frac{3}{4}} \right) \right]^2} d\theta,$$

$$m_D = \int_0^{\frac{\pi}{6}} \frac{\sin^2 \theta + \cos \theta \sqrt{\cos^2 \theta - \frac{3}{4}}}{\left[\cos \theta - \left(1 - \frac{2t_{eq}}{\varepsilon_{eq}d_e} \right) \left(\frac{1}{2} + \sqrt{\cos^2 \theta - \frac{3}{4}} \right) \right]^2} d\theta.$$

If a three piecewise-linear path is considered, as illustrated in Fig. 6.6b, then

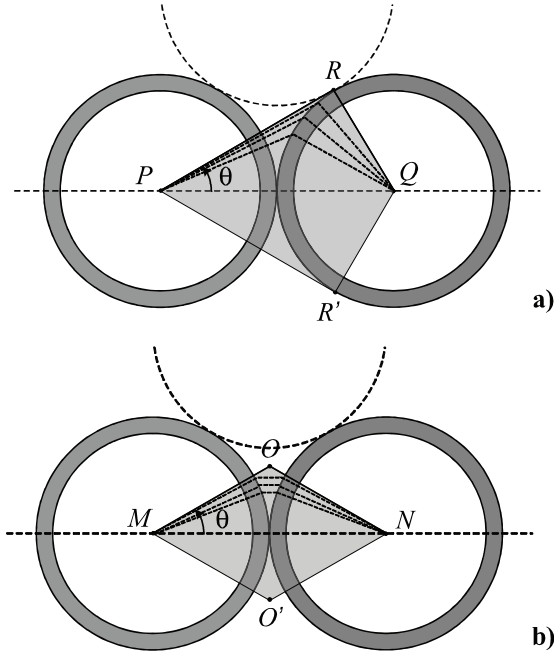


Figure 6.6: Basic cells for the calculation of the turn-to-turn capacitance. According to Koch's approach, (a) the electric field lines are assumed radial, until they reach the surface of the adjacent turn, [190]. The integration path proposed by Massarini [177] is shown in (b): the electric field lines follow the shorter path in the air-gap between two adjacent turns.

the resulting capacitance (per unit of length) is given by

$$C_{tt,M} = \varepsilon_{eq} \theta^* \ln^{-1} \left(\frac{d_e}{d_i} \right) + \varepsilon_0 \cot \frac{\theta^*}{2} - \varepsilon_0 \cot \frac{\pi}{12} \quad (6.8)$$

where

$$\theta^* = \arccos \left(1 - \frac{1}{\varepsilon_{eq}} \ln \left(\frac{d_e}{d_i} \right) \right).$$

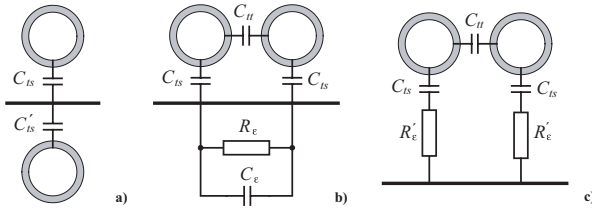


Figure 6.7: (a) Wire to conductive-plane capacitance calculable with the method of images. (b) The properties of the core can be included in the model as a lossy capacitance or (c) as series resistors to the core [191].

6.3 Influence of the Core on the Electric Field Distribution

The simplest winding arrangement is constituted by a single-layer coil wrapped around the magnetic core. In this configuration, the electric flux lines leaving each turn terminate on the adjacent turns and on the core. The latter usually consists of a ferrite material with a certain conductivity σ . The assumption of considering the core as an ideal conductor is useful to calculate the value of the capacitance against the core. The method of images can be used [177] and the formulas for the turn-to-turn capacitance derived in the previous section can be applied (cf. Fig. 6.7a). However, in order to predict the frequency behavior of the systems, it is opportune to include the resistance of the core in the model (cf. Fig. 6.7b).

An example of frequency analysis of ferrite wound components is in [191]. There, it is shown how the equivalent core resistance is responsible for the considerable damping of the frequency resonance peaks due to the self capacitance and leakage inductance of the winding.

Thus, in order to verify the impact of the core resistivity on the transformer's frequency behavior, the parameters of ferrite material of grade N87 [132] of the transformers cores analyzed in the experimental part of this work, have been extracted. For this reason, a ferrite sample between two electrodes has been considered to be a lossy capacitor [?], and the complex permittivity

$$\hat{\epsilon} = \epsilon_0 \epsilon_r = \epsilon_0 (\epsilon' - j\epsilon'') \quad (6.9)$$

describes the relationship between the electrical field, \mathbf{E} , within the material and the electric flux density $\mathbf{D} = \hat{\epsilon} \mathbf{E}$. The real part of the complex permittivity, ϵ' , accounts for the electrical energy stored in the dielectric material while the

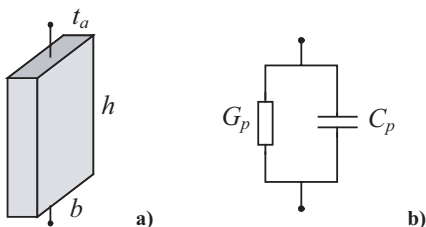


Figure 6.8: (a) Sample shape for measuring the dielectric and conductive properties of ferrite and (b) its equivalent circuit. The parallel capacitance C_p and dielectric loss factor $\tan \delta_\epsilon$ (or D) of a thin ferrite slab for N87 ferrite, having dimensions of $8 \text{ mm} \times 8 \text{ mm} \times 1.52 \text{ mm}$, have been measured using the AGILENT A294A dielectric test fixture.

imaginary part, ϵ'' , accounts for the conduction losses.

The AGILENT A294A test fixture has been used for measuring the dielectric characteristic of the material. The calibration procedure, outlined in the AGILENT A294A manual [192] as well as the sample preparation and size restrictions are the main issues of concern in measuring the ferrite electrical characteristics. The sample has the geometry depicted in Fig. 6.7a and its equivalent circuit used for extracting the material parameters is in Fig. 6.7b.

The ferrite sample is assumed as an ideal parallel-plate capacitor and the calculation of capacitance is performed assuming that the plates that bound the material sample are equipotential surfaces. This assumption is rigorous at DC since the conductive plates cannot support a voltage difference under static conditions. However, under AC excitation it is possible that the conductive plates are not equipotential and consequently also the electric field is not uniform within the sample cross-section and the electric flux density is similarly non-uniform. In order to measure the true material constants, the sample should have a minimum cross-sectional dimension that is a small fraction of the wavelength over the entire frequency range of interest. The tests have been carried out using a tiny slab of material N87 of dimensions $8 \text{ mm} \times 8 \text{ mm} \times 1.52 \text{ mm}$ with the electrodes plated onto opposite $8 \text{ mm} \times 1.52 \text{ mm}$ faces [193]. The capacitive admittance of each thin plate, whose expression is given by

$$Y_p = G_p + j\omega C_p \quad (6.10)$$

is measured using an AGILENT A294A precision impedance analyzer with its dielectric test fixture. The fixture of the impedance analyzer provides both a guarded and an unguarded electrode where the unguarded electrode is intended

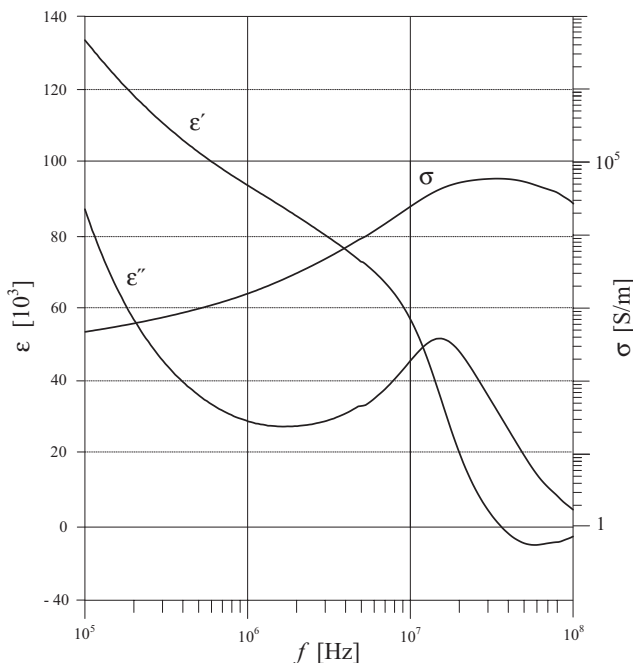


Figure 6.9: Frequency plot of the real and imaginary parts ε' and ε'' of the complex relative permittivity and of the conductivity σ for N87 ferrite at 25°C.

to minimize the effects of fringing near the edges of the guarded electrode. The measured capacitive reactance is used to derive the frequency-dependent real part of the relative permittivity as follows

$$\varepsilon' = \frac{h}{\varepsilon_0 t a b} C_p(f). \quad (6.11)$$

The measured dielectric loss factor, $\tan \delta_\varepsilon$, defined as

$$\tan \delta_\varepsilon = \frac{\varepsilon''}{\varepsilon'} = \frac{G_p}{\omega C_p} = \frac{\frac{\sigma t a b}{h}}{\omega \frac{\varepsilon_0 \varepsilon' t a b}{h}} = \frac{\sigma}{\omega \varepsilon_0 \varepsilon'} \quad (6.12)$$

provides information on both dielectric and ohmic losses, that cannot be empirically split. Actually, the former are dependent on the lossy component of the dielectric constant, ε'' , while the latter on the conductivity of the ferrite.



Figure 6.10: The damping effect of the resistors across the winding's turns is equivalent to the damping effect of the core resistance in wound ferrite components.

The imaginary part of the permittivity and the equivalent conductivity σ of the ferrite are given by

$$\varepsilon'' = \tan \delta_\varepsilon \varepsilon' \quad (6.13)$$

$$\sigma = \omega \tan \delta_\varepsilon \varepsilon_0 \varepsilon' = \omega \varepsilon_0 \varepsilon'' \quad (6.14)$$

The frequency plot of ferrite parameters (ε' , ε'' , σ) is shown in Fig. 6.9. The conductivity assumes a large value over all the considered frequency band [100 kHz - 100 MHz] that is of interest for practical applications. The damping of the frequency resonances peaks and the larger values of the winding impedance over all the frequency bandwidth are due to the large value of the core resistivity, $1/\sigma$, that leads to a value of the core resistance R_ε of some k Ω (cf. Fig. 6.7b). In particular, these effects are more relevant when the coil is directly wrapped on the core, such as the primary winding (cf. Fig. 6.3), but are negligible when the winding is far from the core or a screen is interposed between the core and the winding.

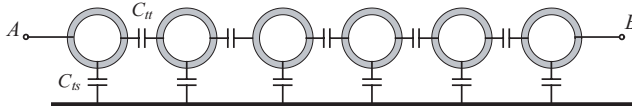


Figure 6.11: Equivalent capacitance network for a single layer coil with a shield or core.

6.4 Capacitance of the Secondary Winding

6.4.1 Single Layer Capacitance

If the presence of a screen or core is considered, and if the capacitance between two nonadjacent turns is neglected, then the resulting equivalent network representing the distributed capacitances between adjacent turns, C_{tt} , and towards the screen, C_{ts} , can be seen as depicted in Fig. 6.11. In the simplest case, if the screen or core is distant from the coil or even absent (air-coil), the resulting capacitance C_{AB} across the terminals $A - B$ is given by

$$C_{AB} = \frac{C_{tt}}{n_t - 1} \quad (6.15)$$

where n_t is the number of turns. For the configuration depicted in Fig. 6.11, the resulting capacitance across the terminals is given by

$$C_{AB}(n_t) = \frac{C_{tt}}{2 + \frac{C_{tt}}{C_{AB}(n_t-2)}} + C_{tt} \quad (6.16)$$

assuming the capacitance to shield C_{ts} is two times larger than the capacitance C_{tt} by virtue of the images method (cf. Fig. 6.7a). Equations (6.15) and (6.16) have already been proposed in [177] and [194]. There, the capacitance C_{AB} depends inversely (6.15) and asymptotically, (6.16) on the number of turns, n_t . Both formulas provide good approximations of the self-capacitance if there are only a few turns or they are well spaced (cf. *d1* Fig. 6.12a). In the case of many turns, tightly wrapped around the core, the influence of the capacitive coupling between nonadjacent turns cannot be neglected and the dependence of C_{AB} on n_t is better expressed by a linear relationship [195], *i.e.* the capacitance increases linearly for increasing number of turns. Fig. 6.12b shows the relationship between the number of turns n_t and the measured capacitance C_{AB} for two different coils made with wire having a diameter of 0.5 mm with insulation thickness of 33 μm and magnetic cores, E47 and E98, of ferrite grade N87. For both cases the following behavior has been empirically registered. As long as the

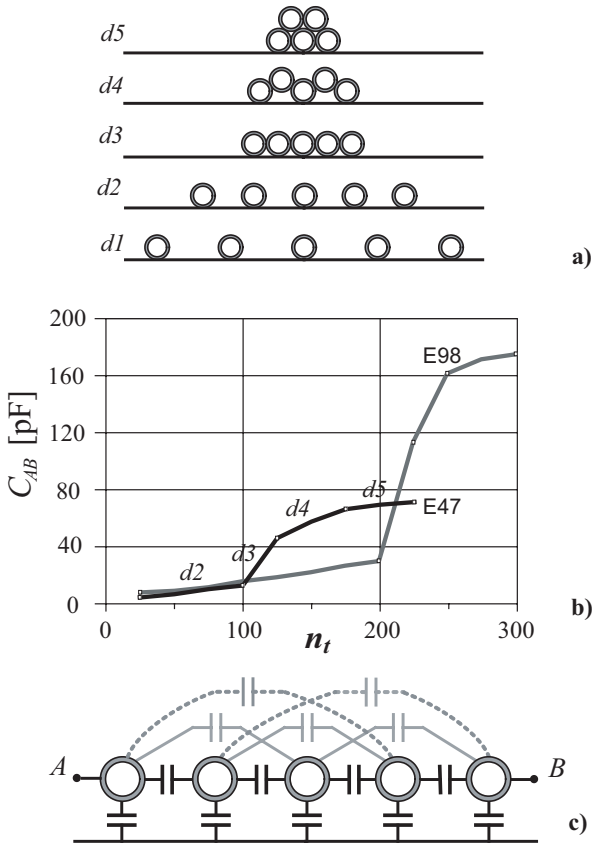


Figure 6.12: Empirical verification of the dependence of the self capacitance of a single layer on the spacing between turns. a) Different spacing between turns $d1 \dots d5$, b) measured self-capacitance of a coil made out of a wire having a diameter of 0.5 mm and insulation thickness of $33 \mu\text{m}$ wound around two different cores, E47 and E98. n_t is the number of turns. c) The electrostatic interactions between nonadjacent turns cannot be neglected for the configurations $d4$ and $d5$.

turns are wound uniformly, each turn close to the next one, a linear dependence of C_{AB} on n_t is observed (cf. $d2$ and $d3$ Fig. 6.12a). In particular, the values of the capacitance measured for the two coils are nearly the same for fewer turns

Table 6.1: Measured and Calculated Winding Capacitance [pF]

	Measured	Calculated with (6.7)	Calculated with (6.8)
Tr # 1	3.84	3.12	3.35
Tr # 2	4.84	4.22	4.47

(cf. Fig. 6.12) because the cores have been wound with the same wire, although the E47 core had a further insulating coating with respect to the E98 core. For a larger n_t , the space between turns becomes tight, the turns start to overlap (cf. *d4* Fig. 6.12a) and a sudden increase of the capacitance C_{AB} is observed. This is because the electrostatic interaction between nonadjacent turns becomes stronger (cf. Fig. 6.12c). As soon as the second layer begins to grow (cf. *d5* Fig. 6.12a), the dependence of C_{AB} on n_t is again linear and less steep, and the trend is the same as that registered for the first layer. This kind of dependence of C_{AB} on n_t can also be observed with more layers. It should be noted that the measurement in Fig. 6.12 could also have been equivalently realized by keeping the number of turns n_t constant while varying the mutual arrangement of the turns.

6.4.2 Layer-to-Layer Capacitance

Starting from the value of C_{tt} provided by (6.7) or (6.8) one can calculate the value of the capacitance between two layers of turns, then of a section of the winding constituted by z layers, and finally of the whole winding made out of q sections (cf. Fig. 6.3). Toward this aim the following formulas provide a good assessment of these capacitances [170]. The layer-to-layer capacitance C_{ll} is given by

$$C_{ll} = \frac{n_t(n_t + 1)(2n_t + 1)}{6n_t^2} l C_{tt} \quad (6.17)$$

where l is the average length of a turn. Then the capacitance C_s of a section is provided by

$$C_s = C_{ll}(z - 1) \left(\frac{2}{z}\right)^2. \quad (6.18)$$

Finally, for the overall winding, constituted by q sections, the capacitance is:

$$C_w = \frac{C_s}{q}. \quad (6.19)$$

Tab. 6.4.2 shows the calculated values of the secondary winding capacitances of transformers # 1 and # 2 whose specifications are given in Tabs. 6.2-6.3.

The use of (6.17) for calculating the layer-to-layer capacitance implies the calculation of the turn-to-turn capacitance C_{tt} by means of (6.7) or (6.8). This computational effort is worthwhile if the number of turns < 10 for layer, but for a larger number of turns it is convenient to use simpler formulas for calculating the capacitances. The winding structure can be modeled as a coaxial cylindrical capacitor, or if the curvature radius r is large (cf. Fig. 6.13), of a parallel plate capacitor:

$$C_{ll} = \varepsilon_0 \varepsilon_r \frac{2\pi w}{\ln\left(1 + \frac{d}{r}\right)} \xrightarrow{r \rightarrow \infty} C_{ll} = \varepsilon_0 \varepsilon_r \frac{2\pi r w}{d} \quad (6.20)$$

where w is the width of the layer, or the breath of each section. Equation (6.20) is valid for a large number of turns with axial symmetry. For only a few spaced turns the calculation of C_{tt} by means of (6.7) or (6.8) has to be the basis for deriving the self-capacitance.

The value of the distance d between two wires of different layers plays a decisive role in the calculation of the capacitance. In general d is not provided by two times the insulation thickness (cf. Fig 6.5), as one can easily and erroneously assume, but it is opportune to use an empirical formula [170] that accounts for the actual mutual position between wires, that are usually not perfectly aligned.

$$d = 1.26 \cdot d_e - 1.15 \cdot d_i \quad (6.21)$$

where d_e and d_i are external and internal wire diameters respectively (cf. Fig. 6.5). Equation (6.21) should provide the length of the average electric flux line between two conductors rather than the insulation thickness. If the conductors are distant or the insulation is thick, then the actual distribution of electric flux lines can be more complex than the ones sketched in Fig. 6.6. Accurate information on the wire's characteristics, such as its insulation thickness and its cross-section, is very important in order to have a good assessment of the equivalent distance d and hence to reduce the error in the final calculation of the capacitance.

The expressions of the static capacitance C_{ll} (6.20) are derived under the assumption of uniform charge distribution over the conductors of each layer disconnected (cf. Fig. 6.13). However, according to the connection among terminals of adjacent layers, *i.e.* the winding strategy, the potential distribution along the turns varies and consequently so does the value of the layer-to-layer capacitance.

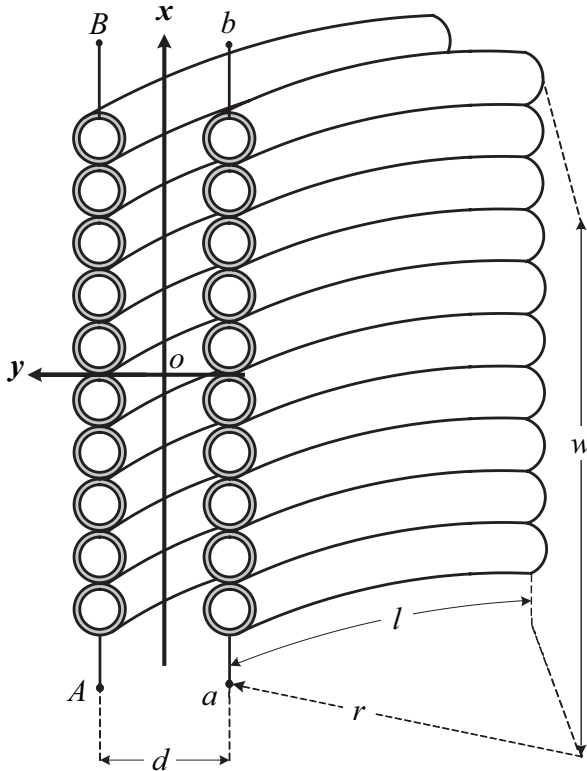


Figure 6.13: Representation of two adjacent layers or single-layer windings.

6.4.3 Effect of the Connection Between Adjacent Layers

An interesting way to derive the value of the equivalent capacitance when different connections of the layers are considered, is provided by the *Principle of Virtual Work (PVW)* ([196], p. 460). If U is the voltage difference between two layers, as those depicted in Fig. 6.13, then the corresponding electrostatic energy W_ϵ stored between the layers is given by

$$W_\epsilon = \frac{1}{2} \int_{Vol} \mathbf{D} \cdot \mathbf{E} dv = \frac{1}{2} C_u U^2 \quad (6.22)$$

Consider the two possible connections between two adjacent layers, *i.e.* layers wound in opposite directions (cf. Fig. 6.14a) or in the same direction (cf. Fig. 6.14c).

According to the PVW, the stored electrostatic energy can be calculated by realizing that no matter what process is used to assemble the system, the final configuration (d and w) and the voltage distribution are the same. For the connection as in Fig. 6.14a, that provides the equivalent voltage distribution shown in Fig. 6.14b, the electric field is given by

$$E(x) = \frac{U}{d} \frac{x}{w} \quad (6.23)$$

and the electrostatic energy stored corresponding to this configuration is given by

$$\begin{aligned} W_\varepsilon &= \frac{1}{2} \int_{Vol} \varepsilon E^2(x) dv \\ &= \frac{1}{2} \varepsilon l d \frac{w}{d^2} \frac{U^2}{3} = \frac{1}{2} \frac{C_{ll}}{3} U^2 \\ &= \frac{1}{2} C_{eq} U^2 \end{aligned} \quad (6.24)$$

where ε is the equivalent dielectric constant of the media interposed between the layers, l the average turn length and C_{ll} is the static interlayer capacitance, (6.20). For the connection in Fig. 6.14c, which provides the equivalent voltage distribution shown in Fig. 6.14d, the electric field and the corresponding stored energy can be derived with the same procedure and are given respectively by

$$E(x) = \frac{U}{2d} \quad (6.25)$$

and

$$\begin{aligned} W_\varepsilon &= \frac{1}{2} \frac{C_{ll}}{4} U^2 \\ &= \frac{1}{2} C'_{eq} U^2 \end{aligned} \quad (6.26)$$

Thus layers wound in the same direction show a lower equivalent capacitance C'_{eq} than the capacitance C_{eq} of layers wound in opposite direction and this is due to the different potential distribution corresponding to the two configurations.

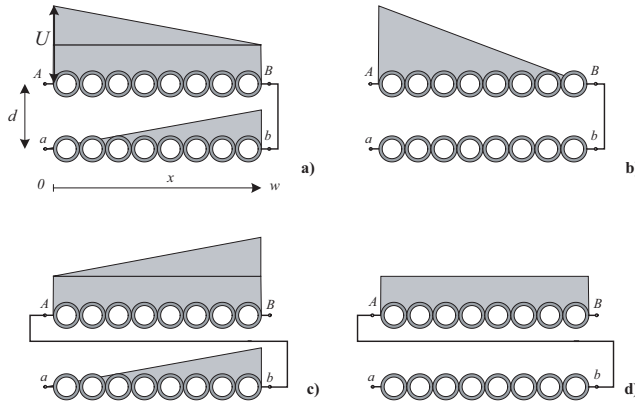


Figure 6.14: Voltage distribution in dependence on the layers connection. Layers wound in opposite direction, (a), and (b) equivalent potential distribution. Layers wound in the same direction, (c), and (d) equivalent potential distribution. The terminal a is grounded.

6.4.4 Effect of the Voltage Ratio and Spacing Between Adjacent Layers

The voltage difference between adjacent layers or windings affects the value of the static capacitance. In Fig. 6.13 the ports AB and ab of two adjacent layers are shown. If the voltages U_{ab} and U_{AB} or U_{Aa} and U_{Bb} are known, the value of the capacitance at one port can be expressed by:

$$C = \frac{C_{ll}}{3U_{ref}^2} [(U_{Aa} + U_{Bb})^2 - U_{Aa}U_{Bb}] \quad (6.27)$$

where C_{ll} indicates the static layer-to-layer capacitance and U_{ref} is a reference voltage [142]. Lets now assume the connection shown in Fig. 6.15a of the two coils, a sketch of which is depicted in Fig. 6.13. If the voltage $U_{AB} = U_{ab}/n$ is taken as reference voltage for the calculation of the capacitance at the terminals AB according to (6.27), the capacitance C_{AB} shown in Fig. 6.15.a is provided by

$$C_{AB} = \frac{C_{ll}}{3}(n - 1)^2. \quad (6.28)$$

where n indicates the voltage ratio. Equation (6.27) is derived under the assumption of potential variation only between the layers. If the variation of the

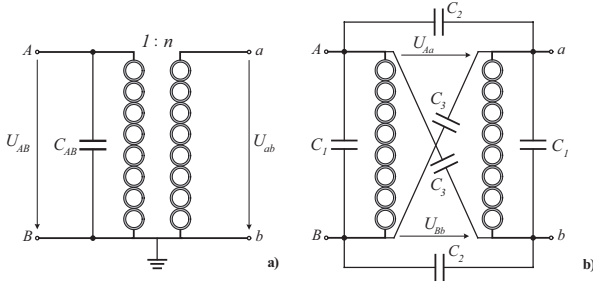


Figure 6.15: (a) Equivalent capacitance C_{AB} of two coils wound in opposite direction, with voltage ratio $n=U_{ab}/U_{AB}$ and one terminal grounded. (b) Lumped capacitances C_1 , C_2 and C_3 associated with a 2-D distribution of the electric field for the configuration depicted in Fig. 6.13.

voltage within the same layer of turns is considered as well, then the electric field has two components (E_x, E_y) rather than just E_x , as assumed so far. The equivalent circuit in Fig. 6.15b shows the six capacitances, of which two are linearly independent, that are associated with a two-dimensional (2-D) electric field distribution for the winding architecture shown in Fig. 6.13. Such a field distribution is strongly dependent on the the distance d between adjacent layers; accordingly, the assumption of 2-D electric field distribution is more valid the larger the distance d . It can be easily proven [197], that these capacitances assume the following values:

$$\begin{aligned} C_1 &= -\frac{C_{ll}}{6} \left(1 - 2\frac{d^2}{w^2}\right) \\ C_2 &= +\frac{C_{ll}}{3} \left(1 - \frac{d^2}{2w^2}\right) \\ C_3 &= +\frac{C_{ll}}{6} \left(1 + \frac{d^2}{w^2}\right) \end{aligned} \quad (6.29)$$

The equivalent capacitance C_{AB} of the two port system corresponding to the connection shown in Fig. 6.15b, under the assumption of 2-D electric field distribution, is provided by:

$$C_{AB} = (C_1 + C_3)(1 + n^2) + C_2(1 - n)^2. \quad (6.30)$$

By substituting the values (6.29) into (6.30), the capacitance C_{AB} becomes a function of the static interlayer capacitance C_{ll} and of the geometric parameters d and w :

$$C_{AB} = \frac{C_{ll}}{3}(1 - n)^2 + \frac{d^2}{3w^2}C_{ll}(1 + n + n^2). \quad (6.31)$$



Figure 6.16: The screen of a Pearson current transformer is gapped, to avoid a magnetic short circuit.

If the equivalent distance d (6.21) between two adjacent layers is small compared to the width w of each layer (cf. Fig. 6.13), then the equation (6.31), derived under the assumption of 2-D electric field distribution, can be simplified to (6.28). This equation corresponds to 1-D field distribution.

6.5 Capacitance towards Screen

The capacitance against the screen is due to the electric energy stored in the gap between the secondary winding and the screen. For this calculation, it is assumed that only the lower layers of the sections contribute to the capacitance, since the electric field between the screen and layers in front of the screen provides the major contribution to the electrostatic energy stored. The distribution of the voltage U across a coil of q sections and z layers per section is shown in Fig. 6.19. The energy stored between each section and the screen is calculated in a similar fashion as in [142] and then all contributions can be summed up to provide the total energy stored between the screen and the conductive layer opposite to the screen. Hence the resulting layer-to-screen capacitance $C_{l,s}$

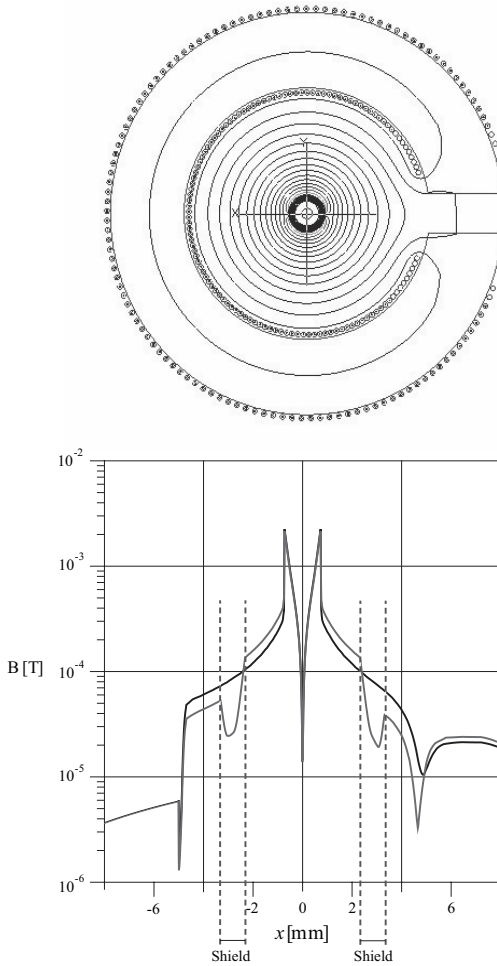


Figure 6.17: Effect of the screen on the field in the transformer window. The magnetic field results reduced.

assumes the following expression:

$$C_{ls} = \sum_{i=1}^q C_{ls,i} \frac{1}{q^2 z^2} \left(\frac{3z^2(i-1)^2 + 3z(i-1) + 1}{3} \right) \quad (6.32)$$

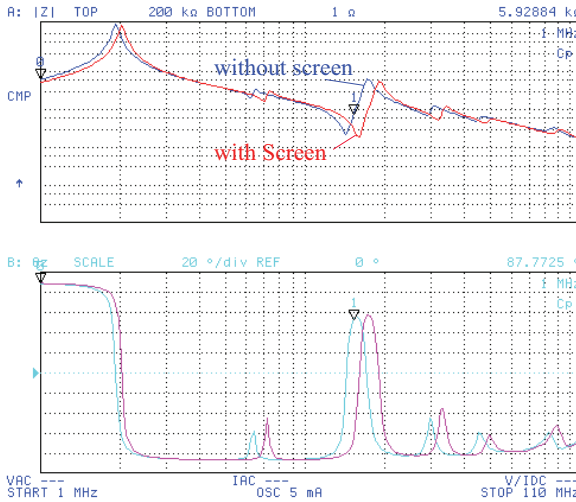


Figure 6.18: Measured effect of the screen on the field in the transformer window.

where $C_{ls,i}$ is the static capacitance between each section of width w and the screen, which can be calculated in a similar fashion as (6.20). For a large number of sections q , the previous formula (6.32) can be simplified into

$$C_{ls} = \frac{C_{ls,i}q}{3} \quad (6.33)$$

where the capacitance $C_{ls,i}$ between each section and the screen can be assumed equal for all the sections, if the width w is the same for all sections (cf. Fig. 6.19). A good approximation for $C_{ls,i}$ (per unit of length) is given by

$$C_{ls,i} = \varepsilon_{eqs} \frac{2\pi w}{\ln\left(1 + \frac{d_s}{a}\right)} \quad (6.34)$$

where ε_{eqs} is the equivalent dielectric constant that accounts for the properties of the insulation of the wires faced to the screen and the air between the layer and screen. The parameter a is the radial distance of the screen from the central axis (cf. Fig. 6.3) and d_s is the distance of the secondary from the screen (cf. Fig. 6.19).

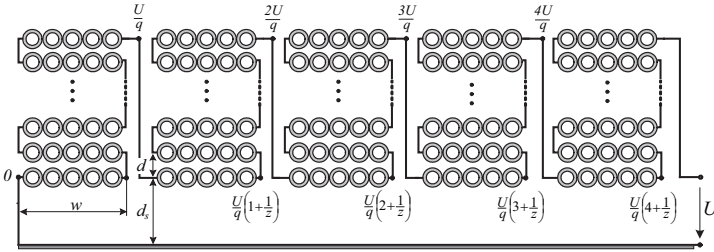


Figure 6.19: Distribution of the voltage U across a coil of $q=5$ sections and z layers per section; d indicates the inter-layer distance while d_s is the distance between the inner layers and the screen.

Table 6.2: Technical Specifications of the Transformer #1 with ER98 Core used for the Experimental Validation

Outer diameter of secondary wire	$d_{e \max}$	0.472 mm
Insulation thickness	h	20 μm
Dielectric constant of insulation	ε	3.55
Number of turns per layer	n_t	5
Number of layers	z	10
Number of sections	q	5
Average turn length	l	$2\pi \cdot 26$ mm
Breath of each section	w	2.5 mm
Distance from screen	d_s	8 mm
Distance screen from axis	a	15.5 mm
Breath of screen	L	52 mm

6.6 Experimental Results

In order to verify the consistency of the procedure for calculating the self-capacitance, measurements and calculations have been performed for three different transformers architectures. The high-voltage transformers possess the same construction characteristics (cf. Fig. 6.3) but different numbers of layers, sections and winding arrangements. The geometrical features of the transformers and the properties of the windings are shown in Tabs. 6.2-6.4.

If one refers all the contributions to the self-capacitance to primary side of the transformer, the capacitances of the secondary windings and the capacitances

Table 6.3: Technical Specifications of the Transformer # 2 with 72/65/39 Core used for the Experimental Validation

Outer diameter of secondary wire	$d_{e \max}$	0.297 mm
Insulation thickness	h	16 μm
Dielectric constant of insulation	ε	3.55
Number of turns per layer	n_t	27
Number of layers	z	5
Number of sections	q	11
Average turn length	l	$2\pi \cdot 31.7$ mm
Breath of each section	w	4 mm
Distance from screen	d_s	10.9 mm
Distance screen from axis	a	18.5 mm
Breath of screen	L	81 mm

Table 6.4: Technical Specifications of the Transformer # 3 with U 93/76/20 Core used for the Experimental Validation

Outer diameter of secondary wire	$d_{e \max}$	0.194 mm
Insulation thickness	h	11.5 μm
Dielectric constant of insulation	ε	3.55
Number of turns per layer	n_t	26
Number of layers	z	20
Number of sections	q	5
Average turn length	l	$2\pi \cdot 40$ mm
Breath of each section	w	5 mm
Distance from screen	d_s	15 mm
Distance screen from axis	a	21.5 mm
Breath of screen	L	41 mm

between secondary windings and screen have to be multiplied by a factor n^2 , where n is the transformer turns ratio (very large for step-up transformers) [197]. In light of this, the contribution of the primary and the inter-windings *mutual* capacitances (between primary and secondary) to the equivalent capacitance can be considered negligible.

The secondary winding impedance has been measured with an Agilent A294A impedance analyzer for the following two conditions. The measurement was first performed without the screen and the magnetic core. In this case the

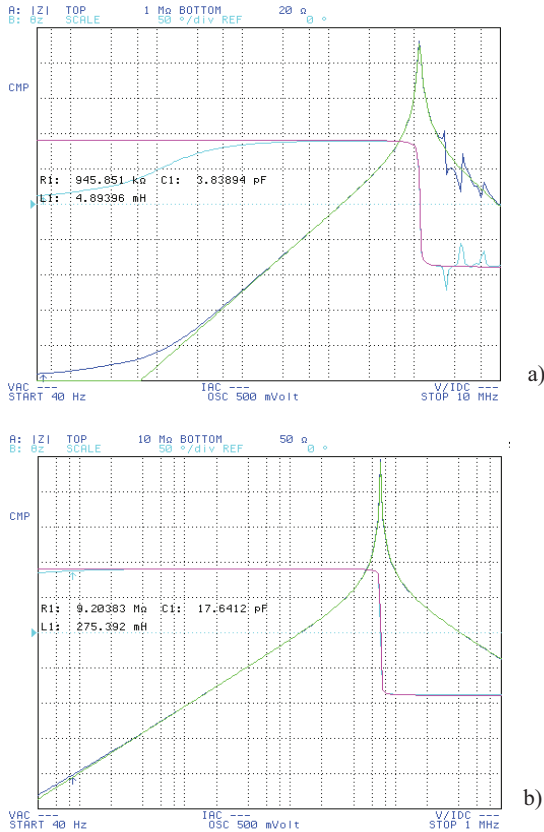


Figure 6.20: Measured self-capacitance of the secondary winding for the transformer # 1 without the screen and the core (a) and measured self-capacitance for the system comprising of the screen and the core (b).

value of the first parallel-resonance frequency f_p , given by

$$f_p = \frac{1}{2\pi\sqrt{LC}} \quad (6.35)$$

is shifted to higher frequencies than for the cored system since the magnetizing inductance L without the core assumes a lower value. Secondly, the impedance

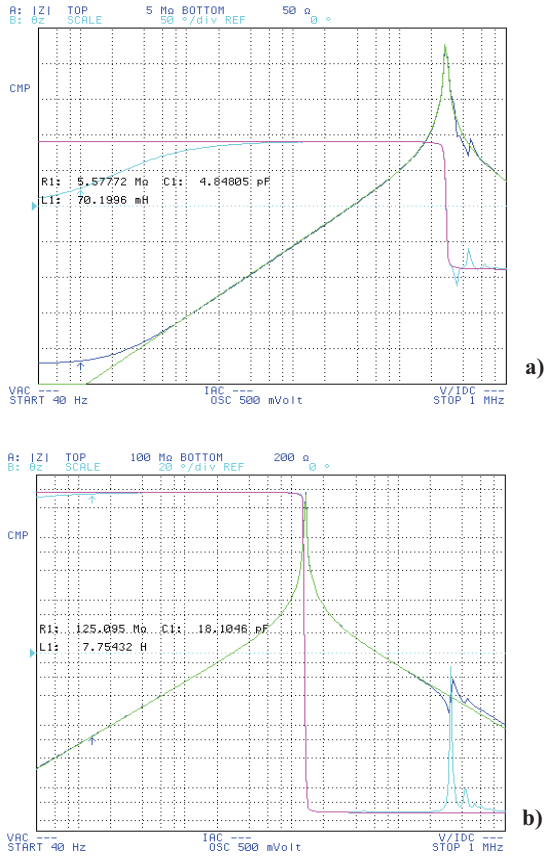


Figure 6.21: Measured self-capacitance of the secondary winding for the transformer # 2 without the screen and the core (a) and measured self-capacitance for the system comprising of the screen and the core (b).

was measured for the system comprising of the core and the screen (cf. Fig. 6.22). The measurement realized without the core and screen provides the self-capacitance of the winding while the measurement performed with connected screen and winding gives the total capacitance, *i.e.* the sum of the winding

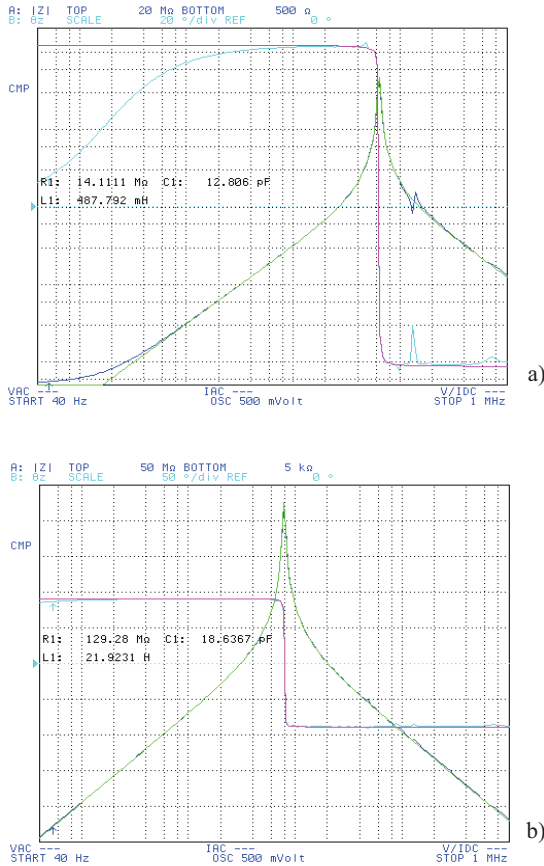


Figure 6.22: Measured self-capacitance of the secondary winding for the transformer # 3 without the screen and the core (a) and measured self-capacitance for the system comprising of the screen and the core (b).

self-capacitance and the capacitance to the screen. From these latter two measurements, the capacitance towards the screen was calculated as the difference. Both measurements with and without core showed that the stray capacitance towards the core can be neglected since the screen is interposed between wind-

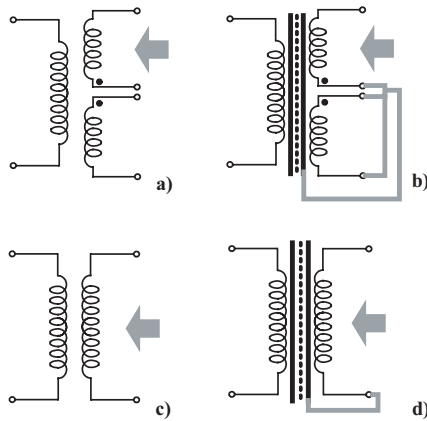


Figure 6.23: Connections of the secondary winding's terminals adopted during the impedance measurement for transformers # 1, (a) and (b), and transformers # 2 and # 3, (c) and (d), respectively.

ings and core for these transformer architectures.

The connections of the secondary winding's terminal adopted during the impedance measurements for the transformers # 1 is shown in Fig. 6.23a-b. This transformer has two secondary windings that are series connected in operation, with one terminal connected to the screen and grounded. Transformers # 2 and # 3 have only one secondary winding, with one terminal grounded and connected to the screen in normal operation (cf. Fig. 6.23c-d).

Tab. 6.5 shows the experimental and analytical results obtained for the three transformers. The winding self-capacitance has been calculated by substituting the formulas (6.20) into (6.18) and (6.19) and considering (6.24) or (6.26) according to the type of connection of the layers. The capacitance against the screen was calculated with equations (6.32), (6.33) and (6.34). For the transformer # 1 having two secondary windings, one of the secondaries has been short circuited during the measurement, to avoid the magnetic coupling between the two secondaries; moreover, the total self-capacitance is given by the sum of two times the winding self-capacitance and the capacitance to the screen. From Tab. 6.5 it is evident that the relative error between calculated and measured self-capacitance is constant. The parameter that mostly affects the calculation of the winding self capacitance is the equivalent distance d between wires (6.21). Furthermore, the analytical results have been obtained assuming that the turns of each layer are aligned as shown in Fig. 6.4a. If the conductors

Table 6.5: Experimental Results [pF]

Transformer # 1				
	Calculated	Measured	Error (%)	
Self-capacitance of secondary winding (2 Secondaries)	3.15	3.84	-17.97	
Self-capacitance towards screen	8.06	9.96	-19.08	
Total self-capacitance	14.36	17.64	-18.59	
Transformer # 2				
	Calculated	Measured	Error (%)	
Self-capacitance of secondary winding	3.97	4.84	-17.98	
Self-capacitance towards screen	10.84	13.26	-18.25	
Total self-capacitance	14.81	18.10	-18.18	
Transformer # 3				
	Calculated	Measured	Error (%)	
Self-capacitance of secondary winding	10.47	12.80	-18.20	
Self-capacitance towards screen	4.75	5.84	-18.66	
Total self-capacitance	15.22	18.64	-18.35	

were orthocyclic, as shown in Fig. 6.4b, the value of the static DC capacitance is two times the value obtained for aligned conductors [?].

The capacitance value is therefore between two case limits with dependence on the the winding arrangement: lowest capacitance value for turns aligned and highest capacitance value for an orthocyclic packing. Since the aligned turns condition was assumed, then the results shown in Tab. 6.5 correspond to minimum capacitance values; the same assumption has been done for the calculation presented in Tab. 6.4.2. A correct assessment of the mutual position of the turns can reduce the calculation error. For the transformers considered, the turns within each section of the windings are not exactly aligned but they are as well not orthocyclically placed. A correcting factor k , defined as

$$1 < k < 2 \tag{6.36}$$

can be introduced and used to take into account the mutual position of the turns

within a section. It was estimated between 1.1 and 1.3 for these transformers and this can be assessed depending on the angle α shown in Fig. 6.4. This factor, once multiplied by the calculated capacitance value, would compensate the calculation error.

The calculation of the capacitance due to screen is also affected by an error of -18% and this is due to the simplification made of modelling the static DC capacitance between winding and screen as an ideal cylindrical capacitor. This approximation is accurate if the secondary winding is divided into several sections with the same characteristics (6.33).

6.7 Conclusion

This chapter presented a comprehensive procedure for calculating the self-capacitance of high-voltage transformers. Such transformers usually find application within isolated DC/DC converters where the transformer's self-capacitance and leakage inductance are used as elements of the resonant tank.

The analytical approach was selected over the FEM approach because there is a good tradeoff between speed in acquiring the results and their accuracy. The proposed procedure of calculation is based on a physical approach and equations for calculating the turn-to-turn, interlayer, section's and winding capacitances, respectively, were explained.

The approach and formulas presented in this chapter can be used for wound components other than just step-up transformers. The influence of the core on the electric field distribution was analyzed and the dielectric characteristics of N87 ferrite grade extracted. Including the core's resistance in the equivalent circuit of the winding is important to correctly reproduce the frequency behavior. Moreover, the dependence of the value of a single layer capacitance on the number of turns was shown.

The two factors that are responsible for the error in the calculation are: the distance d between layers and the turns arrangement, either aligned or orthocyclic.

The *principle of virtual work* was used to show how different potential distributions influence the value of the static interlayer capacitance. It was proven that a six-capacitances equivalent model corresponding to 2-D electric field distribution can be reduced to a conventional single capacitance associated to the 1-D electric field distribution, if the equivalent distance d between layers or adjacent windings is small enough.

The experimental results show that the calculation's procedure is consistent for different transformer architectures and the error remains constant.

The proposed analysis of the electrostatic behavior of high-voltage transformer and the calculation procedure are important from a practical standpoint for

three different purposes:

- a) reducing the capacitance value and hence the dielectric losses (by modifying for instance the winding arrangement);
- b) using the self capacitance of the transformer as an effective circuital parameter (integration);
- c) applying a strategy of capacitance cancellation, that already succeeded for other two-port devices [198].

Chapter 7

Isolated Planar DC Current Transformer

7.1 Introduction

The sensor presented in this chapter uses a planar current transformer (CT) as the main sensing device. For a high upper bandwidth limit the parasitic capacitance and leakage inductance must be small [191]. The number of turns on the sensing coil can therefore be reduced, which also decreases the value of the magnetizing inductance (cf. L_{m1} in Fig. 7.3), thus providing some advantages [82]. The realization cost is lower for a planar transformer rather than a wire wound device. The drawback of this solution is that the lower corner frequency increases with fewer turns. This also happens when core materials with low permeability, a gapped or core-less transformers are used. Therefore, in order to extend the bandwidth to DC while keeping the advantages at high frequency, another device able to sense the DC and low frequency part of the measured signal can be combined with the CT. The technique of matching the frequency characteristics of two sensing devices for broad band current sensing from DC to several MHz has already been proposed in literature [199, 200, 73, 201, 202]. The proposed sensor features a Hall-effect based element for performing the low frequency current sensing. There are at least three well known architectures for combining a Hall-effect sensor and a magnetic core:

1. open loop;
2. closed loop;
3. a combination of open loop and CT.

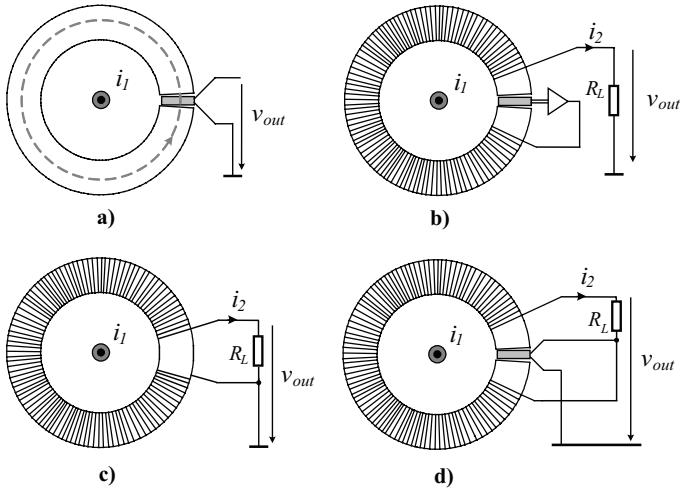


Figure 7.1: Current sensors technologies based on magnetic core: a) open-loop, b) closed loop, c) current transformer and d) the proposed current sensor.

For all three the Hall element is physically inserted into a gapped magnetic structure (cf. Fig. 7.1 a, b, d). A description of each architecture is given in [75]. Closed loop devices are most common and operate on the principle of compensating the low frequency flux in the core with a feedback from a DC to low frequency sensor [201, 203], which is typically a Hall element. Since the magnetic core for a closed loop transducer operates at zero-flux, the operating point of the sensor is also around the zero flux crossing. It is therefore unnecessary for the DC to low frequency sensor to be linear.

The proposed transducer uses a linear Hall element for sensing the current components from DC up to the lower corner frequency of the planar CT. The measured current signal is provided by the sum of the output signal of the Hall element and the CT (cf. Fig. 7.1d). Contrary to the closed loop technology, the proposed solution is passive and does not require feedback or process electronics. As described in detail in the following sections, the matching between the Hall element and the CT is provided without electronics stage, which is usually required for instance in [199]. This chapter presents a planar prototype of the CT that is an improvement of a previous toroidal device [191]. It has been empirically verified that the main characteristics of the DC-planar CT are:

1. frequency bandwidth from DC up to 30 MHz;

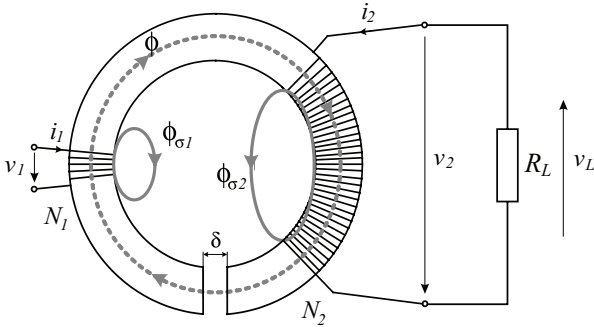


Figure 7.2: Sketch of a gapped current transformer.

2. 40 A (DC) current rating;
3. high dv/dt immunity;
4. thermal stability (linear behavior under temperature variations);
5. compact planar transformer with a multilayer PCB winding;
6. low realization cost.

7.2 Principle of Operation

The driving quantity for the functioning of the sensor is the magnetic flux ϕ . This is because the output signal of the Hall-effect sensor is proportional to the flux and the output voltage of the CT is dependent on the flux rate (cf. Fig. 7.5). For this aim it is opportune to use an equivalent circuit of the transformer which allows to calculate easily the flux and includes also the properties of the magnetic core. The capacitance-permeance analogy based model was chosen. The definitions of the used quantities along with the complete set of transformer's equations are included in the fifth chapter of this Dissertation. We recall hereafter only the formulas needed to explain the principle of operation of the sensor. A sketch of the gapped current transformer is shown in Fig. 7.2. The flux in the core if $\Lambda_g \ll \Lambda_m$ is defined as

$$\phi = \Lambda_g(N_1 i_1 - N_2 i_2). \quad (7.1)$$

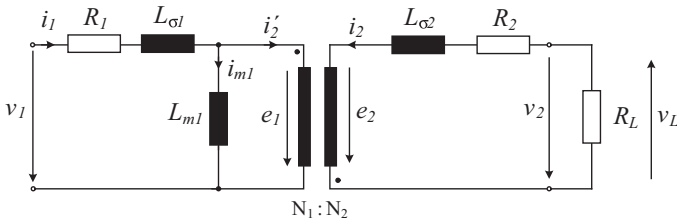


Figure 7.3: Equivalent electric circuit of a current transformer.

The primary and secondary voltages are given respectively by

$$v_1 = R_1 i_1 + L_{\sigma 1} \frac{di_1}{dt} + L_{m1} \frac{di_{m1}}{dt} \quad (7.2)$$

and

$$v_2 = R_2 i_2 + L_2 \frac{di_2}{dt} - M \frac{di_1}{dt} = -i_2 R_L. \quad (7.3)$$

From (7.3) the current ratio can be extracted using the Laplace transform, where s indicates the Laplace operator. The ratio between primary and secondary currents is then provided by:

$$\frac{I_2(s)}{I_1(s)} = \frac{N_1}{N_2} \frac{s \frac{L_{m2}}{R_2 + R_L}}{1 + s \frac{L_2}{R_2 + R_L}}. \quad (7.4)$$

7.2.1 Ideal Sensor

If the leakage inductance $L_{\sigma 2}$ is sufficiently small, which is typical for planar transformer, then

$$L_2 \approx L_{m2} \quad (7.5)$$

and, if the winding resistance R_2 is negligible with respect to the load resistor R_L , then the time constant associated with the secondary winding assumes the form:

$$\tau = \frac{L_2}{R_L}. \quad (7.6)$$

Accordingly, the current ratio (7.4) can be written as

$$\frac{I_2(s)}{I_1(s)} = \frac{N_1}{N_2} \frac{s\tau}{1 + s\tau}. \quad (7.7)$$

The expression of the flux ϕ in the frequency domain is obtained from (7.1) and (7.7):

$$\begin{aligned} \Phi(s) &= \Lambda_g(N_1 I_1 - N_2 I_2) \\ &= N_1 \Lambda_g \left(1 - \frac{N_2}{N_1} \frac{I_2}{I_1} \right) I_1 \\ &= N_1 \Lambda_g \left(\frac{1}{1 + s\tau} \right) I_1. \end{aligned} \quad (7.8)$$

The Hall-effect element measures the DC to low frequency components of the current i_1 . It uses the magnetic flux density B , defined as

$$B(s) = \frac{\Phi}{A} \quad (7.9)$$

generated by the current i_1 , to deflect an *internal* current flowing through a conductor, thus developing a transversal potential. The output voltage signal of the Hall-effect element V_H is thus proportional to B through the sensitivity S_{Hall} , measured in V/T, and is given by

$$V_H = S_{Hall} B. \quad (7.10)$$

The Transfer Function (TF) of the Hall captor V_H/I_1 can finally be derived by substituting (7.8) and (7.9) in (7.10) and assuming $N_1=1$:

$$\begin{aligned} \frac{V_H}{I_1} &= \frac{\mu_0}{\delta} S_{Hall} \left(\frac{1}{1 + s\tau} \right) \\ &= k_H \left(\frac{1}{1 + s\tau} \right). \end{aligned} \quad (7.11)$$

On the other side, the TF of the current transformer V_L/I_1 is derived by (7.4):

$$\begin{aligned} \frac{V_L}{I_1} &= \frac{R_L}{N_2} \frac{s\tau}{1 + s\tau} \\ &= k_L \frac{s\tau}{1 + s\tau}. \end{aligned} \quad (7.12)$$

Let observe that (7.11) is a low pass function and the (7.12) a high pass function having the same corner frequency as depicted in Fig. 7.4.

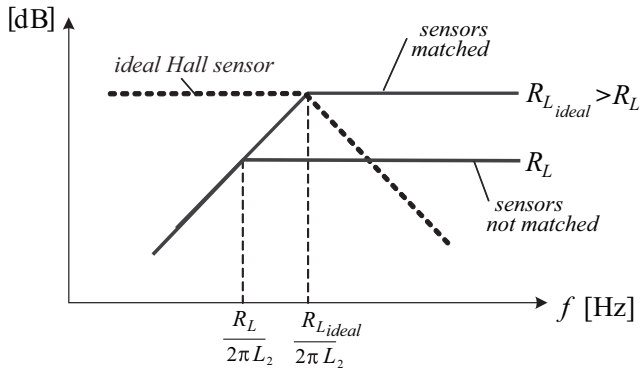


Figure 7.4: Resulting transfer function of the proposed transducer. The matching between the two sensors is achieved by using an opportune value of the transformer’s load resistor R_L (7.15).

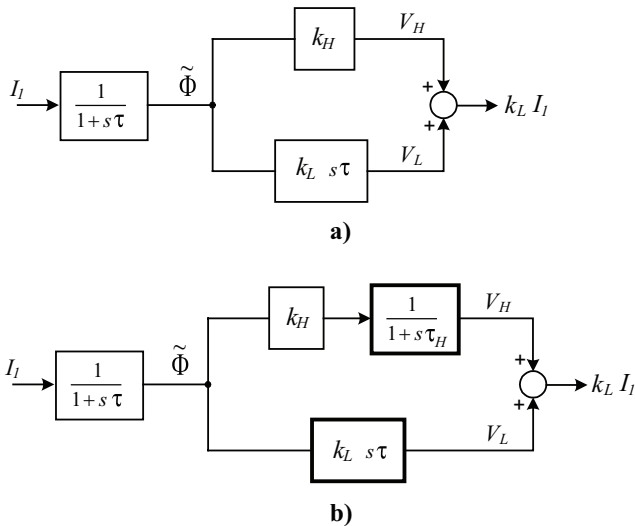
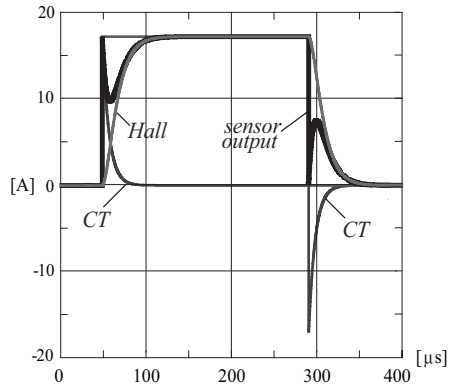
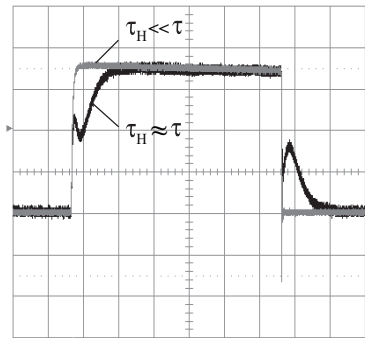


Figure 7.5: Block diagrams explaining the functioning of the proposed current sensor in the frequency domain when $k_H = k_L$: a) ideal and b) real operating.



a)



b)

Figure 7.6: Sensor components that contribute to the formation of the current step; operating principle according to Fig. 7.5b. The sum between the Hall captor and the CT output signals does not reproduce properly the step because $\tau_H \approx \tau$: a) simulation and b) measurement.

In the proposed current sensor the output signal is provided by

$$V_{out} = V_L + V_H \quad (7.13)$$

and these voltages are summed without using process electronics (cf. Fig. 7.1d). If the gain values of the sensor components are designed to be equal, then the

overall transfer function of the sensor, provided by the sum of (7.11) and (7.12) is a flat response over the entire frequency band (cf. Fig. 7.4). Constraining the gain of each of the two transfer functions to be equal in value yields

$$\frac{R_L}{N_2} \equiv \frac{\mu_0}{\delta} S_{Hall} \quad (7.14)$$

If the parameters N_2 , S_{Hall} and δ have already been selected, then the value of the load resistance R_L has to be chosen such that:

$$R_L = \frac{N_2 \mu_0 S_{Hall}}{\delta} \quad [\Omega] \quad (7.15)$$

In Fig. 7.5a the block diagram that explains the functioning of the sensor is shown. There, a quantity proportional to the flux $\tilde{\Phi}$ drives both the Hall-effect element and the current transformer, whose output signals, V_H and V_L , are summed to provide in output a constant gain equal to

$$V_{out} = k_L I_1. \quad (7.16)$$

7.2.2 Real Sensor

The ideal functioning of the sensor has been derived under the assumption of constant sensitivity of the Hall captor (7.10). Actually, the Hall sensor is better characterized by a low pass function as:

$$V_H = \frac{S_{Hall}}{1 + s\tau_H} B. \quad (7.17)$$

where τ_H is the time constant of the device. The block diagram that describes the real functioning of the sensor is depicted in Fig. 7.5b. If the Hall element corner frequency f_H ,

$$f_H = \frac{1}{2\pi\tau_H} \quad (7.18)$$

is at least one decade larger than the CT's lower corner frequency f given by

$$f = \frac{1}{2\pi\tau} = \frac{R_L}{2\pi} \frac{\delta}{\mu_0 N_2^2 A} \quad (7.19)$$

such that the condition

$$f_H \gg f \quad (7.20)$$

is verified, then matching between the output signals of Hall element and CT occurs correctly, similar to the matching behavior presented in [204]. Equation (7.20) ensures that the Hall-element operates in the linear part of its characteristic curve and that no further attenuation occurs by the matching point.

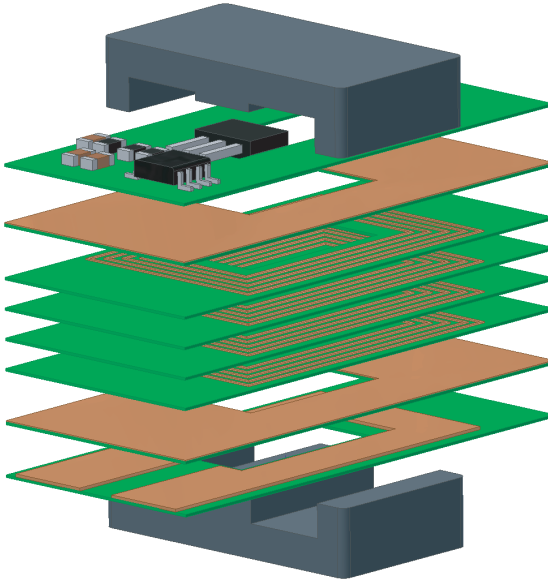


Figure 7.7: Exploded drawing of the DC planar-CT indicating the placement of the layers.

In case

$$\tau_H \approx \tau \quad (7.21)$$

then the Hall captor output signal is affected by delay, as shown in the simulation in Fig. 7.6a and in the measurement Fig. 7.6b, and the sum between the signal components of Hall and CT does not reproduce properly the current step. Therefore, the values of R_L and L_2 must be selected carefully to obtain a corner frequency f sufficiently smaller than f_H .

Moreover, the parameters $L_{\sigma 2}$ and R_2 affect the real operation of the sensor and it is opportune to include them in the design and model. Although a planar transformer shows a smaller leakage inductance than a toroidal device, the $L_{\sigma 2}$ plays an increasing role at high frequency and it determines with the winding self capacitance C the upper bandwidth limit of the transformer. The value of winding resistance R_2 is dependent on the cross-section of the secondary turns; although a compact secondary coil is desirable to obtain a small device, a larger wire cross section ensures a lower winding resistance, hence a lower corner frequency f , (7.19).

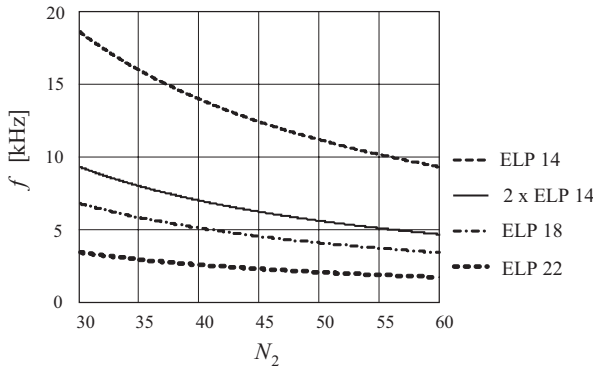


Figure 7.8: Dependency of the planar CTs' lower corner frequency f according to (7.19) on the number N_2 of secondary turns for different ELP cores.

In [191] a high-frequency permeance based model of the CT was presented. Here, since the matching between the transfer functions (TF) of the two sensor components occurs in the kHz range, the presented low-frequency model of the transformer is suitable for analyzing the proposed signal matching. Accordingly, skin and proximity effects in the windings, rotational magnetic losses and the secondary winding self capacitance have been neglected.

7.3 Realization of the Prototype

A toroidal prototype of the proposed current sensor was shown in [191]. The device was made out of a toroidal gapped magnetic core and a Hall element positioned in the air gap. An electric screen between the primary was used to split the interwinding capacitance and to decrease the value of the leakage inductance [205]. The choice of the planar shape rather than the toroidal one leads to a significant improvement of the frequency behavior of the device and brings with it the following advantages while still retaining all the features of the toroidal prototype:

1. a low profile;
2. an embedded primary conductor in the component, and better control over parasitics;
3. better manufacturability;

7.3. REALIZATION OF THE PROTOTYPE

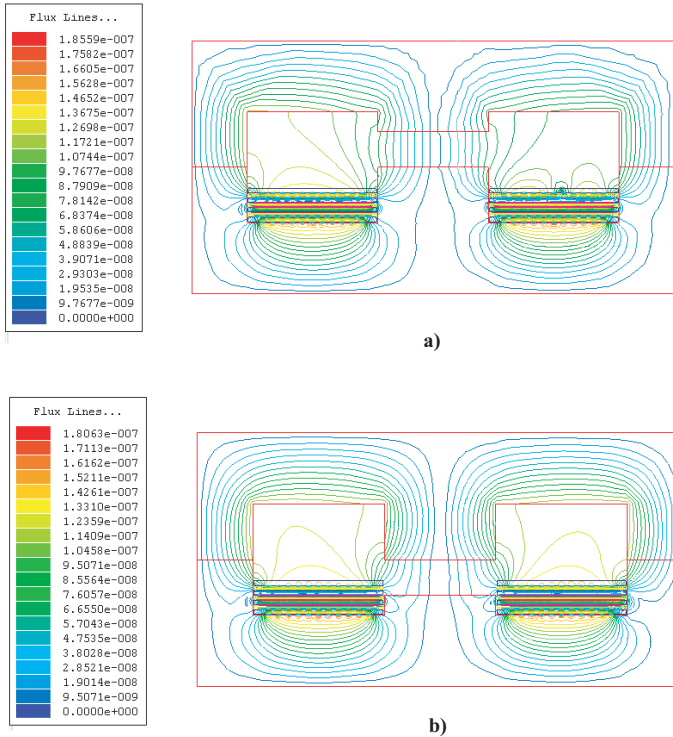


Figure 7.9: Magnetic flux lines distribution within the core for a frequency of 1 kHz. This frequency corresponds to the end of the operating region of the Hall element and the beginning of the transformer's one. It is important that the flux lines are linked with the Hall-effect element and remain within the air gap. Therefore the solution a) of having the air gap far from the winding-PCB layer is more convenient than having the air gap aligned with the winding PCB b).

4. the ability to integrate all the main parts, i.e. windings, EM screens, process electronics into a compact and mechanically robust device;
5. higher frequency bandwidth.

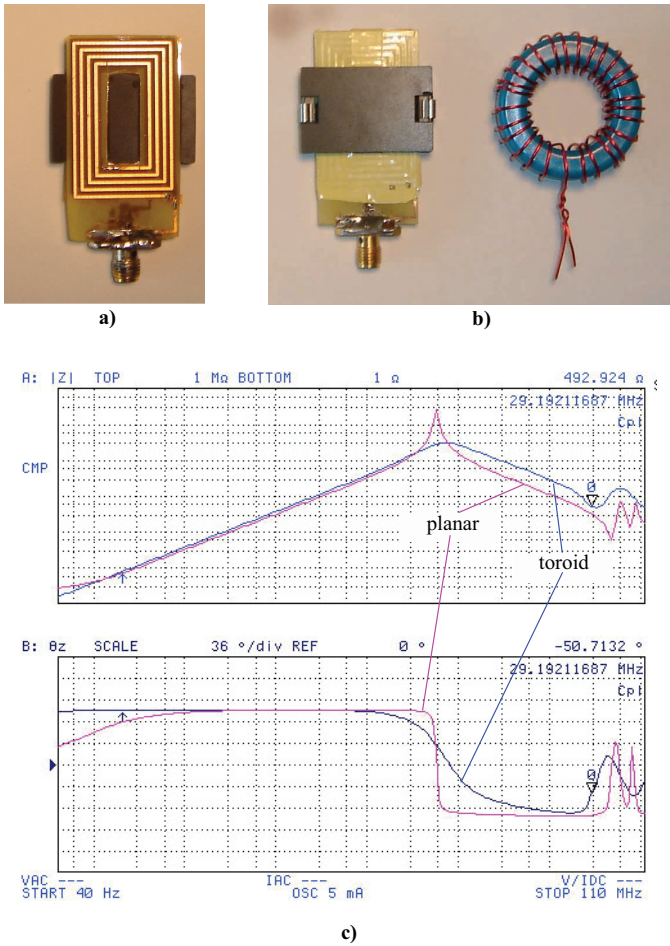


Figure 7.10: Planar and toroidal current transformer prototypes. a) Particular of the winding of a planar ELP current transformer, b) devices having the same magnetizing inductance and c) the measurement of their impedance, showing the same inductance, but a higher stray capacitance for the planar prototype.

With these aims in mind, a planar magnetic core in combination with an eight-layers PCB was built: four layers host the secondary coil of 45 turns, one layer

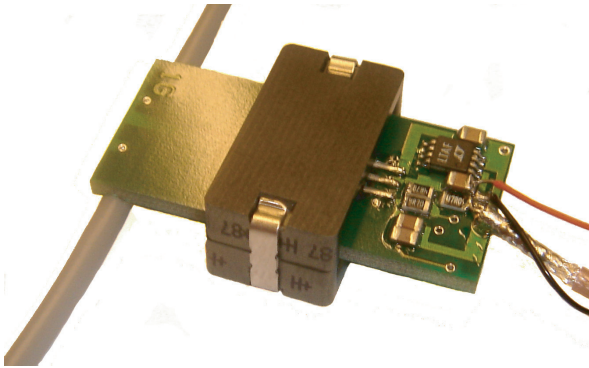


Figure 7.11: Photograph of the proposed DC planar-CT featuring a planar ELP18 core.

for the primary, one for the output stage electronics, and the remaining two layers for ground plane and screen. An exploded view of the sensor structure is shown in Fig. 7.7. The core consists of two E-cores with an air gap of 1.4 mm. In order to design a sufficiently compact planar prototype, the smallest commercial ELP ferrite cores were selected [132]. They are ELP14, ELP18 and ELP22. To reduce the parasitics associated with the windings and to decrease the number of layers of the PCB, the number of secondary turns was selected to be the minimum possible for proper sensor operation. For this aim, the value of the corner frequency f has been calculated as a function of the number N_2 of secondary turns for four different planar cores. The results of the calculations are shown in the curves of Fig. 7.8. Since a sufficiently large value of the inductance L_2 is desired in order to fulfill (7.20), the solution of taking two ELP14 cores has also been considered. An Allegro A3515 Hall element [197] was chosen for its linear characteristic up to 30 kHz. Therefore only two cores, ELP18 and ELP22, with a number of turns larger than 40 fulfill (7.20) and present lower corner frequencies below 5 kHz. Moreover, it is important that the flux lines link the Hall element and remain within the cross-section of the air gap until the CT start working within the linear part of its frequency characteristic: this was verified by FEM simulations shown in Fig. 7.9. On the basis of these considerations, 18 different prototypes were built, with different combinations of winding strategies and layers arrangements. A photograph of the proposed DC planar-CT that features a ELP18 planar core is shown in Fig. 7.11.



Figure 7.12: Current step response experimental setup

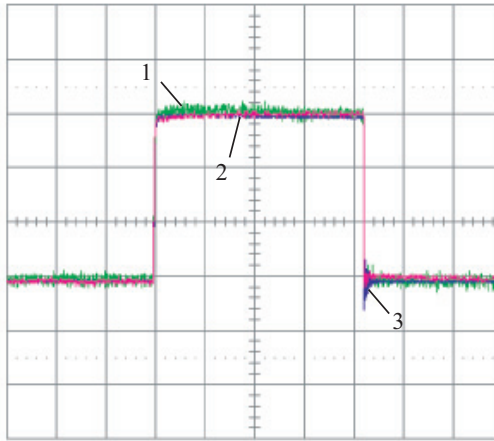
7.4 Experimental Results

7.4.1 Current Step Response

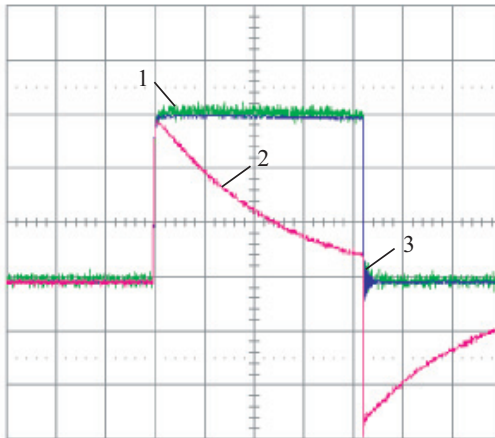
A rectangular shaped current waveform contains more harmonic components than other waveforms, for instance a triangular one, and is therefore a very effective test for a current sensor. The current step response of the proposed planar DC CT was compared with three other wide-bandwidth devices: a Tektronix A6312 probe (100 MHz), a Shunt LEM 25/10 (10 MHz) and a HOKA Probe (50 MHz) [199]. The experimental setup is described in [204]. The measurement results are shown in Figs. 7.13-7.16, and the performance of the proposed sensor compares equally well to the other more expensive and well established current transducers. The high upper bandwidth limit of the CT, measured 30 MHz according to the procedure presented in [191], allows faithful reproduction of the rising and falling edges of the current step (cf. Figs. 7.13-7.17) while the Hall-element detects the stationary edges of the signal.

7.4.2 Core Saturation

A closed loop implementation of the sensor ensures that the magnetic core saturates at higher rating of primary current than an open loop architecture. For a closed loop sensor, the magnetic field in the core is compensated by the feedback action of the DC to low frequency sensor whose output signal is injected

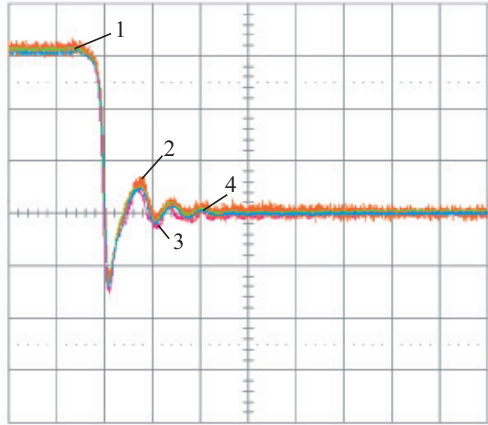


a)

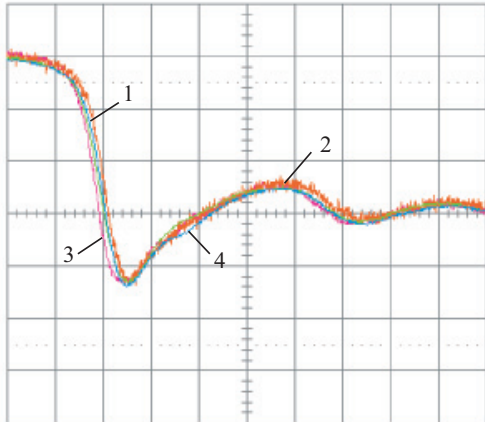


b)

Figure 7.13: a) Current step response where the sensors are respectively: 1) Shunt LEM 25/10, 2) proposed DC planar-CT current sensor, 3) Tektronix A6312 Probe. Vertical scale: 5 A/div, time scale: 50 μs /div. In b) the Hall sensor signal is not present; only the planar current transformer is sensing.



a)



b)

Figure 7.14: Current step response where the sensors are respectively: 1) Shunt LEM 25/10, 2) Tektronix A6312, 3) proposed DC planar-CT current sensor, 4) HOKA sensor [199]. Vertical scale 5 A/div, time scale: a) 0.5 μs/div, b) 0.1 μs/div. Furthermore b) shows 20 ns delay of the Tektronix probe.

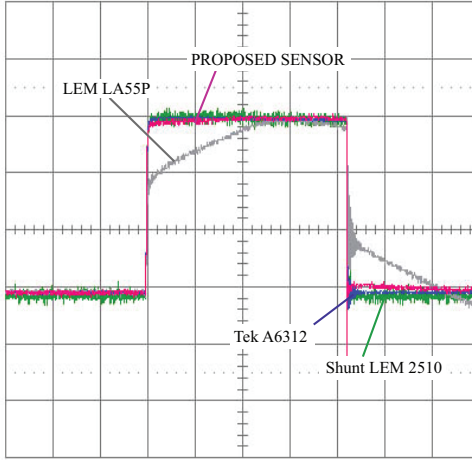


Figure 7.15: Current step response. Vertical scale 5 A/div, time scale: 0.5 $\mu\text{s}/\text{div}$.

in the secondary winding to oppose the primary MMF (cf. Fig. 7.1b). If the primary current i_1 is stationary (DC) or not sufficiently compensated by the effect of the secondary current, there is no flux rate, hence the CT is inhibited and does not provide any output signal.

An issue for the proposed sensor is the saturation of the magnetic core, since no compensation loop is implemented. However, the quite large air-gap, necessitated by the physical dimensions of the Hall element, reduces the effects of the non linear magnetic characteristic of the core and stabilizes the value of the inductance L_{m1} . This latter becomes less dependent from the core parameters, (5.9), and decreases in value, because the equivalent permeability of the gapped system is smaller than the core permeability.

Since the volt-seconds necessary to saturate a magnetic circuit (starting from $B = 0$) are

$$\begin{aligned}\varphi_S &= N_1 B_S A \\ &= L_{m1} i_S,\end{aligned}\tag{7.22}$$

increasing the air-gap length reduces the inductance value according to (5.8) and (5.9), whereas the current i_S , for which saturation occurs, increases. φ_S and

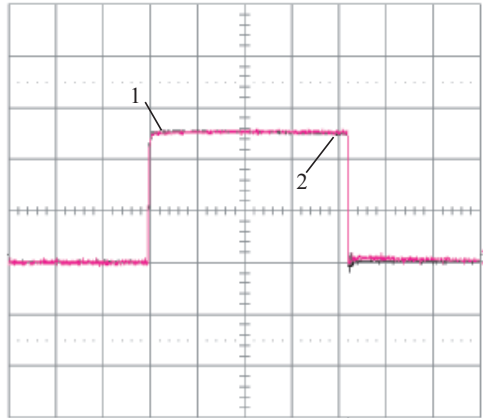


Figure 7.16: Current step response where the sensors are respectively: 1) proposed DC planar-CT current sensor, 2) 1 Shunt LEM 25/10. Vertical scale: 20 A/div, time scale: 50 μ s/div.

B_S indicate saturation flux and induction, respectively. Fig. 7.16 shows a 0.2 ms current step of 50 A in amplitude; the sensor is able to measure such current steps. By means of similar tests, an excellent linear behavior has been registered up to 40 A DC.

7.4.3 dv/dt Immunity Test

The interwinding capacitance of the CT couples the primary and secondary windings. Whenever there is a high dv/dt in the primary or near the secondary, the disturbance is transferred to the secondary in the form of a common mode current. This disturbance can also appear, if the current sensor is placed closely to a fast switching MOSFET: the sensor is stressed with severe dv/dt . In this case v represents the drain to source voltage. One measurement result of dv/dt immunity is shown in Fig. 7.18. The measurement setup adopted to produce the voltage step was similar to the one used to generate the current step. However, a faster switching FET was used and a series connection of resistors of total 3 k Ω was inserted in the primary to reduce the flowing current in the primary to nearly zero as well as the stray capacitance of the resistors. In this way, the current measured by the sensors under test was just due to the parasitic capacitances that couple the transients dv/dt into the output of the sensor. The

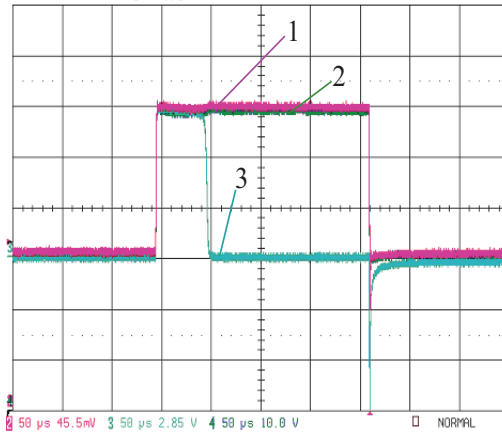


Figure 7.17: Current step response where the sensors are respectively: 1) proposed DC planar-CT current sensor, 2) Tektronix A6312 current probe and 3) Pearson. Vertical scale: 5 A/div, time scale: 0.5 $\mu\text{s}/\text{div}$.

distortion registered in output of the proposed sensor for 16 $\text{kV}/\mu\text{s}$ voltage rate is comparable to the performance of a Tektronix A6312 used as reference device (cf Fig. 7.18).

7.5 Conclusion

This chapter has presented a novel isolated current sensor made out of the combination of a Hall-effect element, positioned in the air gap of the magnetic structure, and a planar current transformer with a multilayer PCB winding. The Hall captor is sensitive to the DC to low frequency components of the measured current, whereas the higher frequencies, to which the Hall sensor is insensitive, are detected magnetically by the CT. The matching between the Hall element and the CT is performed without electronic stage.

The functioning has been explained analytically by means of a permeance model of the transformer. This model allows access to the flux, flux rate and MMF besides the electrical quantities. Furthermore, it allows time and frequency simulations on electrical network simulators of electro-magnetic networks; it allows implementation of frequency dependent components, complex permeability and direct core losses extraction.

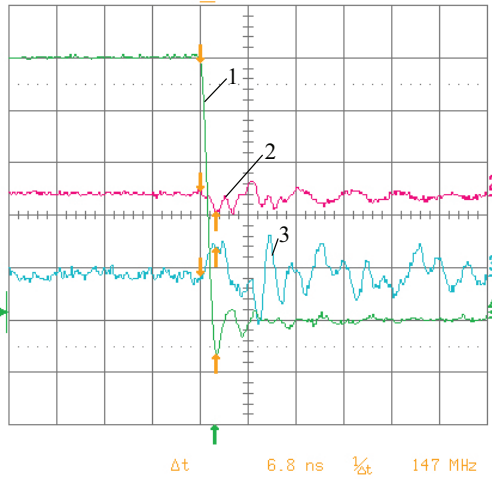


Figure 7.18: dv/dt immunity test. 1) voltage step (16 kV/ μ s), 2) proposed DC planar-CT current sensor, 3) Tektronix A6312. Time scale: 20 ns/div; voltage scale: 20 V/div; current scale 0.5 A/div.

Simulations and FEM results have been presented for verification.

It has been shown that the appropriate dimensioning of the magnetic system, and especially the accurate selection of the corner frequency f of the CT transfer function is important to grant the correct functioning of the sensor.

The choice of the planar magnetic structure led to the following advantages, while still retaining all the features of a former toroidal prototype [191]: higher frequency bandwidth, low profile, better manufacturability and compatibility with integration processes.

Furthermore, a planar prototype has been shown and the following features have been verified experimentally: frequency bandwidth from DC up to 30 MHz, high current rating (40 A DC), superior linearity, high immunity against dv/dt transients.

All these performances, in particular accuracy and low realization cost, comply with the requirements necessary for the application of the sensor within the latest generation of converters and drives.

Chapter 8

Conclusion

8.1 Dissertation Summary

In Chapter 2, a novel hysteresis current control concept for three-phase three-level PWM rectifiers is presented. The proposed control is based on a virtual connection of the output center point and the mains star point and achieves a decoupling of the three phases. This control technique, besides having the advantages of a classical hysteresis control, provides a more regular switching of the power transistors and an intrinsic stability of the output center point voltage, and allows a full utilization of the modulation range. The novel control concept is discussed and compared to conventional current control techniques. The current control is digitally implemented and experimental results for controlling a Vienna Rectifier are presented. Furthermore, a pre-control signal for the hysteresis band is implemented to obtain coordinated switching between the phases and results in a near constant switching frequency and a current ripple performance that is similar to conventional carrier-based PWM controllers. Theoretical analysis of the control method is presented and the performance of the phase decoupling is experimentally verified.

In Chapter 3 deals with the center-point voltage balancing issue for three-level converter topologies. The balancing of the output center-point voltage of a hysteresis current-controlled three-level PWM rectifier is realized by adding an offset to the input current-reference. It is shown that the strategy of augmenting the current reference by an offset in direct (hysteresis) modulated three-level rectifiers is equivalent to the utilization of the redundant switching-states in indirect (voltage-oriented) PWM modulation. The main characteristics of direct and indirect current-control methods for three-phase active rectifiers are

presented, with particular emphasis on the degree-of-freedom one can use to balance the center-point in three-level topologies. The space-vector representation of the input rectifier voltage and current is chosen to explain the effect of the current offset injection on the output center-point voltage. The influence of the current offset injection on the mains currents as well as the control and center-point characteristics are analyzed and verified by measurements. Finally, the design of the center-point controller is presented and its dynamic performance is experimentally demonstrated.

In Chapter 4, the implementation and experimental verification of two discontinuous pulse-width modulation (DPWM) methods for three-phase, three-level rectifiers are presented. DPWM's features, such as improved waveform quality, lower switching losses and reduced AC-side passive component size, are investigated and compared to the conventional continuous pulse-width modulation (CPWM). These features allow higher power density and/or efficiency to be achieved and are important targets for the next generation of power rectifiers. The implementation of the two DPWM strategies is explained by means of space-vectors representation and modulation functions. A detailed analysis of both AC-side and DC-side current waveforms is presented, and there is excellent agreement between the analytical, simulated and experimental results for the mains current ripple amplitude and output center point current over the practical modulation range. Finally, the control of the center point voltage is discussed.

In Chapter 5, the frequency dependent characteristics of a gapped toroidal structure are extracted empirically over a bandwidth that exceeds 30 MHz. The analysis is complicated due to non-linear flux distributions, magnetic properties of the core material, leakage inductance, stray capacitances and eddy currents in the windings. A permeance model of the core is implemented to model the magnetic circuit. The model includes a linear lumped element equivalent circuit to approximate the non-linear complex permeability of the core, which was measured empirically. Stray capacitance and inductance of the winding are also modeled. A gyrator is used to couple the electric and magnetic models for circuit simulation. The measured and simulated results of open-circuit impedance from the secondary winding and the transimpedance gain (V/A) of the current sensor are compared and discussed. The Chapter deals also with the high frequency characterization of ferrite material. The flux distribution within the ferrite is modeled using the electromagnetic wave propagation theory and the dimensional resonance effect is explained. Derivations for the losses in the core and in the winding are included in the Chapter. A review of the literature dealing with the calculation of the frequency-dependent winding resistance is presented and the winding impedance for the case-study is calculated by a modified Dowell formula.

Chapter 6 deals with the electrostatic analysis of wound ferrite components, and a particularly complex architecture, the high-voltage transformer, is selected to analyze with a broad perspective, the electric field distributions. The calculation of transformer's parasitics, in particular of its self capacitance, is fundamental for predicting the frequency behavior of the device, to reduce the capacitance's value and moreover for more advanced aims of capacitance integration and cancellation. The chapter presents a comprehensive procedure for calculating all contributions to the self-capacitance of high-voltage transformers and provides a detailed analysis of the problem, based on a physical approach. The advantages of the analytical formulation of the problem rather than a finite element method analysis are discussed. The approach and formulas presented have general validity and can be used for other wound components rather than just step up transformers. Analytical and experimental results are presented for three different high-voltage transformer architectures.

Chapter 7 presents a novel, planar current sensor, comprised of a magnetic current transformer and a Hall-effect element. The sensor has a broad frequency bandwidth from DC up to 30 MHz, a high current rating (40 A DC), superior linearity, high EMI immunity, small size, robustness and low realization cost. The main design formulae are given; simulations and finite element results are presented for verification. Experimental results of current step response and dv/dt immunity are included.

8.2 Dissertation Conclusion

The main advantage of the Decoupling Hysteresis Control (DHC) for three-level PWM rectifiers is to eliminate the phase interaction and stabilize the switching frequency. This is achieved by injecting a zero-sequence signal at a control level or, specifically, by augmenting the current reference by a zero-sequence current that would circulate if the mains star point and the rectifier output center-point are connected. Since the connection between the mains star point and the rectifier output center-point is only virtually established, the zero sequence voltage between these two points can be used as a degree of freedom in the modulation, and can be shaped suitably in order to extend, for instance, the modulation range. The decoupling signal injection to stabilize the switching frequency of hysteresis current controllers, has also been successfully combined with a virtual flux based reference current generation method for use in grid connected inverters [206, 207]. Furthermore, the technique of synchronization of the switching pulses around a common clock reference frequency for the DHC has the advantage that the waveform quality is similar to the conventional carrier based current controller.

The center-point voltage control for three-level rectifiers has been achieved by augmenting the current reference value by a common offset, which has a loading effect on the center-point. The essential advantages of the control concept are (1) the very straightforward realizability by practical circuits and (2) the possibility of a direct inclusion into a high-dynamic (analog) hysteresis control of the mains current. Therefore, the method can be applied also for low-power rectifier systems and for systems with switching frequencies greater than 100 kHz.

For practical realization of the current control of three-level rectifier, discontinuous modulation is preferred over continuous modulation, especially if high power density and/or low filtering effort and/or small size of the AC-side passive components are required. Since the advantages of the discontinuous modulation are recognized for higher modulation indices, it may be a good strategy to swap between different modulation strategies according to rectifier's operating point, thus realizing a high-performance adaptive modulation algorithm [108, 103].

In order to predict and reproduce the impedance and the transimpedance frequency characteristics of the current sensor, a transformer model based on the permeance-capacitance analogy [191, 137] has been introduced in the Dissertation. This model presents numerous advantages, such as (1) the implementation of frequency dependent components and complex permeability; (2) the simulation of a magnetic network by an electrical circuit; (3) it allows access to the flux rate and the magneto-motive force; (4) geometry and number of turns are included in the model; (5) since a resistance element in the permeance model represents core losses (unlike the conventional magnetic reluctance model where resistance represents energy storage), core losses could be also extracted using this method [126].

The upper bandwidth limit of the study-case, constituted by the gapped current transformer, is mostly dependent on the winding impedances, in particular the stray winding capacitances [165], and this was also verified by measurements.

The two factors that are responsible for the error in the parasitic capacitance calculation are: the distance d between layers of turns and the turns arrangement, either aligned or orthocyclic.

The proposed calculation procedure for determining the self-capacitance of wound components is important from a practical standpoint for three different purposes: (1) reducing the capacitance value and hence the dielectric losses (by modifying for instance the winding arrangement); (2) using the self capacitance of the transformer as an effective circuital parameter (integration); (3) applying a strategy of capacitance cancellation, that already succeeded for other two port devices [198].

The proposed planar current sensor has a commercial potential in virtue of the following experimentally verified performance: frequency bandwidth from DC up to 30 MHz, high current rating (40 A DC), superior linearity, high immunity against dv/dt transients.

All these performance measures, in particular accuracy and low realization cost, comply with the requirements necessary for the application of the sensor within the latest generation of converters and drives.

8.3 Recommendations for Future Work

The limitations for the digital implementation of a modulation method in an industrial rectifier system are dictated by the computation capability of the presently available Digital Signal Processors (DSPs). The increase of the switching frequency, which is the traditional approach to increase the power density and to improve the dynamic performance of the controller, is possible but limited by the speed of the DSP. The modulation strategies implemented in this Dissertation have been using an Analog Devices ADSP-21991 DSP, which is specified as a 160 MIPS processor. The implemented software (non-optimized) leads to an upper switching frequency of 25 kHz for the implementation of the Space Vector Modulation for the three-level rectifier. Therefore, the optimization of the code for a more efficient utilization of the computation capability of the DSP should be undertaken.

There are applications that require a high switching frequency, such as rectifiers in modern aircraft. The rectifiers are currently implemented using multi-pulse passive rectifier circuits. The trend is to increase the power density and lower the weight of the future more-electric-aircraft and therefore the active rectification will have an increasing importance. The modern aircraft now operate with a mains fundamental frequency that has a range from 360 to 800 Hz. The standards require that the current quality is assessed up to the 61st harmonic. Therefore, the active rectifier requires a switching frequency in the order of 100kHz and a current controller bandwidth of at least 50 kHz. Therefore, high performance current controllers are necessary and an investigation into the applicability of the controllers presented in this Dissertation should be undertaken for these new aircraft applications.

An alternative to the conventional Space Vector Modulation is represented by a direct modulation strategy, such as the presented Decoupling Hysteresis Control, which has an excellent dynamic performance. Further research can be addressed to improve the harmonic impact of hysteresis-based modulation strategies and to stabilize the switching frequency.

The performance and accuracy of the hysteresis current controller is de-

pendent on the accuracy of the current sensor. Further research is necessary to develop prototypes of the current sensors with better EMI performance and with a simple layout and easy to reproduce characteristics.

The thermal dependence, the linearity, the offset compensation and the current derating characteristics are all aspects of the design, especially for magnetic core based current sensor architectures, that need further investigations.

Appendix

A.1 Switch Signal and Input Rectifier Voltage for the First Sector

Fig. 8.1 shows the switch gate signals of the *Vienna* rectifier for the first sector.

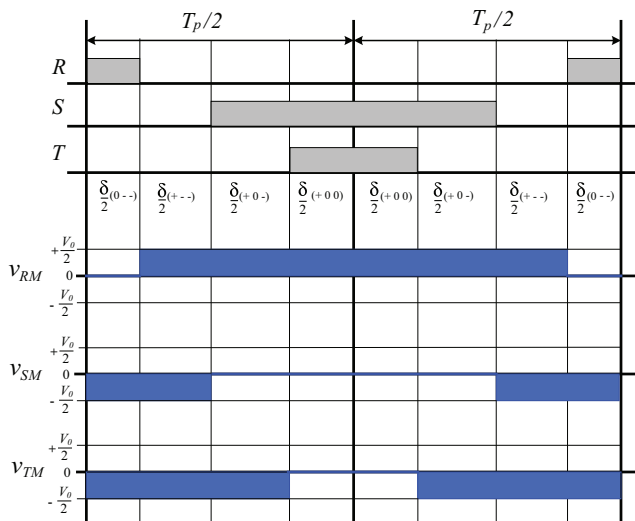


Figure 8.1: *Vienna* Rectifier switch gate signals and rectifier input voltages for one switching period T_p in the first sector.

From the switching pattern and the duty cycles of the applied vectors, the input rectifier to center point average voltages are shown and are given by

$$\begin{aligned}
 v_{RM} &= \frac{1}{2}V_o(1 - \delta_{(0--)}) \\
 v_{SM} &= -\frac{1}{2}V_o(\delta_{(0--)} + \delta_{(+-)}) \\
 v_{TM} &= -\frac{1}{2}V_o(1 - \delta_{(+00)}).
 \end{aligned} \tag{8.1}$$

A.2 Space Vectors Duty Cycle Calculation for the First Sector

The sector border angles φ_1 and φ_2 shown in Fig. 8.2 are dependent on the modulation index M and defined as

$$\begin{aligned}
 \varphi_1 &= \frac{\pi}{3} - \varphi_2 \\
 \varphi_2 &= \arcsin \frac{1}{\sqrt{3}M}
 \end{aligned} \tag{8.2}$$

The voltage reference phasor V^* is given by the time average over one switching period T_p of the space vectors available in Sector 1

$$\begin{aligned}
 V^*(\varphi) &= \delta_{(0--)}v_{(0--)} + \delta_{(+-)}v_{(+-)} \\
 &+ \delta_{(+0-)}v_{(+0-)} + \delta_{(+00)}v_{(+00)}.
 \end{aligned} \tag{8.3}$$

where in the first sector the space vectors are

$$\begin{aligned}
 v_{(0--)} &\equiv v_{(+00)} = \frac{1}{3}V_0 \\
 v_{(+-)} &= \frac{2}{3}V_0 \\
 v_{(+0-)} &= \frac{1}{\sqrt{3}}V_0 e^{j\frac{\pi}{6}}
 \end{aligned} \tag{8.4}$$

and the duty cycles in a switching period T_P add up to unity

$$1 = \delta_{(0--)} + \delta_{(+-)} + \delta_{(+0-)} + \delta_{(+00)}. \tag{8.5}$$

A complex modulation index is defined as

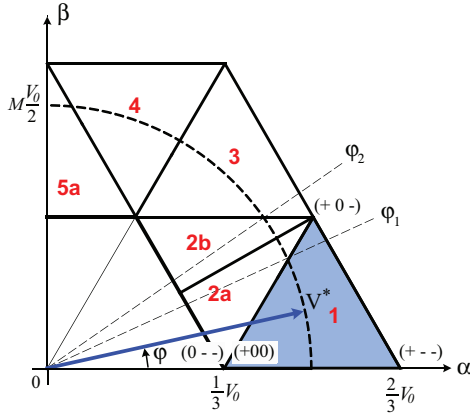


Figure 8.2: Representation of the M dependent border angles φ_1 and φ_2 between two sectors and, in particular, of the space vectors available in sector 1.

$$\frac{V^*}{\frac{1}{2}V_0} = m_\alpha + jm_\beta \quad (8.6)$$

By replacing (8.4) in (8.3) and considering (8.5) and (8.6) it follows that the real and imaginary parts of the complex modulation function are given by:

$$m_\alpha = 1 + \frac{1}{3}\delta_{(+--)} - \frac{1}{3}\delta_\rho \quad (8.7)$$

$$m_\beta = \frac{1}{\sqrt{3}}\delta_{(+0-)} \quad (8.8)$$

where $\delta_\rho = \delta_{(0--)} + \delta_{(+00)}$. Hence the space vectors duty cycle for the Sector 1 can be expressed as a function of the modulation index as

$$\begin{pmatrix} \delta_\rho \\ \delta_{(+--)} \\ \delta_{(+0-)} \end{pmatrix} = \begin{pmatrix} 2 & -1 & -1 \\ -1 & 1 & -1 \\ 0 & 0 & -2 \end{pmatrix} \tilde{m} \quad (8.9)$$

where

$$\tilde{m} = \begin{pmatrix} 1 \\ \frac{3}{2}m_\alpha \\ \frac{\sqrt{3}}{2}m_\beta \end{pmatrix} = \begin{pmatrix} 1 \\ \frac{3}{2}M\cos\varphi \\ \frac{\sqrt{3}}{2}M\sin\varphi \end{pmatrix}. \quad (8.10)$$

The expression of the duty cycles as a function of the modulation index, exemplarily shown for the first sector, is the basis for the calculation of the current ripple (4.25)-(4.27) as well as of the capacitor current (4.31), calculated in Appendix D.

A.3 Switching Loss Calculation

Assuming sinusoidal mains currents, the switching losses are defined as

$$P_T = \frac{1}{\pi} \int_0^\pi f_P k_f |i(\varphi)| d\varphi. \quad (8.11)$$

For CPWM, with $\rho = 0.5$, the switching occurs continuously over the entire fundamental period $[0, 2\pi]$. The product $k_f |i(\varphi)|$ relevant for the switching losses in CPWM is plotted in Fig. 8.3a for the phase R and is normalized by $k_f f_P \hat{I}$. The losses can be calculated integrating the function $k_f |i(\varphi)|$ according to (8.11) and setting the appropriate integration intervals, resulting in (4.21). Observe that for DPWMA the phase switches are clamped over defined intervals, hence the switching losses are zero and therefore $k_f = 0$. The resulting product $k_f |i(\varphi)|$ is shown in Fig. 8.3b for DPWMA and $M = 0.8$. For DPWMA the section angles (8.2) defining the clamping intervals are dependent on M . For DPWMB the clamping intervals are different than for DPWMA and independent of M . The function $k_f |i(\varphi)|$ for DPWMB is shown in Fig. 8.3c. Therefore contrary to DPWMA, the factor of possible frequency increase for DPWMB is independent of M (4.23)-(4.24).

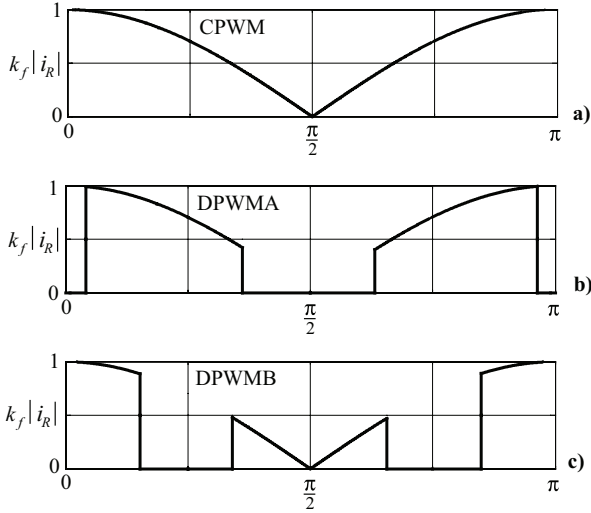


Figure 8.3: Normalized functions $k_f|i(\varphi)|$ relevant for the calculation of the switching losses represented over half mains period for a) CPWM, b) DPWMA and c) DPWMB. The function $k_f|i(\varphi)|$ for DPWMA is represented for $M = 0.8$ and the clamping intervals are dependent on M according to (8.2).

A.4 Output Capacitors RMS Current

The average value over a switching period of the current $i_{+,avg}$ in the positive bus bar within the interval $[0, \frac{\pi}{3}]$ can be defined as a function of ρ_- (4.14) and for Sectors 1, 2a, 2b and 3 as follows

$$\begin{aligned}
 i_{+,avg,1}(\varphi) &= (\delta_{(+--)} + \delta_{(+0-)} + \rho_-(\delta_{(+00)} + \delta_{(0--)}))i_R \\
 i_{+,avg,2a}(\varphi) &= (\delta_{(+0-)} + \rho_-\delta_{(+00)} + \delta_{(0--)})i_R \\
 i_{+,avg,2b}(\varphi) &= (\delta_{(+0-)} + \delta_{(0--)})i_R \\
 &\quad + \rho_-(\delta_{(++0)} + \delta_{(00-)})(i_R + i_S) \\
 i_{+,avg,3}(\varphi) &= \delta_{(+0-)}i_R \\
 &\quad + (\delta_{(+++)} + \rho_-(\delta_{(++0)} + \delta_{(00-)}))(i_R + i_S)
 \end{aligned} \tag{8.12}$$

where the method to calculate the space vectors duty cycles is shown in Appendix 8.3. The integration of the currents (8.12) gives the global average of the current in the positive bus bar. If the distribution ρ_- is set according to the scheme DPWMA , then

$$\begin{aligned}
 I_{+,avg,DPWMA} = & \frac{1}{\frac{\pi}{3}} \left(\int_0^{\varphi_1} |i_{+,avg,1}(\varphi)|_{\rho=1} d\varphi \right. \\
 & + \int_{\varphi_1}^{\frac{\pi}{6}} |i_{+,avg,2a}(\varphi)|_{\rho=1} d\varphi \\
 & + \int_{\frac{\pi}{6}}^{\varphi_2} |i_{+,avg,2b}(\varphi_N)|_{\rho=0} d\varphi \\
 & \left. + \int_{\varphi_2}^{\frac{\pi}{3}} |i_{+,avg,3}(\varphi)|_{\rho=0} d\varphi \right) \quad (8.13)
 \end{aligned}$$

where φ_1 and φ_2 are defined as shown in Fig. 8.2. In order to calculate the rms-value of the positive bus bar current, the squared values of the currents have to be considered in (8.12) averaged over the switching period. The squared current can be written for each sector in a general form analogous to (8.12), and integrated similar to (8.13) referring to the integration intervals for DPWMA.

Finally, the rms-current into the upper output capacitor (C_+ in Fig. 4.1) can be calculated as

$$I_{C+,rms}^2 = I_{+,rms}^2 - I_{+,avg}^2 \quad (8.14)$$

and this yields to (4.31), which is a result independent of the modulation scheme.

A.5 FEM Formulation in Terms of Weighted Residuals

A general physical problem is expressed by a function $g(x)$, where $x \in \mathbb{R}^n$ and $g \in \mathbb{C}^n$. The dynamics of the problem is described by a partial differential equation

$$Ag(x) - f = 0 \quad (8.15)$$

where A is a linear operator and f is a constant vector. Under the assumption that A is linear, symmetric and positive defined, (8.15) represents the stationary condition of the functional $F(x)$, defined as

$$F(x) = \frac{1}{2} \langle A(g(x)), x \rangle - \langle f, x \rangle \quad (8.16)$$

where $\langle \cdot \rangle$ indicates the spatial average (dot product). The weak form of (8.15) in terms of residual weighted by test functions $h(x)$ is

$$\int_{\Gamma} [A(g(x)) - f] \cdot h(x) dx = 0 \quad \forall \quad h(x) \in \mathbb{R}^n \quad (8.17)$$

Lets take N nodes on the domain Γ and follow the Galerkin's method:

- approximate the problem's solution $g(x)$ in the form:

$$g(x) = \sum_{i=1}^N u_i \Phi_i(x) \quad (8.18)$$

where u_i represent the weights and Φ_i are the shape functions;

- write N equations like (8.17), using the shape functions $\Phi_i(s)$ as test functions:

$$h(x) = \Phi_i \quad i = 1, 2, \dots, N \quad (8.19)$$

There results a system of N algebraic equations in the unknowns u_i , with $i = 1, 2, \dots, N$

$$\langle A(\sum_i u_i \Phi_i) - f, \Phi_i \rangle = 0 \quad (8.20)$$

where $A(\sum_i u_i \Phi_i) - f$ represents the mismatch or error on the equation $A(x) - f = 0$.

By (8.20) the orthogonality between the mismatch and the shape functions is imposed, i.e. the projection of the error in the space of the approximating functions is zero.

The initial problem has been simplified into the solution of a system of N linear algebraic equations in the N unknowns u_i . The crucial steps of this procedures

Appendix

are the creation of the mesh and the choice of suitable shape functions Φ_i .

Bibliography

- [1] T. G. Wilson. The evolution of power electronics. *IEEE Trans. on Power Electronics*, 15(3):439–446, 2000.
- [2] Johann W. Kolar. Lecture notes on power electronics. *Swiss Federal Institute of Technology Zurich*, 2006.
- [3] R. W. Erickson and D. Maksimovic. Fundamentals of power electronics - Second edition. *Kluwer Academic Publisher*, 2001.
- [4] S. Round, M. Heldwein, J. W. Kolar, A. Melkonyan, and I. Hofsjager. A SiC JFET driver for a 5 kW, 150 kHz three-phase PWM converter. *Proc. Industrial Applications Society Conf.*, pages 410–416, 2005.
- [5] V. Caliskan, D. J. Perreault, T. M. Jahns, and J. G. Kassakian. Analysis of three-phase rectifiers with constant-voltage loads. *IEEE Trans. Circuits Systems*, 50(9):1220–1226, Sept. 2003.
- [6] D. J. Perreault, K. K. Afridi, and I. A. Khan. Automotive applications of power electronics. *Power Electronics Handbook- Book Chapter*, pages 791–816, 2001.
- [7] A. R. Prasad, P. D. Ziogas, and S. Manias. An active power factor correction technique for three-phase diode rectifiers. *IEEE Trans. Power Electronics*, 6(1):83–92, Jan. 1991.
- [8] J. W. Kolar, H. Ertl, and F. C. Zach. A comprehensive design approach for a three-phase high frequency single-switch discontinuous-mode boost power factor corrector based on analytically derived normalized converter component ratings. *IEEE Trans. Industry Applications*, 31(3):569–582, May/June 1995.
- [9] M. C. Klaubunde, Y. Zhao, and T. A. Lipo. Current control of a 3-level rectifier/inverter drive system. *Proc. Industry Applications Society Conf.*, pages 859–866, 1994.

BIBLIOGRAPHY

- [10] E. Mehl and I. Barbi. An improved high-power factor and low-cost three phase rectifier. *IEEE Trans. Industry Applications*, 33(2):485–492, 1997.
- [11] P. Barbosa. Three phase power correction circuits for low-cost distributed power systems. *Ph.D. Thesis, Virginia Polytechnic Institute and State University*, 2002.
- [12] G. Gong, M. Lobo Heldwein, U. Drofenik, J. Miniboeck, K. Mino, and J. W. Kolar. Comparative evaluation of three-phase high-power-factors AC-DC converter concepts for applications in future more electric aircrafts. *IEEE Trans. Industrial Electronics*, 52(3):688–695, June 2005.
- [13] J. W. Kolar and F.C. Zach. A novel three-phase three-switch three-level PWM rectifier. *Proc. Power Conversion Conf.*, pages 125–138, 1994.
- [14] M. Liserre. Innovative control techniques of power converters for industrial automation. *Ph.D. Thesis, Politecnico di Bari, Italy*, 2001.
- [15] F. Daniel, R. Chaffai, K. Al-Haddad, and R. Parimelalagan. A new modulation technique for reducing the input current harmonics of a three-phase diode rectifier with capacitive load. *IEEE Trans. Industry Applications*, 33(5):1185–1193, 1997.
- [16] R. L. Steigerwald. Power electronic converter technology. *Proc. the IEEE*, 89(6):890–897, June 2001.
- [17] R. Naik, M. Rastogi, and N. Mohan. Third-harmonic modulated power electronics interface with three-phase utility to provide a regulated DC output and to minimize line-current harmonics. *IEEE Trans. Industry Applications*, 31(3):598–602, 1995.
- [18] P. Pejovic. *Low-harmonic three-phase diode bridge rectifiers based on the current injection principle*. Belgrade: Academic Mind, 2005.
- [19] L. Malesani and P. Tomasin. PWM current control techniques of voltage source converters - a survey. *Proc.Industrial Electronics, Control and Instrumentation Conf.*, pages 670–673, 1993.
- [20] M. P. Kazmierkowski and M. A. Dzieniakowski. Review of current regulation methods for VS-PWM inverters. *Proc.Int. Symposium on Industrial Electronics*, pages 448–456, 1993.
- [21] M. L. Heldwein, T. Nussbaumer, F. Beck, and J. W. Kolar. Novel three-phase CM/DM conducted emission separator. *Proc. Applied Power Electronics Conf.*, pages 797–802, 2005.
- [22] G. Laimer. *Ultra-Compact 10kW/500kHz Three-Phase Rectifier*. Ph.D. Thesis, Swiss Federal Institute of Technology Zurich, 2005.
- [23] S. Round, P. Karutz, M. L. Heldwein, and J. W. Kolar. Towards a 30 kW/liter, three-phase unity power factor rectifier. *Proc. Power Conversion Conf.*, 1:1251–1259, 2007.

- [24] M. P. Kamizierkowski and L. Malesani. Current control techniques for three-phase voltage-source PWM converters: a survey. *IEEE Trans. Industrial Electronics*, 45(5):691–703, Oct. 1998.
- [25] L. Malesani and P. Tenti. Three-phase AC/DC PWM converter with sinusoidal AC currents and minimum filters requirements. *IEEE Trans. Industry Applications*, IA-23(1):71–77, 1987.
- [26] J. W. Dixon, A. B. Kulkarni, and M. Nishimoto. Characteristics of a controlled-current PWM rectifier-inverter link. *IEEE Trans. Industry Applications*, 23:1022–1028, Nov/Dec 1987.
- [27] O. Boon-Teck, J. W. Dixon, A. B. Kulkarni, and M. Nishimoto. An integrated AC-drive system using a controlled-current PWM rectifier/inverter link. *IEEE Trans. Industry Applications*, 3:64–71, Jan. 1988.
- [28] J. Holtz. Pulsewidth modulation - a survey. *IEEE Trans. Industrial Electronics*, 39(5):410–420, Dec. 1992.
- [29] F. Jenni and D. Wüest. *Steuerverfahren für selbstgeführte Stromrichter (trans. Modulation strategies for self commutated converters)*. B. G. Teubner, Stuttgart, 1995.
- [30] J. W. A. Wilson. The forced commutated inverter, a regenerative rectifier. *IEEE Trans. Industry Applications*, 1A-14:335–340, Jul./Aug. 1978.
- [31] L. Malesani, P. Mattavelli, and S. Buso. Robust dead-beat current control for PWM rectifiers and active filters. *IEEE Trans. Industry Applications*, 35(3):613–620, May/June 1999.
- [32] J. Holtz. Pulsewidth modulation for electronic power conversion. *Proc. IEEE*, 82:1194–1214, Dec. 1994.
- [33] A. B. Plunkett. A current controlled PWM transistor inverted drive. *Proc. Industry Applications Society Conf.*, pages 785–792, 1979.
- [34] C. Chiarelli, L. Malesani, S. Pirondini, and P. Tomasini. Single-phase, three-level, constant frequency current hysteresis control for UPS applications. *Proc. European Power Electronics Conf.*, pages 180–185, 1993.
- [35] Q. Yao and D. G. Holmes. A simple, novel method for variable hysteresis band current control of a three-phase inverter with constant switching frequency. *Proc. Industry Applications Society Conf.*, pages 1122–1129, 1993.
- [36] L. Malesani and P. Tenti. A novel hysteresis control method for current-controlled voltage-source PWM inverters with constant modulation frequency. *IEEE Trans. Industry Applications*, 26(1):88–92, Jan./Febr. 1990.
- [37] L. Malesani, P. Tenti, E. Gaio, and R. Piovani. Improved current control technique for VSI PWM inverters with constant modulation frequency

BIBLIOGRAPHY

- and extended modulation range. *IEEE Trans. Industry Applications*, 27(2):365–369, Mar./Apr. 1991.
- [38] L. Malesani, P. Mattavelli, and P. Tomasin. High performance hysteresis modulation technique for active filters. *IEEE Trans. Power Electronics*, 12(5):876–884, Sept. 1997.
- [39] M. P. Kazmierkowski, R. Krishnan, and F. Blaabjerg. *Control in Power Electronics - Selected Problems*. Academic Press, 2002.
- [40] E. H. Ismail and R. W. Erickson. Application of one-cycle control to three-phase high quality resonant rectifier. *Proc. Power Electronics Specialists Conf.*, pages 1183–1190, 1995.
- [41] M. Malinowski, M. P. Kazmierkowski, S. Hansen, F. Blaabjerg, and G. D. Marques. Virtual-flux-based direct power control of three-phase PWM rectifiers. *IEEE Trans. Industry Applications*, 24(7):1019–1027, Jul./Aug. 2001.
- [42] M. Malinowski, M. Jasinski, and M. P. Kazmierkowski. Simple direct power control of three-phase PWM rectifier using space vectors (DPC-SVM). *IEEE Trans. Industrial Electronics*, 51(2):447–454, Apr. 2004.
- [43] M. Malinowski and M. P. Kazmierkowski. Control of three-phase PWM rectifiers. *Control in Power Electronics - Book Chapter*, pages 419–459, July 2002.
- [44] J. Holtz and S. Stadtfeld. A predictive controller for the stator current vector of ac machines fed from a switched voltage source. *Proc. International Power Electronics Conf.*, pages 1665–1675, 1983.
- [45] D. Wüest and F. Jenni. Space vector based current control schemes for voltage source inverters. *Proc. Power Electronics Specialists Conf.*, pages 986–992, 1993.
- [46] E. H. Ismail and R. W. Erickson. A single transistor three-phase resonant switch for high quality rectification. *Proc. Power Electronics Specialists Conf.*, pages 1341–1351, 1992.
- [47] E. H. Ismail and R. W. Erickson. A new class of low cost three phase high quality rectifiers with zero-voltage switching. *Proc. Applied Power Electronics Conf.*, pages 182–189, 1993.
- [48] M.H. Kheraluwala and D. M. Divan. Optimal discrete pulse modulation waveforms for resonant link inverters. *Proc. Power Electronics Specialists Conf.*, pages 567–574, 1988.
- [49] G. Venkataramanan, D. M. Divan, and T. M. Jahns. Discrete pulse modulation strategies for high-frequency inverter systems. *IEEE Trans. Power Electronics*, 8(3):279–287, July 1993.

- [50] J. W. Kolar, H. Ertl, and F.C. Zach. Analysis of on- and off-line optimized predictive current controllers for pwm converter systems. *IEEE Trans. Power Electronics*, 6(3):451–462, July 1991.
- [51] Y. Xiaojie, L. Yongdong, H. Rixiang, and C. Zhiguang. Predictive current control of three-phase PWM rectifier under the condition of non-ideal source voltage. *Proc. Power Electronics and Drive Systems Conf.*, pages 586–590, 2003.
- [52] R. Wu, S. B. Dewan, and G. R. Slemon. Analysis of a PWM AC to DC voltage source converter under the predicted current control with a fixed switched frequency. *IEEE Trans. Industry Applications*, 27(4):756–764, 1991.
- [53] S. Hiti, D. Borojevic, R. Ambatipudi, R. Zhang, and Y. Jiang. Average current control of three-phase PWM boost rectifier. *Proc. Power Electronics Specialists Conf.*, pages 131–1137, 1995.
- [54] U. Drogenik and J. W. Kolar. Comparison of not synchronized sawtooth carrier and synchronized triangular carrier phase current control for the VIENNA rectifier. *Proc. Symposium Industrial Electronics*, pages 13–19, 1999.
- [55] M. Liserre, A. Dell’Aquila, and F. Blaabjerg. Design and control of a three-phase active rectifier under non-ideal operation conditions. *Proc. Industry Applications Society Conf.*, pages 1181–1188, 2002.
- [56] C. T. Rim, N. S. Choi, G. C. Cho, and G. H. Cho. A complete DC and AC analysis of three-phase controlled-current PWM rectifier using D-Q transformation. *IEEE Trans. Power Electronics*, 9:390–396, July 1994.
- [57] S. Saetieo and D. A. Torrey. Fuzzy logic control of a space vector PWM current regulator for three-phase power converters. *IEEE Trans. Power Electronics*, 13:419–426, May 1998.
- [58] J. W. Dixon and J. M. Contardo. Fuzzy logic control of a space vector PWM current regulator for three-phase power converters. *IEEE Trans. Power Electronics*, 13:419–426, May 1998.
- [59] M. Jasiniski, M. Cichowlas, M. Liserre, and F. Blaabjerg. Fuzzy logic current controller for PWM rectifiers. *Proc. Industrial Electronics Conf.*, pages 1300–1305, 2002.
- [60] A. Dell’Aquila, M. Liserre, C. Cecati, and A. Ometto. A fuzzy logic CC-PWM three-phase AC/DC converter. *Proc. Industry Applications Conf.*, pages 987–992, 2003.
- [61] A. Dell’Aquila, M. Liserre, C. Cecati, and A. Ometto. A fuzzy-logic-based controller for active rectifiers. *IEEE Trans. Industry Applications*, 39:105–112, Jan./Febr. 2003.

BIBLIOGRAPHY

- [62] S. Busquetes-Monge, G. Soremekun, E. Hertz, C. Ragon, J. Zhang, D. Borojevic, Z. Gurdal, D. K. Linder, and M. Arpilliere. Design optimization of a boost power factor correction converter using genetic algorithms. *Proc. Applied Power Electronics Conf.*, pages 1177–1182, 2002.
- [63] A. Dell’Aquila, M. Liserre, and F. Blaabjerg. Genetic-algorithm-based design of the active damping for a LCL-filter three-phase active rectifier. *Proc. Applied Power Electronics Conf.*, pages 234–240, 2003.
- [64] F. Costa, P. Poulichet, F. Mazaleyrat, and E. Labouré. The current sensors in power electronics, a review. *EPE Journal*, 11(1):7–18, Oct 2001.
- [65] D. Y. Qiu, S. C. Yip, H. Shu-Hung Chung, and S. Y. Ron Hui. On the use of current sensors for the control of power converters. *IEEE Tran. Power Electronics*, 18(4):1047–1052, July 2003.
- [66] L. A. Kojovic. Guidelines for current transformers selection for protection systems. *Proc. Power Engineering Society Summer Meeting*, pages 593–598, 2001.
- [67] J. R. Stack, T. G. Habetler, and R. G. Harley. Bearing fault detection via autoregressive stator current modeling. *IEEE Tran. Industry Application*, 40(3):740–747, May-June 2004.
- [68] C. Oates, A. J. Brunett, and C. James. The design of high performance Rogowski coils. *Proc. Power Electronics, Machines and Drives Conf.*, pages 568–573, 2002.
- [69] L. Zhao, J. D. van Wyk, and W. G. Odeendal. Planar embedded pick-up coil sensor for integrated power electronics modules. *Proc. Applied Power Electronics Conf.*, pages 945–951, 2004.
- [70] G. Laimer and J. W. Kolar. Design and experimental analysis of a DC to 1 MHz closed loop magnetoresistive current sensor. *Proc. Applied Power Electronics Conf.*, pages 1288–1292, 2005.
- [71] L. Di Rienzo, R. Bazzocchi, and A. Manara. Circular arrays of magnetic sensors for current measurements. *IEEE Tran. Instrumentation Measurements*, 50(5):1093–1096, Oct. 2001.
- [72] K. Bohnert, H. Braendle, M. G. Brunzel, P. Gabus, and P. Guggenbach. Highly accurate fiber-optic current sensor for the electrowinning industry. *IEEE trans. Ind. Applic.*, 43(1):180–187, Jan./Febr. 2007.
- [73] L. Ghislanzoni and J. A. Carrasco. A DC current transformer for large bandwidth and high common mode rejection. *IEEE Tran. Industrial Electronics*, 46(3):631–636, June 1999.
- [74] LEM. Current sensors. *Available Online: www.lem.com*, 2005.

- [75] E. Favre and W. Teppan. State of the art in current sensing technologies. *Proc. Power Electronics and Intelligent Motion Conf.*, pages 549–554, Nov. 2003.
- [76] C. Xiao, L. Zhao, T. Asada, W. G. Odendaal, and J. D. van Wyk. An overview of integratable current sensors technologies. *Proc. Power Electronics Specialist Conf.*, pages 1252–1257, 2003.
- [77] P. Ripka. Current sensors using magnetic materials. *International Journal of Optoelectronics and Advanced Materials*, 6(2):587–592, June 2004.
- [78] F. Costa, E. Labouré, F. Forest, and C. Gautier. Wide bandwidth, large AC current probe for power electronics and EMI measurements. *IEEE Tran. Industrial Electronics*, 44(4):502–511, Aug. 1997.
- [79] H. G. Sauer. Influence of the dc current on the operating of a current transformer. *Messen+Prüfen/Automatik (in German)*, pages 267–275, June 1975.
- [80] G. Laimer and J. W. Kolar. Wide bandwidth low complexity isolated current sensor to be employed in a 10kW/500kHz three-phase unity power factor PWM rectifier system. *Proc. Power Electronics Specialist Conf.*, pages 1065–1070, 2002.
- [81] J. Pankau, D. Leggate, D. Schlegel, R. Kerkman, and G. Skibiniski. High frequency modelling of current sensors. *IEEE Tran. Industrial Applications*, 35:1374–1382, Nov.-Dec. 1999.
- [82] M. Zhu, D. J. Perreault, V. Caliskan, T. C. Neugebauer, S. Guttowski, and J. G. Kassakian. Design and evaluation of feedforward active ripple filters. *IEEE. Tran. Power Electronics*, 20(2):276–285, March 2005.
- [83] C. Xiao, G. Chen, and W. G. Odendaal. Overview of power loss measurement techniques in power electronics systems. *IEEE Trans. on Industry Applications*, 43(3):657–664, 2007.
- [84] C. T. Pan and T. Y. Chang. An improved hysteresis current controller for reducing switching frequency. *IEEE Trans. Power Electronics*, 9(1):97–104, Jan. 1994.
- [85] J. W. Kolar, U. Drogenik, and F. C. Zach. Space vector based analysis of the variation and control of the neutral point of hysteresis current controlled three-phase/switch/level PWM rectifiers. *Proc. Power Electronics Drive Systems Conf.*, 2:22–33, 1995.
- [86] J. A. Houldsworth and D. A. Grant. The use of harmonic distortion to increase the output voltage of a three phase pwm inverter. *IEEE Trans. Industry Applications*, IA-20(5):1224–1228, Sep./Oct. 1984.

BIBLIOGRAPHY

- [87] S. Ogasawara and H. Akagi. Analysis of variation of neutral point potential in neutral-point-clamped voltage source PWM inverters. *Proc. Industry Applications Conf.*, 2:965–970, 1993.
- [88] L. Dalessandro, U. Drogenik, S. D. Round, and J. W. Kolar. A novel hysteresis current control for three-phase three-level rectifiers. *Proc. Applied Power Electronics Conf.*, 1:501–507, 2005.
- [89] L. Malesani, P. Mattavelli, and P. Tomasin. Improved constant-frequency hysteresis current control of VSI inverters with simple feedforward bandwidth prediction. *IEEE Trans. Industry Application*, 33(5):1194–1202, Sep./Oct. 1997.
- [90] M. Liserre, A. Dell’Aquila, and F. Blaabjerg. An overview of three-phase voltage source active rectifiers interfacing the utility. *Proc. Bologna Power Tech Conf.*, 3:1–7, 2003.
- [91] C. Klumpner, F. Blaabjerg, and P. Thoeegersen. Alternate ASDs: evaluation of the converter topologies suitable for integrated motor drives. *IEEE Ind. Applications Magazine*, 12(2):71–83, 2006.
- [92] W. A. Tabisz, M. Jovanovic, and F. C. Lee. Present and future of distributed power systems. *Proc. Applied Power Electronics Conf.*, pages 11–18, 1992.
- [93] A. Siebert, A. Troderson, and S. Ebner. AC to DC power conversion now and in the future. *IEEE Trans. Industry Applications*, 38(5):934–940, Jul./Aug. 2002.
- [94] G. Gong, M. L. Heldwein, U. Drogenik, J. Miniboeck, K. Mino, and J. W. Kolar. Comparative evaluation of three-phase high-power-factors AC-DC converter concepts for applications in future more electric aircraft. *IEEE Trans. Industrial Electronics*, 52(3):688–695, June 2005.
- [95] Y. Zhao, Y. Li, and T. A. Lipo. Forced commutated three-level boost type rectifier. *IEEE Trans. Industry Applications*, 31(1):155–161, Jan./Febr. 1995.
- [96] N. Celanovic and D. Boroyevich. A comprehensive study of neutral-point voltage balancing problem in three-level neutral-point-clamped voltage source PWM inverters. *IEEE Trans. Power Electronics*, 15(2):242–249, 2000.
- [97] J. Pou, D. Boroyevich, and R. Pintado. New feedforward space-vector PWM method to obtain balanced AC output voltages in a three-level neutral-point-clamped converter. *IEEE Trans. Industrial Electronics*, 49(5):1026–1034, 2002.

- [98] O. Ojo and S. Konduru. A discontinuous carrier-based PWM modulation method for the control of neutral point voltage of three-phase three-level diode clamped converters. *Proc. Power Electronics Specialists Conf.*, 2:1652–1658, 2005.
- [99] S. Busquets Monge, S. Somavilla, J. Bordonau, and D. Boroyevich. Capacitor voltage balance for the neutral-point-clamped converter using the virtual space vector concept with optimized spectral performance. *IEEE Trans. Power Electronics*, 22(4):1128–1135, 2007.
- [100] D. Zhou and D. G. Rouaud. Experimental comparisons of space vector neutral point balancing strategies for three-level topology. *IEEE Trans. Power Electronics*, 16(6):872–879, 2001.
- [101] F. Springmeier and J. K. Steinke. Control of the DC link neutral potential of a three-level GTO inverter as a part of the Direct Self Control. *Proc. Power Electronics and Motion Control Conf.*, pages 479–483, 1990.
- [102] O. Ojo. The generalized discontinuous PWM scheme for three-phase voltage source inverters. *IEEE Trans. Industry Applications*, 51(6):1280–1289, 2004.
- [103] T. Brückner and D. G. Holmes. Optimal pulse-width for three-level inverters. *IEEE Trans. Power Electronics*, 20(1):82–89, 2005.
- [104] B. K. Bose. An adaptive hysteresis-band current control technique of a voltage fed PWM inverter for machine drive system. *IEEE Trans. Industrial Electronics*, 27(5):402–408, 1990.
- [105] W. McMurray. Modulation of the chopping frequency in DC coppers and PWM inverters having current hysteresis controllers. *Proc. Power Electronics Spec. Conf.*, pages 295–299, 1983.
- [106] D. M. Brod and D. W. Novotny. Current control of VSI-PWM inverters. *Proc. Industry Application Society Conf.*, pages 418–425, 1984.
- [107] I. Nagy. Improved current controller for PWM inverter drivers with the background of chaotic dynamics. *Proc. Internat. Conf. on Industrial Electronics Control and Instrumentation.*, pages 561–566, 1994.
- [108] A. M. Hava, R. J. Kerkman, and T. A. Lipo. A high-performance generalized discontinuous PWM algorithm. *IEEE Trans. Industry Applications*, 34(5):1059–1071, 1998.
- [109] C. B. Jacobina, A. M. Lima, and E. R. da Silva. Digital scalar pulse-width modulation: a simple approach to introduce non-sinusoidal modulation waveforms. *IEEE Trans. Power Electronics*, 16(3):351–359, 2001.
- [110] B. P. McGrath, D. G. Holmes, and T. A. Lipo. Optimized space vector switching sequences for multilevel inverters. *IEEE Trans. Power Electronics*, 18(6):1293–1301, 2003.

BIBLIOGRAPHY

- [111] J. W. Kolar, H. Ertl, and F. C. Zach. Influence of the modulation method on the conduction and switching losses of a PWM converter system. *IEEE Trans. Industry Applications*, (6):1063–1075, 1991.
- [112] A. M. Trzynadlowski and S. Legowski. Minimum-loss vector PWM strategy for three-phase inverters. *IEEE Trans. Power Electronics*, 9(1):26–34, 1994.
- [113] D. Chung and S. Sul. Minimum-loss strategy for three-phase PWM rectifier. *IEEE Trans. Industrial Electronics*, 46(3):517–526, 1999.
- [114] M. Depenbrock. Pulse width control of a three-phase inverter with non-sinusoidal phase voltages. *Proc. ISPC Conf.*, pages 399–403, 1977.
- [115] A. M. Hava, R. J. Kerkman, and T. A. Lipo. Carrier-based PWM-VSI overmodulation strategies: Analysis, comparison and design. *IEEE Trans. Power Electronics*, 13(4):674–689, 1998.
- [116] L. Asiminoaei, P. Rodriguez, and F. Blaabjerg. A new generalized discontinuous PWM strategy for active power filters. *Proc. Applied Power Electronics Conf.*, pages 315–321, 2007.
- [117] J. W. Kolar, H. Ertl, and F. Zach. Design and experimental investigation of a three-phase high power density PWM rectifier employing a novel semiconductor module. *Proc. Applied Power Electronics Conf.*, 2:514–523, 1996.
- [118] N. Celanovic and D. Boroyevich. A comprehensive study of neutral-point voltage balancing problem in three-level neutral-point-clamped voltage source PWM inverters. *IEEE Trans. Power Electronics*, 15(2):242–249, 2000.
- [119] M. Marchesoni, P. Segarich, and E. Soressi. A new control strategy for neutral-point-clamped active rectifiers. *IEEE Trans. Industrial Electronics*, 52(2):462–470, 2005.
- [120] J. W. Kolar and U. Drogenik. A new switching loss reduced discontinuous scheme for a unidirectional three-phase/switch/level boost-type PWM (Vienna) rectifier. *Proc. Int. Telecommunication Energy Conf.*, pages 490–499, 1999.
- [121] F. Wang. Sine-triangle versus space-vector modulation for three-level PWM voltage-source inverters. *IEEE Trans. Industry Applications*, 38(2):500–506, 2002.
- [122] K. Zhou and D. Wang. Relationship between space-vector modulation and three-phase carrier based PWM: a comprehensive analysis. *IEEE Trans. Industrial Electronics*, 49(1):186–196, 2002.

- [123] G. Laimer and J. W. Kolar. Wide-bandwidth low-complexity isolated current sensor to be employed in a 10 kW/500 kHz three-phase unity power factor PWM rectifier system. *Proc. Power Electronics Specialist Conf.*, pages 1065–1070, 2002.
- [124] C. Graziano, R. De Leo, V. M. Primiani, S. Pennesi, and P. Russo. Wide-band characterization of current probes. *IEEE Tran. Electromagnetic Compatibility*, 45(4):616–625, Nov. 2003.
- [125] C. R. Paul. *Electromagnetics for Engineers with Applications*. New Jersey: Wiley, 2004.
- [126] J. L. Thompson and S. A. Stigant. Overvoltages in transformers due to the self-capacity of the windings. *Elect. Rev.*, 76:25–37, 1915.
- [127] R. W. Buntenbach. Analogs between magnetic and electrical circuits. *Electronics Products*, pages 108–113, Oct. 1969.
- [128] A. E. Fitzgerald, C Kingsley, and S. D. Umans. *Electric Machinery*. McGraw Hill, 2003.
- [129] E. C. Snelling. *Soft Ferrites: Properties and Applications*. London: Butterworth & Co, 2nd edition, 1988.
- [130] G. R. Skutt. High frequency dimensional effects in ferrite-core magnetic devices. *Ph.D. Thesis, Virginia Polytechnic Institute and State University, Blacksburg, Virginia*, Oct. 1996.
- [131] F. G. Brockman, P. H. Dowling, and W. G. Steneck. Dimensional effects resulting from a high dielectric constant found in a ferromagnetic ferrite. *Physical Review*, 77(1):85–93, 1950.
- [132] EPCOS, Ferrites. *Datasheets and Accessories*, 2005. Available online: www.epcos.com.
- [133] R. Prieto, V. Bataller, J. A. Cobos, and J. Uceda. Influence of the winding strategy in toroidal transformers. *Proc. of the Industrial Electronics Society Conf.*, 1:359–364, Aug.-Sep. 1998.
- [134] P. N. Murgatroyd, A. K. Y. Chu, G. K. Richardson, D. West, G. A. Yearley, and A. J. Spencer. Making Rogowski coils. *Meas. Sci. Technol. (2) (Design Note)*, pages 1218–1219, 1991.
- [135] R. L. Stoll. Method of measuring alternating currents without disturbing the conducting circuit. *IEE Proc.*, 122(10):1166–1167, Oct 1975.
- [136] D. G. Pellinen and P. W. Spence. A nanosecond risetime megampere current monitor. *The Review of Scientific Instruments*, 42(11):1699–1701, Sep. 1971.
- [137] R. W. Buntenbach. Analogs between magnetic and electrical circuits. *Electronic Products*, pages 108–113, Oct. 1969.

BIBLIOGRAPHY

- [138] P. G. Blanken and J. J. L. M. Van Vlerken. Modeling of electromagnetic systems. *IEEE Tran. Magnetics*, 27(6):4509–4515, Nov. 1991.
- [139] J. J. L. M. Van Vlerken and P. G. Blanken. Lumped modeling of rotary transformers, heads and electronics for helical scan. *IEEE Tran. Magnetics*, 31(2):1050–1055, March 1995.
- [140] B. Cogitore, J. P. Keradec, and J. Barbaroux. The two-winding transformer: an experimental method to obtain a wide frequency range equivalent circuit. *IEEE Tran. Instrumentation and Measurement*, 43(2):364–371, Apr. 1994.
- [141] A. Schellmanns, P. Fouassier, J. P. Keradec, and J. L. Schanen. Equivalent circuits for transformers based on one-dimensional propagation: Accounting for multilayer structure of windings and ferrite losses. *IEEE Tran. Magnetics*, 36(5):3778–3784, Sep. 2000.
- [142] W. T. Duerdoth. Equivalent capacitance of transformer windings. *Wireless Engineer*, 23:161–167, June 1946.
- [143] P. Han, G. R. Skutt, J. Zhang, and F. C. Lee. Finite element method for ferrite coreless calculation. *Proc. Applied Power Electr. Conf.*, 1:348–353, March 1995.
- [144] G. R. Skutt and F. C. Lee. Characterization of dimensional effects in ferrite core magnetic devices. *Proc. Power Electr. Specialists Conf.*, 2:1435–1440, June 1997.
- [145] M. Urling, V. A. Niemela, G. R. Skutt, and T. G. Wilson. Characterizing high frequency effects in transformer windings - a guide to several significant articles. *Proc. Power Electronics Specialists Conf.*, pages 373–385, 1989.
- [146] Xi Nan and C. R. Sullivan. An improved calculation of proximity-effect loss in high-frequency windings of round conductors. *Proc. Power Electronics Specialists Conf.*, 2:853–860, 2003.
- [147] M. K. Kazimierczuk, G. Sancineto, G. Grandi, U. Reggiani, and A. Maszarini. High-frequency small-signal model of ferrite core inductors. *IEEE Trans. Magn.*, 4185-4191(5):35, Sept. 1999.
- [148] R. Prietro, J. A. Cobos, O. García, P. Alou, and J. Uceda. Study of 3-d magnetic components by means of "double 2-d" methodology. *IEEE Trans. Industrial Electronics*, 50(1):183–192, Febr. 2003.
- [149] P. L. Dowell. Effects of eddy currents in transformer windings. *Proc. IEE*, 113(8):1387–1394, Aug. 1966.
- [150] E. Bennett and S. C. Larson. Effective resistance to alternating currents of multilayers windings. *AIEE Trans.*, 59:1010–1017, 1940.

- [151] T. H. Long. Eddy-current resistance of multilayer coils. *AIEE Trans.*, 64:712–718, Oct. 1945.
- [152] J. A. Ferreira. Improved analytical modeling of conductive losses in magnetic components. *IEEE Trans. Power Electronics*, 9(1):127–131, Jan. 1994.
- [153] F. Robert, P. Mathys, and J-P. Schauwers. The layer copper factor, although widely used and useful, has no theoretical base. in *Proc. Power Electronics Specialists Conf.*, 3:1633–1638, 2000.
- [154] W. G. Hurley, E. Gath, and J. G. Breslin. Optimizing the ac resistance of multilayer transformer windings with arbitrary current waveforms. *IEEE Trans. Power Electronics*, 15(2):369–376, March 2000.
- [155] B. Carsten. High frequency conductor losses in switchmode magnetics. *Proc. High Frequency Power Conversion Conf., Intertec Communications Inc., Ventura, CA, and Proc. Power Conversion Intell. Motion Conf., Germany*, pages 161–182, May and Nov. 1986.
- [156] J-P. Vandelac and P. D. Ziogas. A novel approach for minimizing high-frequency transformer copper losses. *IEEE Trans. Power Electronics*, 3(3):266–277, July 1988.
- [157] M. P. Sayani, G. R. Skutt, and P. S. Venkatraman. Electrical and thermal performance of pwb (printed wiring board) transformers. *Proc. Applied Power Electronics Conf.*, pages 533–542, March 1991.
- [158] J-P. Keradec, E. Laveuve, and J. Roudet. Multipolar developments of vector potential for parallel wires. application to the study of eddy currents effects in transformer windings. *IEEE Trans. Magn.*, 27(5):4242–4245, Sept. 1991.
- [159] W. G. Odendaal. A generic approach for the modelling of high power density magnetic components. *Ph. D. Thesis, Rand Afrikaans University*, May 1997.
- [160] P. Wallmeier. Improved analytical modeling of conductive losses in gapped high frequency inductors. *IEEE Trans. Industry Application*, 37(4):1045–1054, July/August 2001.
- [161] F. Robert, P. Mathys, and J-P. Schauwers. A closed-form formula for 2-d ohmic losses calculation in smps transformer foils. *IEEE Trans. Power Electronics*, 16(3):437–444, May 2001.
- [162] J. Lammeraner and M. Štafl. Eddy currents. *Illiffe Books, London*, 1966.
- [163] R. L. Stoll. The analysis of eddy currents. *Clarendore Press, Oxford*, 1974.
- [164] L.D. Landau, E.M. Lifshitz, and L.P. Pitaevskii. Electrodynamics of continuous media, second edition. *London: Pergamon Press*, 8, 1984.

BIBLIOGRAPHY

- [165] P. Wallmeier, P. Ide, J. Kunze, and B. Margaritis. Effects in magnetic components for switched mode applications in the MHz range. *Proc. of the Applied Power Electronics Conf. and Exposition*, 2:964–970, 2004.
- [166] W. Lenz. Calculation of the free period of a single layer coil. *Annalen der Physik*, 43:749–97, 1914.
- [167] D. Maurice and R. H. Minns. Very-wide band radio frequency transformers. *Wireless engineers*, 24:169–177, 209–216, June, July 1947.
- [168] R. Feldkeller. *Theory of Coils and Transformers*. Stuttgart: Hirzel Verlag, 1971. In German.
- [169] P. A. Abetti. Survey and classification of published data on the surge performance of transformers and rotating machines. *AIEE Trans.*, 77:1403–1414, Dec. 1958.
- [170] H. Zuhrt. Simple approximate formulas for the self capacitance of multi-layer coils. *Elekrotechnische Zeitschrift*, 55:662–665, July 1934. In German.
- [171] R. G. Meldhurst. High-frequency resistance and self-capacitance of single layers solenoids. *Wireless Engineer*, 24:35–43, Feb. 1947.
- [172] P. A. Abetti and F. J. Maginiss. Natural frequencies of coils and windings determined by equivalent circuit. *AIEE Trans.*, I:495–504, June 1953.
- [173] R. C. Degeneff. A general method for determining resonances in transformer windings. *IEEE Trans. Power App. Syst.*, PAS-96(2):423–430, Mar.-Apr. 1977.
- [174] L. F. Casey, A. F. Goldberg, and M. F. Schlecht. Issues regarding the capacitance of 1-10 MHz transformers. *Proc. Applied Power Electronics Conf. and Exposition*, pages 352–359, 1-5 Feb. 1988.
- [175] S. Wang, F. C. Lee, and W. G. Odendaal. Single layer iron powder core inductor model and its effects on boost PFC EMI noise. pages 874–852, 2003.
- [176] L. Zhao, J. T. Strydom, and J. D. van Wyk. Wide band modelling of integrated power passive structures: the series resonator. pages 1283–1288, 2002.
- [177] A. Massarini and M. K. Kazimierczuk. Self-capacitance of inductors. *IEEE Trans. Power Electronics*, 12(4):671– 676, July 1997.
- [178] T. Duerbaum and G. Sauerlander. Energy based capacitance model for magnetic devices. 1:109–115, 2001.
- [179] B. Ackermann, A. Lewalter, and E. Waffenschmidt. Analytical modelling of winding capacitances and dielectric losses for planar transformers. 1:2–9, 2004.

- [180] T. Duerbaum. Capacitance model for magnetic devices. 3:1651–1656, 2000.
- [181] H. Y. Lu, J.G. Zhu, S. Y. R. Hui, and V. S Ramseden. Measurement and Modeling of stray capacitances in high frequency transformers. *Proc.Power Electronics specialists Conf.*, pages 763–769, 1999.
- [182] H. Y. Lu, J. G. Zhu, and S. Y. R. Hui. Experimental determination of stray capacitances in high-frequency transformers. *IEEE Trans. Power Electronics*, 18(5):1105–1112, Sept. 2003.
- [183] F. Cavalcante and J. W. Kolar. Design of a 5 kW high-output voltage series-parallel resonant DC-DC converter. *Proc. Power Electronics Specialists Conf.*, pages 1807–1814, 2003.
- [184] F. Cavalcante and J. W. Kolar. Small-signal model of a 5 kW high-output voltage capacitive-loaded series-parallel resonant DC-DC converter. *Proc. Power Electronics Specialists Conf.*, pages 1807–1814, 2005.
- [185] S.D. Johnson, A.F. Witulski, and R.W Erickson. Comparison of resonant topologies in high-voltage DC applications. *IEEE Transactions on Aerospace and Electronic Systems*, 24(3):263–274, May 1988.
- [186] J. Sun, M. Nakaoka, and H. Takano. High-voltage transformer parasitic resonant PWM DC-DC high power converters and their performance evaluations. *Proc. Int. Symp. Industr. Electronics*, pages 572–577, 1997.
- [187] B. Tala-Ighil, J.-M. Noybe-Yome, P. Gouton, and C. Glaize. On the utilization of the transformers parasitic capacitances as a resonant element in high-voltage converters operating above resonance with variable frequency. *IEE Colloquium on Static Power Conversion*, 3:1–5, 1992.
- [188] J.A. Collins. An accurate method for modelling the transformer winding capacitances. pages 1094–1099, 1990.
- [189] M. Albach and J. Lauter. The winding capacitance of solid and Litz wires. pages 1–5, 1997.
- [190] J. Koch. Berechnung der Kapazität von Spulen, insbesondere in Schalenkernen. *Valvo Berichte*, 14(3):99–119, 1968.
- [191] L. Dalessandro, W. G. Odendaal, and J. W. Kolar. HF characterization and non linear modelling of a gapped toroidal magnetic structure. *IEEE Trans. Power Electronics*, 21(5):1167–1175, Sept. 2006.
- [192] Agilent impedance analyzer.
- [193] F. G. Brockmann, P. H. Dowling, and W. G. Steneck. Dimensional effects resulting from a high dielectric constant found in a ferromagnetic ferrite. *Physical Review*, 77(1):85–93, 1950.

BIBLIOGRAPHY

- [194] G. Grandi, M. K. Kazimierczuk, A. Massarini, and U. Reggiani. Stray capacitances of single-layer solenoid air-core inductors. *IEEE Trans. on Industry Applications*, 35(5):1162–1168, Sept./Oct. 1999.
- [195] E. Labouré, F. Costa, and F. Forest. Current measurement in static converters and realization of a high frequency passive current probe. pages 478–483, 1993.
- [196] M. Zahn. *Electromagnetic Field Theory - A problem solving approach*. Krieger Publisher, 2003.
- [197] E. Laveuve, J.-P. Keradec, and M. Bensoam. Electrostatic of wound components: analytical results, simulation and experimental validation of the parasitic capacitance. *Proc. Industry Applications Society Annual Meeting*, 2:1469–1475, Oct. 1991.
- [198] R. Chen, J. D. van Wyk, S. Wang, and W. G. Odendaal. Application of structural winding capacitance cancellation for integrated EMI filters by embedding conductive layers. pages 2679–2686, 2004.
- [199] N. Karrer and P. Hofer-Noser. A new current measuring principle for power electronics applications. *Proc. Information Storage and Processing Conf.*, pages 279–282, 1999.
- [200] L. Ghislanzoni. Magnetic coupled current sensing techniques for spacecraft systems. *Proc. European Space Power Conf.*, pages 323–327, 1989.
- [201] K. Unser. Beam current transformers with DC to 200 MHz range. *IEEE Tran. Nuclear Science*, (16):934–938, June. 1969.
- [202] J. Weber. *Oscilloscope probe circuits*. Tektronix Inc., 1969.
- [203] S. Ogasawara, K. Murata, and H. Akagi. A digital current sensor for PWM inverters. *Proc. the Industrial Application Society Conf.*, pages 949–955, 1992.
- [204] N. Karrer. *Hochdynamische Erfassung elektrischer Ströme über stossfrei verkoppelte Wandler*. Nr. 946, Reihe 8, VDI, Düsseldorf, 2002.
- [205] E. Labouré, F. Costa, and F. Forest. Current measurement in static converters and realization of a high frequency passive current probe. *Proc. European Power Electronics Conf.*, pages 478–483, 1993.
- [206] L. Serpa, Round S., and J.W. Kolar. A virtual-flux decoupling hysteresis current controller for mains connected inverter systems. *IEEE Trans. on Power Electronics*, 22(5):1766–1777, Sept. 2007.
- [207] L. Serpa and J.W. Kolar. Extendend virtual-flux decoupling hysteresis controller for mains connected three-level npc inverter systems. *Proc. Brazilian Power Electronics Conf.*, pages 1–7, Sept. 2007.

Curriculum Vitæ

Luca Dalessandro was born in Bari, Italy, on April 29, 1978.

From 1996 to 2001 he studied Electrical Engineering at the Politecnico di Bari, Italy where he received his M.Sc. Degree with first class honors and and praise of the jury.

His thesis on "Continuum Electromechanics" was supervised by Prof. Dr. Antonio DeSimone (currently ISAS, Trieste, Italy) and refereed by Prof. Dr. Salvatore Marzano (Rector of the Politecnico di Bari) and Prof. Dr. Francesco Vacca. From 2001 to 2002 he was a Researcher at the Max-Planck-Institute for Mathematics in the Sciences (MPI-MIS) in Leipzig, Germany, where he focused his research on continuum mechanics, electromechanical systems modeling and control and finite-element methods.

From the Fall 2002 to the Summer 2006 he held the position of Research and Teaching Assistant at the Swiss Federal Institute of Technology (ETH) in Zurich, Switzerland, with the Power Electronic Systems Laboratory (PES). In July 2006, under a post-doctoral fellowship grant provided by the Industry, he joined the National Science Foundation Engineering Research Center (NSF-ERC) for Power Electronics Systems (CPES) at the Virginia Polytechnic Institute and State University, Blacksburg, VA.

In Fall 2006 he was appointed Adjunct Professor at the Bradley Department of Electrical and Computer Engineering at the Virginia Tech, where he taught an advanced course on Electromagnetic Fields (ECE 3106). Since the Fall 2007 he is an Associate Researcher at the Power Systems and High-Voltage Technology Institute (EEH) of the ETH.

His research interests include all disciplines of electric power engineering, in particular power electronics, electric machines and drives, applied electrodynamics, electromagnetic compatibility, continuum electromechanics, high-voltage technology, power systems analysis and electrical measurements.

He is the recipient of several awards and fellowships and is listed in *Who's Who in Science and Engineering*. In particular, in 1994, he was awarded by UNESCO-Pineider in the prestigious "Salone dei Cinquecento", Palazzo Vec-

chio, Florence, for his graphical contribution to the International Year of Family.

He has been a visitor and an invited lecturer at several recognized Companies and Institutions including the European Center for Nuclear Research (CERN), Switzerland, the Laboratory for Electromagnetic and Electronic Systems (LEES) at the Massachusetts Institute of Technology (MIT), Cambridge, MA, the ABB Corporate Research Center, Baden-Dättwil, Switzerland, TOSHIBA, Japan, and the National Japanese Institute for Advanced Industrial Science and Technology (AIST), Japan.

In 2007 he served as an External Scientific Advisor the Swiss Embassy to Italy. In November 2007, after a designation of the Rectorate, he represented the ETH Zurich at the International Economical Conference "The Meeting 2007".

He serves as a Reviewer for numerous International Journals and Conferences in his fields of interest, in particular for the IEEE Transactions on Power Electronics, IEEE Transactions on Industry Applications and IEEE Transaction on Industrial Electronics.

He is a IEEE Member and a Registered Professional Engineer in Italy.

He speaks fluently English, German and Italian and he is proficient in French, Spanish and Portuguese. He is an University sport athlete, for the disciplines rowing and track & field and a Senior Member of the Italian University Sport Center (CUSI).

(Update: November 2007)